Development of Multiphase and Multiscale Mathematical Models for Thermal Spray Process

Spyros Kamnis

A Thesis submitted for the degree of Doctor of Philosophy

School of Engineering and Applied Science

Aston University

October 2007

Supervisor: Dr Sai Gu

Abstract

High velocity oxyfuel (HVOF) thermal spraying is one of the most significant developments in the thermal spray industry since the development of the original plasma spray technique. The aim of this thesis is to provide the thermal spray community, computational approaches and view points in an effort to improve the technology and advance the quality and efficiency of the HVOF thermal spray systems. The first investigation in this thesis deals with the combustion and discrete particle models within the general purpose commercial CFD code FLUENT to solve the combustion of kerosene and couple the motion of fuel droplets with the gas flow dynamics in a Lagrangian fashion. The effects of liquid fuel droplets on the thermodynamics of the combusting gas flow are examined thoroughly showing that combustion process of kerosene is dependent on the initial fuel droplet sizes. The second analysis in this thesis cope with the full water cooling numerical model, which can assist on thermal performance optimisation or to determine the best method for heat removal without the cost of building physical prototypes. The numerical results indicate that the water flow rate and direction has noticeable influence on the cooling efficiency but no noticeable effect on the gas flow dynamics within the thermal spraying gun. The third investigation in this thesis deals with the development and implementation of discrete phase particle models. The improvement of the existing models, including the detailed phase change methods and predictions of oxide layer growth on the surface of metal particles, is presented allowing for better process optimization. The results indicate that most powder particles are not melted upon hitting the substrate to be coated. The oxidation model confirms that HVOF guns can produce metallic coating with low oxidation within the typical standing-off distance about 30 cm. Physical properties such as porosity, microstructure, surface roughness and adhesion strength of coatings produced by droplet deposition in a thermal spray process are determined to a large extent by the dynamics of deformation and solidification of the particles impinging on the substrate. Therefore, is one of the objectives of this study to present a complete numerical model of droplet impact and solidification. The modelling results show that solidification of droplets is significantly affected by the thermal contact resistance/substrate surface roughness.

Contents

List of Figures

List of Tables

Aknowledgement

I would like to take this opportunity to express my thanks and appreciations to my supervisor, Dr Sai Gu, for his guidance, encouragement, financial support and for providing me with first class resources.

I would like to express my deep thanks to my colleague and good friends Nicola Zeoli and Kosta Papadiki for their useful comments and discussions throughout the three (and a half) years leading to the submission of this thesis.

I would also like to extend my special acknowledgment to Maria and my parents Helen and Christopher for their interest and support throughout my years as a student. My Father, Christopher, in the first place is the person who put the fundament my learning character, showing me the joy of engineering ever since I was a child. My Mother, Helen, is the one who sincerely raised me with her caring and gently love.

One more practical note, I'm indebted to the Engineering and Physical Sciences Research Council and Aston University for their continued funding of my postgraduate studies.

Nomenclature

Section 4.1

textitGeneral symbols

A constant in eddy dissipation model = 4.0
A_0 constant in realizable $\kappa - \varepsilon$ model = 4.04
A_s Coefficient in realizable $\kappa - \varepsilon$ model
B constant in eddy dissipation model = 0.5
C_1 constant for the linear pressure-strain model = 1.8
C_2 constant for the linear pressure-strain model = 0.6
$C_{1\varepsilon}$ constant for the turbulent dissipation of energy = 1.44
$C_{2\varepsilon}$ constant for the turbulent dissipation of energy = 1.92
C_μ coefficient for turbulent viscosity
c_p specific heat capacity (J/KgK)
E enthalpy (J/Kg)
G generation of turbulence energy (Kg/ms)
K thermal conductivity (W/mK)
k kinetic energy (m^2/s^2)
$M_{\omega,j}$ molecular weight of species j
$M_{\omega,R}$ molecular weight of species i
N number of chemical species in the system
p pressure (Pa)
$R_{i,r}$ net rate of production of species i due to reaction r
S source term
T temperature (K)
U mean velocity (m/s)
u velocity (m/s)
$v_{j,r}$ stoichiometric coefficient for product j in reaction r
$v_{i,r}$ stoichiometric coefficient for reactant i in reaction r

$v_{R,r}$ stoichiometric coefficient for a particular reactant R in reaction r
Y_M contribution of the fluctuating dilatation to the overall dissipation rate (Kg/ms^2)
Y_P mass fraction of product P
Y_R mass fraction of a particular reactant, R

Greek symbols

δ Kronecker symbol
ε turbulence dissipation rate (m^2/s^3)
μ viscosity (Kg/ms)
ρ density (Kg/m^3)
σ Prandtl number
τ deviatoric stress tensor

Subscripts

eff effective value
h heat source for the conservation of heat
i, j, l co-ordinate indices
k kinetic energy
t turbulent context
ε turbulence dissipation rate

Section 4.2

General symbols

A constant in eddy dissipation model = 4.0
A_0 constant in realizable $\kappa - \varepsilon$ model = 4.04
A_p surface area of the droplet (m^2)
A_s coefficient in realizable $\kappa - \varepsilon$ model
B constant in eddy dissipation model = 0.5
C_D drag coefficient
C_1 constant for the linear pressure-strain model = 1.8
C_2 constant for the linear pressure-strain model = 0.6
$C_{i,s}$ vapor concentration at the droplet surface $(Kg/molm^3)$
$C_{i,\infty}$ vapor concentration at the bulk gas $(Kg/molm^3)$

$C_{1\varepsilon}$ constant for the turbulent dissipation of energy = 1.44

$C_{2\varepsilon}$ constant for the turbulent dissipation of energy = 1.92

C_{μ} coefficient for turbulent viscosity

c_p specific heat capacity (J/KgK)

$D_{i,m}$ diffusion coefficient of vapor in the bulk (m^2/s)

d diameter (m)

d_p particle diameter (m)

E enthalpy (J/Kg)

F_D drag force per unit particle (N)

F_x additional acceleration (N)

G_k generation of turbulence energy due to mean velocity gradients (Kg/ms^2)

G_b generation of turbulence energy due to buoyancy (Kg/ms^2)

g_x x component of gravitational acceleration (m^2/s)

h convective heat transfer coefficient (W/m^2K)

K thermal conductivity (W/mK)

K_c mass transfer coefficient (m/s)

$K_{\propto}$ thermal conductivity of the continous phase (W/mK)

k kinetic energy (m^2/s^2)

$M_{w,i}$ molecular weight of species i

$M_{\omega,i}$ molecular weight of reactant i

$M_{\omega,j}$ molecular weight of product j

$M_{\omega,R}$ molecular weight of reactant R

m_p mass of particle (Kg)

N number of chemical species in the system

N_i molar flux of vapour ($Kgmol/m^2s$)

Nu Nussel number

p pressure (Pa)

p_{op} operating pressure (Pa)

p_{sat} saturated pressure (Pa)

Pr Prandtl number

Re relative Reynolds number

Re_d Reynolds number based on particle diameter

$R_{i,r}$ net rate of production of species i due to reaction r

S source term

S_c Schmit number

s path of particle

T temperature (K)

T_L Langrangian integral time

T_∞ local temperature of the continous phase (K)

t time (s)

U mean velocity (m/s)

u velocity (m/s)

$v_{j,r}$ stoichiometric coefficient for product j in reaction r

$v_{i,r}$ stoichiometric coefficient for reactant i in reaction r

$v_{R,r}$ stoichiometric coefficient for reactant R in reaction r

Y_M contribution of the fluctuating dilatation to the overall dissipation rate (Kg/ms^2)

Y_P mass fraction of product P

Y_R mass fraction of a particular reactant, R

X_i spatial co-ordinate

Greek symbols

δ Kronecker symbol

ε turbulence dissipation rate (m^2/s^3)

ε_p particle emissivity

Θ_R radiation temperature

μ viscosity (Kg/ms)

ρ density (Kg/m^3)

σ Prandtl number

τ deviatoric stress tensor

ν molecular kinematic viscosity

ϕ shape factor

Subscripts

eff effective value in reference to the addition of turbulent and non-turbulent contribution of a variable

i, j, l co-ordinate indices

k kinetic energy

p particle

t turbulent context

ε turbulence dissipation rate

Section 4.3

General Symbols

C_μ coefficient for turbulent viscosity
c_p specific heat capacity (J/KgK)
E enthalpy (J)
h sensible enthalpy (J)
k thermal conductivity (W/mK)
k_P turbulence kinetic energy at point (P)
k_s thermal conductivity of the solid ((W/mK)
Δn distance between wall surface and the solid cell center (m)
P stress production term for the Reynolds stress model
Pr molecular Prandtl number
Pr_t turbulent Prandtl number
$\dot{q}$ heat flux (W/m^2)
T temperature (K)
T^* logarithmic mean temperature
T_P temperature at the cell adjacent to wall (K)
T_w temperature at the wall (K)
t time (s)
U_c mean velocity magnitude at $y^* = y_T^*$
U_P mean velocity of the fluid near wall
y^* non-dimensional viscous sublayer thickness
y_T^* non-dimensional thermal sublayer thickness
y_P distance to the wall
Greek symbols

μ dynamic viscosity of the fluid (Ns/m^2)
ρ density $(Kg/m^3$)
$\vec{v}$ velocity vector (m/s)

Section 5.3

General Symbols

A_p particle area (m^2)

Bi Biot number
c_p specific heat capacity (J/KgK)
h heat transfer coefficient (W/m^2K)
h_{se} sensible enthalpy (J)
H total heat (J)
ΔH latent heat content
k thermal conductivity (W/mK)
k_p particle thermal conductivity W/mK
L latent heat (J/Kg)
r radial distance (m)
r_0 particle radius (m)
Ste Stefan number
S_h enthalpy source term
t time (s)
T_{liquid} liquidius temperature (K)
T_{solid} freezing temperature (K)
$T_{surface}$ particle surface temperature (K)
T_{ref} reference ambient temperature (K)
T_∞ ambient temperature (K)
T dimensionless temperature
$T_G$temperature (K)
u velocity (m^2/s)
x radial phase front position within the particle (m)
β liquid fraction
ρ density (kg/m^3)
ρ_p particle density (kg/m^3)
τ dimensionless time (s)

Section 5.4

General Symbols

A0 model constant (A/s)
CD drag coefficient
Cp specific heat capacity (J/KgK)
E energy (J/Kg)
f solid fraction

g gravity acceleration (m/s^2)
h convective heat transfer coefficient (W/m^2K)
H total heat transfer coefficient (W/m^2K)
H_sf latent heat (J/Kg)
H_ox heat of oxidation (J/Kg)
Nu non-dimensional Nusselt number
u fluid velocity (m/s)
p pressure (Pa)
Q model constant (eV)
K0 model constant $(eV/torr)$
k_s thermal conductivity of particle (W/mK)
k_ox thermal conductivity of oxide layer (W/mK)
k_b Boltzman constant;
k_g thermal conductivity of gas (W/mK)
K_eff effective thermal conductivity (W/mK)
P_O2 Partial pressure of O2 $(Torr)$
Pr Prandtl number;
R particle radius (m)
Re Reynolds number;
T temperature (K)
T_L liquidus temperature (K)
T_S solidus temperature (K)
T_k melting temperature of the primary element (K)

Greek symbols

α thermal diffusivity (m^2/s)
ρ density (Kg/m^3)
τ deviatoric stress tensor;
δ oxide layer thickness (A)
μ coefficient of viscosity (N/sm^2)
$\psi(T)$ Correction function;
Δt time step (s)
Δx gird nodes distance (m)

Subscripts

p particle;
eff effective;
g gas;
ox oxide;
i,j cartesian directions;

Section 6.1

General Symbols

CD drag coefficient
C_p particle specific heat capacity (J/KgK)
D barrel diameter (m)
d_p particle diameter (m)
F_D drag force per unit particle (N)
g_x x component of gravitational acceleration (m^2/s)
H convective heat transfer coefficient (W/m^2K)
H_sf latent heat (J/Kg)
k_g gas thermal conductivity (W/mK)
k_s particle thermal conductivity (W/mK)
k_c partition coefficient
Pr Prandtl number
Re Reynolds number based on particle diameter
St Stokes number
R particle radius (m)
T temperature (K)
T_L liquidius temperature (K)
T_S solidus temperature (K)
T_k primary element melting temperature (K)
t time (s)
up particle velocity (m/s)
u_g gas velocity (m/s)

Greek symbols

A thermal diffusivity (m^2/s)
μ_g gas viscosity (Kg/ms)

ρ_p particle density (Kg/m^3)
ρ_g gas density (Kg/m^3)
ϕ shape factor

Section 7.1

General symbols

A porosity coefficient
c_p specific heat capacity
C porosity constant
E_c Eckert number
F_{vol} surface tension source term (N)
g gravity vector (m^2/s)
h sensible heat (J)
H total heat (J)
ΔH latent heat (J/Kg)
k thermal conductivity (W/mK)
C_μ coefficient for turbulent viscosity
L latent heat of freezing (J/Kg)
$\hat{n}_\omega$ unit vector normal to the wall
p Pressure (Pa)
q heat flux (W/m^2)
R substrate surface roughness (m)
S_h enthalpy source term
S_y moment source term
t time (s)
$\hat{t}_\omega$ unit vector tangential to the wall
T temperature (K)
u velocity (m^2/s)
t time (s)
U_0 droplet impact velocity (m^2/s)

Greek symbols

α coefficient in numerical scheme
β liquid fraction

η small constant to avoid division by zero
θ_ω contact angle (θ)
λ porosity
μ dynamic viscosity (Kg/ms)
ρ density (Kg/m^3)
σ surface tension (N)
τ Marangoni stress
φ volume fraction

Subscripts

i, j, l co-ordinate indices
liquid liquid material
ref reference point
solid solid material
w wall

Mathematical operators

∂ partial differential operator
∇ del operator
Δ difference between two quantities of a variable
$\rightarrow$ vector form of variable

Chapter 1

Introduction

High velocity oxyfuel (HVOF) thermal spraying is one of the most significant developments in the thermal spray industry since the development of the original plasma spray technique. From the fluid dynamics point of view, the process is very complex and involves two-phase discrete particle flow coupled with turbulence, heat transfer, chemical reaction and compressible supersonic transitions. The first HVOF method was introduced in 1982, however there has been limited effort, compared to plasma spraying, on understanding the effects of process parameters on the coating quality. Several experimental procedures and diagnostic tools have been developed to measure the main parameters that influence the characteristics of coating deposition. These diagnostic tools are able to measure direct thermal spray properties such as external jet temperature and particle dynamics; however, measurements and analysis of the gas and particle behaviour within the system is not feasible.

Computational fluid dynamics (CFD) is a valuable tool that can provide information on parts of the system or phenomena happening within the system that would not otherwise be visible. Numerical modelling gives a mean of visualizing and enhanced understanding of the designs. Predictions under a given set of circumstances, can answer many (what if?) questions very fast by giving the variables and receiving the outcomes. In short time, the design performance can be predicted and thereafter can be improved by testing many design variation. With numerical modelling, process and design optimization can be done before physical prototyping and testing. The foresights gained can result in better design and faster understanding of the process parameters involved in HVOF thermal spraying technology. Difficult and expensive physical prototyping is bypassed leading to shorter design cycles, products get to the market faster and consequently time and money are saved. The aim of this thesis is to provide the thermal spray community, new computational approaches and view points in an effort to improve the technology and advance the quality and efficiency of the HVOF thermal spray systems.

Thermal spray coatings are often applied for better corrosion and wear resistance. Therefore, low porosity and good adhesion are desired properties of the coating. High velocity processes, such as HVOF spraying, are the most potential methods for producing a good quality coating with low porosity. Over the decades, many HVOF numerical models have been developed and are able to provide insight to the gas flow, in-flight particle dynamics and even droplet impingement or coating formation. However, most of the modelling work is based on the gas fuelled HVOF systems. The technology of high velocity oxygen fuel (HVOF) thermal spraying has been transforming from gas fuelled towards liquid fuelled systems. An apparent benefit from that development is to use low cost fuels such as kerosene. The combustion of liquid fuels is a very challenging computational task and has rarely been documented in open literature. The first investigation in this thesis deals with the combustion and discrete particle models within the general purpose commercial CFD code FLUENT to solve the combustion of kerosene [1] and propane [2] by coupling the motion of fuel droplets with the gas flow dynamics in a Lagrangian fashion. The effects of liquid fuel droplets on the thermodynamics of the combusting gas flow are examined thoroughly in section 4.2.

The combustion generates the heat and momentum input to powder particles during the HVOF process in which gas temperature reaches over 3000 K within the spraying gun. Active cooling is normally required to protect the spraying gun from overheating by using water as heat transfer media. The cooling process needs to be carefully controlled to protect the gun, retain sufficient heat for powder particles and achieve energy efficiency during operation. A good understanding of the underlying heat transfer process is essential to design such multifunctional cooling mechanism. To date such detailed information is not available and system operation is primarily based on trial and error methods. The second analysis in this thesis (section 4.3) cope with the full water cooling numerical model [3], which can assist on thermal performance optimisation or to determine the best method for heat removal without the cost of building physical prototypes.

As a critical element of the process; combustion generates the required energy and momentum for powder heating and acceleration. The quality of coating is directly related to the particle parameters such as velocity, temperature, oxidation and state of melting or solidification. In order to obtain this particle data, consistent mathematical models need

[1]Published: S. Kamnis and S. Gu. 3-D modelling of kerosene-fuelled HVOF thermal spray gun. Chemical Engineering Science, Volume 61, Issue 16, August 2006, Pages 5427-5439

[2]Published: S. Kamnis and S. Gu. Numerical modelling of propane combustion in a high velocity oxygen-fuel thermal spray gun Chemical Engineering and Processing, Volume 45, Issue 4, April 2006, Pages 246-253

[3]Published: S. Kamnis and S. Gu. Computational fluid dynamic modelling of water-cooling mechanism during thermal spraying process. Int. J. Modelling, Identification and Control, Vol. 2, No. 3, 2007

to be developed to predict particle dynamic behaviour. Most of the already developed models are based on several assumptions excluding from the predictions phenomena such as oxidation and melting of the powder particles. A review of the existing models is presented in section 2.4. The third analysis in this thesis deals with the development and implementation of discrete phase particle models into FLUENT, which are able to predict accurately the particle dynamics, by overcoming the limitations of previous models. The improvement of the existing models, including the detailed phase change methods [4] and predictions of oxide layer growth [5] on the surface of metal particles, is presented in chapter 5 allowing better process optimization. The particle transport equations are solved in a Lagrangian manner and coupled with the three-dimensional, chemically reacting, turbulent gas flow and the in-flight results are presented in chapter 6.

The ultimate goal of research efforts in thermal spraying field is to establish predictive correlations between the processing parameters and the properties (quality) of the coatings. Physical properties such as porosity, microstructure, surface roughness and adhesion strength of coatings produced by droplet deposition in a thermal spray process are determined to a large extent by the dynamics of deformation and solidification of the particles impinging on the substrate. A well developed model can provide insight into the underlying physics of the process by overcoming the technical constrains imposed by experiments. Therefore, is one of the objectives of this study to present a complete numerical model of droplet impact and solidification [6]. A review of the existing droplet impingement models is provided in section 2.4 where several limitations are underlined and possible improvements alongside with the results are provided in chapter 7.

In attempting to provide a comprehensive review of existing models and methods chapter 2 contain summaries of others people work while chapter 3 present important models, physical phenomena and definitions related to this work. In general the amount of reworking is minimal on these summaries. However the evaluation of methods and models has been worked out. Appendix A contains an overview of the basic fluid flow and turbulence models which are implemented into FLUENT. The particular models were not developed or modified by any means all the way through this study. This is an applied thesis and in addition to presenting author's work, it is hoped that this document provides a useful summary and comprehensive critique of existing work giving enough detail to serve as a useful reference.

[4] S. Kamnis, S. Gu, and N. Zeoli. Mathematical Modelling of Inconel 718 Particles in HVOF Thermal Spraying. Surface and Coatings Technology

[5] N. Zeoli, S. Gu and S. Kamnis Numerical simulation of in-flight particle oxidation during thermal spraying. Computers and Chemical Engineering, 19 August 2007

[6] Published: S Kamnis and S.Gu. Numerical modelling of droplet impingement. 2005 J. Phys. D: Appl. Phys. 38 3664-3673

Chapter 2

Literature Review

2.1 HVOF Thermal Spray Process

Thermal spraying is a general term to describe all methods in which the coating is formed from melted or semi-melted droplets. In thermal spraying the material is in the form of powder, wire or rod and is fed into the flame produced by a spray gun, where it is heated and the particles are accelerated towards the substrate to be coated. The thermal and kinetic energy of the flame can be produced either with burning mixtures of fuel gas and oxygen, or by using an electrical power source. Based on the energy source, thermal spray methods can be divided into a few main groups: plasma spray methods, flame spray methods, high velocity oxy-fuel methods, electrical arc methods, and, as the latest technology, cold gas methods [1, 2, 3]. In thermal spraying the coating is produced by rapid solidification of the melted or semi-melted droplets attached to the substrate. A typical structure for the coating is a pancake-like lamellar structure, where the flattening degree and adhesion between the lamellas, together with the coating material itself, define the main properties of the coating. The adhesion and porosity of the coating is mainly defined by the particle melting behaviour and the velocity when attaching to the surface. In addition, due to the fast cooling rate of the particles, some special features, such as residual stresses and the metastable phases can be observed in the thermally sprayed coatings [1, 2, 3].

When better corrosion and wear resistance are the desired properties, thermal spray coatings are often applied and especially HVOF (High velocity oxy-fuel) spraying is the most potential method for producing such a coating. The required thermal energy, for heating powder particles, in HVOF is produced by the combustion of mixtures of oxygen and fuels. Typical fuels mainly used are: hydrogen, kerosene, propane, propylene, natural gas or acetylene. Due to convergent-divergent nozzle design a jet with supersonic speed is produced. The main difference between HVOF and other commonly used processes,

such as (ASP), is the relationship between the kinetic and thermal energy of the process described by the particle velocity and the flame temperature. In Atmospheric Plasma Spray (APS), the energy is based on the plasma produced by ionizing an inert gas, typically a mixture of argon and helium, between the anode and the cathode in the spray gun. The resulting plasma flame temperature, is very high compared to this in HVOF process. Due to the high process temperature, APS enables good melting of the ceramic particles and is often used to produce ceramic coatings. However, HVOF has also demonstrated the ability to deposit dense ceramic coatings [4, 5, 6, 7].

The main feature of HVOF process is the ability to produce dense coatings, preventing excess phase transformations and oxidation due to short in-flight time of powder particles in relatively cold flame. It is extensively used to produce metal coatings , while the use of thermal spray coatings, has traditionally been based on extending the life of the sprayed component. The aerospace industry was the first manufacturing section that recognized the great value of the process and was largely responsible for driving the development and its confidence. Applications include jet engine components such as compressor air seals, compressor stators and fan duct segments and stiffeners. Despite the extensive industrial utilization of thermal spraying, the process is a very complex and includes number of variables. A better understanding of the relationship of these variables and their effect on the coating properties must be obtained in order to apply thermal spray coating to "prime reliant" applications.

2.2 HVOF Methods and Technology

In typical HVOF process fuel and oxygen are led to the combustion chamber together with the spray powder (figure 2.1). The combustion of the gases produces a high temperature and high pressure in the chamber, which causes the supersonic flow of the gases through the nozzle and supersonic expansions outside the gun in the free jet region. The powder particles are heated up through the thermal interaction with the combusting gases in the combustion chamber and during the flight through the nozzle. The flame temperature varies in the range of 3000K - 3500K, depending on the fuel, the fuel gas/oxygen ratio and the gas pressure. In the HVOF process the particles melt completely, partially or even remain solid, depending on the overall system design, flame temperature, material's melting point and powder feeding method. These are adjustable process parameters and they affect the properties of the coating [1].

Great attention has been given to produce coatings using a wider range of materials. For those powder materials that are sensitive to phase transformations due to evaporation or oxidation, HVOF spray is very potential coating method due to the process condition,

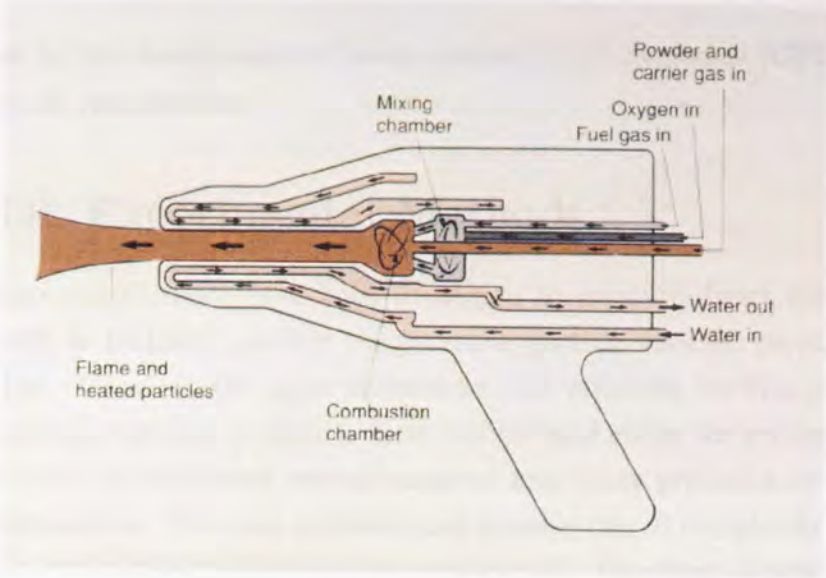

Figure 2.1: Schematic representation of a typical HVOF gun

which combines a relatively low flame temperature with a low exposure time in the flame. A few different HVOF spray systems exist with quite different gun designs and capacities. Each one has differences in design, but all are based on the same fundamental principles. The combination of high pressure (over 4 bar) and gas flow rates of several hundred litters per minute generate hypersonic gas velocities [7]. These systems can be roughly divided into the first, second and third generation. In all first and second generation guns the pressurized burning of gaseous fuel with oxygen is used to produce an exhaust jet travelling at a speed of about 1500 to 2000 m/s. Spray systems belonging to this category are Jet Kote, Diamond Jet (DJ), HV-2000 and CDS. Under standard spray conditions the systems are operated at a power level of about 80 kW and are capable of spraying about 2-3 kg/h of WC-Co. The third generation systems are for power levels ranging from 100 to 200 kW, being capable of spray rates up to about 10 kg/h. The difference between the third generation systems (JP-5000 and DJ Hybrid) and the previous ones is the operation at higher gas/fuel flows and higher chamber pressures (8 to 12 bar versus to 3 to 5 bar) [7, 8, 9].

Despite the fact that the first HVOF method was introduced in 1982, there has only been limited effort towards understanding the effect of process parameters on the structure and properties of the coating compared to the work carried out in the field of plasma spraying. The main reason for this is that in plasma spraying the process parameters are specified by the powder manufacturers, since the process is mainly controlled according to powder particle properties. Recently, more interest in understanding the HVOF process and the effect of process variables on the coating quality has arisen due to the

growing interest in the development of computational fluid dynamics (CFD) tools for process control and optimization.

2.3 HVOF Experimental Methods

Different experimental methods have been developed to measure direct thermal spray jet properties such as enthalpy, particle temperature, particle velocity, particle size and total particle flux. These are the main parameters that influence the characteristics of the deposited coating. On-line diagnostic tools can be used either for process optimization of thermal spray coating with certain material and spray processes or for process control during deposition. The most sophisticated systems due to complexity are mainly used for process optimization rather than process control. Therefore, a large number of simple, fast, and cost effective systems for the measurement of the jet shape and direction, ignoring information on single particles, have been developed, such as Particle Flux Imaging-PFI, DifRex M, Plume Spector and SDC [10]. Measurements in the jet can be done by using probes specially developed for the measurement of temperature and velocity of gas. This technology gives overall information on the jet properties, but, depending on the spray material, no detailed information on the particle conditions or other spray conditions, such as gas pressure [11].

For process optimization detailed information on single particle is required. More sophisticated tools are based on the measurement of thermal emission of the particles. In these systems fast CCD cameras are used to track the particle velocity, while two-colour pyrometer is employed to determine the temperature [12]. For single particle measurements, the method is limited to low particle load in the jet to observe the light emitted without intrusion from surrounding particles. In real HVOF production work this method is not very accurate due to high powder feeding rates (5-10 kg/h).

Only a few commercial equipment applications are suitable when detailed information on particles is required for different spray conditions in order to optimize spray parameters. Temperature measurement is based on the optical system and on the fact that objects emit electromagnetic radiation, in which the intensity and wavelength depend on the temperature of the object; the radiation is shifted towards shorter wavelengths during heating. Measurement is based on the two colour pyrometer measuring the radiance of hot, incandescent particles. Two colour pyrometer is a method for optical temperature measurement that is based on the measurements of the light emitted by the object in two separate wavelength ranges. The method eliminates the effect of particle size, emissivity and non-ideal focusing, and is, therefore, usable with all materials without material specified calibration [13]. For lack of better information, the particles are generally assumed to

behave as grey body emitters [16]. This will cause some inaccuracy in the measurements, especially in the case of metal particles where the error can be up to 273K [13]. The measurement of particle velocity is generally performed by laser Doppler velocimetry or by transit timing techniques [14].

DPV-2000 is based on two-colour pyrometry at two different spectral ranges in the near IR wavelength region around 790 nm and 990 nm,18 respectively. The particle velocity is determined by the in-flight technique during the passage of particles in front of a two-slit mask [15]. The mean and standard deviation of the particle temperature distribution can be obtained from observations of sufficient numbers of individual particles [16]. The measurement spot is small and the positioning must be performed carefully. The measurement is also relatively insensitive to spatial movement of the spray pattern. If information through the whole flame is required, the measurement must be performed by scanning the probe, which increases the measurement time for several minutes per condition. The benefit of the system is in its ability to measure dimensional information on single particles.

SprayWatch is based on the CCD camera. The particles are imaged onto a CCD camera sensor with the aid of spectrally resolving optics. Particle velocity is measured using the time-of-flight method. The length of the particle traces on the CCD detector is measured by the image processing algorithm, and is then converted to velocity by dividing it by the known camera shutter time [17]. The temperature of the particles is measured with two-color pyrometry. The benefit of this technique is the possibility to obtain information through the whole jet. A disadvantage is that the information is always an average, and, therefore, the temperature values are lower than the values obtained by DPV-2000 when measured from the centre of the jet. It is shown that particle velocity and temperature varies widely at different positions in the jet, and monitoring of particle properties at one single position in the jet is not sufficient for describing the complete particle jet [18].

PIV The principle of the PIV system is based on the fact that flying particles are illuminated by two laser flashes following each other in quick succession and the backscattered light is detected by a camera. Hence, there are two possibilities to acquire the images: either two images are taken (for each laser flash one) or one image is double exposed. By analysis of PIV images, a particle appears as a particle image pair. From the spatial distance of the partners of a pair, the known time difference of the laser pulses and the flight direction of the particle the magnitude and the direction of a velocity vector can be calculated. The so-called particle tracking is one methodology for PIV image analysis. This methodology involves a wide range of techniques for determining which particle images belong to the same particle. On the basis of these results, particle image pairs for

calculation of particle velocities can be formed. However, particle tracking is normally only applicable for low particle densities, since it requires a detection of the individual pairs [19].

2.4 Research Development on Modelling

2.4.1 Gas Dynamics

The earliest quantitative analysis of the gas dynamics and particle dynamics of HVOF spraying was conducted by [20]. They analyzed the internal and external flow of a newly designed HP/HVOF torch from Hobart TAFA Technologies. They computed the energy release from an equilibrium chemistry model of heptane and oxygen, assuming no influence from the gas motion. They used one-dimensional isentropic flow assumptions to compute the flow through a converging/diverging section of the nozzle. One-dimensional flow assumptions were then used to compute the effect of viscosity in the constant diameter barrel of the torch. External to the torch they used simple linear shock-expansion theory to calculate the under-expanded supersonic jet flow, ignoring mixing with the ambient air. Particle trajectories were also calculated, assuming no interaction with the gas stream.

The first CFD simulations of the HVOF spraying process have been conducted by [21, 23]. They modelled both the internal and external flow of the Metco Diamond Jet torch. Their CFD simulation included the standard $\kappa - \varepsilon$ turbulence model and combustion chemistry. Their chemistry model included dissociation of the reaction products using an approximate equilibrium model and seven gas species: $C_3H_6, O_2, N_2, H_2O, CO_2, CO$, and H_2. The finite difference equations, using a density based formulation, were solved by an explicit time iterative scheme. Particles of various sizes were injected inside the gas flow but these particles did not interact in any way with the gas stream. They were tracking particles responding to the local gas velocity and temperature but without being coupled with the flow. Their analysis also did not account for any phase change of the particles.

More recent analyses have used modern computational fluid dynamic (CFD) methods to simulate more complex physics in two dimensions. An analysis by [24] performed where the internal and external computational domains were fully coupled by using the finite volume method implemented in a commercial CFD code originally designed for aerospace applications. An iterative, segregated solution method with a Semi-Implicit Method for Pressure-Linked Equations was used. The combustion model used was a one-dimensional approximate equilibrium chemistry model including the dissociation of the gaseous products.

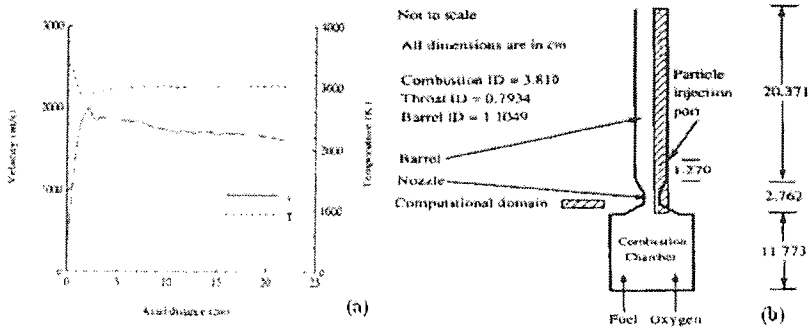

Figure 2.2: Axial gas velocity and temperature along the centreline (a) and schematic of HVOF torch used (b) [25]

The computational study [25] included more reactions and species in the combustion model so as to predict a more accurate flow field regarding the flame temperature and speed of the premixed methane. A schematic representation of the HVOF torch used is shown in figure 2.2(b). The free jet outside the torch is not included in the simulation assuming that most particle heating and acceleration occur in the barrel; however, deceleration and cooling of the particles at the free jet should not be ignored. The combustion chamber also is not included for simplicity. The combustion chamber exit conditions are determined by equilibrium conditions, assuming complete combustion of the fuel. This assumption in conjunction with the absence of the free jet region is responsible for the fact that the calculated gas and particle temperatures are slightly higher than the experimental results. A complete simulation of spray combustion in the combustion chamber is necessary as well as three-dimensional studies for heavier particle loading rates or different torch geometries. The accuracy and numerical stability of the highly compressible flow relies heavily on the discretization schemes used to resolve the conservation equations. In many studies the first order of accuracy upwind scheme is employed making difficult the capture of the shock diamonds inside the nozzle and free jet. Figure 2.2(a) clearly shows that the compressibility effects inside the torch are purely simulated, where only one shock diamond is captured.

A second order of accuracy scheme employed by [26] to capture HVOF shock diamonds however only two diamonds were observed in their results. Only recent third-order schemes such as the well-known QUICK [27] are able to successfully capture the compressibility effects at the free jet region. Although QUICK scheme can increase the accuracy of the solution still the solution may display unphysical oscillations and unacceptable unbounded values for turbulence quantities or species concentrations. More accurate results for the gas flow were obtained by a number of researchers recently using higher order discretization schemes [28, 34, 35].

A comprehensive 2-D model that allows for an appropriate representation of compressibility effects in the flow, combustion, and turbulence was published by [28] in 2001. The improved renormalization group (RNG) $\kappa - \varepsilon$ turbulence model [29] was used to account for the effect of turbulence with standard semi-empirical wall functions in the cells adjacent to walls to represent turbulent boundary conditions. High-order interpolation schemes were employed to resolve compressibility effects in the supersonic jets. The geometry used is shown in figure 2.3. Since experimental measurements are rather limited in HVOF, a comparison of results for a supersonic air jet, for which data are available in the literature, was used to validate the model indirectly. This comparison showed a good agreement. An approximate, single-step, equilibrium formula that takes into account the effect of dissociation was used to treat the combustion process. Propylene and oxygen assumed to react immediately upon entering the calculation domain. Propylene is a fast burning fuel therefore the assumption of infinitely rapid reaction rate was reasonable and become necessary in view of the fact that detailed multi-step reaction kinetics are very complex and speed limitations of the computers make it very difficult to simulate numerically. A list of studies with different assumptions regarding the reaction rate, are: (1) infinitely fast reaction rate [24, 28, 30]; (2) finite reaction rate in Arrhenius form [31, 32, 40]; (3) finite reaction rate limited by turbulent mixing [34, 35].

The authors have shown that the most sensitive parameters affecting the process are fuel flow rate, total flow rate of oxygen and fuel (oxyfuel flow rate), total inlet gas flow rate, and barrel length. Increasing the total inlet gas flow rate has limited effect on the gas velocity and temperature inside the nozzle however; increasing the total inlet gas flow rate increases the total thermal inertia and momentum inertia. Increasing the oxyfuel flow rate significantly increases flame velocity and temperature, particularly after exiting the nozzle.

Despite the good results provided by the authors the model has several drawbacks. A 2-D axisymetric domain can be implemented only in the case of symmetric torques. This case is rather limited and imposes constrains on the torque design and powder feeding methods. The prediction of 5 shock diamonds compared (figure 2.3) with the approximately eight diamonds observed experimentally (figure 2.4) denotes that much work have to be done to increase the accuracy. The standard wall functions implemented by the authors are based on relatively simple empirical laws and in highly compressible flows may not accurately predict the local flow quantities. An immediate defect is the inaccurate prediction of the flame stretch and thickness inside the combustion chamber. The model validation was based only on the supersonic jet expansion excluding any validation of the combustion model through the free jet temperature.

A good comparison between the numerical and experimental results of gas temper-

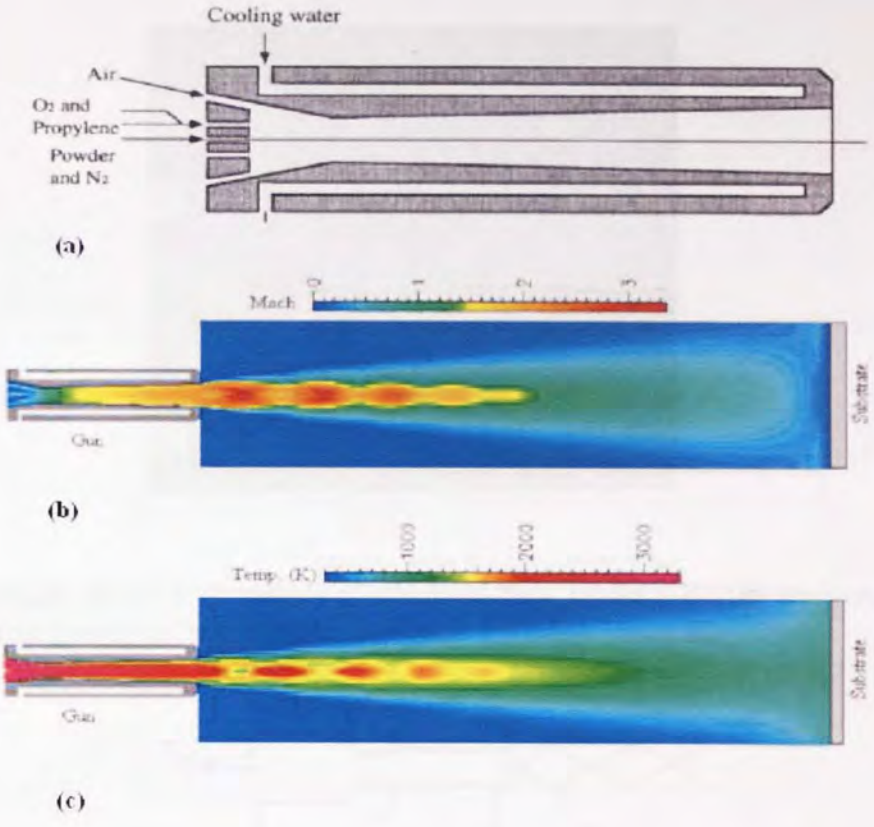

Figure 2.3: Geometry (a) Mach number contours (b) gas temperature contours (c) (b) [28]

ature and velocity is provided by [26]. Figure 2.5(a) shows schematically the JP-5000 torch design and figure 2.5(b) shows the comparison between computational prediction and experimental measurement of gas temperature in the radial direction at the barrel's exit.

Summarizing, the combustion process has been modelled by several groups successfully; however 3-D liquid fuelled HVOF systems have not being examined by any research group. Modelling turbulence using the $\kappa - \varepsilon$ model is adequate to the problem of HVOF process while discretization schemes of third order of accuracy as well as finer grids at the free jet region are needed to capture adequately the supersonic jet expansion.

2.4.2 Particle Modelling

Models describing the in-flight behaviour of particles during HVOF spraying are well documented [24, 25, 30, 33, 37]. From the viewpoint of solution methods of governing equations for two-phase systems, three types of models may be considered: coupled,

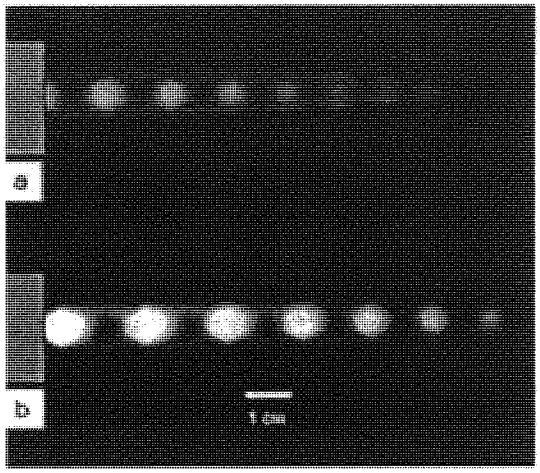

Figure 2.4: Images of shock diamonds of a Hobart-Tafa JP-5000 HVOF equipment operated at chamber pressures of 0.65MPa (top) and 0.91Mpa (bottom)

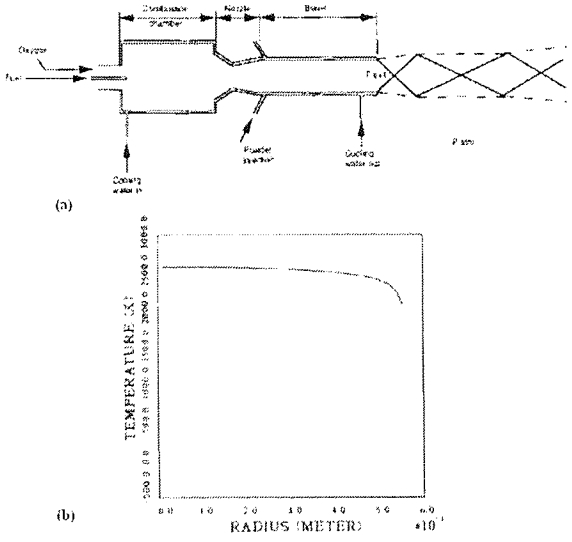

Figure 2.5: Schematic of the high pressure HVOF gun and flow field (a) and experimental versus numerical results for gas temperature (b) [26]

semi-coupled [24, 25, 31, 37] and decoupled [30]. Since the coupled method, Eulerian approach, is not used in HVOF processes, only Lagrangian methods are discussed. In most of the numerical model available in literature the temperature gradient inside the particle is neglected and consequently propagation of the melting front towards the centre of the particle is not considered. A consistent semi-coupled Lagrangian numerical simulations of HVOF spraying particles has been presented by [38]. The torch diagram

and computational domain are shown in figure 2.6.

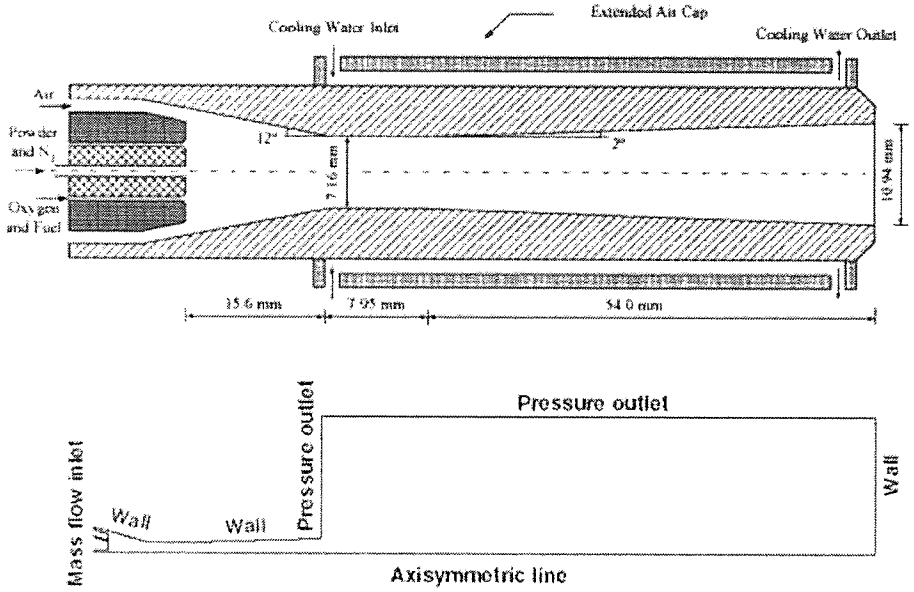

Figure 2.6: Torch diagram and computational domain [38]

In this model it is assumed that the particles are heated with negligible internal resistance and the internal particle temperature gradients can be ignored due to the small Biot number (ratio of heat transfer coefficient on the boundary to the internal heat conductance) of good heat-conducting particles. Assuming no internal resistance is a reasonable assumption for temperatures lower than the melting pointing of powder particles. When the particle temperature reaches the melting point the current model assumes that the phase change occurs instantly (figure 2.7). In reality transition from solid to liquid stage is not infinitely fast and the phase change time is a function of the latent heat of fusion. During phase change (Stefan problem) a melting front develops inside the particle that allows for a temperature gradient between the surface and the centre of the particle.

In an other study of the same authors [35] the particle melting and solidification is included in their model. The heating of the particle is described by the following equations:

$$m_p c_{p_p} \frac{dT_p}{dt} = \begin{cases} hA_p(T_g - T_p), (T_p \neq T_m) \\ 0, (T_p = T_m) \end{cases} \tag{2.1}$$

$$\Delta H_m m_p \frac{df_p}{dt} = \begin{cases} hA_p(T_g - T_p), (T_p = T_m) \\ 0, (T_p \neq T_m) \end{cases} \tag{2.2}$$

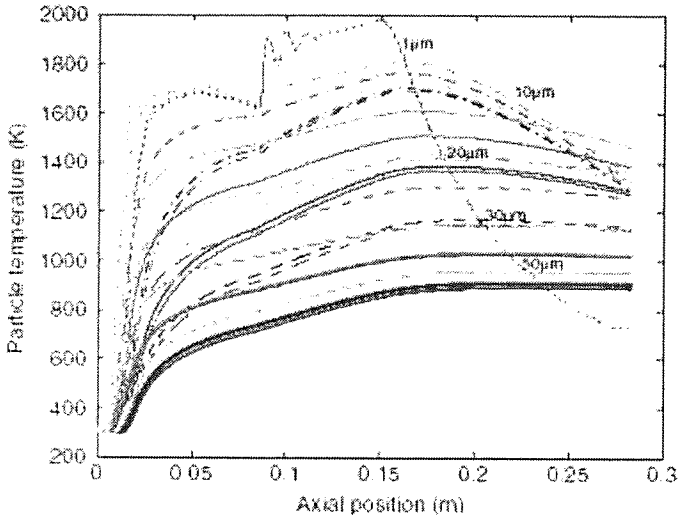

Figure 2.7: Profiles of temperature of different size particles injected at five different locations as a function of axial position [38]

where T_p is the temperature of the particle, A_p is the surface area of the particle, T_m is the melting point of the particle, ΔH_m is the enthalpy of melting and f_p is the ratio of the melted mass to the total mass of the particle. The melting ratio of the particles along the centreline is shown in figure 2.8.

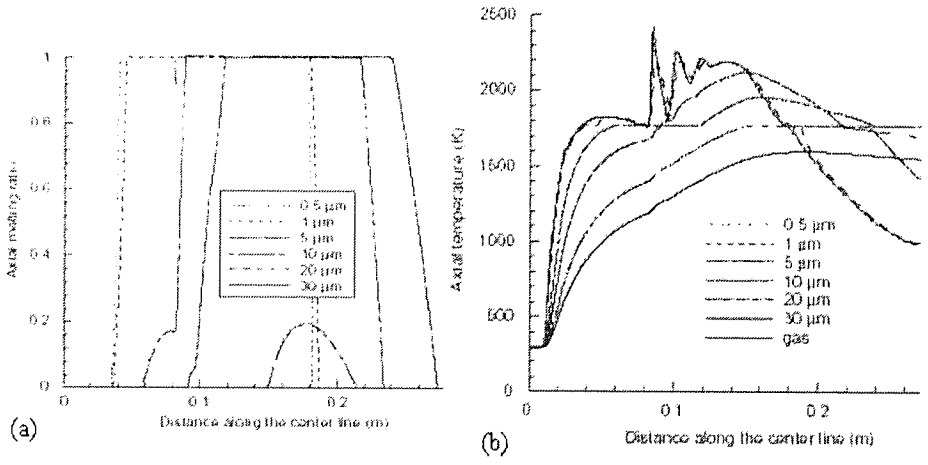

Figure 2.8: Profiles of melting ratio along the centreline (a) and temperature of particle along the centreline (b)[38]

In this model the particle is assumed to have negligible internal thermal resistance and the melting ratio is a result of the average particle temperature. During phase change is assumed that the particle has constant temperature which is equal to liquidus

temperature. In reality as the phase change front moves towards the centre, the surface temperature of the particle is changing according to convective heat transfer from the surrounding fluid. Consequently the model presented by the authors tends to under predict the average particle temperature during melting and over predict it during solidification. The most significant limitation of this model is that allows melting and solidification at a single temperature. This assumption can not be valid when the powder particle material is an alloy. In the case of alloys melting and solidification takes place within a range of solidus and liquidus temperatures. Similar work including the same assumption of uniform particle temperature on the thermal behaviour of the powder particles was contacted by [25, 40].

The in-flight behaviour of powder particles has been examined extensively the last two decades mainly for plasma spray applications. Soon after the developed plasma spray models have been modified and applied to HVOF process. The dynamic behaviour of the powder particles was modelled successfully by many research groups; however, the thermal behaviour models either neglected or used simplified assumptions on the particle heating and phase change. Those models are able to predict the temperature and velocity history of in-flight particles by coupling the simulation of gas and particle flows, however, the phenomena of oxidation on metal powders have hardly been addressed in open literature. The improvement of the existing models, including the detailed phase change methods and predictions of oxide layer growth on the surface of metal particles, is deemed necessary allowing for better process optimization.

2.4.3 Powder Particle Impingement, Flattening and Solidification

The desired coating properties are dictated by the applications. High density coatings, for example, are required to provide wear or corrosion resistance, whereas thermal barrier coatings should have a relatively high percentage of porosity (close porosity) to ensure thermal shock resistance. The ultimate goal of research efforts in thermal spraying field is to establish predictive correlations between the processing parameters and the properties (quality) of the coatings. Physical properties such as porosity, microstructure, surface roughness and adhesion strength of coatings produced by droplet deposition in a thermal spray process are determined to a large extent by the dynamics of deformation and solidification of the particles impinging on the substrate, the cooling rate of the resulting splats, and the interactions of these splats with the surface. Better control of the process requires a fundamental understanding of the fluid flow and heat transfer that occurs during the impact, spreading, and solidification of molten droplets. A well developed

model can provide insight into the underlying physics of the process by overcoming the technical constrains imposed by experiments.

Throughout years numerous efforts have been made to develop droplet impingement models. The early work by [41] oversimplifies the impingement process, neglecting both viscous and surface tension effects in their modelling. Later phase change is introduced in the impingement models [42, 43, 44] by considering an order of magnitude balance between inertial, viscous and surface tension. More recent numerical models [45, 46, 47, 48] incorporate both MAC and VOF methods [49] in order to closely represent the detailed physics.

Despite the advance in developing numerical methods, the accuracy of existing droplet impingement models is severely limited by many assumptions being made. For example, the models developed by [50] and [51] assume that solidification starts only after droplet spreading is finished. Simultaneous spreading and solidification are incorporated into the splash models [52, 53], however, the thermal contact resistance at the liquid-solid interface in those models is neglected and liquid-solid contact angle is given an arbitrary constant value, which could bring in a certain degree of error into the model as the research by [54] demonstrates that the value of contact angle could significantly influence the accuracy of model predictions.

Finite element methods are used by [55] to solve droplet impingement, however the capillary forces at the liquid-solid angle is not included in their model. More recently, [56] presented a splash model with improvement on the governing equations with modified initial conditions, however this model is only applicable to fast solidification due to the assumption that solidification occurs within a time during the beginning of impact process. Latest research includes a 3-D model developed by [57] who use experiment-based input parameters to simulate the impact of droplets on the tip of a pin projecting from a flat surface. Nevertheless the accuracy of the 3-D model is affected by the following factors: the shrinkage effect caused by the density discrepancy between liquid and solid materials is not considered; no-slip wall is employed instead of using more realistic boundary condition; and the possibility of air entrapment between splat and substrate is ignored.

As stated in the last section, previous models of droplet impact either neglected or used simplifying assumptions when dealing with: capillary effects during droplet impact; simultaneous solidification and its effects on arresting droplet spread; and droplet-substrate thermal contact resistance, heat transfer to the substrate, and their effects on the transient deformation and solidification of the splat. It is, therefore, one of the objectives of this study to develop a complete numerical model of droplet impact and solidification that considers capillary effects at both liquid-substrate and liquid-solid interfaces, sim-

ulates simultaneous solidification and heat transfer to the substrate during the impact dynamics, and considers thermal contact resistance at the surface of the substrate. The complete model can be used to analyze the formation of a coating layer made from one droplet impact as a function of processing parameters in a thermal spray process. The processing parameters include the shape, pressure, velocity, and temperature distribution within the droplet and substrate during the impact, which can be obtained only by a complete solution of the continuity, momentum, and energy equations.

Chapter 3

Concepts and Definitions

3.1 Turbulence Modelling

This chapter attempts to provide a better understanding of the HVOF process parameters from both the physical and theory standpoint. This chapter shall discuss and define the relevant terms and concepts and is not intended as a complete overview, but only as a partial list of definitions and concepts, which shall be referred to throughout this work. Background information about the turbulent-compressible flow is given in sections 3.1 with reference to appendix A for the mathematical presentation of the physical phenomena. Section 3.2 provides the most important concepts of compressibility effects in the nozzle and jet while definitions on premixed flames are given in section 3.3.

Based on the assumption of continuum the basic equations of fluid dynamics are derived according to the Reynolds's transport theorem:

$$\begin{bmatrix} rate\ of\ change\ of \\ total\ property\ in\ V \end{bmatrix} = \begin{bmatrix} rate\ of\ property \\ being\ created\ in\ V \end{bmatrix} + \begin{bmatrix} property\ flowing \\ in\ V\ surface \end{bmatrix} + \begin{bmatrix} property\ flowing \\ out\ of\ V\ surface \end{bmatrix}$$

which states the conservation of a flow quantity inside an arbitrary volume (Control Volume Method). The dynamic behaviour of fluid flow is completely described by the conservation of three quantities: mass, momentum and energy. An important feature of the fluid flow is the turbulence. The borderline for laminar flow existence is delimited by non-dimensional parameters such as Reynolds number, Taylor number, Grashof number and Richardson number. The complex and chaotic flow that arise outside this range is called turbulent. Even if much is known about turbulence this is still one of the most difficult and challenging area for the scientific community. Brilliant monographs are available in the open literature both for experimental [68, 69] and numerical analysis

[70, 71, 72, 73]. The inherent features of turbulent flow can be summarized in:

1. Three dimensional random fluctuation in the values assumed by the flowfield variables (velocity, pressure, temperature)

2. Presence of eddies of different size, from a characteristic dimension (ex: in the free shear flow δ = shear layer thickness) to the Kolmogorov length scale $L = (\mu^3\delta/\rho^3 v^3)^{1/4}$

3. The small eddies dissipated by viscosity are replaced are replaced by the production of new ones, in a self sustaining mode.

An immediate effect of turbulence is the strong increase in the mixing behaviour (i.e. transport of mass, momentum and energy) of the flow compared to the solely molecular diffusion acting in laminar state. This means also that due to the higher rate of interaction of molecules with the wall the heat transfer and skin friction (at the same conditions) are increased. From a mathematical point of view, the mixing activity is directly related to the presence of gradients in the time-averaged flow.

The set of equations given in appendix A is a complete description of the turbulent flow but unfortunately does not have an analytical solution: the only way to obtain a complete description of the flow field (velocity and pressure as functions of time and space) is to solve numerically the Navier-Stokes equations. This approach is called direct numerical simulation (DNS) and as indicated in [74] 'is a research tool, and not a brute-force solution to the Navier-Stokes equations for engineering problems'. The main concern about DNS is related to the rapid increase in the instantaneous range of length and timescale with the Reynolds number, so that for usual engineering application the range of scales to solve directly is too wide. Considering the flow of air at 3.3 m/s passing a flat plate: the smallest eddy has a diameter of about 0.04 mm, consequently to solve a shear layer of 10 cm over a 2.9 m^2 plate it is necessary to employ a grid with 5 trillion points (the size of the biggest mesh realized is around 100 million nodes). For such reason, the common approach for turbulent flow does not solve the instantaneous flow field but is based on its statistical description ($\approx$ approximate solution).

It is possible to subdivide the entire turbulence models in three main groups: the so called first order closure (algebraic, one equation and multiple equations), second order closure (Reynolds-stress model, RSM) and Large eddy simulation (LES). The closure is the main drawback of statistical description: the equations derived for this method contain some additional terms so they need to be modeled. The first order closure models are based on the linear eddy viscosity hypothesis introduced by Boussinesq or the non linear extension proposed by Lumley. Boussinesq hypothesis is not generally valid. It

is not accurate in cases like sudden variation in the mean strain rate, secondary flows, separated flow, rotating and stratified flows. The limit of this approach relies on the assumptions of local equilibrium between turbulence and main strain and of system rotation independence.

RSM models employ the exact equations for the Reynolds-stresses while the closure is necessary for higher order correlation terms. Those two classes of model belong to a more general approach, called RANS (Reynolds Averaged Navier Stokes equations). The most used 2 equations model is the $\kappa - \varepsilon$ and a detailed description can be found in [77]. It relies on the solution of two additional transport equations, one for the turbulent kinetic energy κ and the other for its dissipation rate ε. Finally the Large Eddy Simulation solves the large structure (vortex with high energy content) while model the influence of small structure (based on the observation they have more homogeneous and universal character).

3.2 HVOF Shock Patterns in Nozzle and Jet

3.2.1 Nozle Shock Paterns

During thermal spray process the combustion products are accelerated towards a Converging-Diverging nozzle and after a short distance the gas flow is expanded forming a supersonic jet at the barrel's exit. In this section some of the important aspects of internal and external supersonic-compressible flows are described based on the current HVOF design (figure 3.1).

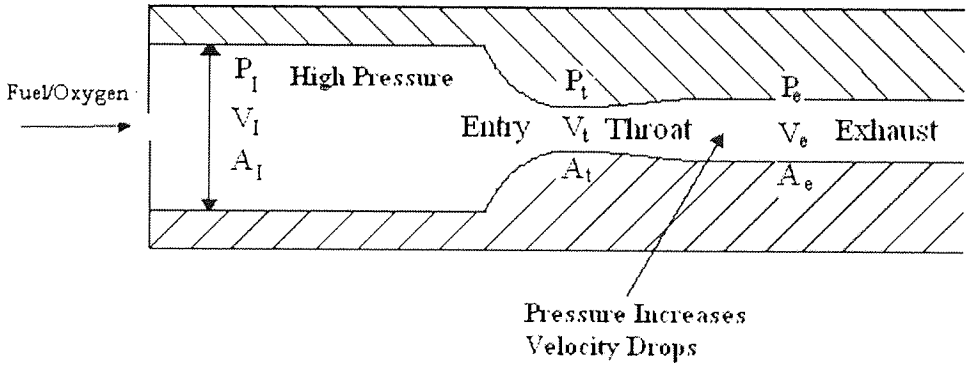

Figure 3.1: HVOF *de Laval* nozzle

The most important type of duct is the *de Laval* nozzle, which consists of a converging entry section and a diverging exhaust section. When the gas is under high pressure inside the combustion chamber and escapes through such a nozzle two possibilities arise.

The first is that the flow, after being expanded in the entry section, is compressed in the exhaust section and remains subsonic throughout. When the pressure inside the combustion chamber exceeds the critical value, the other alternative occurs. The flow becomes supersonic on passing the throat and continues to expand from this point. The HVOF gun design examined in this work allows for high pressure development inside the combustion chamber and thus supersonic expansion through the nozzle and at the barrels exit.

To understand the adjustment of the flow in the jet it is better first to revert to the shock patterns occurring within the nozzle. In the simplest description these shock fronts would be curved discs across the nozzle perpendicular to the nozzle wall. The actual shock front is, however different. The shock front is oblique and consequently changes the direction of the flow abruptly, that is, the sock front leads to jet detachment (figure 3.2(a)). The shock front is cut-off by a Mach shock disc perpendicular to the axis. Behind the incident and mach shock front a reflected shock front and a discontinuity surface develop. The flow, velocity, density and temperature are discontinuous across this contact surface. This slip discontinuity arises because the thermodynamic pathway through the incident and reflected shocks does not equal the pathway through the Mach disc. By Bernoulli's principle the total specific energy remains constant along a streamline, therefore when the two adjacent fluid elements arrive at the contact surface they must still have the same total specific energy. They must also have the same pressure since they are still adjacent. However their entropies and densities are different. Bernoulli's principle implies that the fluid element close to the triple point must have lower kinetic energy and hence flow velocity, than the adjacent element. The slip discontinuity results exactly from this difference in flow velocities.

When the chamber and exhaust pressure difference increase the place of detachment moves towards the rim of the nozzle while the shock front leaving the rim becomes longer (figure 3.2 (b)). For further increase of the pressure difference between the chamber and exhaust the tips of the shock fronts approach each other and eventually the two shocks intersect each other (figure 3.2 (c)). For similar wave pattern see Hartmann and Lazarus [79, 78]. The jet boundary curves slightly inward up to the place where the intercepting shock meets the boundary. At this point the shock front is reflected as a rarefaction wave (sound wave) and the jet boundary diverges again. The whole process repeats itself. By the action of viscosity at the jet boundary this periodic pattern dissipates eventually.

3.2.2 Jet Shock Patterns

The characteristic structure of a slightly underexpanded supersonic jet, that is, one for which the pressure of the gas at the nozzle orifice is slightly greater than the ambient gas

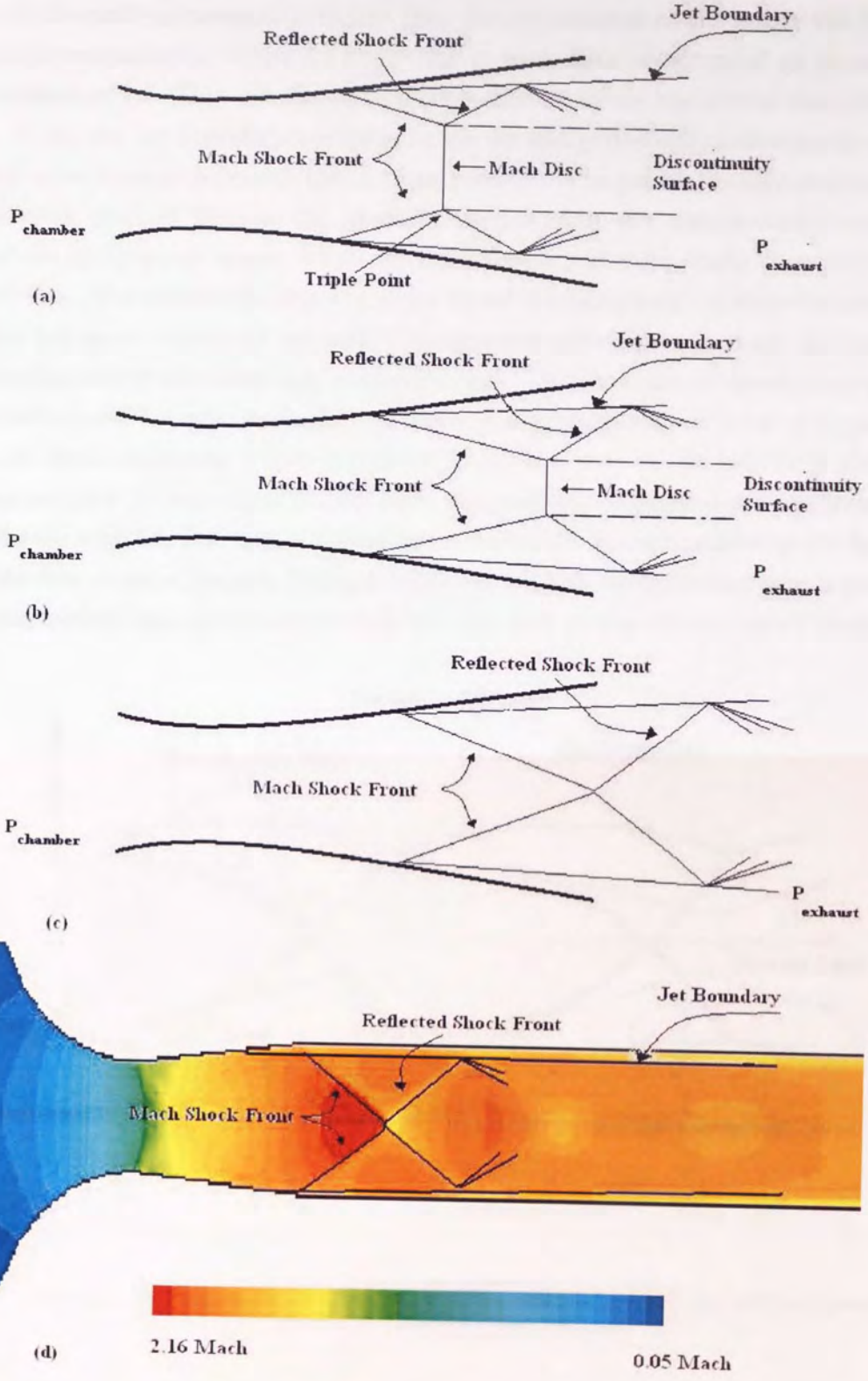

Figure 3.2: Shock patterns in *de Laval* nozzle

pressure (if the ambient pressure is higher than the gas pressure at the nozzle the jet is reffered as overexpanded). Figure 3.3 shows the characteristic structure of an underexpanded supersonic jet. This complicated axisymmetric structure has several remarkable features. First, the jet boundary oscillates as the jet gas periodically overexpands and econverges in its attempt to match the ambient pressure. The gas continually overshoots the equilibrium position because the effects of the boundary arc communicated to the interior of the jet by sound waves, which, by definition, travel more slowly than the bulk supersonic flow. The characteristic paths of the sound waves converge to form the second remarkable feature of the jet, the network of crisscrossed shock waves, or shock diamonds. These standing shocks alternate with rarefaction fans. The gas in the jet interior expands and cools as it flows through the rarefaction fans and is compressed and heats as it passes through the shock diamonds. Figure 3.3 clearly illustrates that the jet interior is always out of step with the jet boundary. For example, the positions of greatest gas compression do not coincide with the positions of minimum jet diameter. The streamlines in the figure indicate the flow paths of the gas. The gas bends out towards the boundary as it is passes through rarefaction fans and bends towards the axis as it passes through shock fronts.

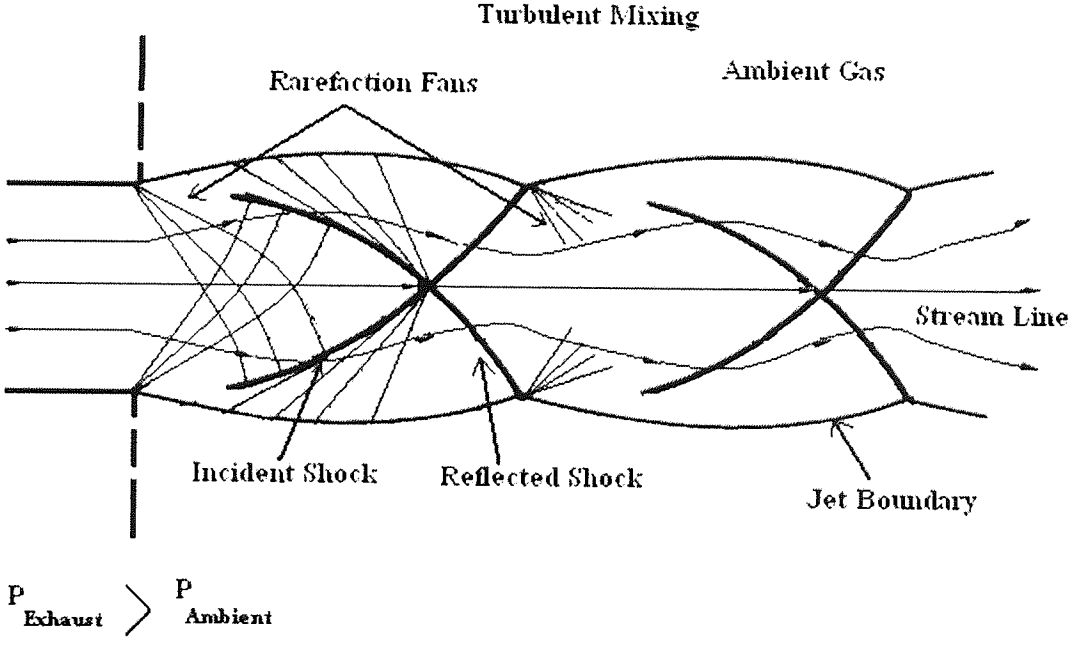

Figure 3.3: Regular reflection and the pattern of crisscrossed shocks in an underexpanded jet.

The shock structure can be understood in terms of characteristics. As the gas leaves the nozzle, it expands and a rarefaction fan starts from the nozzle orifice. The gas

overexpands, and the pressure of the ambient gas at the boundary pushes the jet back towards the axis. These characteristics form a converging conical shock. When this so-called incident shock reaches the jet axis it undergoes a regular reflection forming a diverging shock. At the point where this reflected shock reaches the jet boundary it knocks the boundary outward, creating a new rarefaction fan and the process begins all over again. The angle between the incident shock and the jet axis determines the type of reflection: small angles of incidence yield the regular reflections and large angles of incidence yield Mach reflections. When gas passes through a shock its velocity component normal to the shock is greatly reduced while its parallel component remains unchanged. Thus shocks with large angles of incidence relative to the flow axis are more effective at slowing down the flow than shocks with small angles of incident.

The jet structures shown in figure 3.3 in reality do not have sharp, stable boundaries but turbulent boundaries where jet and ambient gases mix. Near the orifice, where the pressure mismatch is large, Mach reflections occur but further downstream the reflections are regular. The mixing layer which grows eats its way into the supersonic core of the jet. When the mixing layer reaches the axis of the jet the flow is subsonic and fully turbulent.

3.3 Premixed Combustion

Being a critical element of the process, combustion not only generates the required energy for powder heating but also affects the multiphase flow pattern. Subsequently, fuel is the main driven force for the evolution of HVOF thermal spray systems. The gas fuel system namely HVOGF, is an early stage product and consumes gas fuel such as propylene or hydrogen. Most recently, the liquid fuel system namely HVOLF has been given much attention due to their advantages, such as, cheap fuels namely kerosene or propane, high momentum output with the design of convergent-divergent nozzle, and high flow rate.

In combustion processes, fuel and oxidizer are mixed and burned. The combustion categories are based upon whether the fuel and oxidizer is mixed first and burned later (premixed) or combustion and mixing occur simultaneously (non-premixed). In the present study oxygen and fuel are mixed prior entering the combustion chamber. The advantage of premixed combustion is that much greater control of the combustion is possible. By premixing flame temperature can be better controlled and under lean conditions soot formation is restricted. Despite the advantages, premixed combustion must be used carefully because of the potential of accidental burn of the premixed reactants, which could result in an uncontrolled explosion. Premixed flames can be adequately described with the proper definition of the inner flame structure, the kinematics of flame and flow, the stretching of flame and the flame thickness. This introduction is based on a number of

excellent reviews of theoretical and numerical combustion . Poinsot and Veynante [80] is an excellent introductory book and many topics discussed in this section are given a fuller treatment in this book.

3.3.1 Inner Flame Structure

A schematic representation of the inner structure of the propane premixed flame is shown in figure 3.4. A large amount of fuel and oxidizer is present at the unburnt side of the flame, whereas this amount is significantly reduced at the burnt side. The opposite holds for carbon dioxide. This flame region can be divided into three zones. Going through the flame from the side of the unburnt gases to that of the burnt gases, one encounters the preheat zone first, then the inner layer, and finally the oxidation layer. The preheat zone can be considered as chemically inert. In this zone, the unburnt gases are heated up by heat transport from the reaction layer. The reaction layer can be divided into the inner and oxidation layer. In the inner layer, or fuel-consumption layer, the fuel is consumed and converted into hydrogen and carbon monoxide, and the radicals are depleted by chain-breaking reactions. The oxidation layer is located downstream of the reaction layer in which the oxidation takes place of hydrogen and carbon monoxide to water and carbon dioxide. The effect of the oxidation layer on the other two upstream layers is weak. The thickness of the inner layer is small compared to the thickness of the preheat zone and the oxidation layer.

As the flame front moves, combustion of the unburnt occurs, converting them to burnt products. The turbulent combustion modelling is based on the work of [81, 82, 83, 84] The flame front propagation is modelled by solving a density-mean reaction progress variable, denoted by c.

$$\frac{\partial}{\partial t}(\rho c) + \nabla\left(\frac{\mu_t}{Sc_t}\nabla c\right) + \rho S_c \tag{3.1}$$

where:

c = mean reaction progress variable

Sct = turbulent Schmidt number

Sc = reaction progress source term

The reaction progress source term is modelled as follows:

$$\rho Sc = \rho_u u_f |\nabla c| \tag{3.2}$$

where :

ρ_u = density of unburnt mixture

u_f = turbulent flame speed

The mean reaction progress variable is defined as the ratio of the mass fraction of product species over the equilibrium mass fraction of product species:

$$c = \frac{\sum_{i=1}^{n} Y_i}{\sum_{i=1}^{n} Y_{i,eq}} \tag{3.3}$$

where:

n= number of products

Y_i= mass fraction of product species

$Y_{i,eq}$= equilibrium mass fraction of product species

According to the definition above the unburnt mixture has a progress variable of zero and the burnt mixture progress variable of one.

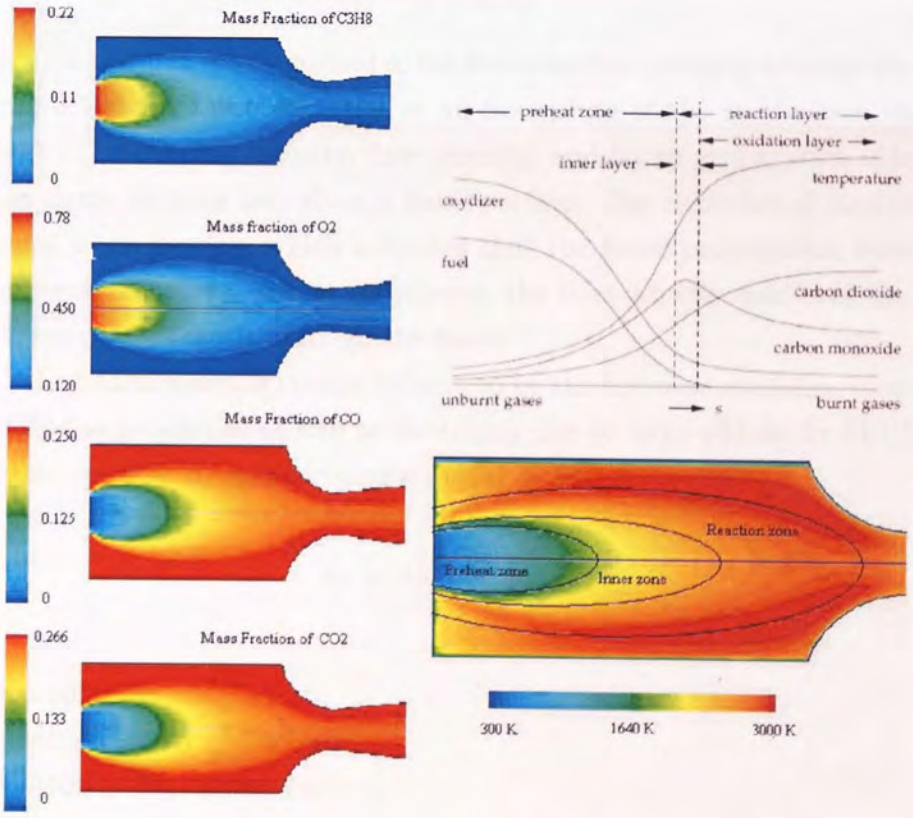

Figure 3.4: Schematic representation of the inner structure of HVOF propane premixed flame with s being the coordinate normal to the flame surface

3.3.2 Flame Speed

A premixed flame is a region in space where the combustion variables vary. These combustion variables are the temperature, density, and species mass fractions. A flame surface inside this flame can be defined as an iso-surface of a certain combustion variable that increases or decreases continuously going from the unburnt to the burnt side of the flame. The choice of the combustion variable is not crucial for the flame analysis, because the iso-surfaces obtained from the different combustion variables have almost matching orientations and they move with almost identical speed. In this description, the choice was made to define the flame surfaces as iso-surfaces of the temperature. The propagation of a flame surface in the normal direction and relative to the gases into the unburnt mixture is due to the chemical reactions that occur and is called the local burning velocity s_L. The velocity at which the flame surfaces move is called the flame propagation velocity u_f. This flame propagation velocity u_f can be obtained from the local balance between the flow velocity u and the local burning velocity s_L:

$$u_f = u + s_L n_f \tag{3.4}$$

in which n_f is the unit vector normal to the flame surface pointing towards the unburnt gases. Figure 3.5 shows these velocities at an iso-surface of the combustion variable Y (temperature). The burning velocity, flow velocity, and flame propagation velocity can vary between flame surfaces and along a flame surface. The structure of laminar flames hardly changes while moving, which indicates that the flame propagation velocity field is almost uniform. However, due to turbulence, the flow velocity field and the burning velocity field vary significantly through the flame.

The turbulent flame speed is mainly influenced by the fuel concentration, temperature, molecular diffusion properties as well as stretching due to large eddies. In FLUENT the turbulent flame speed is computed using a model by [81].

$$u_f = Au' \left(\frac{\tau_t}{\tau_c} \right)^{1/4} \tag{3.5}$$

where

A= model constant

α= thermal diffusivity $\frac{k}{\rho c_p}$(m2/sec)

u'= flow velocity fluctuation (m/sec)

l_t= turbulence length scale (m)

U_l= laminar flame speed (m/sec)

$\tau_t = \frac{l_t}{u'}$= turbulence time scale (s)

$\tau_c = \frac{\alpha}{U_l^2}$= chemical time scale (s)

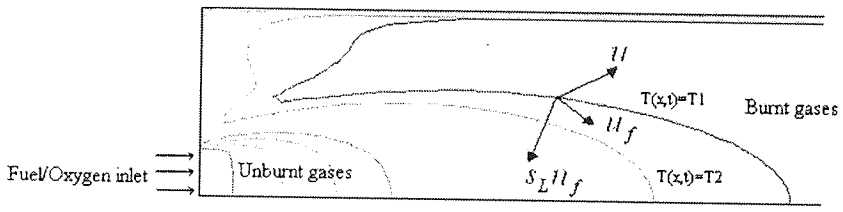

Figure 3.5: Schematic representation of the burning velocity s_L,the flame propagation velocity u_f and the flow velocity u at an iso-surface of the combustion temperature.

3.3.3 Premixed Flame Thickness

Defining and estimating a flame thickness before computation is an obvious requirement for many numerical combustion problems because this thickness controls the required mesh resolution. In most combustion approaches the flame structure must be resolved and enough points must be clustered within the flame thickness. Prior to simulation some simple approximation scaling laws can be used. The classical definition of the flame thickness δ_f is based on a geometrical approach. In this case, the flame thickness is the interval of the steepest tangent to the temperature profile between the unburnt and adiabatic temperature (figure 3.6).

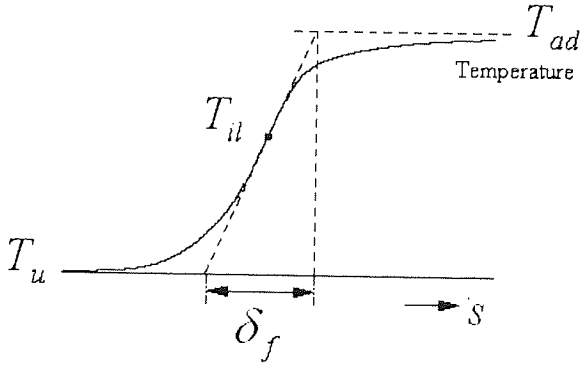

Figure 3.6: Geometrical definition of the flame thickness

$$\delta_f = \frac{T_{ad} - T_u}{(dT/ds)|_{T_{il}}} \tag{3.6}$$

with T the temperature, s the coordinate perpendicular to the flame surface, and the subscripts ad, il, and u denoting the adiabatic case, the inner layer, and the unburnt gases, respectively.

3.3.4 Flame Stretch

Stretching of a flame can lead to variations of the flame behaviour compared to a flat flame with a purely one-dimensional flow and transport. This concept of flame stretch was first introduced by [85]. The main causes of these stretch effects are the curvature of a moving flame surface and a gradient of the flow along this surface. A variable that takes the stretch effects into account is the flame stretch rate K_A. A generally accepted definition of the flame stretch rate K_A was first suggested by [86].

$$K_A = \frac{1}{A}\frac{dA}{dt} \tag{3.7}$$

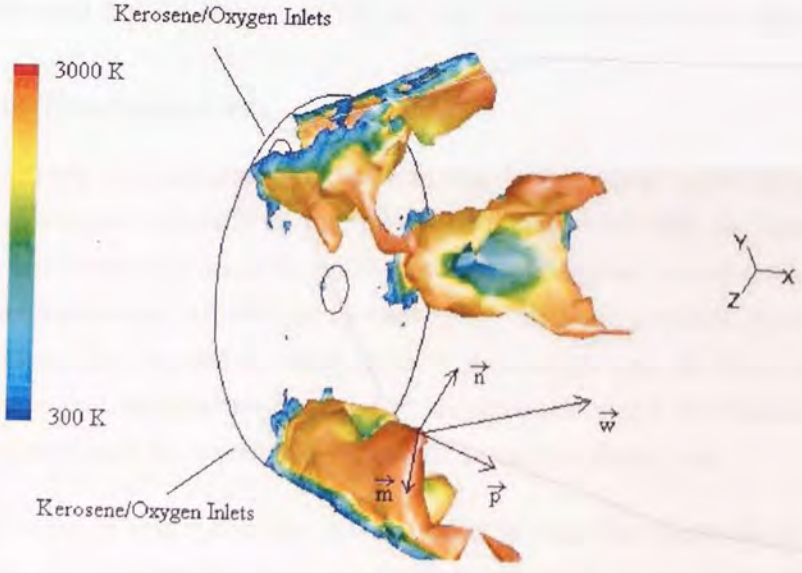

Figure 3.7: Definition of flame stretch. The temperature contours are plotted on iso-vorticity where $\vec{n}$ is the unit vector normal to the flame surface, $\vec{w}$ is the velocity of the flame surface and $\vec{m}$, $\vec{p}$are two orthonormal vectors belonging to the local tangent plane of the flame

The stretch rate represents the fractional area change of a small flame surface element A which moves with the flame propagation velocity (figure 3.7). From this definition more sophisticated expressions have been derived [80].

To take the flame stretching into account the burning velocity S_L is multiplied by a

stretch factor G [84]. The stretch factor G is obtained by integrating normal distribution of the turbulence dissipation rate ε:

$$G = \frac{1}{2} erfc \left\{ -\sqrt{\frac{1}{2\sigma}} \left[\ln\left(\frac{\varepsilon_{cr}}{\varepsilon}\right) + \frac{\sigma}{2} \right] \right\} \tag{3.8}$$

where erfc the error function and ε_{cr} and σ are defined as (σ is the standard deviation of the distribution of ε):

$$\sigma = \mu_{str} \ln\left(\frac{L}{n}\right) \tag{3.9}$$

where μ_{str} is the stretch factor coefficient for dissipation, L is the turbulent integral length scale, and n is the Kolmogorov length scale.

ε_{cr} is the turbulence dissipation rate at the critical rate of strain:

$$\varepsilon_{cr} = 15 \upsilon g_{cr}^2 \tag{3.10}$$

Further details and a good theory review on the flame stretch can be found in [80].

3.3.5 Flame Stabilization

A well-known property of turbulent premixed flames is that their speed of propagation correlates to the turbulent intensity in the unburned mixture [87, 88]. As a consequence, premixed flames are inherently unstable when propagating against a turbulent flow whose intensity increases upstream but decays downstream. To have a stable flame for either laboratory analysis or for a practical combustor requires some type of flame stabilization mechanism. A variety of approaches are used to stabilize premixed turbulent flames [89]. The two main mechanisms to stabilize a turbulent premixed flame are:

1. Low speed zone. Creating a low speed region in the flow field allows the flame stabilization. In this case the turbulent flame speed is able to maintain the incoming flow velocity leading to flame stabilization. This objective is generally achieved by inducing a large recirculation zone anchored to the mixture injector lip (figure 3.8).

2. Continuous ignition. In this case, the reactants are continuously ignited through a heat source.

The formation of recirculation zones is a result of the boundary layer separation of the free-shear flow and can be described according to the mixing-layer theory. Typical streamlines in the viscous mixing region and a representative velocity profile are shown in figure 3.8. The uniform stream of velocity mixes with a dead-air region. The mixing

layer thickness (dividing streamline) grows parabolically with distance. In the formation of recirculation zone the essential mechanism is considered to be a balance between air mass scavenged from the dead-air region by the mixing layer and mass flow reversed back into the dead-air region.

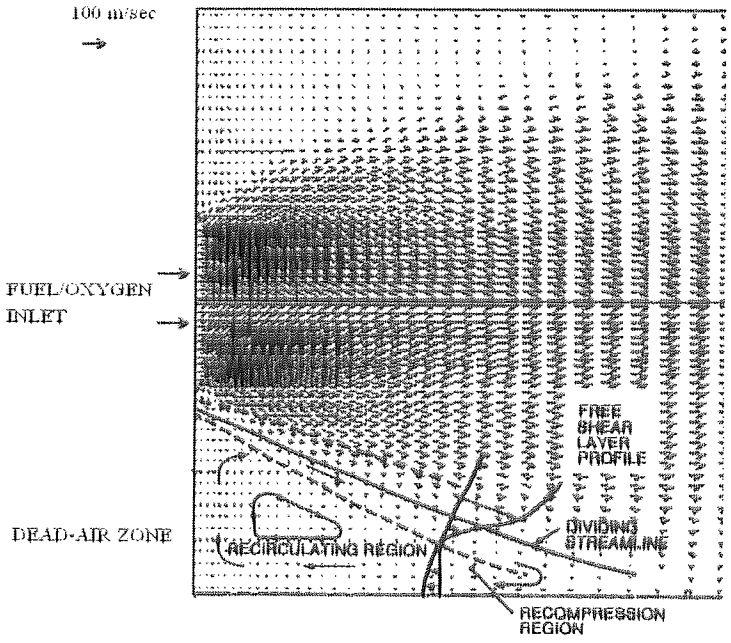

Figure 3.8: Formation of recirculation zones inside the combustion chamber of propane fuelled HVOF system.

3.3.6 Combustion of Liquid Fuels

The combustion of liquids is typically accomplished by injecting through an orifice into a gas-phase combustion chamber. Turbulence inside of the liquid stream causes the emerging liquid fuel to break up into a dense cloud of droplets that along with the oxidizer pass through the combustion zone. Heat transfer to the droplet increases vapour pressure, and thus full evaporation into the gas phase. A non-premixed flame surrounds the droplet or droplet group where vapour and not the liquid itself is what ultimately burns. The three phases of droplet combustion are:

1. Heating Phase: Heat from the gas phase causes the droplet surface to heat up. The heat is convected into the droplet until the entire droplet reaches the boiling temperature.

2. Fuel Evaporation Stage: Fuel evaporates into the gas phase and combustible mixture is created.

3. Combustion Phase: The mixture ignites and burns as a spherically symmetric laminar non-premixed flame.

Noting that the combustion of sprays is a complex interaction of many different processes such as droplet heating, evaporation, combustion with turbulent flow field is evident that spray combustion is a challenging task. The overall model of liquid combustion consists of a wide array of interacting submodels.

According to [90] four combustion modes of droplet cloud are identified. If the spray cloud is very dense the inner core of the spray is saturated and the droplets do not evaporate. Close to the surrounding oxidizer evaporation takes place and cloud of fuel vapour that is formed diffuses into the oxidizer, forming a non-premixed flame. This mode is known as the "external group combustion with sheath vaporization". When the cloud density is lower all the droplets evaporate, but still the flame zone is at the boundary between the fuel vapour and the surrounding oxidizer ("external group combustion with standoff flame"). Finally for dilute sprays some of the droplets are in environment with excess of oxidizer and as result single droplet combustion occurs ("internal group combustion"). The kerosene combustion that is described in the next chapter falls into the category of "external group combustion with standoff flame". A qualitative consideration on the effect of droplet combustion can be found in [91]. Ignition of reactive mixture of fuel vapour and oxidizer is connected by emergence of a flame front in the vicinity of the droplet. Depending on the flow conditions two different types of the flame occur: the envelope flame and the attached flame. The first is characteristic of dense sprays while the second of coarse droplets in a gas flow with high relatively velocities.

Chapter 4

Modelling of Gas Flow Dynamics

4.1 Propane Fueled HVOF System

The thermal process of HVOF is very complicated with combustion, supersonic flow expansion, turbulent mixing and gas-solid interaction. Being a critical element of the process, combustion not only generates the required energy for powder heating but also affects the multiphase flow pattern. Subsequently, fuel is the main driven force for the evolution of HVOF thermal spray systems. The gas fuel system namely HVOGF, is an early stage product and consumes gas fuel such as propylene or hydrogen. Most recently, the liquid fuel system namely HVOLF has been given much attention due to their advantages, such as, cheap fuels namely kerosene or propane, high momentum output with the design of convergent-divergent nozzle, and high flow rate. Numerical modelling has become an important tool in the study of HVOF systems. A well-developed model can provide insight into the underlying physics of the process by overcoming the technical constrains imposed by experiments. In the present study, a wide range of combustion models and numerical methods are examined for a HVOLF gun consuming liquid propane.

4.1.1 Model Development

The studied HVOLF gun is represented schematically in figure 4.1. Fuel and Oxygen are injected axially into the combustion chamber, where the fuel burns and the combustion products are accelerated down through the convergent-divergent nozzle and the long parallel-sized barrel. The gun is protected by cooling water to avoid over-heating. Powder particles are injected into the barrel through a tapping angle by a carrier gas in the front of the barrel, this design can effectively reduce the overheating of the powder particle. The study is focused on the combustion process and subsequent gas flow pattern, while

particle dynamics and gas-particle interaction are not included. The commercial finite volume code FLUENT is used for the numerical study.

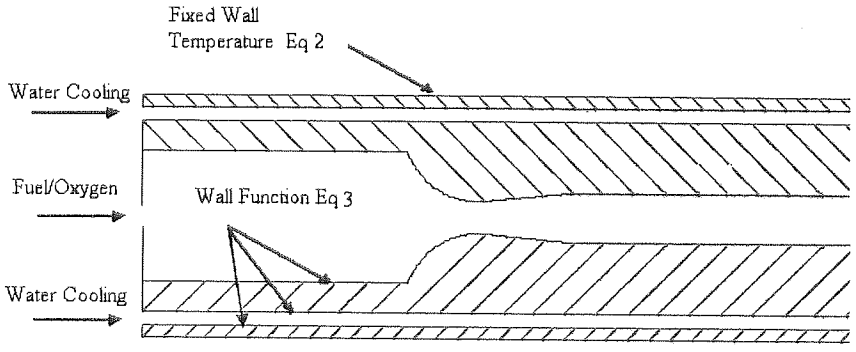

Figure 4.1: Schematic representation of the HVOLF gun geometry.

As illustrated in figure 4.1, the HVOLF gun has an axis-symmetric geometry and a two-dimensional model is employed to reduce the complexity and computational time. The governing equations for the 2-D model in the Cartesian tensor form are:

mass conservation equation

$$\frac{\partial \rho}{\partial t} + \frac{\partial}{\partial x_i}(\rho u_i) = 0 \tag{4.1}$$

momentum conservation

$$\frac{\partial}{\partial t}(\rho u_i) + \frac{\partial}{\partial x_j}(\rho u_i u_j) = -\frac{\partial p}{\partial x_i} + \frac{\partial}{\partial x_j}(\tau_{ij})_{eff} + \frac{\partial}{\partial x_j}(-\overline{\rho u_i' u_j'}) \tag{4.2}$$

energy transport equation

$$\frac{\partial}{\partial t}(\rho E) + \frac{\partial}{\partial x_i}[u_i(\rho E + p)] = \frac{\partial}{\partial x_j}\left(k_{eff}\frac{\partial T}{\partial x_j} + u_i(\tau_{ij})_{eff}\right) + S_h \tag{4.3}$$

where the deviatoric stress tensor is given by

$$(\tau_{ij})_{eff} = \mu_{eff}\left(\frac{\partial u_j}{\partial x_i} + \frac{\partial u_i}{\partial x_j}\right) - \frac{2}{3}\mu_{eff}\frac{\partial u_i}{\partial x_i}\delta_{ij} \tag{4.4}$$

the effective thermal conductivity is

$$K_{eff} = K + \frac{c_p \mu_t}{\sigma_t} \tag{4.5}$$

Liquid fuel and oxygen are pre-mixed before being sprayed into the combustion chamber. In this numerical study, it is assumed that liquid propane evaporates to gas state

and mixed perfectly with oxygen before combustion. This assumption is only valid to liquid propane due to its unique characteristics of extremely low boiling point. When kerosene is used in HVOLF applications, a numerical model needs to include the effect of droplets evaporation and interaction, which will be addressed in the next section.

4.1.2 Model Grid and Computational Domain

This study uses a structured grid based on the following reasons: i) a relatively simple geometry; ii) optimisation of computing cost; iii) effective convergence control at higher order discretization schemes; iv) easy generation of fine local grid by varying nodal point distribution. The computational domain of this axis-symmetric flow includes the gun and external free jet region as illustrated in figure 4.2. The internal grid is composed of 30 radial nodes, 70 axial nodes in the combustion chamber, 170 axial nodes in the converging-diverging nozzle and 200 axial nodes in the barrel. The internal domain is meshed with 40,000 cells. The external domain for the free jet covers the stand-off distance region, typically 200-300 mm from the nozzle exit in axial direction, with 27,000 cells. The cells attached to the pressure outlet faces of the domain are in total 300 while the wall adjusted cells are 350. The O/F inlet mesh faces are 20. Fine meshes are employed to the sensitive areas such as, the nozzle entrance and exit, the barrel exit and the free-jet centreline where high gradients are expected and great accuracy is required in order to capture the compressibility effects. The finer nodal point distribution towards the centreline of the domain is achieved by specifying a distribution factor. The average cell area inside the combustion chamber is 0.000001 m^2 and at the regions close to the O/F inlet and the nozzle entrance the average cell area drops to 0.0000001 m^2. In the free jet region the minimum cell area is 0.000000008 m^2 and is increased to 0.000001 m^2 close to the domain exit. Along the barrel the mesh is more coarse with maximum cell face area at the centre of 0.000003 m^2.

The gas exhausts from the gun to air, where external pressure boundary is applied to the ambient temperature of 300 Kelvin and atmospheric pressure. The interior surfaces of the gun are protected by the cooling water and defined as no-slip wall with a constant temperature of 330 Kelvin which is the measured temperature for the outflow water. In reality, a temperature distribution is expected when water flow through the gun and the water temperature is expected to increase gradually. The heat transfer process of water cooling is not the focus of this study and a heat transfer model solving the water cooling mechanism will be reported in the third section of this chapter.

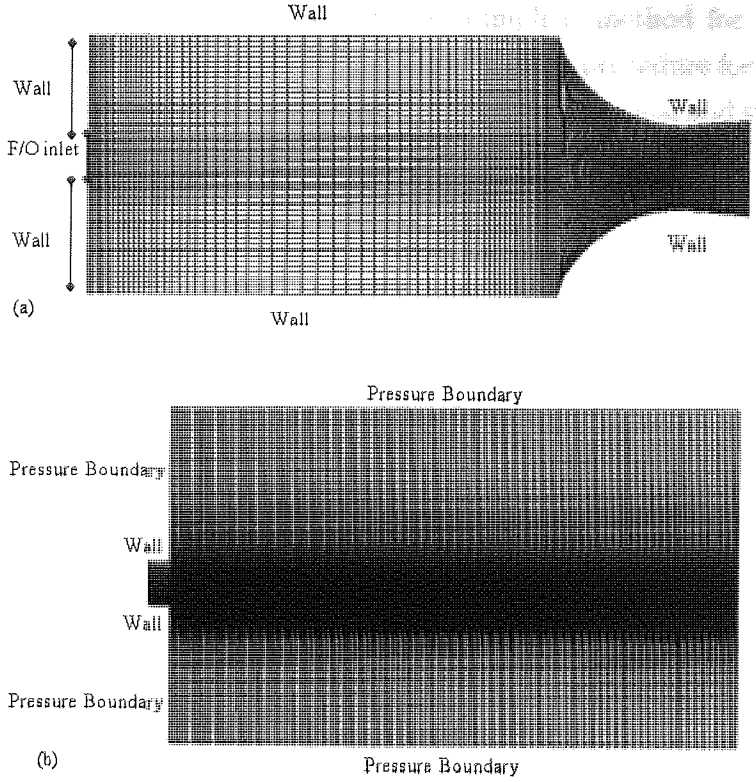

Figure 4.2: Computational grid and boundary conditions being used in the HVOLF model: (a) Internal domain including the combustion chamber and the convergent-divergent nozzle), (b) External domain

4.1.3 Solver Formulation

The numerical method used in this study is a segregated solution algorithm [92] with a control volume based technique. The segregated solution is chosen, due to the advantage over the alternative method of strong coupling between the velocities and pressure. This can help to avoid convergence problems and oscillations in pressure and velocity fields. This technique consists of an integration of the governing equations of mass, momentum, species, energy and turbulence on the individual cells within the computational domain to construct algebraic equations for each unknown dependent variable. The pressure

and velocity are coupled using the SIMPLE (semi-implicit method for pressure linked equations) algorithm [93, 94] which uses a guess-and-correct procedure for the calculation of pressure on the staggered grid arrangement. It is more economical and stable compared to the other algorithms.

The QUICK (quadratic upwind interpolation) scheme [27] is used for the discretization of the model equations. As a higher order scheme, the QUICK method can minimize false diffusion errors, but it is less computationally stable. In contrast, a first/second order upwind scheme is always bounded and provides stability for the discretization of the pressure-correction equation. However, the upwind scheme will produce erroneous results when the flow is not aligned with the grid lines. A comparison of both schemes is discussed in the result section.

4.1.4 Turbulence Modelling

A wide variety of flow problems can be calculated by using the standard $\kappa - \varepsilon$ model [95] based on the presumption that an analogy between the action of viscous stresses and Reynolds stresses on the mean flow exists. Although it is usually acceptably accurate for simple flows, inaccuracies could rise from the turbulent–viscosity hypothesis and from the equation of turbulence dissipation rate for complex flows. Improvement has been made to the standard $\kappa - \varepsilon$ model, a recent development is the realizable $\kappa - \varepsilon$ model [29]. The transport equations for the realizable $\kappa - \varepsilon$ model are:

turbulent kinetic transport equations

$$\frac{\partial}{\partial t}(\rho k) + \frac{\partial}{\partial x_i}(\rho k u_j) = \frac{\partial}{\partial x_i}\left[\left(\mu + \frac{\mu_t}{\sigma_k}\right)\frac{\partial k}{\partial x_j}\right] + G_k + G_b - \rho\varepsilon - Y_M + S_k \tag{4.6}$$

rate of dissipation of energy from the turbulent flow

$$\frac{\partial}{\partial t}(\rho \varepsilon) + \frac{\partial}{\partial x_j}(\rho \varepsilon u_j) = \frac{\partial}{\partial x_j}\left[\left(\mu + \frac{\mu_t}{\sigma_\varepsilon}\right)\frac{\partial \varepsilon}{\partial x_j}\right] + \rho C_1 S_\varepsilon - \rho C_2 \frac{\varepsilon^2}{k + \sqrt{\nu\varepsilon}} + C_{1\varepsilon}\frac{\varepsilon}{k} C_{2\varepsilon} G_b + S_\varepsilon \tag{4.7}$$

where the turbulent viscosity is

$$\mu_t = \rho C_\mu \frac{k^2}{\varepsilon} \tag{4.8}$$

the coefficient of dynamic viscosity is

$$C_\mu = \frac{1}{A_0 + A_s \frac{kU}{\varepsilon}} \tag{4.9}$$

In comparison with the standard $\kappa - \varepsilon$ model, the realizable $\kappa - \varepsilon$ model contains a new formulation of the turbulent viscosity where the dynamic viscosity coefficient is no longer constant.

4.1.5 Combustion Models

The end products of propane combustion can be regarded as carbon dioxide and water in an ideal reaction at stoichiometric ratio.

$$C_3H_8 + 5O_2 -> 3CO_2 + 4H_2O$$

However when temperatures in excess of 2000 K are reached, CO2 and H2O will dissociate into a number of species with light molecular weight due to strong thermal atomic vibration. In the present work the effects of dissociations and intermediate reactions are represented by an equilibrium formulation as follows. The equilibrium formula is calculated using the Stanjan Equilibrium Reaction Model. The input required is a set of mixing variables and a linearized heat loss. The Stanjan equilibrium package then computes chemical equilibrium for the given system. The software returns the values for the species variables at chemical equilibrium including max flame temperature, pressure, density, mixture molecular weight, heat capacity, and species mole fractions.

$C_3H_8 + 5O_2 -> 1.211CO_2 + 2.789H_2O + 1.788CO + 0.842OH + 0.864O_2 + 0.429O + 0.556H_2 + 0.466H$

The eddy dissipation model [96] is used to solve this global reaction. This approach is based on the solution of transport equations for species mass fractions. The reaction rates are assumed to be controlled by the turbulence instead of the calculation of Arrhenius chemical kinetics. The net rate of production for species i due to reaction r, is given by the smaller of the two expressions below:

$$R_{i,r} = \upsilon_{i,r} M_{w,i} A \rho \frac{\varepsilon}{k} \min\left(\frac{Y_R}{\upsilon_{R,r} M_{\omega,R}}\right) \tag{4.10}$$

$$R_{i,r} = \upsilon_{i,r} M_{w,i} A B \rho \frac{\varepsilon}{k} \left(\frac{\sum_P Y_P}{\sum_j^N \upsilon_{j,r} M_{\omega,j}}\right) \tag{4.11}$$

Two more combustion models are tested for a good comparison, namely the laminar finite rate model which computes the chemical source terms using the Arrhenius expressions without the effects of turbulent fluctuations, and the finite rate eddy dissipation model which computes both the Arrhenius rate and mixing rate, and uses the smaller of the two with the effects of turbulence.

4.1.6 Results and Discussions

The results presented in this section are from the gun geometry and grids shown in figures 4.1 and 4.2 at the baseline conditions as listed in Table 4.1.

Attributes	Definition
Combustion model	Eddy dissipation model
Turbulent model	Realizable $\kappa - \varepsilon$ model
Solution algorithm	SIMPLE
Discretization scheme	QUICK
Fuel to oxygen ratio	Stoichiometric ratio
O/F mass flow rate	0.022Kg/s

Table 4.1: Baseline model specification.

Flow Dynamics Inside the Gun

The flame structure is shown by the temperature contours plot in figure 4.3. The fuel-plus-oxygen (inlet temperature 300K) stream creates a cold jet initially and then the mixture is burned to accelerate downstream the combusting products. The orientation of the contours indicates that the flame twist slightly away from the wall towards the nozzle of the gun. The maximum temperature in the chamber is 3095 K with the hottest regions being allocated in two right hand corners. The flow pattern represented by the velocity vector plot in figure 4.4 clearly demonstrates a recirculation in the transverse direction near the fuel-oxygen inlet. The flow transition from subsonic to supersonic conditions through the convergent-divergent nozzle is vividly shown by the Mach number plot in figure 4.5. The subsonic flow is accelerated in the convergent region, the flow reaches sonic state at the throat and further accelerated to supersonic condition in the divergent region. On entering the barrel, the supersonic flow further expands through a series of shock waves and becomes stabilized. The flow development is reflected quantitatively by the centreline results in figure 4.6(a).

External and Overall Flow Dynamics

The expansion of the supersonic free jet outside the gun is illustrated in figure 4.7(a). It is shown that, upon entering the ambient environment, the gas flow immediately expands and is accelerated up to Mach number 2. The high-speed jet goes through a series of compression and expansion before it declines rapidly. Six shock diamonds are captured in the region of elevated velocity, temperature and pressure, which shows a close resemblance

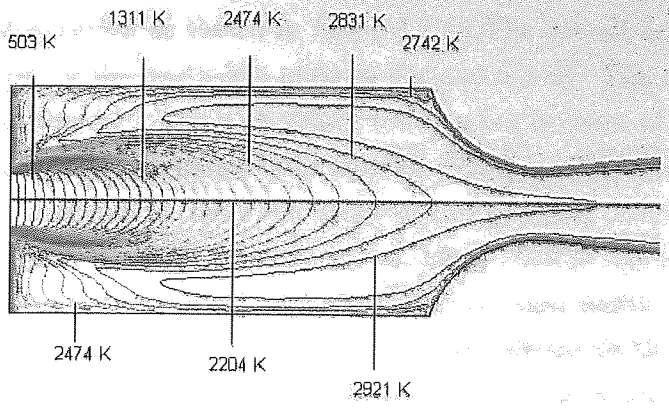

Figure 4.3: Predicted temperature contours within the combustion chamber by the baseline model.

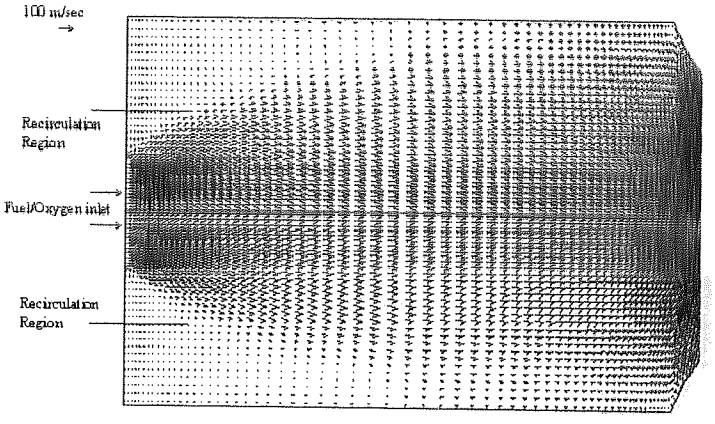

Figure 4.4: Predicted velocity vectors within the combustion chamber by the baseline model.

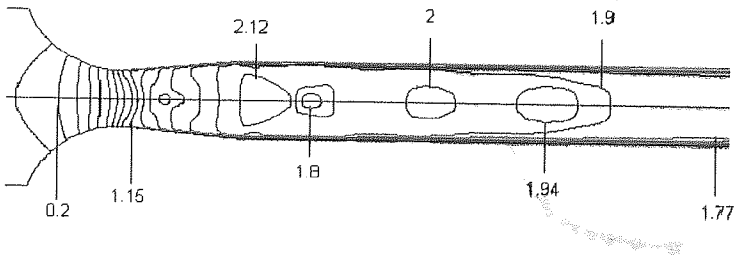

Figure 4.5: Predicted Mach number contours in the convergent-divergent nozzle by the baseline model.

to the experimental observation as shown in figure 4.7(b).The overall flow dynamics are quantitatively presented by the centreline plots in Figures 6(a-d). The gas temperature increase sharply within the combustion chamber and reaches an area of stability within the barrel before decaying in the external environment. The gas velocity increases sharply in the convergent-divergent nozzle, develops maxima and minima, decreases marginally across the barrel and again develops maxima and minima outside the barrel where the free jet is developed. This pattern of expansion and compression waves is repeated until mixing with the surrounding atmosphere which eventually dissipates the supersonic jet. The pressure remains high within the combustion chamber, decreases sharply in the convergent-divergent nozzle and reaches near atmospheric level in the barrel.

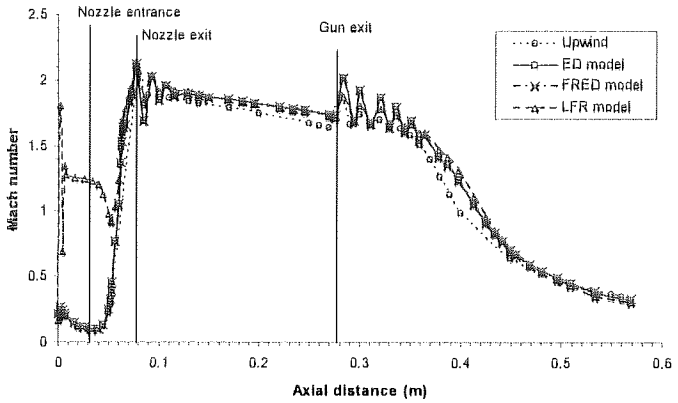

(a) Mach number

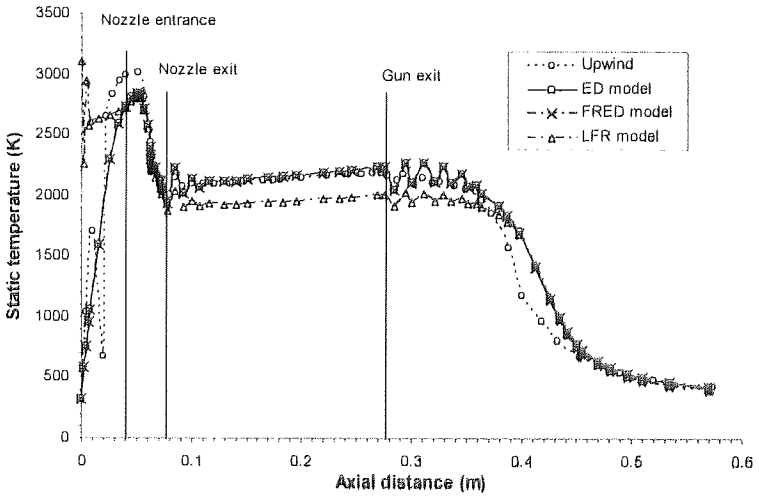

(b) Static temperature)

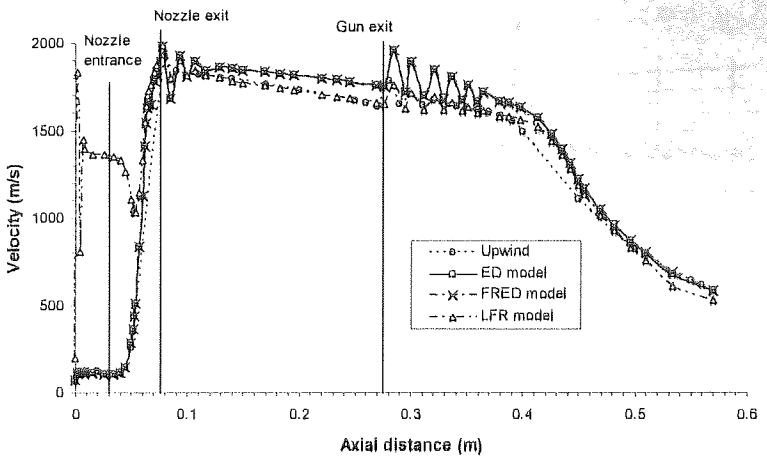

(c) Velocity)

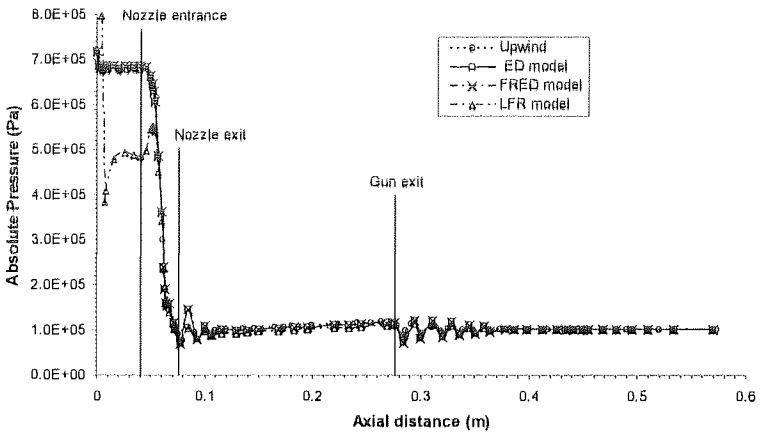

(d) absolute pressure

Figure 4.6: Predicted gas profiles along the centreline (a) Mach number (b) Static temperature (c) Velocity (d) Absolute pressure

Effect of Discretization Schemes

In the present work two discretization schemes are examined, namely, the upwind and QUICK scheme. The employed upwind scheme based on the backward differencing formula has a first order accuracy in terms of the Taylor series truncation error. The QUICK scheme based on the quadratic function uses a three-point upstream-weighted quadratic interpolation for cell face values and has a third order accuracy in structured grids. By examining the results from both schemes, considerable discrepancies are found in the free jet region. The upwind scheme can only generate two shock diamonds as shown in figure 4.7(c) while the QUICK scheme is able to capture a close to reality, six shock diamonds,

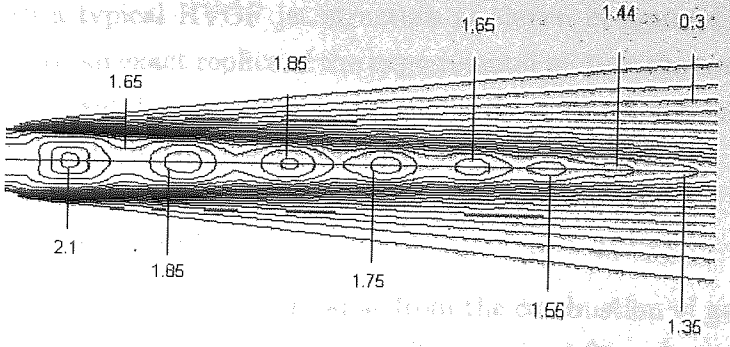

(a)Mach number contours predicted by the baseline model

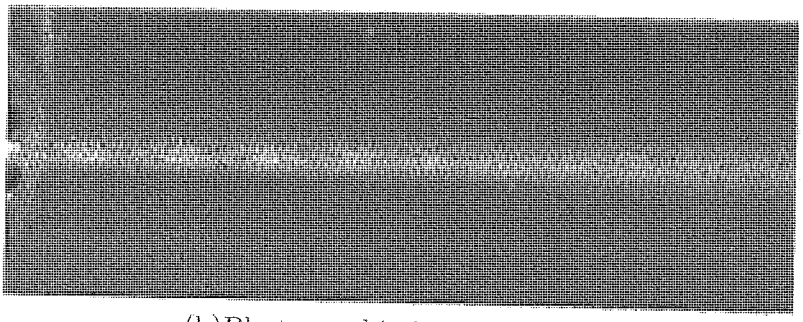

(b)Photographic image of gas jet

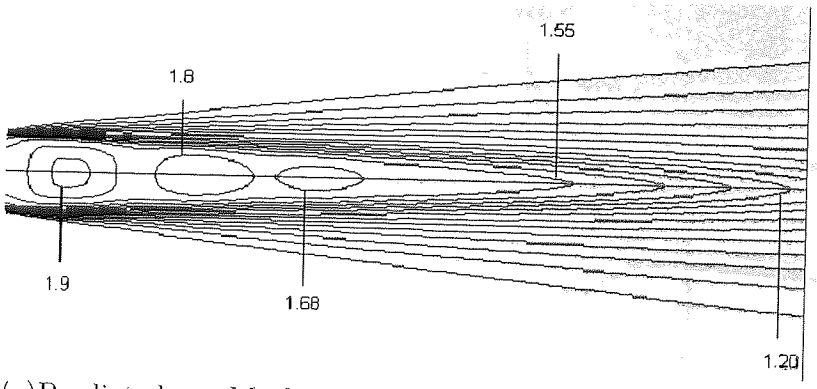

(c)Predicted gas Mach number contour using upwind scheme

Figure 4.7: Gas jet structures outside the HVOLF gun

which is further proved by the centreline plots. The capture of six shock diamonds is the best result being reported in the open literature and is close to experimental observation. Despite the discrepancy, both schemes predict a similar trend and flow characteristics in the centreline as illustrated in figures 4.6(a-d). It is implied that the upwind scheme tends to smooth the shocks in the supersonic region for high-speed compressible flow and the QUICK offers a more realistic prediction. The prediction of six shock diamonds is

compared well with a typical HVOF jet structure as shown in figure 4.7(b). Since the numerical model is not an exact replice of the experimental picture the comparison is only aiming to provide a qualitative agreement and similarity in shock number and structure instead of a detailed quantitative comparison.

Effect of Combustion Models

The premixed flames applied to this work arise from the combustion of gaseous reactants which are perfectly mixed prior to combustion. The premixed flame is a rapid, essentially constant-pressure as shown in figure 4.6(d), and exothermic reaction. Three combustion models, namely laminar finite rate (LFR), eddy dissipation (ED) and finite rate-eddy dissipation (FRED) are tested to evaluate their performance in the HVOF application. A detailed examination of the predictions from ED and FRED models shows similar flow patterns, which are represented by the identical results for the centreline as illustrated in figures 4.6(a-d). On the contrary, LFR model predicts a completely different flow pattern. Instead of the conical shape flame representing the natural evolution of cold inlet stream to hot flame as depicted by the ED model in Figure 4.3, the temperature contours generated by LFR model in figure 4.8 shows the flame is confined to a thin region around the centre without turbulence effects.

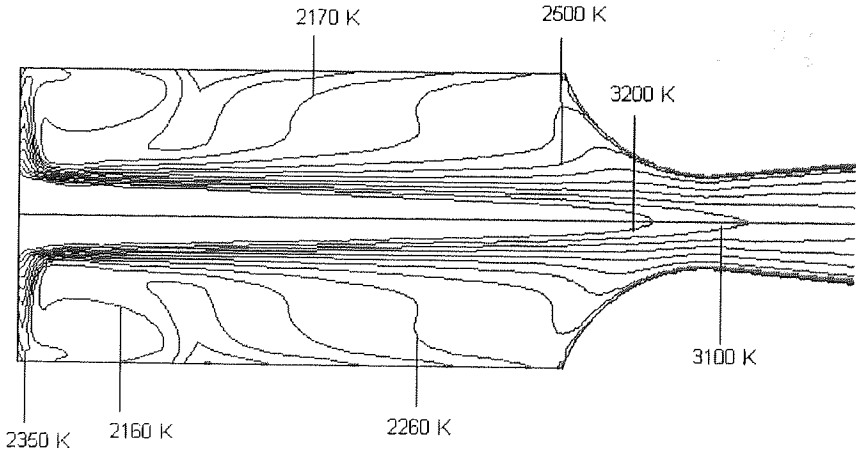

Figure 4.8: Predicted temperature contours within the combustion chamber by LFR model

The laminar model predicts an instantaneous reaction and the flame reaches the maximum temperature immediately after the inlet. Without the turbulent dissipation, a higher maximum flame temperature is found and most the gas flow is concentrated in the centerline region which results in an extremely higher gas velocity in the center

compared to the other regions of the combustion chamber, as illustrated in figure 4.9. Practical experience on operating HVOF systems shows that blockage may occur inside the gun with a configuration as shown in figure 4.10, where the powder particles are injected into the center of the combustion chamber. Examination on the blocked gun shows powder particles accumulate on the internal surfaces of the combustion chamber. It is widely understood that small particles generally follow the gas flow pattern and their profiles of temperature and velocity are close to that of the gas flow, in the case, small powder particles are more easily to reach melting state and projected towards the internal surfaces by the gas flow. The existence of powder particles on the internal surface of the combustion chamber implies that the gas flow spreads in the combustion chamber instead of being confined to the center. The current HVOF design in figure 4.1 moves the powder injection behind the combustion chamber to effectively avoid the blockage and particle overheating. The experience on other HVOF systems implies that the flow pattern predicted by LFR model without turbulent dissipation could not be valid.

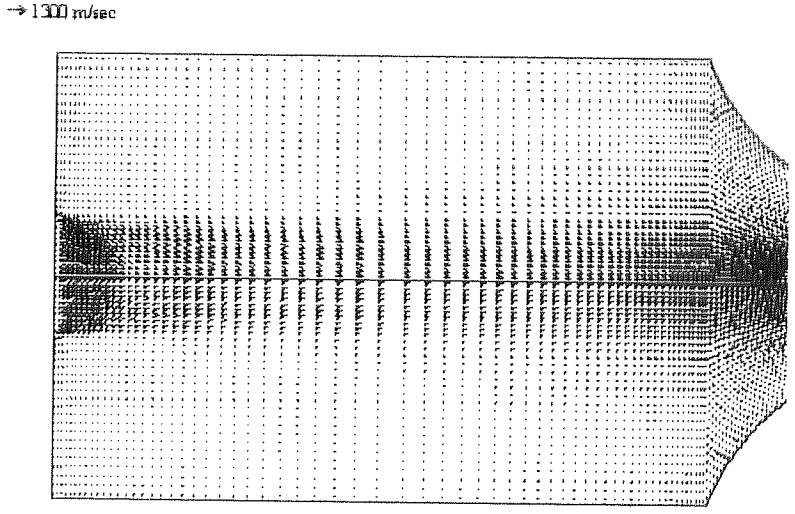

Figure 4.9: Predicted velocity vectors within the combustion chamber by LFR model

One of the important criteria to evaluate combustion models is to examine flame temperature. Although the combustion process in HVOF applications is not adiabatic while some heat is taken away by the cooling water, the well-documented data on adiabatic flame temperature could be used for qualitative evaluation of the combustion model. Here the maximum flame temperature within the combustion chamber is compared with the adiabatic flame temperature of propane produced by [97, 98] as shown in figure 4.11. It should be noted that the adiabatic temperature from Hewitt [97] is produced at one atmospheric pressure and the NASA data is calculated at the combustion chamber pres-

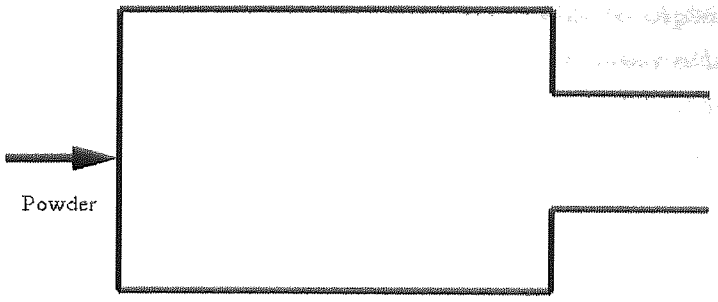

Figure 4.10: Schematic representation of the combustion chamber design where powder particles are injected into the centre of HVOF gun

sure which is 7 times atmospheric pressure. Both results show the same trend that the flame temperature increases according to the rise of oxygen ratio, peaks at 90% and then decreases slightly till the stoichiometic ratio.

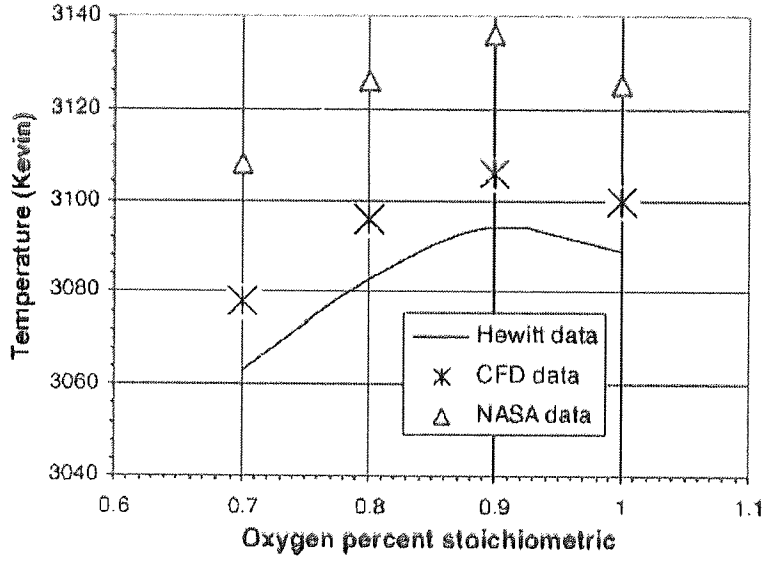

Figure 4.11: Comparison of CFD predicted maximum flame temperature with documented adiabatic flame temperature.

4.1.7 Conclusions

A CFD model has been presented to investigate the combustion and gas dynamics in an HVOF thermal spray gun using the liquid fuel propane. The following conclusions have been obtained in this study:

1. The third-order discretization scheme (QUICK) is able to capture the supersonic shock diamonds closely aligned with the experimental observation in the free jet region. In contrast the first order upwind scheme found to be inadequate to capture the detailed characteristics of the flow. The model predicts that shock waves also exist inside the HVOLF gun where the high-pressure gas flow accelerates through the convergent-divergent nozzle and expands in the front of the barrel.

2. The prediction of reacting flow in the combustion chamber is critically affected by turbulent fluctuations. Without the turbulent effect, the laminar finite rate combustion model predicts that the gas flow is confined to a narrow region around the center of the gun. This computational phenomenon is not consistent with experimental evidences in other HVOF guns that indicate small powder particles travel towards the internal surface of the gun as a result of gas flow dynamics. Both eddy dissipation and eddy dissipation-finite rate combustion models generate similar results with a conical shape flame naturally spreading in the combustion chamber.

3. The global reaction model of propane combustion is able to give a reasonable prediction on heat generation, in term of flame temperature. The same trend is found for the predicted maximum flame temperature and documented adiabatic flame temperature by varying fuel to oxygen ratio.

4.2 Kerosene Fueled HVOF System

Liquid fuelled high velocity oxy-fuel (HVOF) thermal spraying systems are capable of generating more momentum output to powder particles in comparison with gas fuelled systems. The use of low cost fuel such as kerosene makes this technology particular attractive. High quality coating requires thermal spraying systems delivering consistent performance as a result of the combustion during HVOF spraying. The combustion of kerosene is very complicated due to the variation of fuel composition and subsequently makes it extremely challenging for process control. This section describes a three-dimensional simulation using mathematical models available in FLUENT. The combustion and discrete particle models within the numerical code are applied to solve the combustion of kerosene and couple the motion of fuel droplets with the gas flow dynamics in a Lagrangian fashion. The effects of liquid fuel droplets on the thermodynamics of the combusting gas flow are examined thoroughly.

The employed turbulent, combustion and spray models have been vigorously tested against experimental data respectively in the open literature and have demonstrated

accurate predictions in thermal fluid applications including turbulent flame propagation [99], engine combustion [100, 101] and spray atomisation [102]. The prediction of kerosene fuelled HVOF process is validated against the documented experimental measurement of [103]. The geometry of this simulation is based on a commercial HVOF system (MetJet III, Metallisation UK). The results are focused on kerosene combustion and subsequent gas dynamics within the spraying gun. The development of supersonic free jet outside the gun has been described in the previous section and is not included in this section. The solver formulation, turbulence and combustion models were also mentioned previously.

4.2.1 Model Description

In this HVOF system as shown in figure 4.12, premixed fuel and oxygen are injected into the combustion chamber through three evenly distributed holes 8mm from the centre. The hot gas accelerates down through the nozzle which contains a convergent-divergent session and a long parallel-sized barrel. Powder particles are injected into the barrel through a tapping angle by a carrier gas in the front of the barrel. During operation, the gun is protected by cooling water to avoid over-heating. To correctly represent the gas flow dynamics, a three-dimensional model is employed in the study to give accurate predictions. This study is focused on the two phase combustion process where fuel droplet evaporation, mixing and chemical reaction are modelled and subsequent gas flow pattern is described.

The compressible turbulent chemically reacting flow model has been described in the previous sections and only a brief introduction is given here. For the combustion of kerosene, $C_{12}H_{26}$ is used to have a representative average value for the individual components. The combustion kinetics is represented by one global reaction scheme which takes dissociations and intermediate reactions into account.

$$C_{12}H_{26} + 17.75O_2 > 5.039CO_2 + 7.66H_2O + 7.26CO + 3.24OH + 3.041O_2 + 1.31O + 1.29H_2 + 0.924H$$

These coefficients are dependent on variables such as the combustion chamber pressure, fuel to oxygen ratio, mass flow rate or even the torch geometry. To derive those coefficients, an iterative approach based on the Stanjan chemical equilibrium model is employed to make sure the coefficients representing the correct pressure level and thermal flow field. The eddy dissipation model is used to solve this global reaction. This approach is based on the solution of transport equations for species mass fractions. The reaction rates are assumed to be controlled by the turbulence instead of the calculation of Arrhenius chemical kinetics (equations 4.10,4.11).

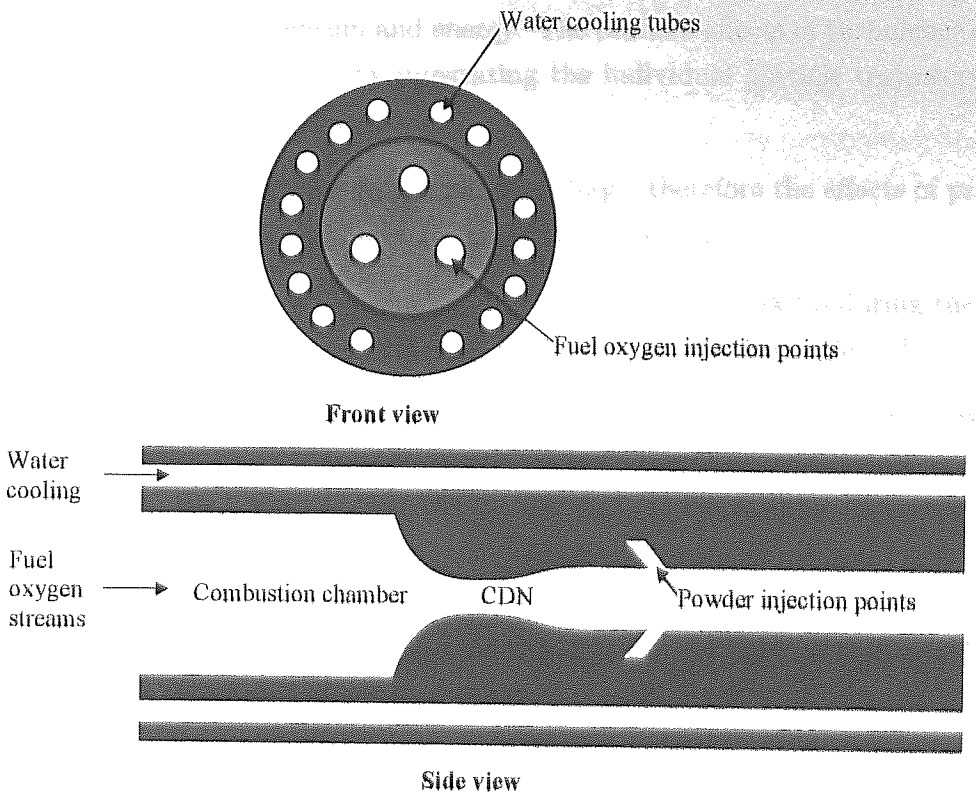

Figure 4.12: Schematics of liquid fuelled HVOF thermal spray gun.

The powder particle dynamics and gas-particle interaction driven by the gas flow are not included in this study and will be examined in the next chapter. The history of fuel droplets are computed with a Lagrangian formulation where the finite inter-phase transport rates and effects of turbulence interactions between the droplet and gas phases are considered. By using this treatment the evaporation history and temperature change for droplets can be calculated. For the accurate prediction of droplet velocity and concentration, a large amount of droplet trajectories are used to better represent the aerosol mixture.

The droplets are injected into the computational domain from the inlet boundary surface with uniform size distribution. The study is intended to shed lights on the importance of fuel atomisation process. However the physical atomization process and the resulted droplet diameter distribution prior to injection are out of the scopes of this study. The conditions under which each droplet has a set of governing equations are:

1. The liquid droplet and oxygen gas phases have their own initial continuous velocity and temperature and co-exist at each location in the flow field.

2. Liquid phase has its own turbulent fluctuations that result in turbulent droplet

transport of mass, momentum and energy. The random effects of turbulence on the particle motion are counted by integrating the individual particle trajectory with the instantaneous fluid velocity.

3. The density ratio for droplet to gas phases is large, therefore the effects of pressure gradients, virtual mass and Saffman forces are neglected.

4. The droplet collisions are neglected and droplets do not break up during the evaporation process while chemical reaction in the droplets is also neglected.

The operation parameters are 0.00351 kg/s for kerosene and 0.0129 kg/s for oxygen.

4.2.2 Particle Models

Equations of Motion

The equation of motion for particles can be written as a force balance that equates the droplet inertia with forces acting on the droplet:

$$\frac{du_p}{dt} = F_D\left(u - u_p\right) + \frac{g_x\left(\rho_p - \rho\right)}{\rho_p} \tag{4.12}$$

the drag force per unit particle mass is:

$$F_D = \frac{18\mu}{\rho_p d_p^2}\frac{C_D Re}{24} \tag{4.13}$$

the drag coefficient CD given by [104]:

$$C_D = \frac{24}{Re_d}\left(1 + b_1 Re_d^{b_2}\right) + \frac{b_3 Re_d}{b_4 + Re_d} \tag{4.14}$$

$b_1 = \exp\left(2.3288 - 6.4581\phi + 2.4486\phi^2\right)$
$b_2 = 0.0964 + 0.5565\phi$
$b_3 = \exp(4.905 - 13.8944\phi + 18.4222\phi^2 - 10.2599\phi^3)$
$b_4 = \exp\left(1.4681 + 12.2584\phi - 20.7322\phi^2 + 15.8855\phi^3\right)$

the shape factor given by [105] is:

$$\varphi = \frac{s}{S} \tag{4.15}$$

the relative Reynolds number is defined as:

$$Re = \frac{\rho d_p \left|u_p - u\right|}{\mu} \tag{4.16}$$

Turbulent Effects on Particles

The turbulent dispersion of particles is predicted by a stochastic tracking approach. The random effects of turbulence on the particle motion are counted by integrating the individual particle trajectory with the instantaneous fluid velocity. Equation (4.17) describes the time spent in turbulent motion along the particle path ds.

$$T = \int_0^\infty \frac{u_p'(t)u_p'(t+s)}{\overline{u_p^2}} ds \tag{4.17}$$

The Lagrangian integral time, T_L, can be obtained by matching the diffusivity of particles $\overline{u_i' u_j'} T_L$ with the predicted diffusion rate $\frac{\nu_t}{\sigma}$ by the realizable $\kappa - \varepsilon$ turbulence model as follow:

$$T_L \approx 0.15 \frac{k}{\varepsilon} \tag{4.18}$$

Heat and Mass Transfer

The droplet heating law is applied when the droplet temperature is lower than the vaporization temperature where a heat balance is applied:

$$m_p c_p \frac{dT_p}{dt} = hA_p(T_\infty - T_p) + \varepsilon_p A_p \sigma(\theta_R^4 - T_p^4) + S \tag{4.19}$$

When the droplet temperature is below the evaporation point the source term S in equation 4.19 is zero while above the evaporation temperature is: $\frac{dm_p}{dt} L$

The heat transfer coefficient is evaluated using the Ranz [106] correlation:

$$Nu = \frac{hd_p}{k_\infty} = 2.0 + 0.6 Re_d^{1/2} \Pr^{1/3} \tag{4.20}$$

When the droplet temperature reaches the vaporization temperature the vaporization Law is activated. The droplet mass reduction is calculated according to:

$$m_p(t + \Delta t) = m_p(t) - N_i A_p M_{\omega,i} \Delta t \tag{4.21}$$

where:

$$N_i = K_c(C_{i,s} - C_{i,\infty}) \tag{4.22}$$

The mass transfer coefficient is calculated according to:

$$Nu_{AB} = \frac{K_c d_p}{D_{i,m}} = 2.0 + 0.6 Re_d^{1/2} Sc^{1/3} \tag{4.23}$$

and

$$C_{i,s} = \frac{p_{sat}(T_p)}{RT_p}, C_{i,\infty} = X_i \frac{p_{op}}{RT_\infty} \tag{4.24}$$

4.2.3 Model Grid and Computational Domain

A 3-D computational model is developed to represent the configuration shown in figure 4.12. Unstructured grid is deployed throughout the domain and the mesh is refined along the centreline and in the nozzle region. Figure 4.13 shows the grid structure within the combustion chamber and the nozzle part. After the examination of grid dependence, the final grid has total tetrahedral mesh cells of 1,108,000. The numerical methods and mathematical models are first applied to a kerosene fuelled 2-D geometry based on the JP-5000 (Praxair, US) HVOF gun. The predicted results are compared with the gas flow measurement [103] and a reasonable agreement is achieved as shown in figure 4.14. The numerical validation was made for the conditions of [103]. The validated numerical approach is then deployed to the 3-D geometry and the results are described in the following section.

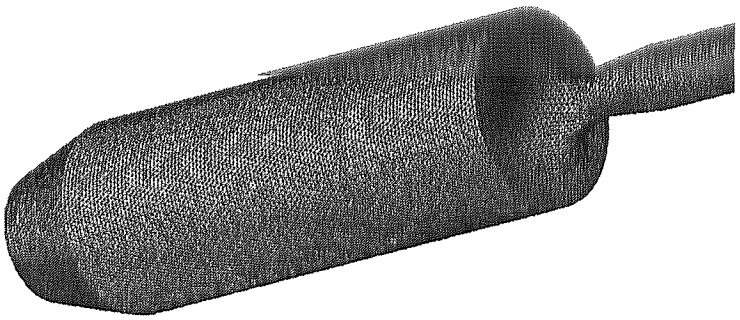

Figure 4.13: Grid structure over the combustion chamber and convergent divergent nozzle part.

4.2.4 Results and Discussions

The development of cold fuel-plus-oxygen streams (given an initial temperature of 300 K as shown in table 4.2) to hot flames are illustrated by the temperature contour plots in figure 4.15. The close distance between the side walls and injection ports tend to shape the flames towards the side walls. Unlike gas fuel which has instantaneous combustion, liquid fuel combustion takes place as fuel droplets evaporate. The evaporation of the droplets is faster in the periphery of the mixture jet and slower at the centre of the jet. Therefore, the flame structure is closely related to the droplet sizes. When fuel droplets

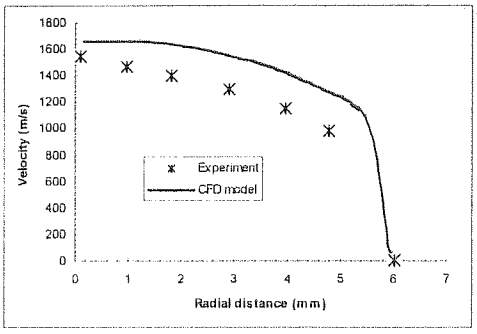

(a) Gas velocity at the exit of the gun

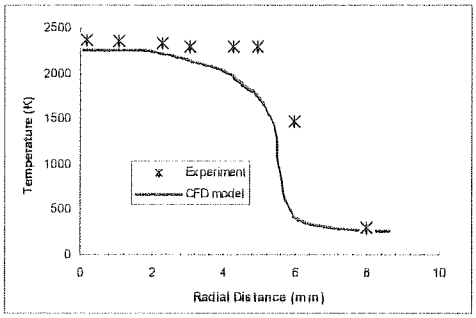

(b) Gas temperature at the exit of the gun

Figure 4.14: Comparison of modelling prediction with gas flow measurement [103].

are very small, rapid heat transfer occurs through the droplet by the surrounding hot gas and the droplets evaporate rapidly, as a result, a combustion process similar to gas fuel could be expected.

Boundaries	**Initial Conditions**
Fuel Inlet	Temperature: 300KMass Flow Rate: 0.00351 Kg/s
Oxygen Inlet	Temperature: 300K Mass Flow Rate: 0.0129 Kg/s
Wall	Temperature: 300K
Pressure Outlet	Pressure: 1 Atm

Table 4.2: Initial boundary values.

In this study, fine droplets of 0.1 μm diameters are injected which generate a confined corn-shape flame and give more uniform temperature profile within the combustion chamber. Further examination is to increase the droplet size to 1 μm diameter, there is no noticeable change of flame structure which implies a marginal variation of droplet

evaporation time. However, the temperature profile within the combustion chamber is changed from a more uniform output to two separate hot spots in the front of combustion chamber. When droplet sizes increase to 6 μm diameters, a more dispersed flame structure is observed as fuel droplets travel much further downstream before being evaporated. For 10 μm diameter droplets, longer droplet evaporation periods further disperse the flames to large fan-shape structure and push the two hot spots toward the centre of combustion. The maximum temperature plots in figure 4.16 confirm the slight reduction of flame temperature as the fuel droplet sizes increase.

Flow Recirculation

The velocity vector plots in figure 4.17 indicate circulation zones between the injection ports. The vector plots show that the location and magnitude of recirculation flow are also dependent on droplet sizes and the recirculation zone slightly moves away from inlet as the droplet size increases. The magnitude and locations of the recirculation regions are more graphically presented by the surface contour plots of vorticity magnitude in figure 4.18. Due to the periodic nature of the geometry, the flow pattern around one injection part shall give a good representation of the overall flow dynamics, in this case, attention should be given to the top injection port. The red regions represent the significance of vorticity (recirculation flow). It is shown that large area of recirculation appear on the side surface and around the top injection hole for 0.1 μm diameter droplets; the recirculation regions has not changed noticeably as the droplets increase to 1 μm; recirculation flows have vanished mostly on the side surface and shrunk slightly around the top injection hole for 6 μm droplets; recirculation flows are reduced further for 10 μm droplets. Overall the results illustrate a substantial reduction of recirculation flows as the droplet size increases.

Droplet Evaporation

The trajectories of fuel droplets at various sizes are vividly shown in figure (4.19). Apparently small droplets only endure short distances and are confined within a more uniform pattern while large droplets travel much further and disperse into the gas flow. The in-flight droplet evaporation along the core of the flames is more quantitatively shown in figure 4.20. The liquid droplets start to evaporate as entering the combustion chamber, the evaporation rate increases rapidly as the droplet are heated up, the evaporation rate peaks when the majority of liquid fuel is transformed into gas and the evaporation slows down to a complete end as liquid fuel dries out. The results confirm that large droplets travel greater distance before disappear. It is interesting to point out that 0.1 and 1 μm droplets share good degree of resemblance in their evaporation histories despite

the substantial difference of their sizes. That confirms the previous discussion that both droplets have similar flame structures in the current operation condition. This result implies that a cost-effective droplet size could be found as the droplet evaporation rate approaches stagnation point. In this case, an ideally designed atomiser for the kerosene fuelled HVOF gun operating in the current flow rate shall produce droplet sizes around 1 μm.

Gas Flow Dynamics

The radial profile of gas velocity within the combustion chamber in figure 4.21 shows that a surge of gas velocity at the fuel/oxygen injection region is found near the inlet (x/H=0.005), the high velocity region spreads outwards in the front of the combustion chamber (x/H=0.05) and gradually transform to more uniform profile with a plateau as the gas flow moves towards the nozzle (x/H=0.7, 1). The variation of fuel droplets has marginal effect to the gas flow near the inlet (x/H=0.005), substantial effect in the front of the combustion chamber (x/H=0.05) and less effect at the end of the combustion chamber (x/H= 1). The radial profile of gas temperature in figure 4.22 shows a similar trend as the velocity, that is, the incoming cold gas gives low temperature profile around the fuel/oxygen injection region near the inlet (x/H=0.005), the temperature variation becomes more substantial as the gas heats up in the front of the combustion chamber (x/H=0.005) and finally more uniform temperature output is achieved at the end of the combustion chamber. The radial profiles of gas dynamics imply a more consistent performance from the current design with a uniform temperature and momentum output despite the variation of fuel droplets. It is mainly due to the three fuel/oxygen injection ports and more importantly a much larger combustion chamber. A design optimization will look into a smaller combustion chamber which consumes less fuel and gives less heat loss to cooling water, and single fuel/oxygen injection port to reduce the carbon deposition. That design optimization will have more stringent requirement on the fuel droplet size which demands a more robust fuel atomiser.

When powder particles are injected, ideally powder particles should be confined within the centre of the gas flow. Therefore it is important to examine the gas dynamics around the centerline region. The velocity profiles in figure 4.23 show a rapid rise of gas velocity in the convergent-divergent section and a slow decline and stabilisation in the parallel section. The droplet variation has almost no effect on the velocity history in the centerline throughout the gun, consequently the acceleration of powder particles and their momentum output will not depend on fuel droplet sizes. The temperature profiles in figure 4.24 show a reversed trend in comparison with the velocity history within the nozzle. However, the droplet size has a considerable effect on the temperature development in the

centerline region. The smaller the fuel droplet, the higher temperature profile is achieved throughout the gun. The decrease of gas temperature according to the increase of the fuel droplet size is more quantitatively shown by the final gas temperature at the gun exit in figure 4.16. It needs to point out that although 0.1 and 1 μm droplets have similar flame structure as discussed before, the variation of fuel droplet size changes the volume ratio of fuel to oxygen which does generate a slight discrepancy on the evaporation rate (shown in figure 4.20) between 0.1 and 1 μm droplets, therefore a slight change of temperature profiles would be expected as more evidently shown in the centerline plot. The results demonstrate that the powder particle heating process is dependent on the fuel droplet size that implies the importance of fuel atomisation process.

Injection angle

The current system implements a parallel injection mechanism to all three ports. The results of droplet motions in figure 4.19 show large droplet stream disperses to great extent and their flames have closer contact with the side wall as shown in figure 4.15. One of the major problems with the three injection ports is the carbon deposition which is a result of closer contact between the flames and walls and has detrimental effect on the operation life of the nozzle. It is interesting to see whether the variation of injection angle affects the combustion and gas dynamics within the gun. In this study, injection angles are varied to 15 degree upward (+) and downward (-) respectively according to the current injection axes. With the fuel droplet size of 1 μm diameter, the flames are closely aligned to the side wall and the two hot spots almost separate completely for upward injection angle as shown in figure 4.15. On the contrary, the downward injection angle generates narrow uniform flames which merge to more uniform temperature profiles within the combustion chamber. The centerline plots in figures 4.23 and 4.24 show the angle variation has no noticeable effect on the gas dynamics around the centre. The results in figures 4.15 and 4.19 clearly show that the contacts between the combusting gas and the wall is reduced by changing the incoming angle of fuel and oxygen stream towards the centre, and subsequently the reduction of carbon deposition could be achieved.

4.2.5 Conclusions

A 3-D combustion flow within a kerosene-fuelled HVOF thermal spray gun has been simulated. The prediction from this numerical model can be summarized as follows:

1. The combustion process of kerosene is dependent on the initial fuel droplet sizes. The small droplets generate a confined corn-shape flame and give more uniform

temperature profile within the combustion chamber while large droplets have dispersed fan-shape flame structure and less uniform temperature profiles.

2. Large areas of recirculation flow are generated around the fuel/oxygen injection ports and the location and magnitude of recirculation flow are dependent on droplet sizes, i.e. recirculation flows decline as the fuel droplet size increases.

3. Generally small fuel droplets only endure short distances and are confined within a more uniform pattern while large droplets travel much further and disperse more widely into the gas flow. With the current gas flow rate, both 0.1 and 1 μm fuel droplets have similar core length of the flames and evaporation rate which implies that an optimized atomizer should produce droplet size around 1 μm to achieve cost-effective operation.

4. The acceleration of powder particle is less sensitive to the variation of fuel droplet size while more dependency is predicted for the particle heating process. The current design of the three fuel/oxygen injection ports with large combustion chamber is able to generate uniform temperature and momentum output despite the variation of fuel droplet sizes.

5. It is possible to overcome the problem of carbon deposition from the current design by changing the incoming angle of fuel and oxygen stream towards the centre, which will effectively reduce the contact between the combusting gas and the internal wall surfaces.

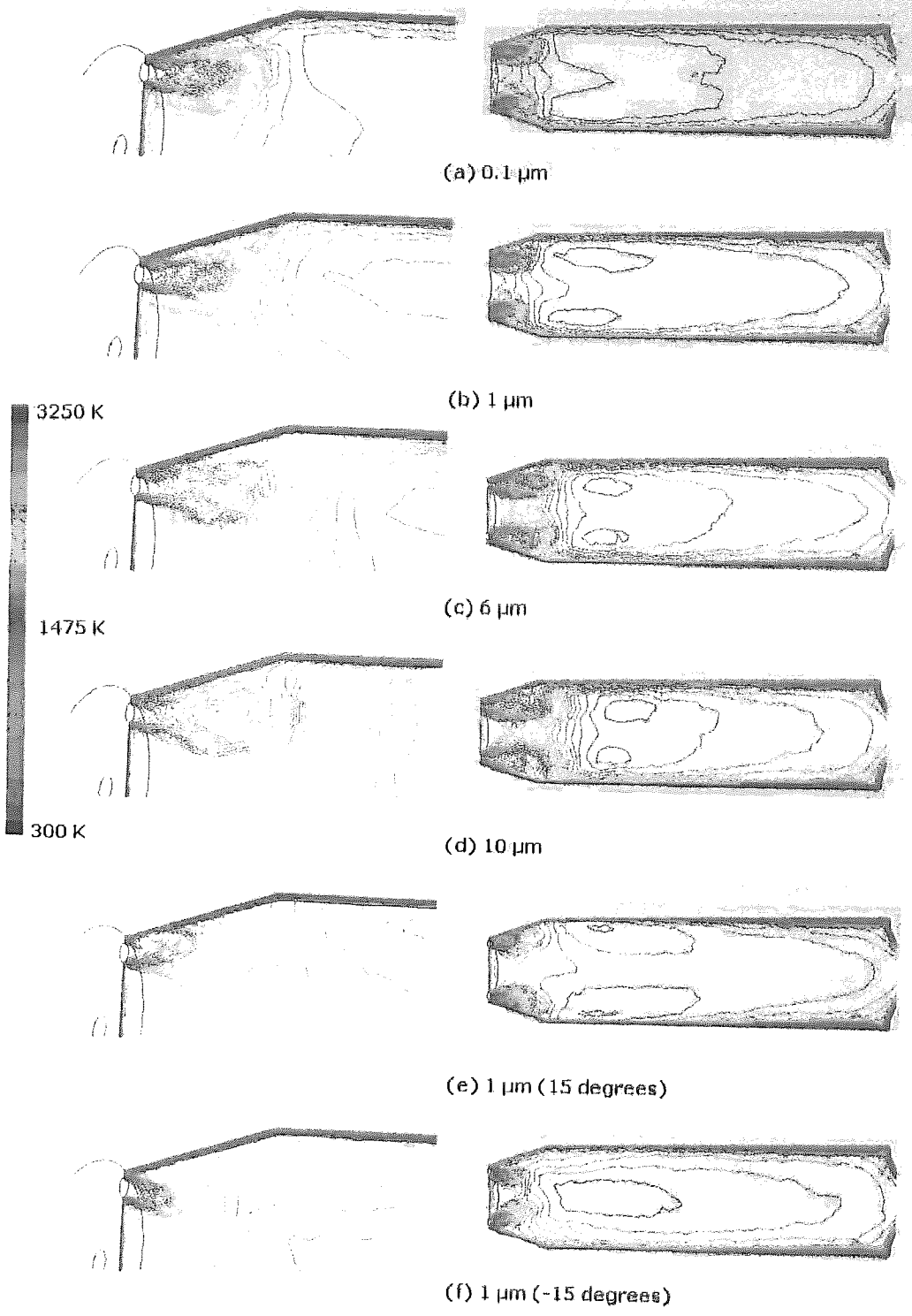

Figure 4.15: Temperature contours within the combustion chamber at different fuel droplet diameters.

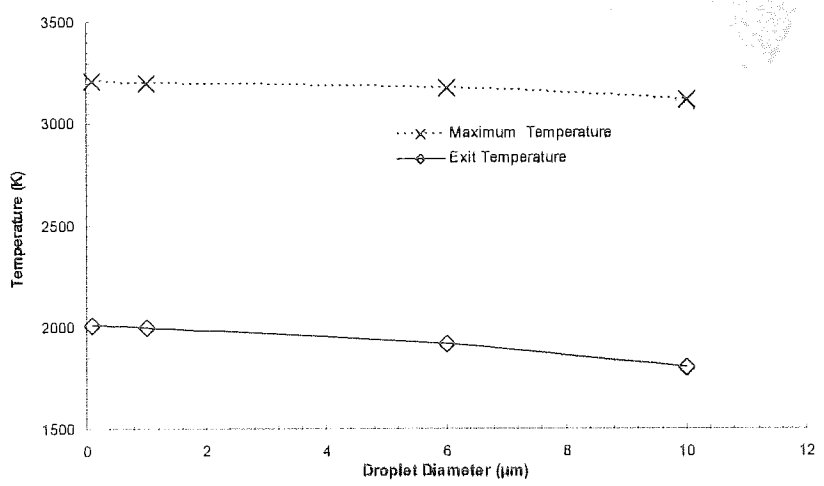

Figure 4.16: Temperature development at different fuel droplet diameters.

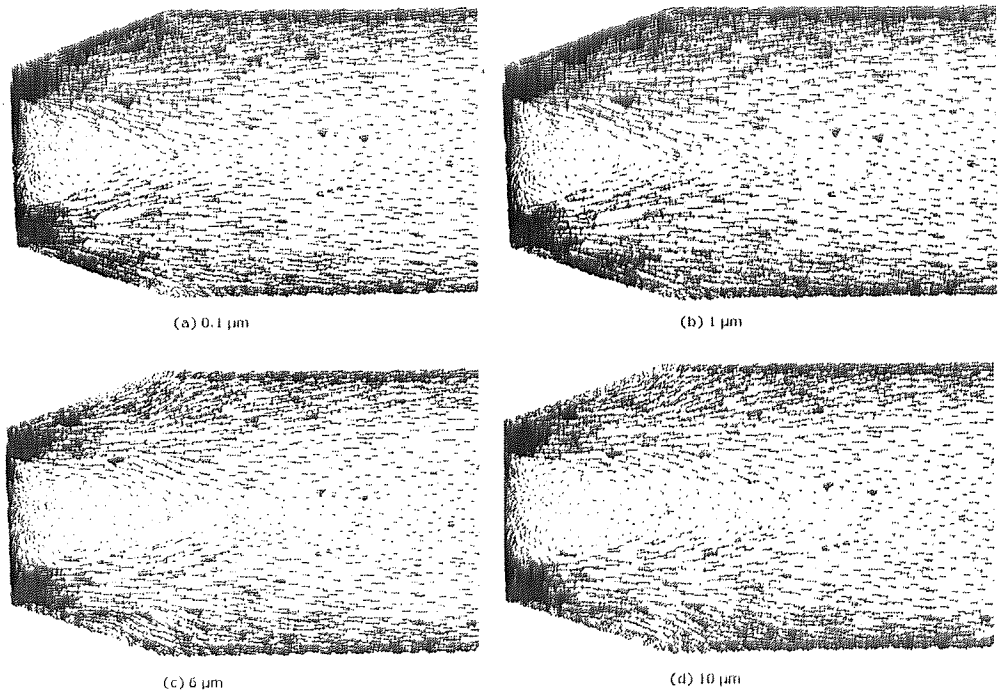

Figure 4.17: Velocity vectors within the combustion chamber for different fuel droplet diameters.

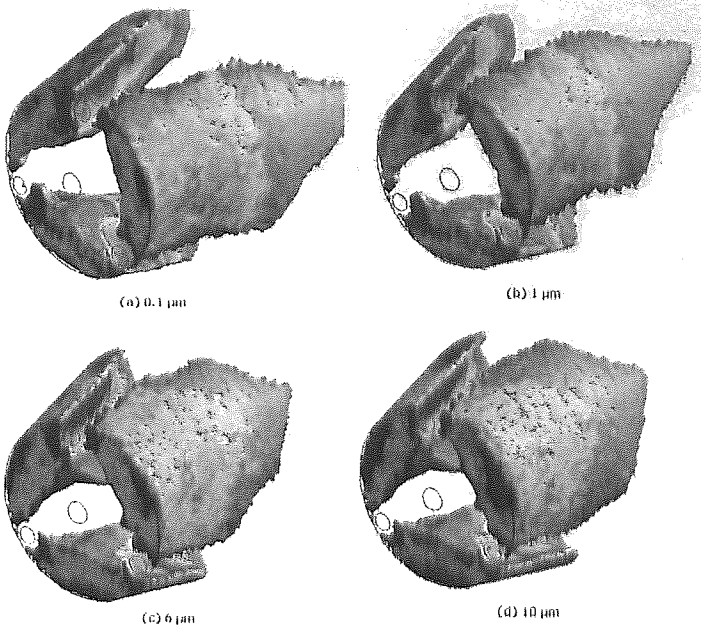

Figure 4.18: Vorticity magnitude plot showing recirculation areas at different fuel droplet diameters.

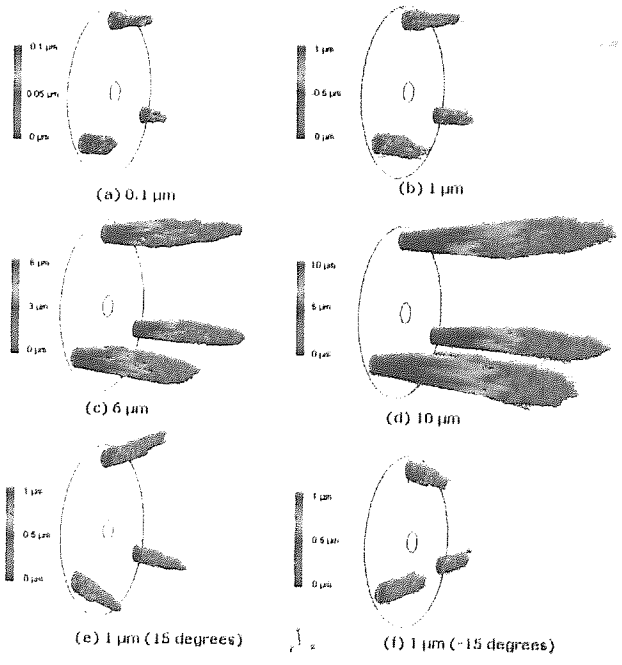

Figure 4.19: Droplet trajectories showing the droplet size evolution.

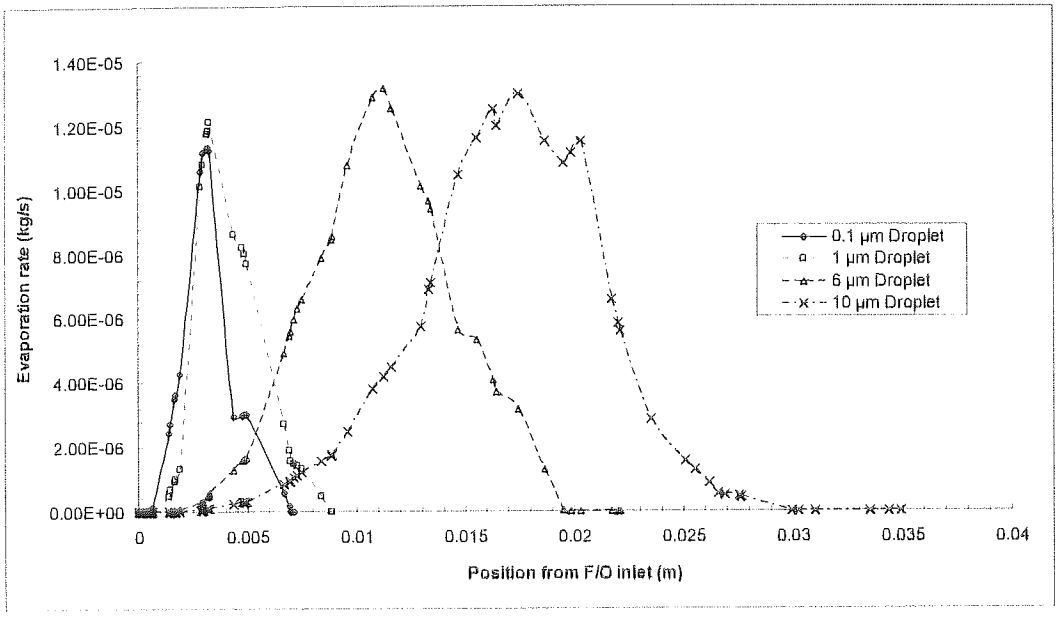

Figure 4.20: Evaporation rates along the core of the flames.

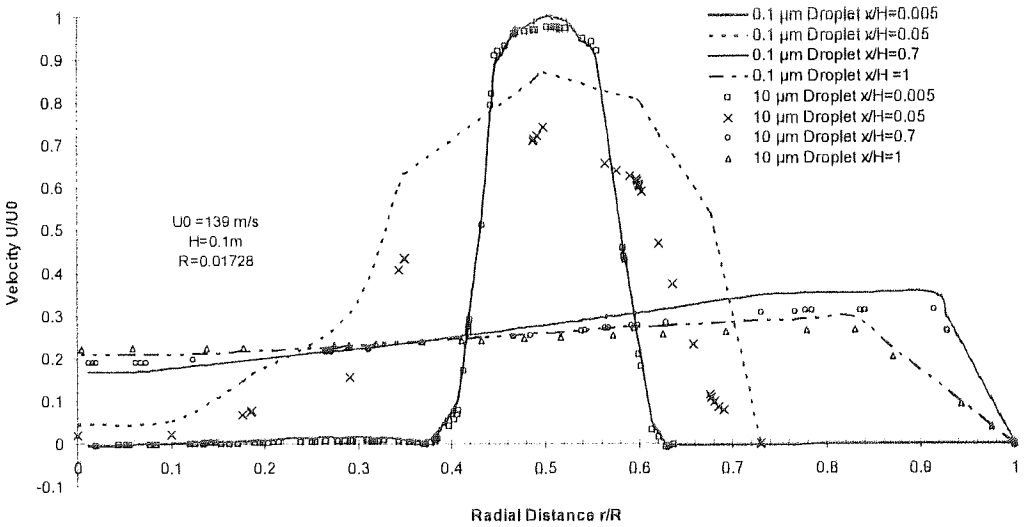

Figure 4.21: Gas velocity radial profiles within the combustion chamber.

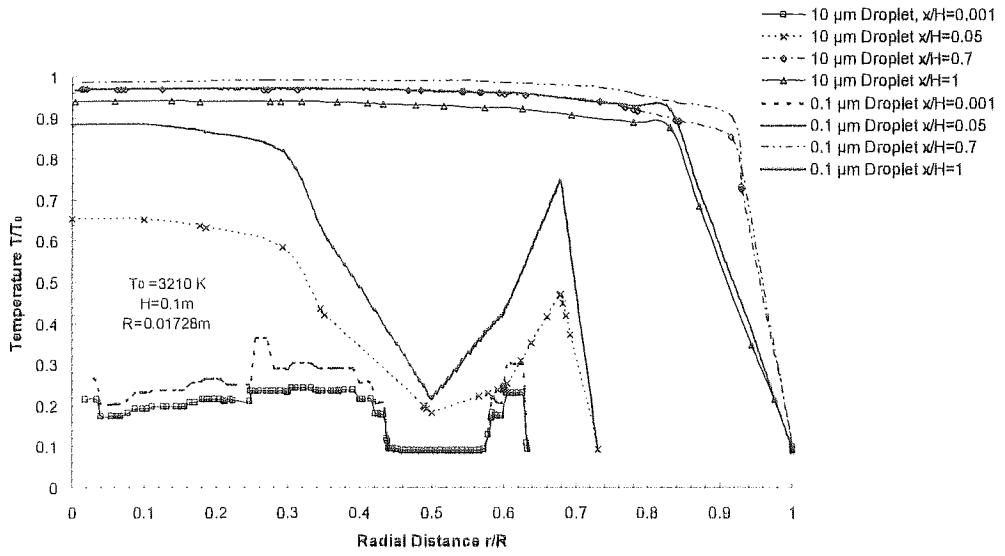

Figure 4.22: Gas temperature radial profiles within the combustion chamber.

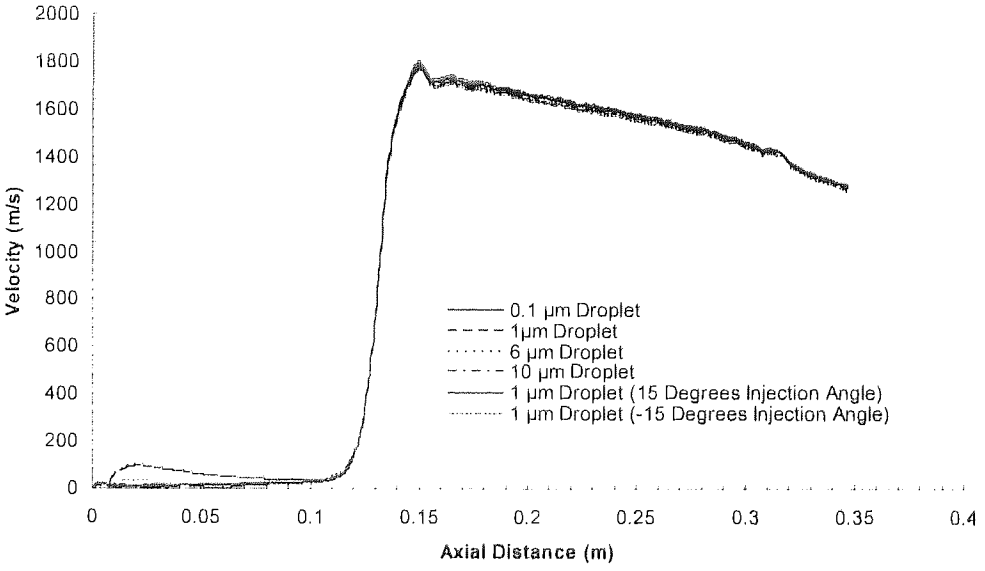

Figure 4.23: Gas velocity profiles along the centreline.

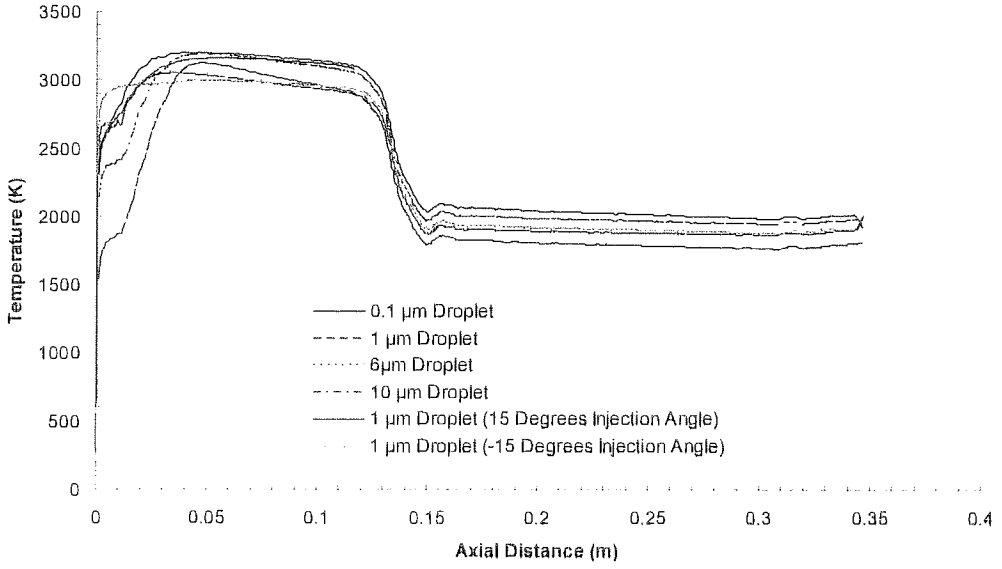

Figure 4.24: Gas temperature profiles along the centreline.

4.3 Water Cooling During Thermal Spraying

The substantial heat and momentum input to powder particles during HVOF process is generated from combustion in which gas temperature reaches over 3000 K within the spraying gun. Active cooling is normally required to protect the spraying gun and powder particles from overheating by using water or gas as heat transfer media. The cooling process needs to be carefully controlled to protect the gun, retain sufficient heat for powder particles to reach molten state, and achieve energy efficiency during operation. A good understanding of the underlying heat transfer process is essential to design such multi-functional cooling mechanism. To date such detailed information is not available and system operation is primarily based on trial and error methods. The research has prioritized on gas/particle flow or coating microstructure whereas heat transfer through the cooling are largely ignored. In most cases, the solid region separating gas flow and cooling water are simplified as a wall boundary adiabatically or with constant temperature/heat flux.

This section aims to examine the detailed heat transfer mechanism within the water-cooled HVOF thermal spray gun, described in the previous section, using numerical approach. The complete HVOF simulation is an integration of numerical water cooling model and gas flow hydrodynamics. The full numerical model will make it possible to

optimize thermal performance or to determine the best method for heat removal without the cost of building physical prototypes. The cooling water flows through a set of holes 33 mm away from the centre of the gun. The holes are not equally spaced, 10 holes on each side of the symmetric plane and the solid sections are left for the fitting of powder injectors. The water cooling configuration shows the holes are located in the same distance away from the gun centreline throughout the gun, therefore, water flows close to the combustion chamber and further away from the barrel. In principle, this design shall give good protection for hot combustion regions where the gun is more venerable and less heat loss to the barrel where powder particles are heated.

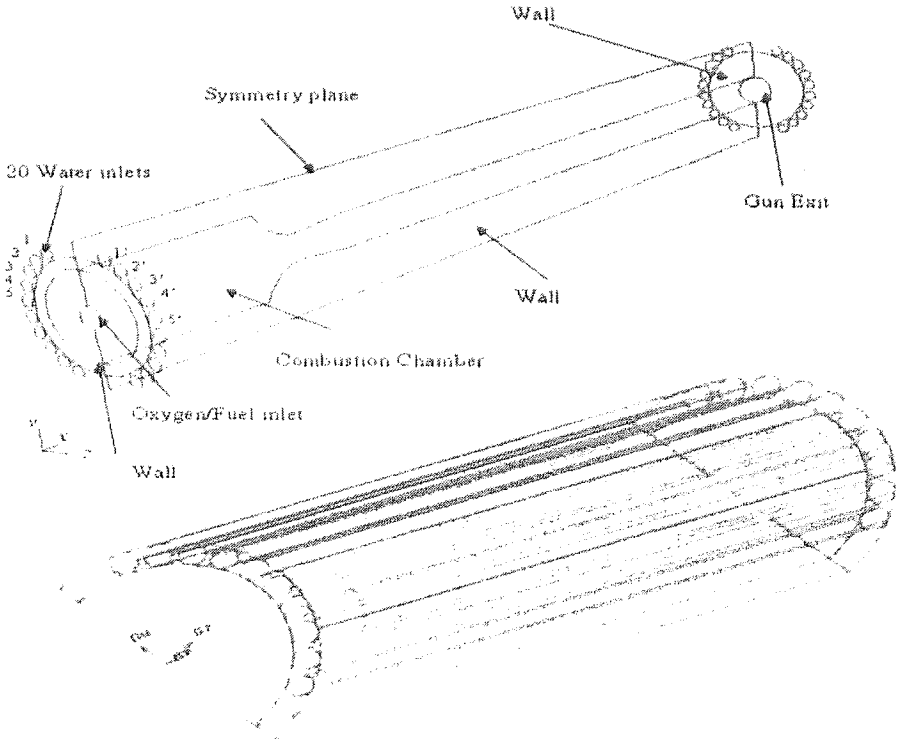

Figure 4.25: Geometric representation of the HVOF gun with water cooling configuration: 2-D schematic on the top, 3-D symmetric CAD drawing.

4.3.1 Model Development

A 3-D computational model is implemented to represent the configuration shown in figure 4.25. The 3-D domain is composed of internal gas flow and the solid gun region where water flow is included. Unstructured grid is deployed throughout the domain including gas, water and the solid regions. After the examination of grid dependence, the final grid has total tetrahedral mesh volumes of 185,000, namely, 120.000 for gas, 20.000 for water

and 45,000 for solid copper. The computing for both the gas flow and solid gun is fully coupled through the distinctive no-slip walls on the internal surface of the gun. The heat transfer model is given the assumptions that the specific heat and thermal conductivity of the copper are assumed to be constant and the heat transfer modes are dominated by convection and conduction in water cooling, therefore, radiation model is not included in the thermal calculation. The numerical methods of pressure-velocity coupling, turbulent and combustion models are the same and have been described in previous section. Only the heat transfer and near-wall models are described in this section thoroughly.

4.3.2 Numerical Models

The gas and water flow are solved numerically in the same manner as described in section 4.1 in which the governing equations, combustion kinetics and the realizable $\kappa - \varepsilon$ turbulent model are detailed. The mathematical models for the solid regions are briefly described as follows.

Energy Equation

In solid regions the energy transport equation has the following form:

$$\frac{\partial}{\partial t}(\rho h) + \nabla \cdot (\vec{v}\rho h) = \nabla \cdot (k \nabla T) \tag{4.25}$$

The term on the right hand side of the equation (4.25) represents the heat flux due to conduction.

Heat Transfer

When the energy equation is solved, the thermal boundary conditions at wall must be defined. The two main thermal conditions that employed in this water cooling model are the fixed temperature and convective heat transfer as illustrated in figure 4.26. The fixed temperature condition is used for the external wall layer that is exposed to room temperature which is given as 300 K. The convective heat transfer wall boundary condition is employed for the cooling tubes where excess thermal energy is absorbed by the water.

The heat transfer to the wall boundary from solid cells is computed as:

$$\dot{q} = \frac{k_s}{\Delta n}(T_w - T_s) \tag{4.26}$$

The fluid side heat transfer coefficient is computed based on the local flow field conditions such as turbulence level, temperature and velocity profiles.

Wall Boundary

When the convective heat transfer coefficient boundary condition at a wall is specified, the law of the wall implemented has the following composite form:

$$T^* \equiv \frac{(T_w - T_P)\,\rho c_p C_\mu^{1/4} k_P^{1/2}}{\dot{q}} \tag{4.27}$$

when $y^* < y_T^*$

$T^* = \mathrm{Pr}\, y^* + \frac{1}{2}\rho\,\mathrm{Pr}\,\frac{C_\mu^{1/4} k_P^{1/2}}{\dot{q}} U_P^2$

when $y^* > y_T^*$

$T^* = \mathrm{Pr}_t \left[\frac{1}{k}\ln(Ey^*) + P\right] + \frac{1}{2}\rho\frac{C_\mu^{1/4} k_P^{1/2}}{\dot{q}}\left[\mathrm{Pr}_t\, U_P^2 + (\mathrm{Pr} - \mathrm{Pr}_t)\, U_c^2\right]$

where P is computed by using the formula given by [107]

$$P = 9.24\left[\left(\frac{\sigma}{\sigma_t}\right)^{3/4} - 1\right]\left[1 + 0.28e^{-0.007\frac{\sigma}{\sigma_t}}\right]$$

The non-dimensional viscous sublayer thickness is calculated as

$$y^* \equiv \frac{\rho C_\mu^{1/4} k_p^{1/2} y_P}{\mu}$$

The non-dimensional thermal sub-layer thickness y_T^* is computed as y^* value at which the linear law and the logarithmic law intersect, given the molecular Prandtl number of the fluid being modelled. Depending on the y^* value at the near wall cells either the linear or the logarithmic profile is applied to compute the wall temperature or heat flux.

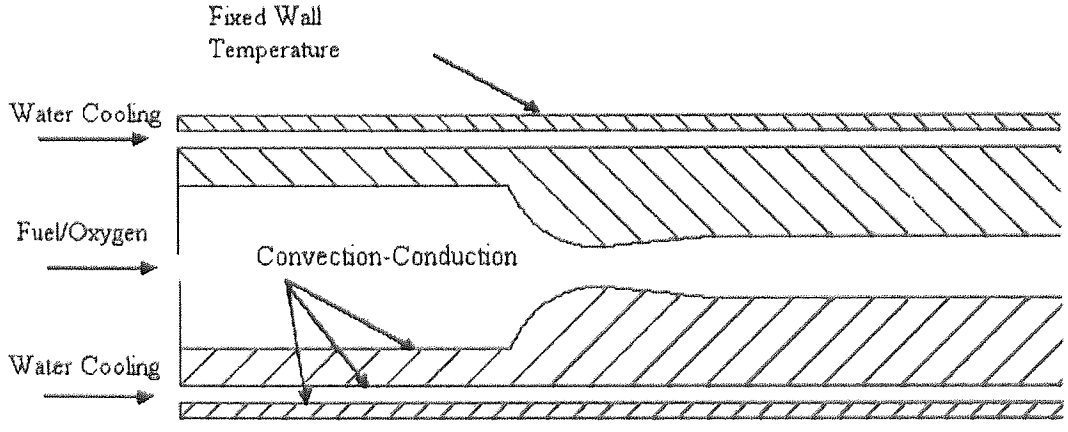

Figure 4.26: 2-D schematic of computational domain with wall boundaries.

4.3.3 Results and Discussions

As described previously the current configuration for water cooling is an array of 20 holes, 10 holes on each side of the symmetric plane and the solid sections are left for the fitting of powder injectors. To examine the heat transfer within each water tube, they are numbered from 1-5 according to the configuration in figure 4.25. The temperature developments along the centreline among those tubes are illustrated in figure 4.27. It is evident that the large spacing between tubes 1 and 1' requires more heat to be carried away for tube 1; the adjacent tube 2 takes less due to the presence of tube 1; heat loss is more evenly distributed for the follow-up tubes. This result shows clearly that heat transfer within each tube is dependent on the geometric arrangement.

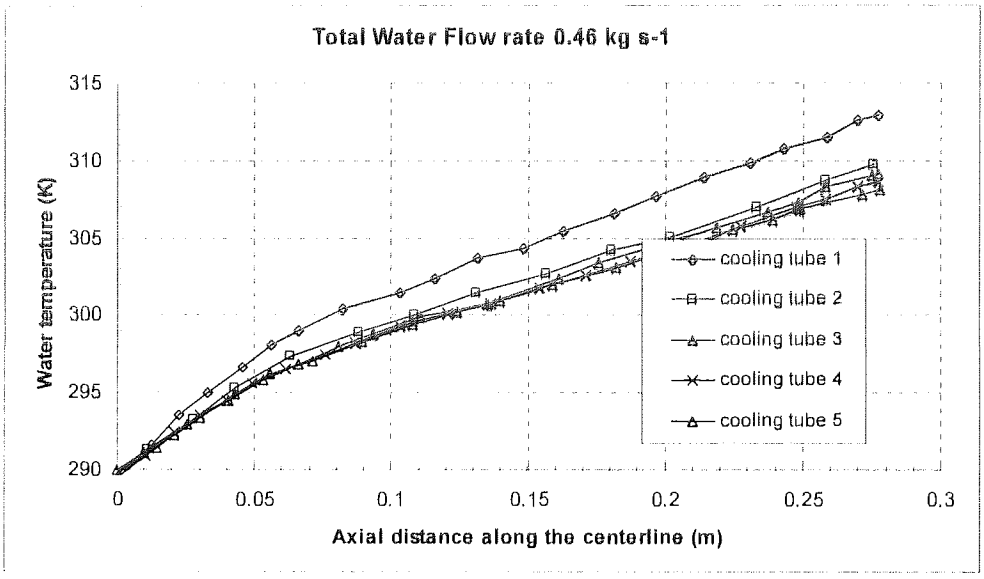

Figure 4.27: Centreline temperature profile of cooling tubes.

The major parameter to control the cooling system is the water flow rate. The effect of water flow rate on heat transfer is evident in figure 4.28 while more heat is taken away as water flow rate increases. Figure 4.28 also shows that a better cooling result is achieved at normal flow direction. The normal flow direction is to inject water from the combustion chamber towards the gun exit while the reverse direction is on the contrary. This discrepancy of heat transfer is a combined result of specific heat and temperature difference. A detailed specific heat profile for the water is given in this model as shown in figure 4.29. To demonstrate the internal temperature development within the water cooling tubes the temperature profile of tube 5 is plotted in figure 4.30. The result in figure 4.27 implies that tube 5 gives a more general representation of the heat transfer

profile of cooling tubes. It is found from figure 4.30 that the wall temperature within the gun is high in the combustion chamber region and low at the nozzle and the profile of water temperature develops differently within the cooling tube by changing the flow direction. As a combination result in this particular case, normal flow direction, namely, water flowing from the combustion chamber towards the gun exit, takes more heat out the gas flow and is more effective in cooling with the current configuration.

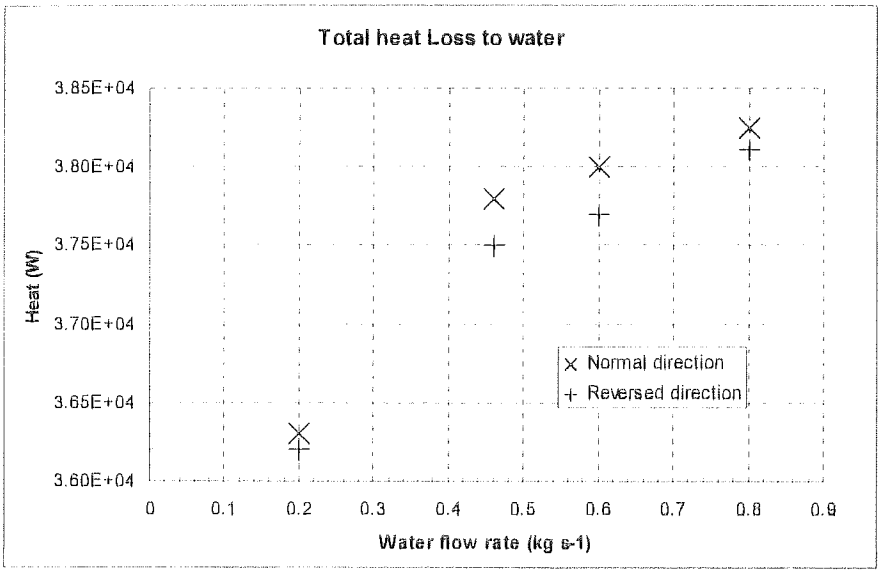

Figure 4.28: Variation of total heat loss to water at different water flow rate and direction.

It is obvious from figure 4.28 that high flow rate take more heat out of the system, which may imply a good protection for the gun. The temperature profiles of internal gun surface at different flow rates in figure 4.31 shows that substantial increase of flow rate from 0.46 to 0.8 Kg/s has not significantly reduce the surface temperature, implying a more cost effective flow rate at 0.46 Kg/s.

The studies in gas and particle dynamics from HVOF guns demonstrate powder particles are predominately entrained in the centre of HVOF guns, therefore the flow pattern within the centre region is critical to coating quality and process control. The temperature profiles along centreline in figure 4.32 show negligible change at various water flow rate. Further examination of the radial temperature profiles in figure 4.33, 0.023 m from the gun inlet, where the maximum combustion temperature occurs, gives a more quantitative comparison. It is evident that increasing water flow rate 3 times has no noticeable effect on the maximum combustion temperature; the profile of high temperature region within the combustion chamber is well remained; and only near wall region is slightly varied on water flow rate. This result proves that the current water cooling mechanism gives

the gun required protection without affecting the gas combustion pattern and thermal hydrodynamics within the HVOF gun. The critical gas flow that subsequently decides the particle dynamics is mainly defined by the internal design of the gun.

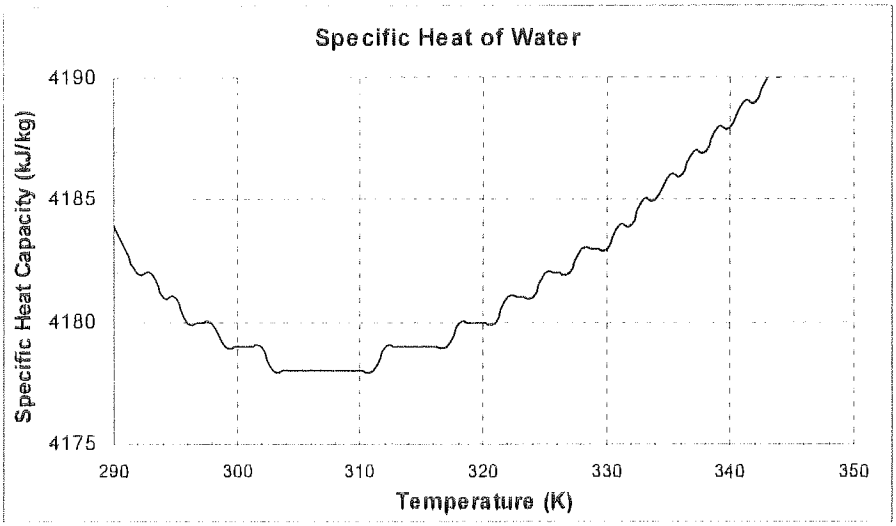

Figure 4.29: Profile of water specific heat at various temperatures

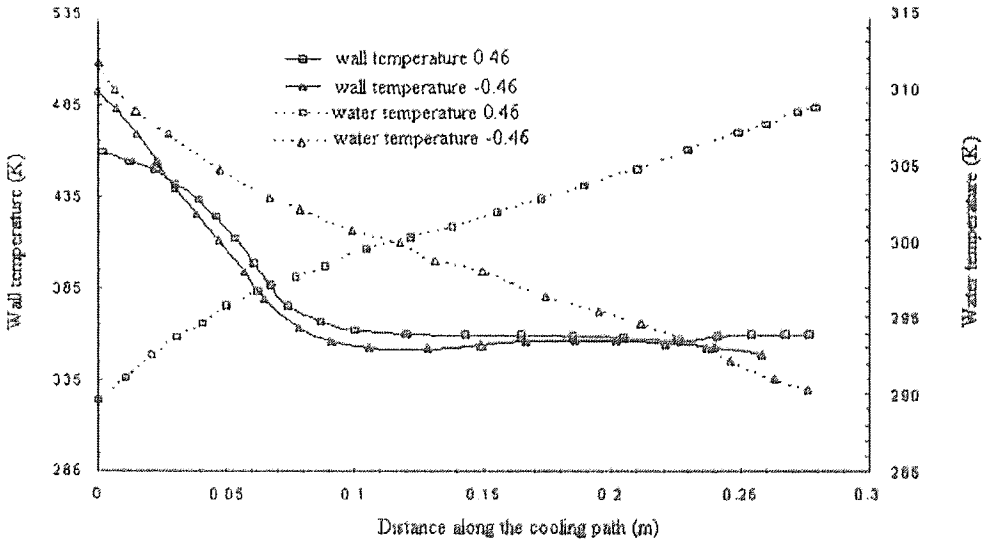

Figure 4.30: Centerline water temperature profile in cooling tube 5 and internal gun surface temperature profile at water flow rates of 0.46 Kg/s and -0.46 Kg/s.

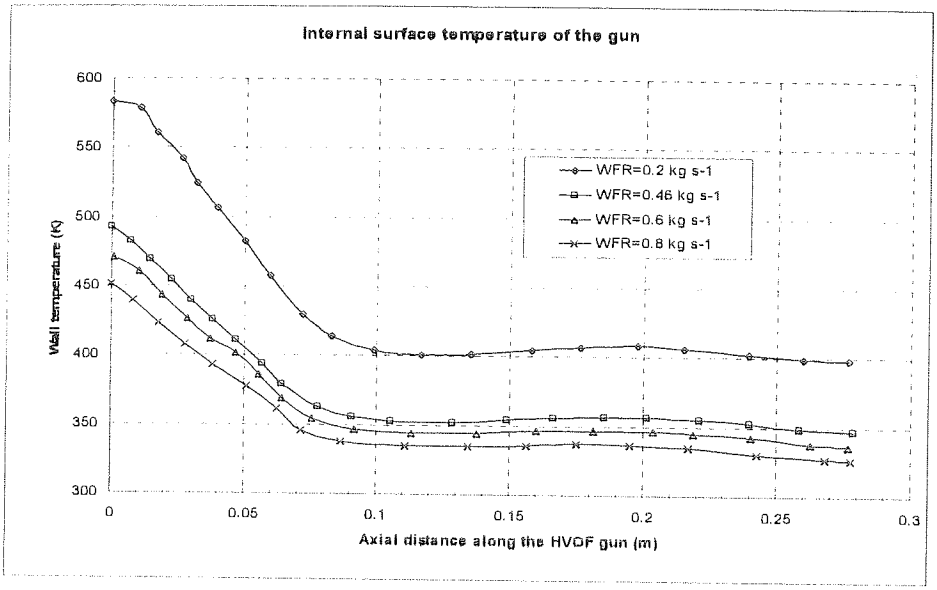

Figure 4.31: Internal surface temperature of the gun at different water flow rate (WFR)

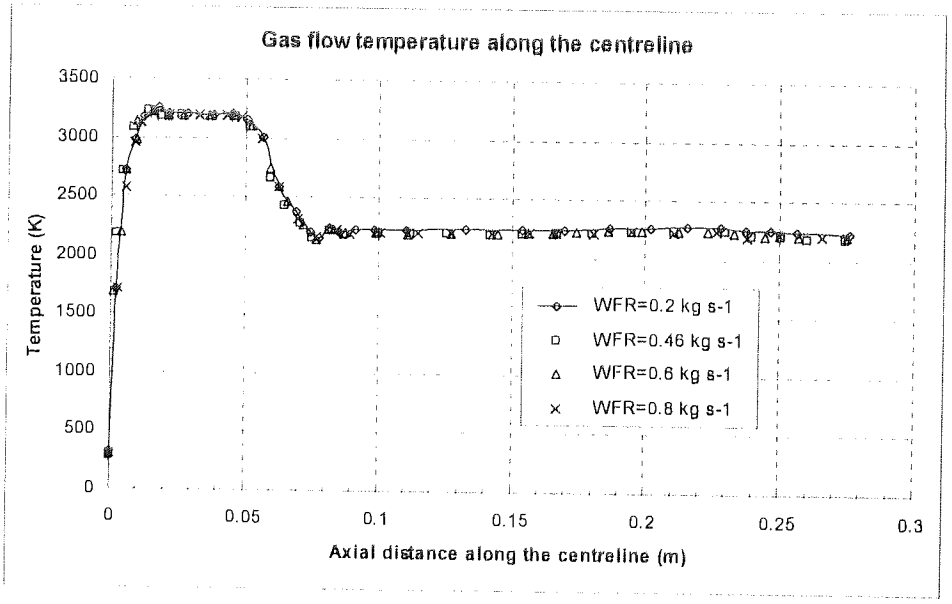

Figure 4.32: Gas flow temperature profiles along the centerline of the gun at different water flow rate (WFR).

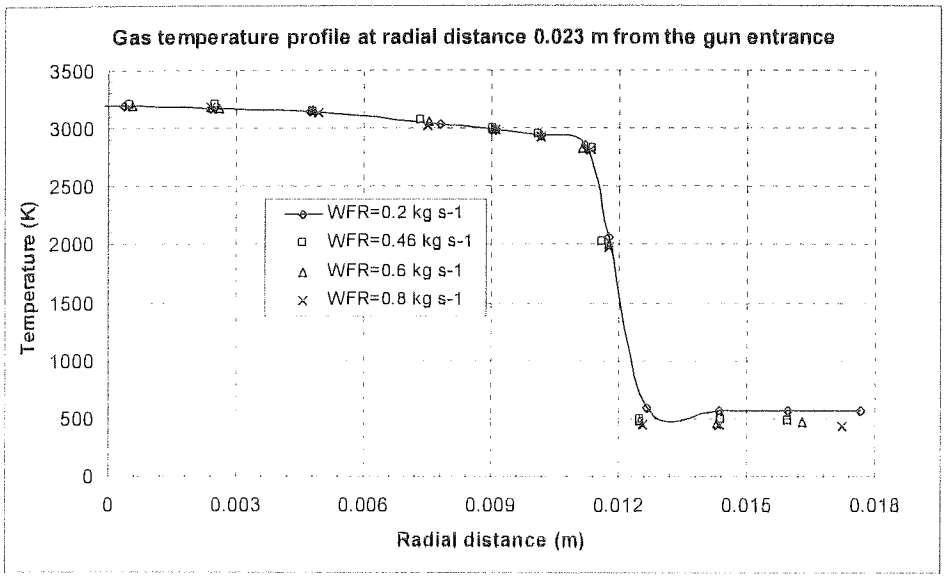

Figure 4.33: Gas temperature profile at radial distance 0.023 m from the gun entrance.

4.3.4 Conclusions

A CFD water cooling model has been presented to examine the heat transfer between the cooling water and the solid copper in a HVOF thermal spray gun. The heat transfer mode is fully integrated with the hydrodynamic gas flow field and gives insights to heat transfer mechanism during the process. The following conclusions have been obtained in this study:

1. The heat loss through water cooling is dependent positively on the water flow rate. The effect of water flow on the temperature of gun surface is more pronounced at low flow rate and less significant at high flow rate. The water flow has no noticeable influence on the gas temperature in the centre of the gun.

2. Flow direction can affect the cooling efficiency. The current cooling configuration points to a better cooling when water flows from combustion chamber towards the exit.

3. The maximum temperature of gas flow within the combustion chamber is independent on water flow rate and direction. The gas flow dynamics relies on the internal design of the thermal spraying gun rather than water cooling configuration.

Chapter 5

Modelling of Powder Particles

5.1 Intorduction to Multiphase Flows

This chapter attempts to provide a description of the multiphase and heat transfer models used for the prediction of powder particles oxidation, melting and solidification during HVOF process. The first section of this chapter gives an introduction to discrete phase modelling. In section 5.3 a developed approximate analytical solution is described thoroughly and validated against other analytical solutions available in literature. The analytical solution is used as a benchmark for the numerical model presented in section 5.4. The numerical model described in this chapter is then implemented as a sub-model into FLUENT and the results on particle melting and oxidation are presented in chapter 6.

Multiphase flows are encountered in many important engineering applications. Because of there commercial importance understanding and improving multiphase processes has become an active area of research. Given the recent advances in computational power, the ability to model complicated phenomena like multiphase flows has never been greater. In this chapter many of the basic assumptions used in the computational modelling are re-examined and alternative approaches particularly in the heat transfer and phase change modelling are implemented.

Multiphase flows are generally divided into four categories: gas-liquid, gas-solid, solid-liquid and three phase flows. Table 5.1 shows some examples for each category. This study focuses on the second type of multiphase flow; gas-solid or dispersed flows. This introduction is based on a number of excellent reviews of gas-solid transport: [108] is a comprehensive introduction to the numerical approaches used to model gas-solid flows, [109] is an excellent introductory book to gas-solid flows.

Gas-liquid flows	Bubbly Flows Separated Flows Liquid Fuel Combustion
Gas-solid flows	Pneumatic Flows Fluidized Beds HVOF Gas-Particle Flow
Liquid-solid flows	Slurry Flows Hydrotransport Sediment Transport
Three-phase flows	Fuel Droplets and Powder Particles in HVOF Gaseous Flow

Table 5.1: Examples and categories of multiphase flows.

5.2 Gas-Solid Phase Overview

Gas-solid multiphase flows are the concurrent flow of solid particles in a gas stream. The gas-solid flows can be subdivided into two categories depending on how the solid particles interact with one another and the gas phase: dilute and dense gas flows. In figure 5.1 the key factors in determining whether a flow is dilute or dense is shown schematically.

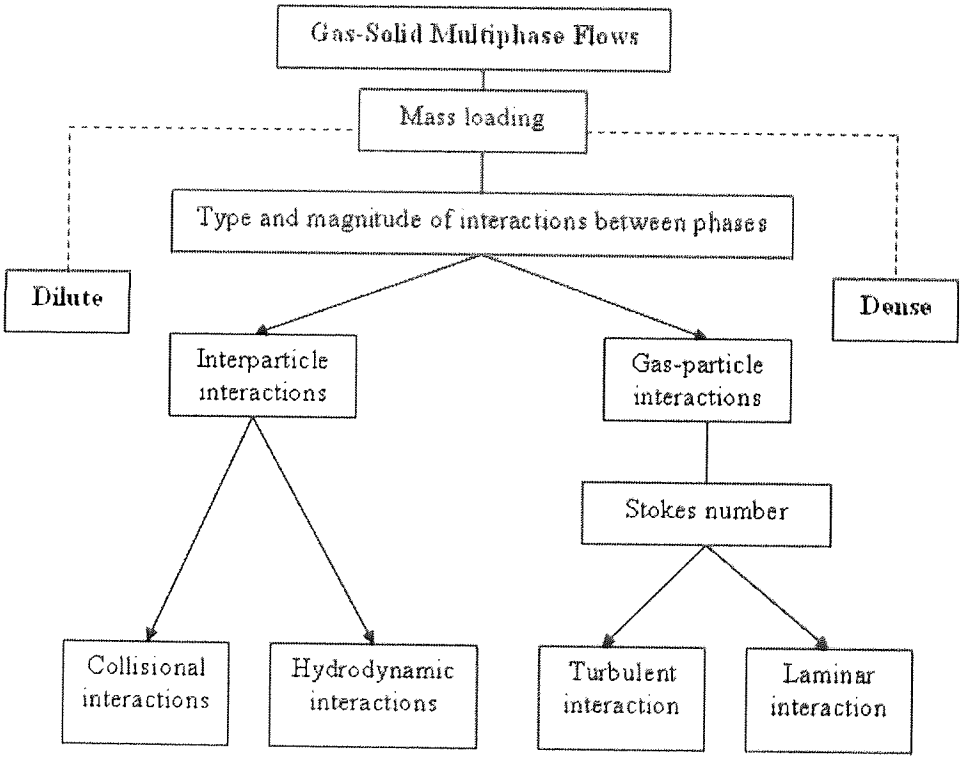

Figure 5.1: Categories and interaction types of gas-solid flows.

The most widely used measure of the gas-solid flow is the mass loading, which is the ratio of the solid phase mass flux to the fluid phase mass flux.

$$Z = \frac{\overline{\rho}_p u_p}{\overline{\rho}_f u_f} \tag{5.1}$$

Here $\overline{\rho}_p = n_p m_p$ and $\overline{\rho}_f = (1 - n_p V C_p)\rho_f$

Using the well known relationship between density, mass and volume and assuming that particles are spherical we can get the relationship:

$$Z = \left[\frac{n_p V_p}{1 - (n_p V_p)}\right]\left[\frac{\rho_p}{\rho_f}\right]\left[\frac{u_p}{u_f}\right] \tag{5.2}$$

In addition to establishing criteria for dilute and dense phase flows, timescale analysis is useful in determining the interactions of single particle with the gas phase. The degree of kinetic equilibrium between the particle and the surrounding gas is given by the ratio of the particle timescale to the fluid timescale.

$$St = \frac{\tau_p}{\tau_f} \tag{5.3}$$

The Stokes number dictates how readily a particle follows the flow. For laminar flows the relationship is simple.

$$St = \frac{n_p \pi \rho_p d_p |u_f - u_p|}{18\mu} \tag{5.4}$$

The expression of Stokes number for turbulent flows is more complicated due to many timescales associated with turbulence and turbulent flow. In turbulent flows the Stokes number represents the importance of turbulence on the particle motion [109]

For both cases of laminar and turbulent cases a Stokes number less than unity means that a particle can respond quickly to flow fluctuations. The appropriate coupling between phases can be selected taking into consideration together the mass loading and Stokes number. Generally phases can be coupled in three ways: mass coupled, momentum coupled and energy coupled. In the case of powder particles in HVOF thermal spray process the particles exchange momentum with the gas flow as well as energy, so they are said to be momentum and energy coupled. In the case of liquid fuel combustion of kerosene (section 4.2) the gas-liquid flow is momentum, energy and mass coupled due to evaporation of liquid droplets. Momentum coupling is the essential link between mass loading, the Stokes number and modelling approaches. In dense flows the momentum transfer (equation (5.5)) increases with increased mass loading (Z). Conversely in dilute flows (small Z) there is a little exchange of momentum from the particles to gas flow.

$$\prod_{mom} \cdot = \frac{Z}{(1 + St)} \tag{5.5}$$

According to mass loading and Stokes number, different modelling approaches are employed to explore gas-solid flows. Dense gas-solid flows such as fluidized beds are modelled using the Eulerian method. The most commonly used Eulerian model is the

two-phase model, which treat the gas and solid as two separate inter-mixed continua. In this approach models have continuity, momentum and energy equations for each phase and are closed with empirical transfer equations.

Dilute flows are modelled using Lagrangian models, which treat the solid phase as discrete particles that are individually tracked through the fluid phase. The most commonly used Lagrangian formulation is the point mass representation of a particle. In this method the particle is much smaller than the grid spacing on which the gas velocity is calculated and does not influence the gas domain or its discretization. The point mass technique is the most appropriate for simulating the thermal and mechanical behaviour of powder particles during thermal spray due to large number of sub-grid micro-size particles. The trajectory of the particles through the gas phase is determined by integration of the particle equation of motion which is based on the forces that are 'assumed' to act on the particle. The application of the point mass method requires grid size larger than the diameter of the particle. When the Reynolds Averaged Navier-Stokes (RANS) methods are used to calculate the gas phase velocities, the point mass approach is modified to cell-averaged model to account for the spatial and temporal turbulence within the grid cell in order to predict their influence on the particle momentum equation.

Migdal et.al.,[110] were the first to propose combining Lagrangian solid particles and Eulerian fluid mechanics for multiphase flows by showing that particles could be treated as sources of mass and momentum in a fluid field. Since then models have been used to study various aspects of gas-solid flows including particle-fluid turbulence interactions [111, 112] hydrodynamic forces between the two phases [113] and particle-particle interactions [114].

The basic particle equations used to simulate the powder particle in-flight behaviour during thermal spray are given in section 6.1.2. For wall bounded flows such as the thermal spray gun, the wall-particle interactions can be important, especially as it relates to such issues as erosion. The particle interacts with the wall through two mechanisms. The first is the hydrodynamic interaction due to proximity of the wall studied by [111]. The second mechanism for wall particle interaction is the mechanical behaviour. The collision between wall and particle can be modelled with either the hard sphere or soft sphere approach. A detailed description of the wall-particles interaction model can be found in FLUENTS's user guide.In FLUENT code the Lagrangian simulation is done in three parts as shown schematically in figure 5.2.

The introduction above gives a very brief description of the multiphase flow modelling. In the following sections an improved analytical approach on the heat transfer and phase change is described thoroughly providing potentially interesting extension to multiphase theory alongside with a numerical model implemented as user defined function in FLUENT.

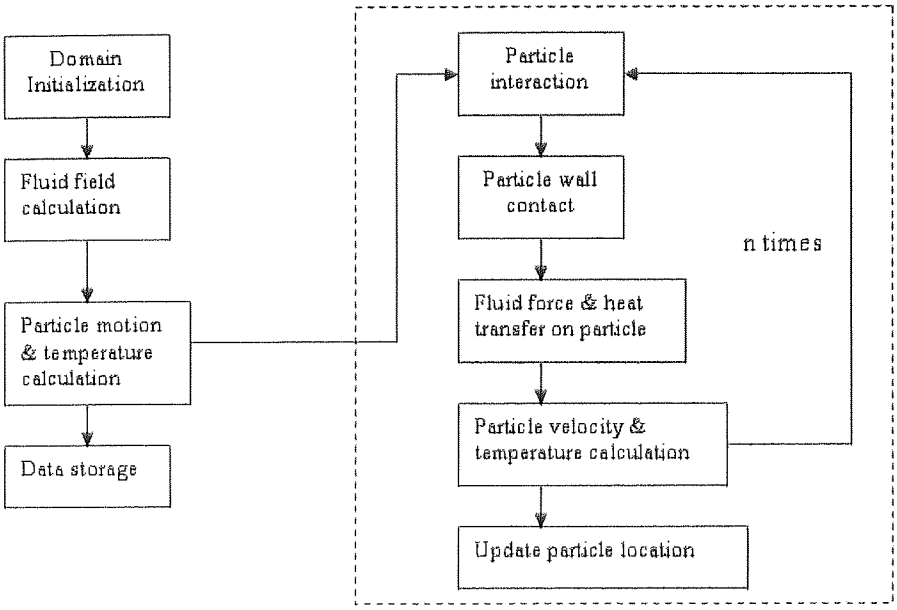

Figure 5.2: Lagrangian simulation flowchart: First the solution of the continuum fluid equations. Second, solution of the equation of motion for each particle and finally the coupling between phases.

5.3 Analytical Particle Models

This section describes an analytical method to find improved approximation of moving boundary as a result of phase change (Stefan problem) based on the perturbation method. All the parameters included in the motion equations are non-dimensional and the solutions can be used for both inward and outward phase change in spherical coordinates. The solution for inward phase change problems is examined thoroughly in this section and the results are compared with well established analytical and numerical solutions. The major advance of the improved analytical solution is to include surface convection without using complex numerical methods. The simplified solutions can be readily incorporated to numerical models in Lagrangian formulation to solve complicated multiscale modeling problems. The current approximation is achieved in a second order perturbation solution, which has proved to be very accurate for the phase change problems with Stefan number below 1.

5.3.1 Review of Existing Models

The powder particles, generally in spherical shapes, are heated and accelerated by the gas stream before impact. The particles are initially heated by the surrounding gas mainly

through convection and then heat is transferred into particles through conduction. In this case, particles are subjected to phase change as a result of heat transfer. A boundary separating two different phases develops and moves in the particle during the process. The moving boundary known as Stefan problem [115] is time-dependent and can only be determined as a function of time and space. The final quality of coating product is closely related to the heating, melting and solidification of powder particles. Better understanding of thermal history of powder particles will enable better control of the process parameters or design optimal configurations for coating systems.

Today, the general thermal profile of particles within gas flow can be readily solved using Lagrangian formulation available in commercial CFD codes. However, the detailed of particle heating and solidification involving phase change can not be obtained in such macro-scale flow simulation. With the assistance of sufficient computational power, the phase change within complicated geometries can be simulated by tracking the moving boundary using numerical methods. One solution is to use fixed grid method where the heat flow is approximated by finite difference to calculate values of temperatures and time. The numerical treatment of the moving boundary can be achieved using the apparent capacity method [116], the effective capacity method [117] the heat integration method [118], the source based method [119], the enthalpy method [120] in the fixed grid, which has been applied to a variety of complex moving boundary problems and is described in chapter 7. A good review of numerical methods on solving Stefan problems can be found in [124, 125].

Sophisticated numerical models can provide details of phase change in multidimensional domain with complex geometries. However, the excessive demand of computing time and computer power limit the wide use of such extensive computing approaches. For instance, in the study of thermal spraying, micro-sized powder particles need to be tracked in a domain of approximate half meter size including thermal spray guns and stand-off distances. It is a challenging computing task to model the phase change within in-flight particles numerically. The detailed description of numerical solution is presented later in this chapter. An alternative solution to such challenging multi-scale modeling problems is to use analytical solutions for the particle heat transfer and phase change, which can be easily incorporated into Lagrangian formulation of particle tracking.

The most well known analytical equations for phase change were developed by Stefan [115] around 1890 and subsequently the moving boundary has been referred as Stefan problem. The Stefan solution is based on the assumption that one phase (liquid) is active and the other stays at melting point. Later Newmann [126] improved the Stefan's solution to more realistic two phase problem with both solid and liquid. The Newmann's solution is based on the assumption of constant imposed temperature and not applicable to constant

imposed flux. More approximate solutions have been developed since then. For instance, Goodman [127] made a better approximation of the overall heat balance by integration of heat conduction based on Karman-Pohlausen's approach [128] of the momentum integral in the boundary-layer theory. Although a variety of analytical equations are available today for solving phase change problems, they are limited with pure heat conduction. This section describes an improved analytical solution to solve the phase change in spherical geometry. The major advantage of this model is its ability to include more realistic surface temperature profile as a result of the convection. The predictions from this analytical solutions show very good agreement with computationally expensive approaches and the dimensionless solutions can be easily implemented into numerical codes for micro-scale particle modeling.

5.3.2 Development of Pertubative Analytical Solution

The analytical approach is based on assumptions as follows: particles do not change shape during the process, particles melt at a fixed temperature, particles have constant density which is an averaged value of solid and liquid states, heat capacity and thermal conductivity of particle is constant.

A schematic of phase change within the particle is shown in figure 5.3. For the initial approximation, the particle inside has a solid temperature T_{solid} and the surface has a constant temperature $T_{surface}$ above the melting point T_{melt}. To generalize the process, non-dimensional variables are introduced as follows:

Non-dimensional position:

$$r = \frac{r}{r_0} \tag{5.6}$$

Non-dimensional time:

$$\tau = \frac{k_p t}{\rho_p c_p r_0^2} \tag{5.7}$$

Stefan number:

$$Ste = \frac{c_p \left(T_{solid} - T_{ref}\right)}{L} \tag{5.8}$$

Biot number:

$$Bi = \frac{h r_0}{k_p} \tag{5.9}$$

Non-dimensional temperature:

$$T = \frac{T(r) - T_{surface}}{T_{solid} - T_{surface}} \tag{5.10}$$

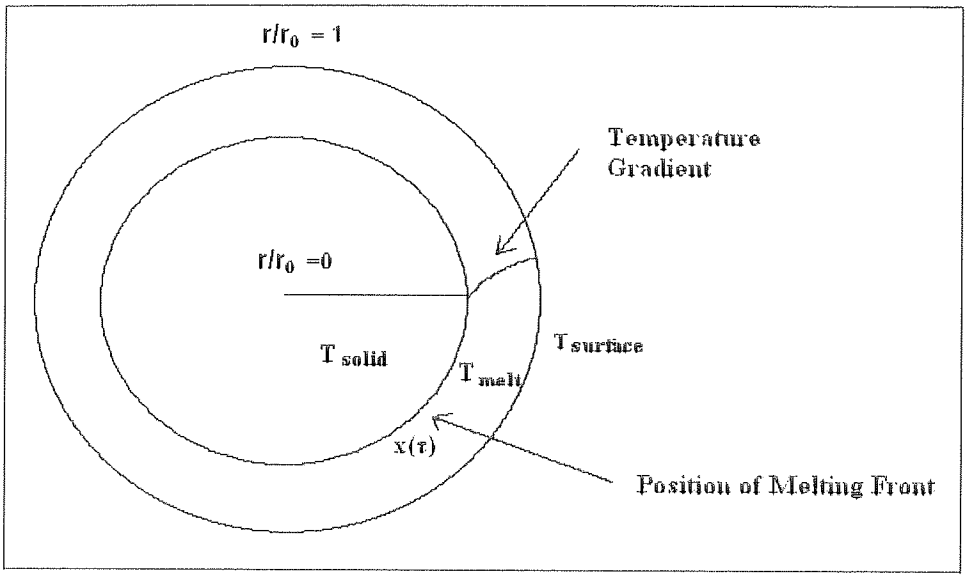

Figure 5.3: Schematic of phase change within particles.

The temperature distribution within the particle is governed by heat conduction equation:

$$\frac{\partial T}{\partial \tau} = \frac{1}{r^2}\frac{\partial}{\partial r}\left(r^2\frac{\partial T}{\partial r}\right), x(\tau) < r < r_0, \tau > 0 \tag{5.11}$$

Boundary conditions are given as:

$$T(r = 1, \tau) = 1, T(r = x(\tau), \tau) = 0 \tag{5.12}$$

$$\frac{\partial x}{\partial \tau} = -Ste\left(\frac{\partial T}{\partial r}\right)_{r=x(\tau)} \tag{5.13}$$

$$\frac{\partial T}{\partial \tau} = \frac{\partial T}{\partial x}\frac{\partial x}{\partial \tau} \tag{5.14}$$

Applying the chain rule (equation (5.14)) and making use of the Stefan boundary condition in Equation (5.13), equation (5.11) can be rewritten as:

$$\frac{1}{r^2}\frac{\partial}{\partial r}\left(r^2\frac{\partial T}{\partial r}\right) = -Ste\frac{\partial T}{\partial x}\left(\frac{\partial T}{\partial r}\right)_{r=x} \tag{5.15}$$

With boundary condition:

$$T(r=1)=1 \tag{5.16}$$

The temperature distribution T can be expressed by the following asymptotic expansion according to Stefan number:

$$T = T_0(r,x) + SteT_1(r,x) + Ste^2T_2(r,x) + ... \tag{5.17}$$

First substitute Equation (5.17) into Equation (5.15) using boundary condition from Equation (5.12), and then equate equal powers of Ste, the governing equations can be found as:

Zero power expressions:

$$\frac{1}{r^2}\frac{\partial}{\partial r}\left(r^2\frac{\partial T_0}{\partial r}\right) = 0, T_0(r=1,x)=1, T_0(r=x,x)=0 \tag{5.18}$$

$$T_{0(r,x)} = \frac{x-r}{(x-r)r} \tag{5.19}$$

$$\frac{\partial T_0}{\partial x} = \frac{r-1}{(x-1)^2 r} \tag{5.20}$$

$$\left(\frac{\partial T_0}{\partial r}\right)_{r=x} = \frac{-1}{(x-1)x} \tag{5.21}$$

First power expressions:

$$\frac{1}{r^2}\frac{\partial}{\partial r}\left(r^2\frac{\partial T_1}{\partial r}\right) = -\frac{\partial T_0}{\partial x}\left(\frac{\partial T_0}{\partial r}\right)_{r=x}, T_1(r=1,x)=0, T_1(r=x,x)=0 \tag{5.22}$$

$$T_{1(r,x)} = \frac{(r-1)(r-2+x)(r-x)}{6(x-1)^3 xr} \tag{5.23}$$

$$\frac{\partial T_1}{\partial x} = \frac{1}{6}(r-1)\frac{-5x^2+2x^3+8rx-4xr^2-2r+r^2}{(x-1)^4x^2r} \tag{5.24}$$

$$\left(\frac{\partial T_1}{\partial r}\right)_{r=x} = \frac{1}{3x^2(x-1)} \tag{5.25}$$

Second power expressions:

$$\frac{1}{r^2}\frac{\partial}{\partial r}\left(r^2\frac{\partial T_2}{\partial r}\right) = -\frac{\partial T_0}{\partial x}\left(\frac{\partial T_1}{\partial r}\right)_{r=x} - \frac{\partial T_1}{\partial x}\left(\frac{\partial T_0}{\partial r}\right)_{r=x} \tag{5.26}$$

$$T_2(r=1,x)=0, T_2(r=x,x)=0 \tag{5.27}$$

$$T_{2(r,x)}=\frac{1}{360}(r-1)(x-r)(r-2+x)\frac{12x^3-17x^2+10x-24rx+12xr^2+6r-3r^2+4}{x^3(x-1)^5r} \tag{5.28}$$

$$\left(\frac{\partial T_2}{\partial r}\right)_{r=x}=\frac{-1}{45}\frac{6x+1}{x^4(x-1)} \tag{5.29}$$

Substitute the first derivatives of temperature in Equation (5.13) by Equations (5.21), (5.26) and (5.29), the solution of the moving boundary is found as

$$\frac{\partial x}{\partial \tau}=-Ste\left(\frac{\partial T_0}{\partial r}+Ste\frac{\partial T_1}{\partial r}+Ste^2\frac{\partial T_2}{\partial r}\right)_{r=x}=$$

$$-\left(\frac{-1}{45}(45x^3-15Stex^2+6Ste^2x+Ste^2)\frac{Ste}{x^4(x-1)}\right) \tag{5.30}$$

The integration of Equation (5.3.2) gives the location of moving boundary with respect to time as:

$$\tau(x)=0.01(x-1)\frac{30x^2+15Ste\times x-15x-2Ste^2-15Ste-15}{Ste} \tag{5.31}$$

Surface Temperature Models

The major advantage of this model is to include the dynamic change of surface convection into the analytical solutions while most existing analytical equations only have constant surface temperature profiles. To derive an approximation for transient surface temperature, a similar procedure as described above is used. To keep the analytical equation in a simple form, the solution is approximated to the first order expansion in Equation (5.17). In comparison to equation (5.12) where only constant temperature is applied, the boundary condition of equation (5.12) is rewritten as:

$$T(r=1,\tau)=f(\tau)=f(x), T(r=x,x)=0 \tag{5.32}$$

The governing equations are derived in the same way as described in section 5.3.2. Zero power expression:

$$\frac{1}{r^2}\frac{\partial}{\partial r}\left(r^2\frac{\partial T_0}{\partial r}\right)=0, T_0(r=1,x)=f(x), T_0(r=x,x)=0 \tag{5.33}$$

$$T_{0(r,x)} = -f(x)\frac{r-x}{(x-1)r} \tag{5.34}$$

$$\frac{\partial T_0}{\partial x} = \frac{f'(x)x^2 - f'(x)x - f'(x)rx + f'(x)r - f(x) + f(x)r}{(x-1)^2 r} \tag{5.35}$$

$$\left(\frac{\partial T_0}{\partial r}\right)_{r=x} = \frac{-f(x)}{(x-1)x} \tag{5.36}$$

First power expression:

$$\left(\frac{\partial T_1}{\partial r}\right)_{r=x} = \frac{1}{6}f(x)\frac{2f(x)}{(x-1)x} \tag{5.37}$$

To start with $f(x)$ being used and later $f(x)$ is substituted by $f(\tau)$, since monotonic functions, to give the expression according to time, the final approximation of the moving boundary can be achieved without the first and second derivatives of $f(x)$. In that case, the position of the moving boundary is expressed as:

$$\frac{\partial x}{\partial \tau} = \frac{-1}{3}Stef(\tau)\frac{Stef(\tau)-3}{x(x-1)} \leftrightarrow \int x(x-1)\partial x = \int \frac{-1}{3}Ste^2 f(\tau)^2 + Stef(\tau)\partial\tau + const \tag{5.38}$$

Oxidation Unreacted-Core Model

The approximate-analytical solution illustrated earlier can be used to track the moving boundary as a result of chemical reaction inside spherical particles (Unreacted-Core model) based on the same perturbation method. The motion of the reaction (freezing) front and species concentration (temperature) are in non-dimensional form similarly to melting and solidification process.

The theoretical approach is based on assumptions as follows: Homogeneity of the spherical particle, an instantaneous reaction occurring at the moving front,constant particle density and reaction is temperature independent. For the initial approximation, the particle inside has a zero diffusing reactant concentration and the surface has a reactant concentration of $C(r,\tau) = C_0$. To generalize the process, non-dimensional variables are introduced as follows:

Non-dimensional position:

$$r = \frac{r}{r_0} \tag{5.39}$$

Non-dimensional time:

$$\tau = \frac{Dt}{r_0^2} \tag{5.40}$$

Perturbation parameter:

$$a = \frac{C_0}{a^*} \tag{5.41}$$

Non-dimensional concentration:

$$C = \frac{C}{C_0} \tag{5.42}$$

The concentration distribution within the particle is governed by modified heat conduction equation where the temperature is replaced by concentration of the diffusing reactant:

$$\frac{\partial c}{\partial \tau} = \frac{1}{r^2}\frac{\partial}{\partial r}\left(r^2\frac{\partial c}{\partial r}\right), x(\tau) < r < r_0, \tau > 0 \tag{5.43}$$

Boundary conditions are given as:

$$\begin{aligned} C(r = x(\tau), \tau) &= 0 \\ C(r = r_0, \tau) &= C \end{aligned} \tag{5.44}$$

$$\frac{\partial x}{\partial \tau} = -a\frac{\partial c}{\partial r}\bigg|_{r=x(\tau)} \tag{5.45}$$

$$\frac{\partial C}{\partial \tau} = \frac{\partial C}{\partial x}\frac{\partial x}{\partial \tau} \tag{5.46}$$

Appling the chain rule from equation (5.46) and make use of the Stefan boundary condition in Equation (5.45), Equation (5.43) can be rewritten as:

$$\frac{1}{r^2}\frac{\partial}{\partial r}\left(r^2\frac{\partial C}{\partial r}\right) = -a\frac{\partial C}{\partial x}\left(\frac{\partial C}{\partial r}\right)_{r=x} \tag{5.47}$$

With boundary condition:

$$C(r = 1) = 1 \tag{5.48}$$

The concentration distribution C can be expressed by the following asymptotic expansion according to α:

$$C = C_0(r, x) + aC_1(r, x) + a^2C_2(r, x) + ... \tag{5.49}$$

Where, in a chemical engineering application, $C(r, \tau)$ is the concentration of the

diffusing reactant, D is the diffusion coefficient, r_0 is the radius of the particle, a^* is the density of non-diflusing reactant in the particle (times a stoichiometric coefficient), C_0 is the maximum concentration outside the particle, $x(\tau)$ is the position of the moving boundary at time τ.

The location of moving boundary with respect to time is similarly:

$$\tau(x) = 0.01(x-1)\frac{30x^2 + 15a \times x - 15x - 2a^2 - 15a - 15}{a} \tag{5.50}$$

The concentration profile behind the moving front can be calculated as:

$$C = \frac{x-r}{(x-1)r} - \frac{1}{6}a(r-1)(x-2+r)\frac{x-r}{(x-1)^3xr} + ... \tag{5.51}$$

Enthalpy Method

To validate the predictions from the analytical solution, numerical model available in FLUENT is employed using fixed grid enthalpy method to calculate the phase change of a spherical particle. In this technique, a variable named as liquid fraction is calculated instead of tracking the melt interface explicitly. The liquid fraction indicates the volume fraction of the cell in liquid form and is associated with each cell in the domain. The liquid fraction is computed at each iteration based on an enthalpy balance. The enthalpy method is described thoroughly in chapter 7 and only the basic equations are provided here.

The enthalpy of the material is computed as the sum of the sensible enthalpy, h_{se}, and the latent heat, ΔH, as follows

$$H = h_{se} + \Delta H \tag{5.52}$$

where

$$h_{se} = h_{ref} + \int_{T_{ref}}^{T} c_p dT_G \tag{5.53}$$

The liquid fraction, β, is defined as:
$\beta = 0$ if $T_G < Tsolid$
$\beta = 1$ if $T_G > liquid$

$$\beta = \frac{T_G - T_{solid}}{T_{liquid} - T_{solid}} if\, Tsolid < T_G < Tliquid \tag{5.54}$$

The Latent heat content is written in terms of the latent heat of freezing, L

$$\Delta H = \beta L \tag{5.55}$$

The energy equation is written as:

$$\frac{\partial}{\partial t}(\rho H) + \nabla \cdot (\rho \vec{u} H) = \nabla \cdot (k \nabla T_G) + S_h \tag{5.56}$$

The source term appears on the right hand-sight is equal to:

$$S_h = \frac{\partial \rho \Delta H}{\partial t} + \nabla (\rho u \Delta H) \tag{5.57}$$

A two-dimensional spherical domain of 3000 cells is used for the numerical simulation.

5.3.3 Discussions and Validation

Equations (5.30) and (5.38) have two real solutions that correspond to locations of the melting front for inward and outward spherical phase change. This solution is focused on the discussion of inward phase change, for instance in the case of particle heating and melting in thermal spray application. A number of analytical solutions are currently available to solve phase change problems with pure conduction. To verify the accuracy of this improved analytical solution, constant surface temperatures are applied according to the conditions in the literature [130, 131, 132, 133, 134, 135] and the results are compared to the documented results. In figure 5.4, AS [130, 131, 132, 133, 134, 135] represent analytical solutions from literature and AS is this improved analytical solution. In the results, the Stefan number is varied from 0.1 to 1. From equation (5.8) Stefan number is dependent on specific heat, temperature difference and latent heat. In the context of particle heating within thermal spray process, sprayed powder particles have same specific heat and latent heat; therefore, Stefan number will be related directly to the temperature difference. The smaller Stefan number corresponds to a smaller temperature difference between the surface and the centre of particle, in that case, a slower phase change is expected and a longer time is required for the particle reaches a complete transformation of phase change.

The results in figure 5.4 demonstrate that completion time for phase change decreases at almost linear fashion as Stefan number increases from 0.3 to 1, but a much slower phase change occurs at Stefan number 0.1. It is apparent that all the models give similar predictions on the general trend of phase development. The closest results to the prediction of improved analytical solution are from [132]and Lin [135]. The solution of [132] is regarded as one of the most accurate for Stefan number below 1 and the equation of Lin [135] is an improved version of quasi-steady solution. The close agreement with both well

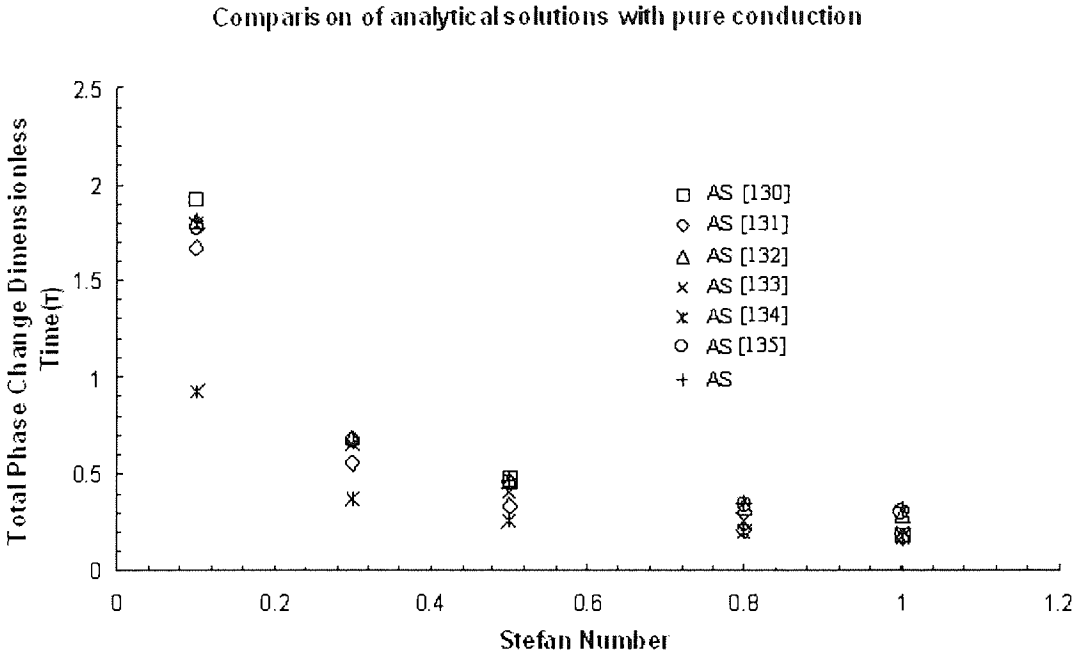

Figure 5.4: Comparison of analytical solutions with pure conduction.

established solutions confirms the accuracy of this new solution to solve phase change with pure conduction.

Development of Phase Front at Constant Surface Temperature

Figure 5.5 shows the development of phase front position in the particle when it is imposed to constant surface temperature. The phase front in the drop moves from the surface $r/r0 = 1$ towards the centre. There are three sets of results given, i.e. Stefan numbers 0.2, 0.3 and 1. The results from the improved analytical solution (AS) are compared with the numerical model (NS) using the enthalpy method. It needs to be noted that the numerical model are also validated with the documented numerical results to make sure the accuracy of model prediction. In figure 5.5, additional results for Stefan numbers 1 are given from a similar enthalpy model used by [136]. Despite the simplicity of the analytical solutions, excellent agreements are reached between the results of the analytical equations and numerical enthalpy model. It needs to point out, the analytical solution is an approximation of a second order of accuracy, in that case, a certain degree of discrepancy will occur at high Stefan number, such as in the result of Stefan number 1. In a general engineering application, the moving boundary problems will occur under Stefan number 1, for instance, powder particles within thermal spraying have Stefan number between 0.3-0.5, therefore the analytical solution developed is able to deliver

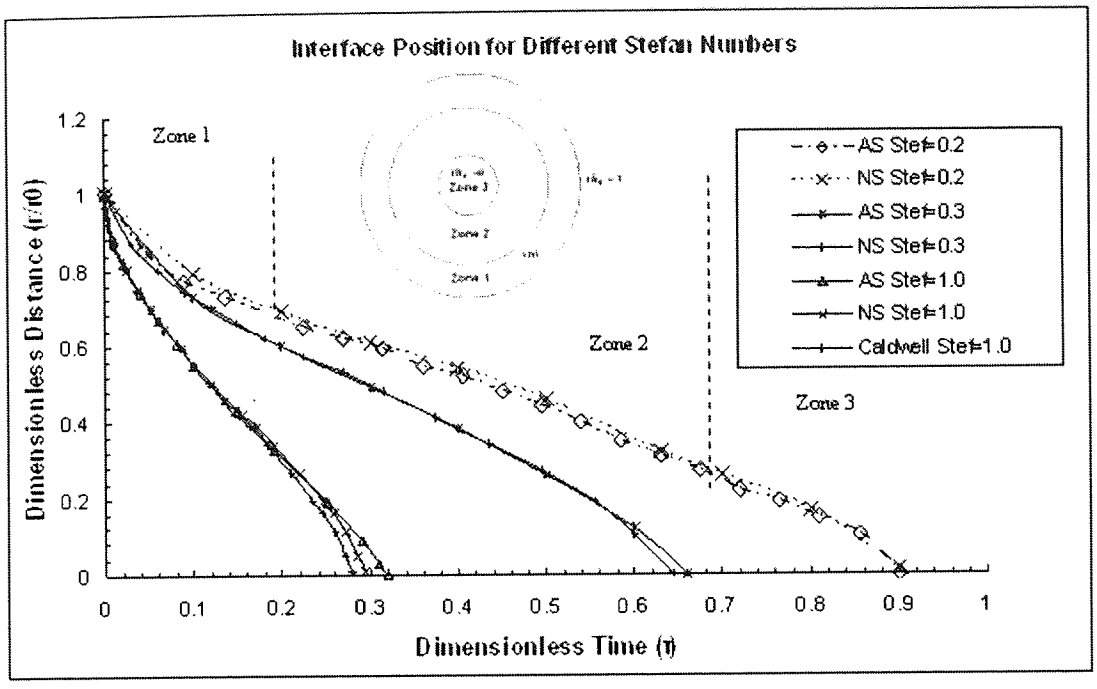

Figure 5.5: Development of moving boundary with pure conduction (AS: analytical solution, NS: numerical solution.

results with good accuracy (>95%) in most engineering applications. For the demand of high Stefan number conditions, high order accuracy from this perturbation method needs to be used. In all the Stefan number conditions plotted, the advance of moving front is not in a linear pattern with respect to time, which indicates the propagation speed of the moving front is not constant.

As described early, low Stefan number corresponds to small temperature difference between the surface and the centre of particle, in that case, phase change develops slowly and the motion of the moving boundary is most identifiable. Among the current results, the heat transfer process is slower enough to give more distinctive regions in the condition of Stefan number 0.2, hereby, the result of Stefan number 0.2 is used for description of phase change development. In the case of particle heat and melting by external gas flow, the particle surface has the maximum high temperature which gives rise to a rapid heating of the adjacent particle regions, as shown in Zone 1. Once the melting front propagates into the particle Zone 2, the effect of conduction on heat transfer becomes significant, which slows down the movement of melting front. As the moving boundary develops further into the core of the particle Zone 3, the area is smaller enough to give a rapid heat transfer and the melting front once again develops very fast in the centre.

The temperature profiles at various stages of the phase change process are shown in

figure 5.6. In the case of particle melting, $T = 1$ is the surface temperature which is above the melt point and $T = 0$ is the melting point. At the beginning of the phase change, there is a high temperature gradient between the surface and the adjacent particle region ($r/r0 = 0.8$), where a rapid propagation of moving front occurs as shown in the Zone 1 of figure 5.5 and described before. As the moving front progresses further inwards, the temperature gradient is reduced at $r/r0 = 0.5$ as the moving front propagation slows down in Zone 2. A sharp temperature gradient is found close to the centre of the particle at $r/r0 = 0.2$, where the moving boundary advances at fast speed as shown in the Zone 3 of figure 5.5.

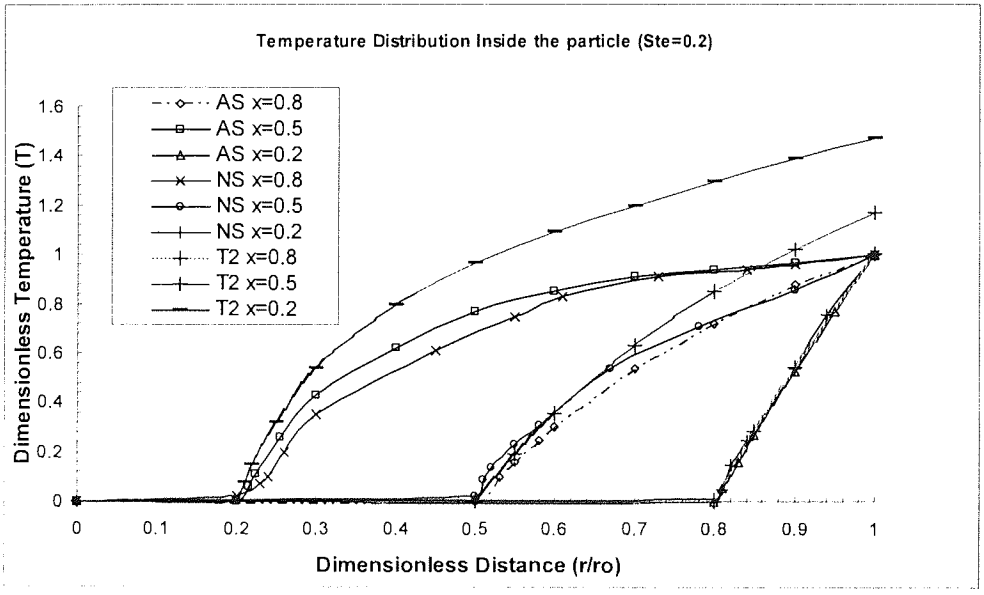

Figure 5.6: Temperature profiles within particles with pure conduction.

Phase Change with Convection and Conduction

For the purpose of model validation, the improved analytical solution is tested at the condition of $Bi = 1$ and $Ste = 0.5$, and the results are compared with the numerical models from literature [137, 138]. In these particular surface convection conditions, phase front moves steadily in the most part of the particle and only accelerates near the centre of the particle. The moving boundary under the effect of convection and conduction develops quite differently from the profile with pure conduction as illustrated in figure 5.5. A more quantitative comparison is given in the following section. It needs to be noted, a "S" shaped profile can be found for all the moving boundary under the condition of constant surface temperature, while the moving boundary profiles are varied under the condition

of transiet surface temperature. The development demonstrated in figure 5.7 is only valid for this specific surface temperature condition.

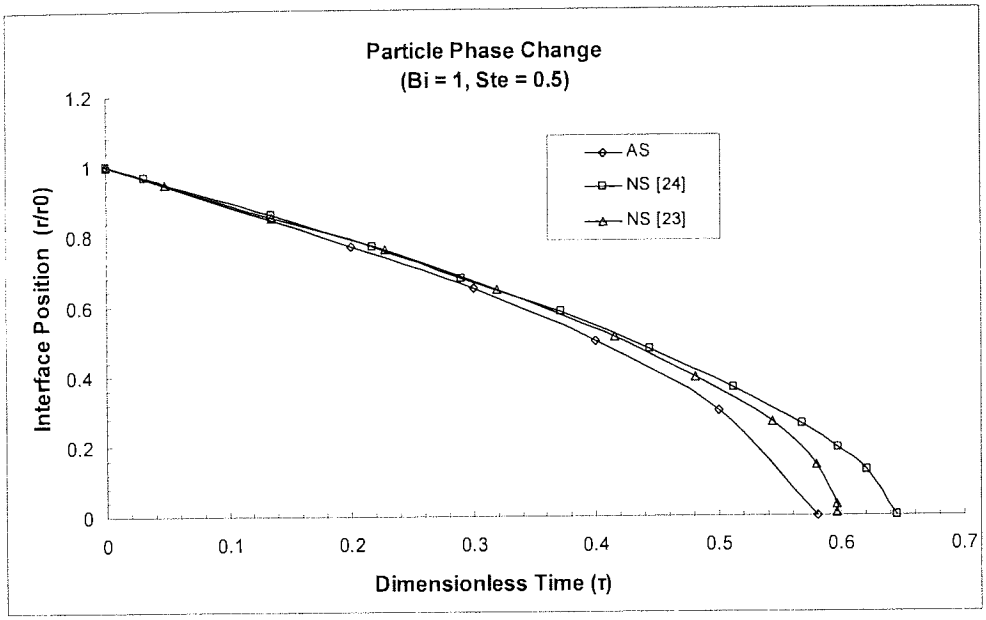

Figure 5.7: Development of moving boundary with convection and conduction.

Development of Phase Front for Variable Surface Temperature

To further investigate the effect of surface temperature on the development of moving boundary, Stefan number 0.2 is used and three different surface temperatures are given. T1 ($f(\tau) = 1$) is with constant surface temperature, T2 ($f(\tau) = 1 + \tau^2$) and T3 ($f(\tau) = \tau^2$) have both variable surface temperatures. The results are compared quantitatively in figure 5.8. An increased heat in T2 only brings a small change of the profile compared to T1 while a much slow development is demonstrated in T3. The development of moving boundary in T1 has been described before and only T3 needs to be addressed here. In the case of particle melting, the surface starts to be heated up from the melting point ($T = 0$), the melting front propagates gradually and progresses inwards steadily as the heat input from surface through convection is balanced by the increased rate of heat required to melt the material. Near the centre of the particle the propagation speed of melting front accelerates as the reduction of area prompts fast heat transfer. The general trend from T3 is similar to the results in figure 5.5. The results in figure 5.8 clearly demonstrate the moving boundary develops differently for different surface temperature conditions. By controlling the heat input or the gas flow pattern around the particle, it is possible to control the process of phase change within the particle, e.g. a constant

propagation speed can be achieved for the moving boundary by removing heat from the particle at the late stage of phase change when a fast propagation is expected. As seen in figure 5.8, the increase of heat input will give rise to high temperature profile for T2 as shown in Figure 5.6 for the location of $r/r0 = 0.5$ and 0.2. In reality, the surface temperature will stagnate once reaches the temperature of surrounding fluid.

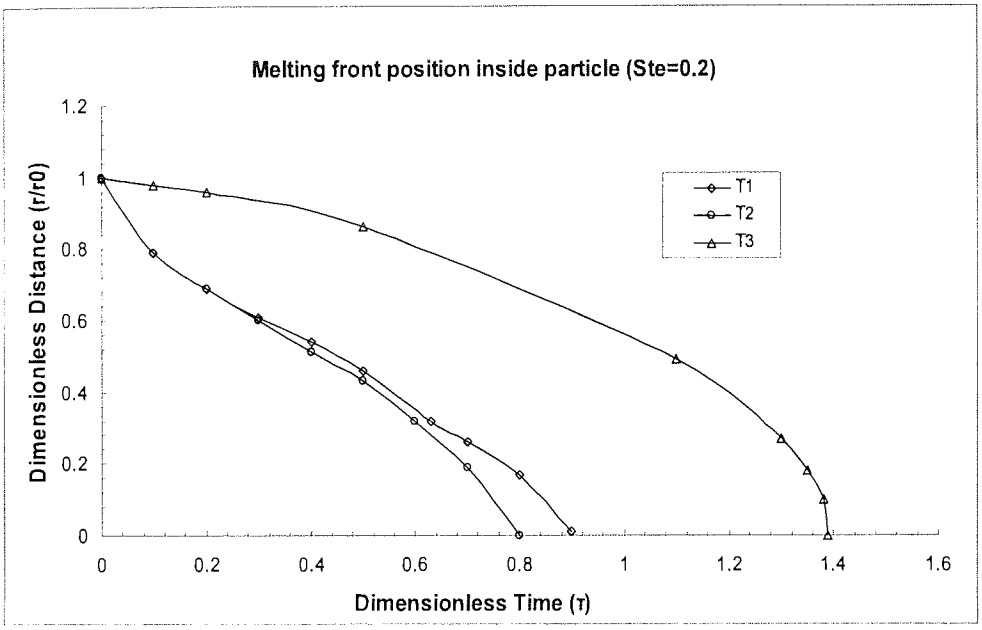

Figure 5.8: Development of moving boundary at different surface temperatures.

5.4 Numerical Phase Change Model

In the previous section an analytical approach on phase change dynamics was described thoroughly and validated. The analytical model is based on several assumptions, such as constant metal properties and single melting temperature which may impose inaccuracies when metal alloys are examined. For pure materials and alloys with eutectic composition, with a definite freezing/melting point, it can be assumed that the freezing-melting front is a surface normal to the direction of propagation. For alloys, the phase transition may take place in a certain temperature range, giving a layer of a certain thickness, the so called mushy zone, which separates the solid from the liquid. In this section an approach that combines the Lagrangian particle modelling with numerical solution within the discrete particles is presented in an attempt to overcome the limitations of the analytical solution. The numerical model presented in this section is a "cheap to

run version" of the expensive fixed grid methods described in section 5.3.1. The concept behind this model is to incorporate an already developed correction function [139] to particle heat transfer equation, which allows for the phase change phenomena to be included.

The high thermal profiles endured for sprayed particles in conjunction with melting give rise to oxidation on the surface of metal powders. Microstructure analysis [140] on as-sprayed coating has clearly identified the oxide layers on deposited metal splats. Metallic oxides are brittle and have different thermal expansion coefficients in comparison to the surrounding metals, therefore, it is generally believed that the oxides in the coating have negative effects on its properties, which undermines the performance of coated products. It is important to understand the development of oxides during thermal spraying in order to achieve better controls of the coating process. Experimental approaches such as microscopic technologies can reveal the final stage of the oxidation after the impact while the critical information of in-flight oxidation development cannot be obtained. Mathematical modelling has been regarded as a cost-effective approach to gain insights of complicated processes. Those models are able to predict the temperature and velocity history of in-flight particles by coupling the simulation of gas and particle flows; however, modelling of oxidation on metal powders have hardly been addressed in open literature. The oxidation model presented in this section is based on the Mott-Cabrera theory for very thin oxide films [141] where it is assumed that oxidation is limited by the ion transport through the oxide layer. The model is implemented as a user defined function (UDF) into FLUENT's source code.

In thermal spray process, the heat transfer due to radiation from the surroundings to particle is negligible compared to the convective heat flux from the gas to the particle. Therefore, particle heating in spherical coordinates is given by:

$$\rho_p C_p \frac{\partial T}{\partial t} = k_S \left(\frac{\partial^2 T}{\partial r^2} + \frac{2}{r} \frac{\partial T}{\partial r} \right) + H_{sf} \rho_p \frac{df}{dt} \tag{5.58}$$

Considering an alloy for which the area of solidification in the phase diagram is approximated by straight lines, Equation (5.58) can be written as:

$$\frac{\partial T}{\partial t} = \frac{\alpha}{\psi(T)} \left(\frac{\partial^2 T}{\partial r^2} + \frac{2}{r} \frac{\partial T}{\partial r} \right) \tag{5.59}$$

Where the function $\psi(T)$ is defined as [139]:

$$\psi(T) = \begin{cases} if\ T_S \leq T \leq T_L & 1 + \frac{H_{sf}(T_k - T_L)^{\frac{1}{1-k_c}}}{C_p(1-k_c)(T_k-T)^{\frac{2-k_c}{1-k_c}}} \\ else & 1 \end{cases}$$

T_K is the melting temperature of the primary element and k is the ratio between solid and liquid concentration. This model assumes infinite velocity for diffusion (equilibrium condition) in liquid phase and zero in the solid [21]. The boundary conditions associated to Equation (5.59) are specified on the boundary and in the center of the particle:

$$\left.\frac{\partial T}{\partial r}\right|_{r=0} = 0; \quad k_s \left.\frac{\partial T}{\partial r}\right|_{r=R} = h(T_g - T_R) \tag{5.60}$$

R represents the radius of the simulated particle, k_s is thermal conductivity of particle, Tg is the gas temperature and h is the convective heat transfer coefficient. The heat transfer coefficient is evaluated using the Ranz and Marshall correlation [106]:

$$Nu = (2 + 0.6Re^{1/2}Pr^{1/3}) \tag{5.61}$$

where Nu is the non-dimensional Nusselt number, defined as:

$$Nu = \frac{hd}{k_g} \tag{5.62}$$

The discretized form of Equation (5.59) is:

$$\begin{aligned} &\alpha\tfrac{\Delta t}{\Delta^2 r}\left(i^{-1}-1\right)T_{i-1}^{n+1} + \left(2\psi_i^n + 2\alpha\tfrac{\Delta t}{\Delta^2 r}\right)T_i^{n+1} - \alpha\tfrac{\Delta t}{\Delta^2 r}\left(i^{-1}+1\right)T_{i+1}^{n+1} \\ &= \alpha\tfrac{\Delta t}{\Delta^2 r}\left(1-i^{-1}\right)T_{i-1}^{n} + \left(2\psi_i^n - 2\alpha\tfrac{\Delta t}{\Delta^2 r}\right)T_i^{n} + \alpha\tfrac{\Delta t}{\Delta^2 r}\left(i^{-1}+1\right)T_{i+1}^{n} \\ &i = 1, 2, ...N-1 \end{aligned} \tag{5.63}$$

N is the number of discretization points along the radius of the droplet and n the time index. After grid sensitivity analyses to all particle sizes the nodal points were set to10. For larger particles more discitization points are required to improve the accuracy of the melting and solidification kinetics. In the same manner, equation (5.60) becomes:

$$-T_{N-1}^{n+1} + \left(1 - \frac{h^n \Delta r}{k_i^n}\right)T_N^{n+1} = \frac{h^n \Delta r}{k_i^n} T_g \tag{5.64}$$

Equation (5.59) in the center (r=0) becomes indeterminate, this means that the relation in Equation (5.63) cannot be used. By applying the theorem of L'Hospital, we obtain:

$$\frac{\partial T}{\partial t} = 3\frac{\alpha}{\psi(T)}\frac{\partial^2 T}{\partial r^2} \tag{5.65}$$

The discretized form of equation (5.65) is:

$$\left(\psi_0^n + 3\alpha\frac{\Delta t}{\Delta^2 r}\right)T_0^{n+1} - 3\alpha\frac{\Delta t}{\Delta^2 r}T_1^{n+1} = \left(\psi_0^n - 3\alpha\frac{\Delta t}{\Delta^2 r}\right)T_0^n + 3\alpha\frac{\Delta t}{\Delta^2 r}T_1^n \tag{5.66}$$

Oxidation on the particle will take place when enough oxygen is available in the surrounding gas flow. Based on the Mott-Cabrera theory, oxidation is controlled by the ion transport through the oxide film, therefore the growth of the oxide layer can be computed by the following relation [142]:

$$\frac{\partial \delta}{\partial t} = 2A_0 \exp\left(\frac{-Q}{k_b T_R}\right)\exp\left(\frac{K_0\sqrt{P_{O_2}}}{k_b T_R}\right) \tag{5.67}$$

It is assumed that the heat released from oxidation is confined to droplet surface, so the boundary condition in Equation (5.63) at location r =R becomes:

$$k_S \left.\frac{\partial T}{\partial r}\right|_{r=R} = \frac{T_g - T_R}{1/h + \delta/k_{ox}} + \rho H_{ox}\frac{d\delta}{dt} \tag{5.68}$$

Equation (5.68) becomes:

$$\begin{aligned} &-T_{N-1}^{n+1} + \left(1 - \tfrac{H^n\Delta r}{k_N^n}\right)T_N^{n+1} = \tfrac{\rho H_{ox}\Delta r}{k_N^n}\tfrac{d\delta^n}{dt} + \tfrac{H^n\Delta r}{k_N^n}T_g \\ &H = \tfrac{1}{(\delta^n/k_{ox})+(1/h)} \end{aligned} \tag{5.69}$$

where H is the total heat transfer coefficient.

At each time step the algebraic system of equations (5.63), (5.64) and (5.66) (without oxidation) and equations (5.63) (5.69) and (5.66) (including oxidation) is solved using the Gauss Seidel iterative method which is implemented as a user defined function in the simulation.

Chapter 6

In-Flight Particle Modelling

6.1 Modelling of Inconel 718 Particles

Powder particles, normally in the size range 5 to 65 μm, are injected into the gas jet so that they are heated and accelerated toward the substrate to be coated. On arrival at the substrate, particles are ideally in a melted or softened state and, on impact, form lenticular splats, which adhere well to the substrate and to one another. The HVOF gun is scanned cross the substrate to build up the required coating thickness in a number of passes. The purpose of this section is to examine particle motion and heat transfer within the gas flow field and to investigate the effect of particle injection parameters.

6.1.1 Model Development

A schematic representation of the HVOF gun is shown in figure 6.1. The mixture of fuel and oxygen stream is injected into the water-cooled combustion chamber, where the gases burn and the combustion products are accelerated down the convergent divergent nozzle and long parallel-sized barrel. Powder particles are injected into the barrel through two holes with a tapping angle in the front of the barrel. The particle laden by gas mixture exits the gun at a high temperature and velocity toward the substrate to be coated.

The three-dimensional simulations are performed in FLUENT. The computational geometry includes the gun and external domain as shown in figure 6.2. The boundary conditions have been described previously. Briefly, a structured grid is used and fine meshes are employed to the sensitive areas such as, the nozzle entrance and exit, the barrel exit and the free-jet centreline where high gradients are expected and great accuracy is required in order to capture the compressibility effects. Grid sensitivity studies have been carried out by doubling the cell number both axially and radially and the numerical solutions from both meshes are almost identical. The compressible turbulent chemically

reacting flow model has been described in (section 4.2).The process parameters employed in the computational modelling are 0.003526 kg/s for kerosene and 0.01197 kg/s. The computation of particle dynamics is achieved by coupling with the Eulerian gas flow. The powder is treated as spherical particles which closely represent the thermally sprayed powder, Inconel 718 which has the thermal properties shown in Table 6.1. The computer model treats the powder feeding as a point injection through the barrel's wall without carrier gas being introduced to the computational domain. Unlike a gas fuelled HVOF system where the carrier gas is injected into the centre of the combustion chamber, the introduction of cross flow carrier gas into a high speed stream has given rise to numerical errors and difficulty to control the convergence of the solutions. Considering that the volume fraction of carrier gas is less than 2% of the total flow rate, the carrier gas is expected to have only marginal effect on the flow pattern and the subsequent effect on the behaviour of particles could be marginal.

Density (ρ_p) [kg/m3]	8200
Solidus temperature (T_S) [K]	1528
Liquidus temperature (T_L) [K]	1610
Primary element melting point (Tk) [K]	1726
Partition coefficient (k_c)	0.3
Specific heat (C_p) [J/kg K]	600
Latent heat (H_{sf}) [J/kg]	227000
Thermal conductivity (k) [W/m K]	T<1000K: 21, 1000<T: 5.8 + 0.016T

Table 6.1: Thermophysical properties for Inconel 718 [143].

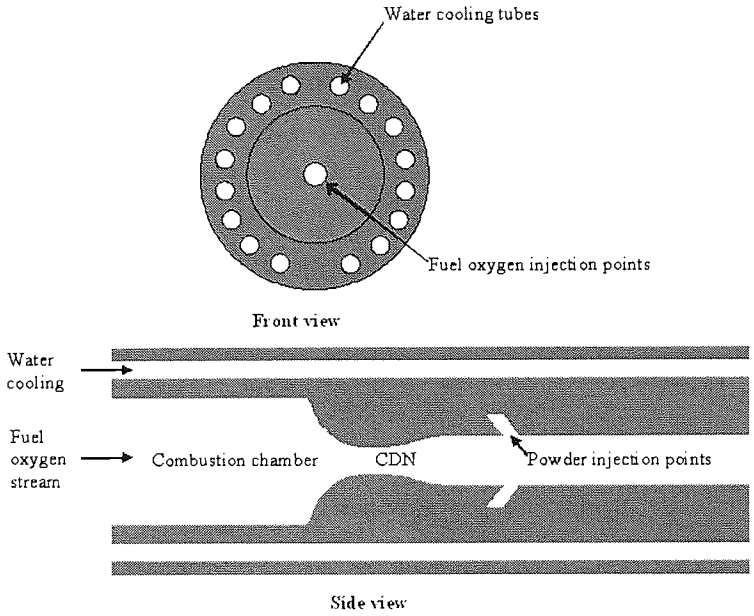

Figure 6.1: Schematic representation of the HVOF gun including combustion chamber, convergent divergent nozzle (CDN) section and parallel-sized barrel.

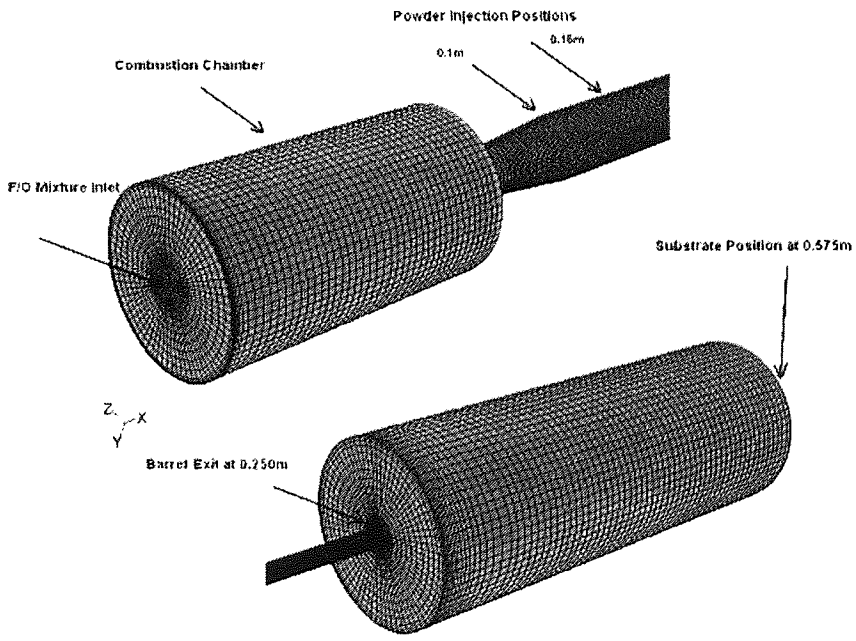

Figure 6.2: Grid and computational domain.

6.1.2 Discrete Phase Mathematical Modelling

The heat transfer models have been described in the previous chapter thus only the momentum transfer modelling is reported in this section. In support of validation both analytical and numerical formulations are reported and compared. The oxide layer growth of the Inconel 718 particles is not included in this section. The oxidation experimental data on Inconel 718 material are very limited in open literature. Instead, the model is implemented for the oxidation level prediction of steel particles where reliable data are available and can be used consistently as input parameters to the model.

Momentum Transfer

The equation of motion for particles can be written as a force balance that equates the droplet inertia with forces acting on the droplet:

$$\frac{du_p}{dt} = F_D\left(u_g - u_p\right) + \frac{g_x\left(\rho_p - \rho_g\right)}{\rho_p} \tag{6.1}$$

The drag force per unit particle mass is:

$$F_D = \frac{18\mu}{\rho_p d_p^2}\frac{C_D Re}{24} \tag{6.2}$$

the drag coefficient CD given by [104]:

$$C_D = \frac{24}{Re_d}\left(1 + b_1 Re_d^{b_2}\right) + \frac{b_3 Re_d}{b_4 + Re_d} \tag{6.3}$$

$$\begin{aligned} b_1 &= \exp\left(2.3288 - 6.4581\phi + 2.4486\phi^2\right) \\ b_2 &= 0.0964 + 0.5565\phi \\ b_3 &= \exp(4.905 - 13.8944\phi + 18.4222\phi^2 - 10.2599\phi^3) \\ b_4 &= \exp\left(1.4681 + 12.2584\phi - 20.7322\phi^2 + 15.8855\phi^3\right) \end{aligned} \tag{6.4}$$

the shape factor is given by [105].
The Reynolds number is defined by:

$$Re = \frac{\rho_g |u_g - u_p| d_p}{\mu_g} \tag{6.5}$$

As the gas flow is turbulent during HVOF spraying, the influence of the turbulence on the particle behavior needs to be evaluated. The effect of turbulent fluctuation on the particle aerodynamic response could be reflected by the Stokes number (St) which is the ratio of the aerodynamic response time to the time scale associated with larger-scale turbulent eddies.

$$St = \frac{\rho_p d_p u_p}{18 \mu_p D}$$

The large Stokes number (St>>1) means a slow response from the particle to the large turbulent eddies. The sprayed powder Inconel 718 with a mean diameter of 20m under the present HVOF flow has the Stokes number:$St \approx 300$, which implies that the turbulence would not have substantial effect on the particles larger than 20m.

6.1.3 Results and Discussions

Influence of Particle Injection Velocity

The particle injection velocity can be manipulated by carrier gas flow rate. In this calculation, 20 μm diameter Inconel 718 particles are injected from the axial distance of 0.12 m. The injection velocities vary in the range 0-40 m/s. The particle trajectories in figure 6.3 show that the particle is driven by the gas flow and travels along the edge of barrel with zero injection speed; the increase of injection velocity will enable the particle travel cross the gas flow and move towards the centre of the jet at injection speed between 8-10 m/s; the particle travels cross the center of the gun and spreads outwards at injection speed of 20 m/s; the particle hits the internal surface of the barrel and the trajectory is changed to opposite direction as the result of elastic collision at 40 m/s. Nozzle wear is most frequently encountered problem for operating HVOF guns and the nozzle needs to be replaced after about 10 hours spraying. Examination of the damaged nozzles reveals the particle pathlines along the internal surface of the barrel and cracks in the nozzle by the impact of high speed particles. The computational results imply that, to spray Inconel 718 powder with a mean diameter of 20 μm, the injection speed needs to be controlled within the range of 8-10 m/s, in that case, and particularly at 8 m/s, most powder particles will stay in the centre of the gun; powder particles will spread outwards by increase of the injection velocity over 10 m/s; the particle is most likely to hit the barrel and give rise to nozzle wear when the injection velocity increased above 20 m/s. Zero injection velocity should also be avoided as the particle travels along the edge of barrel, the particle could make mechanical contacts with the barrel or very small melted particles could stick on the internal surface of the nozzle and generate the blockage.

The advantage of HVOF technology is its ability to accelerate particles to very high speed, therefore, it is desirable to achieve the highest possible velocity of powder particles during spraying. The velocity profiles in figure 6.4 show that the particles reach high velocity when injection velocity is between 8 to 10 m/s. It is known that the gas flow has the highest velocity in the centre; therefore particles will gain more momentum while

traveling in that region. The temperature profiles in figure 6.5 confirm that the particles heated more efficiently for 8-10 m/s injection velocity when the particles travel at the centre of the gas jet.

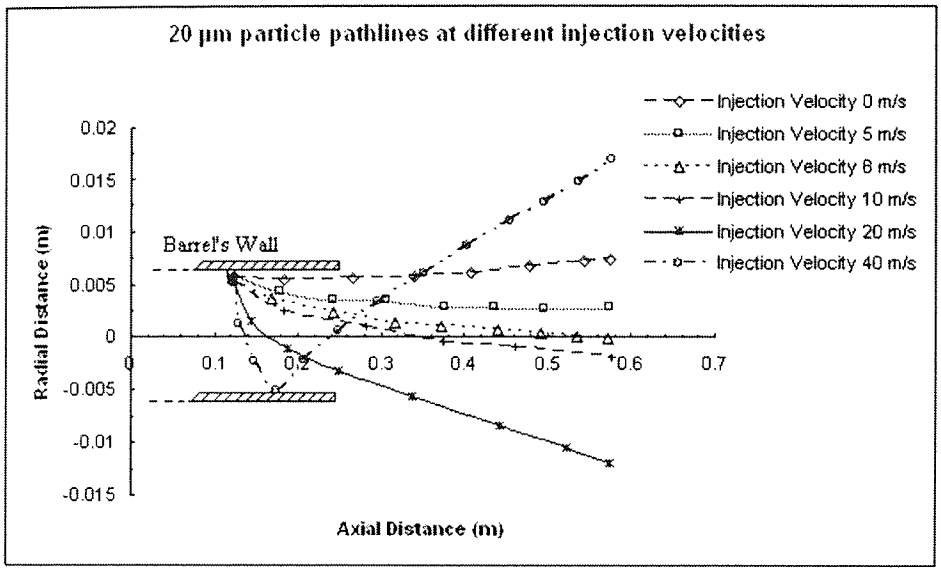

Figure 6.3: Particle trajectories at different injection velocities.

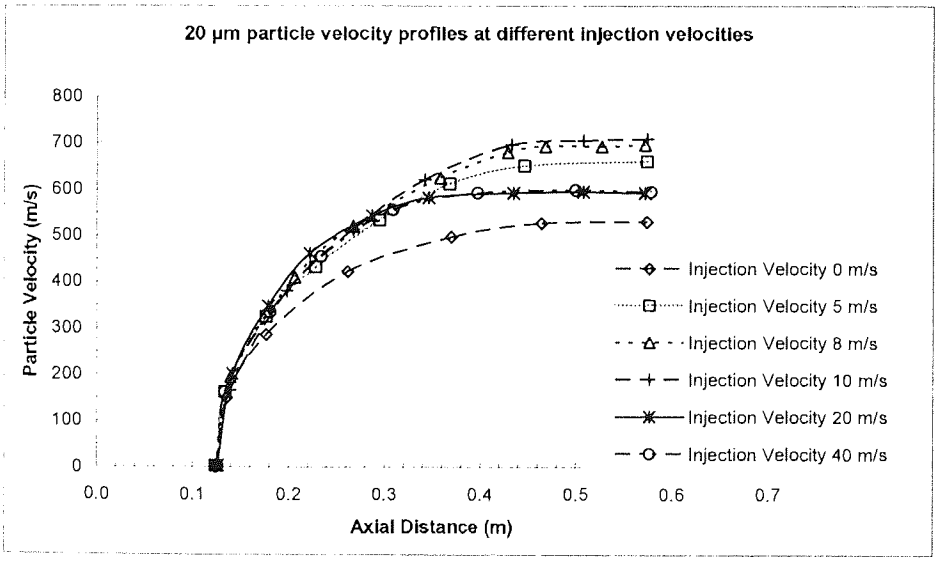

Figure 6.4: Particle velocity profiles at different injection velocities.

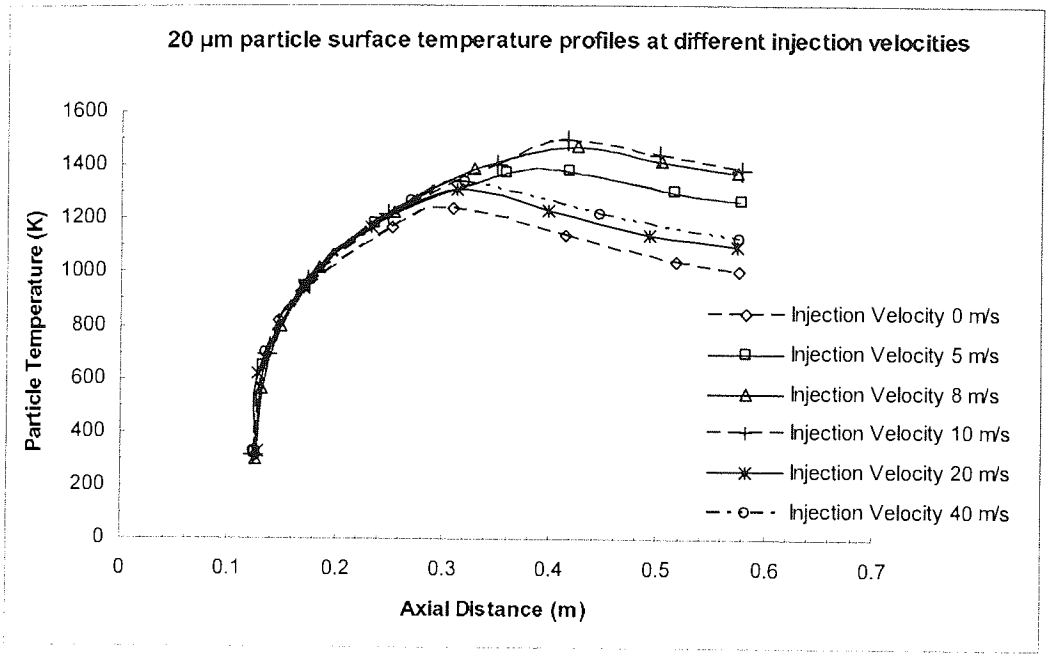

Figure 6.5: Particle surface temperature profiles at different injection speeds.

Influence of Particle Injection Position

The liquid fuelled HVOF gun is designed to inject powders at the front of the barrel instead of feeding the spray powder into the center of the combustion chamber adopted in gas fuelled HVOF systems such as HV2000 (Praxair, US). The advantage of such design is to suppress the contacts between powders and the gas flame to minimize the undesirable oxidation for metal powders. The location of injection is also important to generate consistent coating products. The high pressure gas undergoes drastic expansion and compression in the throat of the nozzle as shown in figure 6.6, the substantial pressure fluctuation makes the control of powder feeding very difficult, therefore, it is not practical to inject powders in the throat region. In this calculation, 20 μm Inconel 718 particles are released from 5 axial locations between 0.10 and 0.15 m in the front of the barrel at injection velocity of 8 m/s which is within the range of optimal injection velocities as stated in the previous section. The predicted paths for these particles plotted in figure 6.7 show that all the particles travel at similar trajectory and reach the centre of the jet at the end of the domain.

The velocity profiles in figure 6.6 demonstrate that the particles accelerate continuously throughout the domain despite the decline of gas jet near the end of the domain. It is known that the longer distance prolongs the residual time of in-flight particle and the particle accelerates more, therefore, it is sensible to inject powder at the earliest possible

point when the gas flow is stabilized. The particle temperature profiles in figure 6.8 show that powder particles are heated rapidly in the barrel and develop steadily from the exit of the gun, the particle temperatures start to decline when the temperature of gas flow drops sharply when cold air penetrates deeply into the gas jet. The computational model has an external domain of 32 cm from the gun exit, which is within the typical range of stand-off distances for the HVOF spray coating. The particle dynamics at the exit of the computational domain (i.e 32 cm from the gun exit) can be regarded as the impact parameters. The particle impact parameters in figure 6.9(a) show that the surface temperatures of particles drop below the melting point (1528K for the Inconel 718 powder). The set of results imply that the particles at the given injection speed will concentrate at the centre of the jet and have similar dynamics from different axial injection distances, while the high impact velocity and temperature will achieve at axial distance closer to the throat of CDN as shown in figure 6.9(b). However, too close to the throat of CDN will give rise to practical issue of controlling the pressure fluctuation for the powder feeder, the axial distance of 0.12 m is adopted in the current design and will be used for the following discussions.

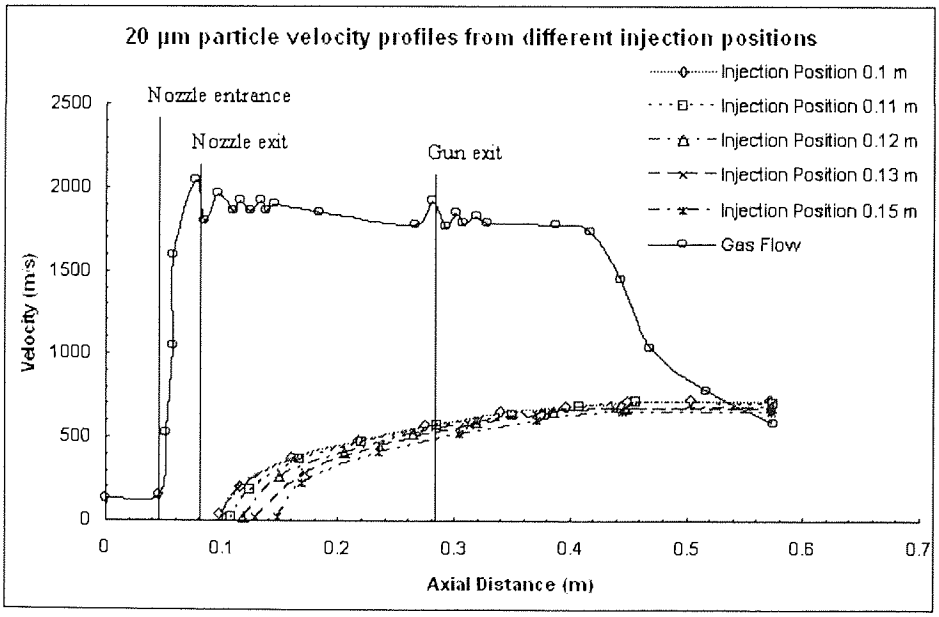

Figure 6.6: Particle velocity profiles from different injection positions.

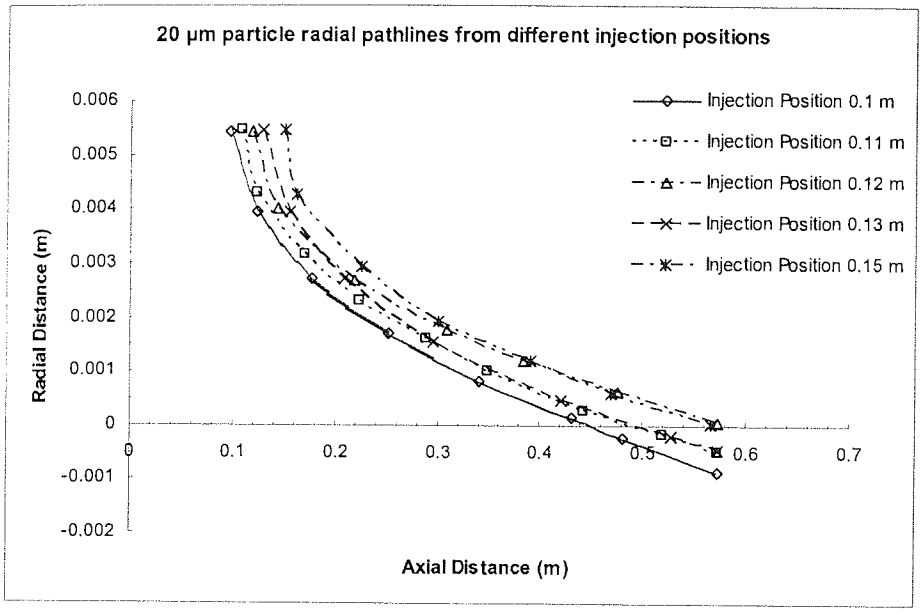

Figure 6.7: Particle trajectories from different injection positions.

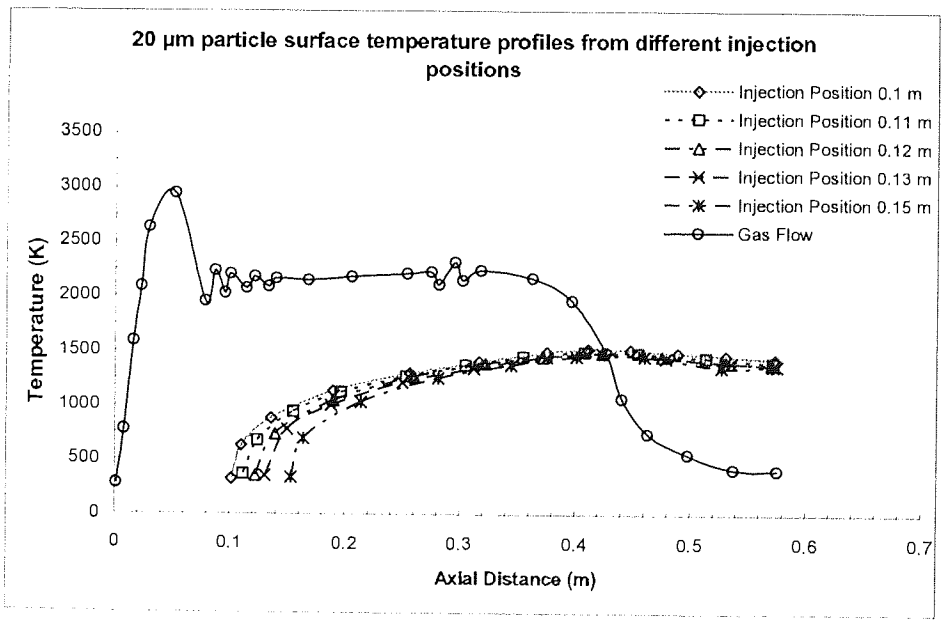

Figure 6.8: Particle surface temperatures from different injection positions.

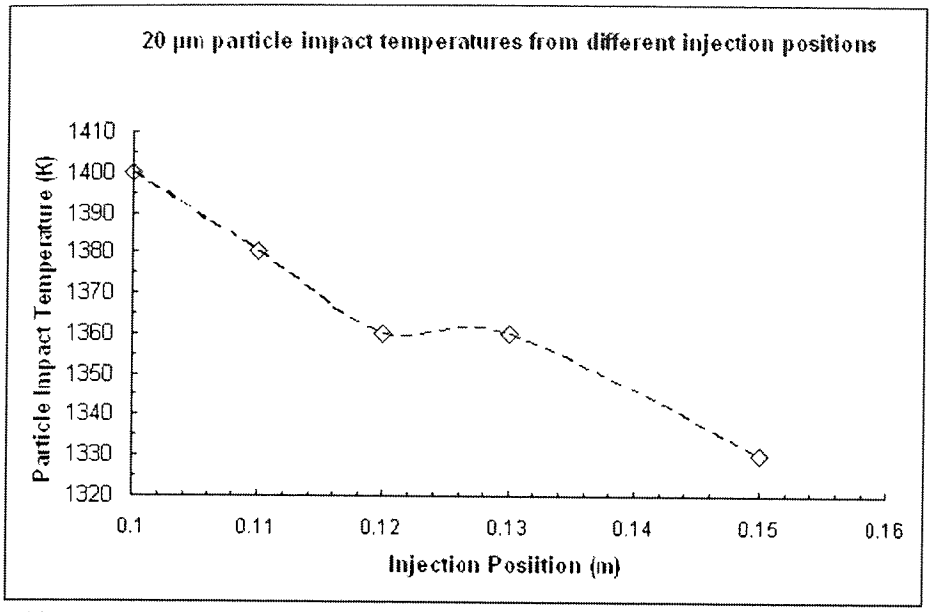

(a)

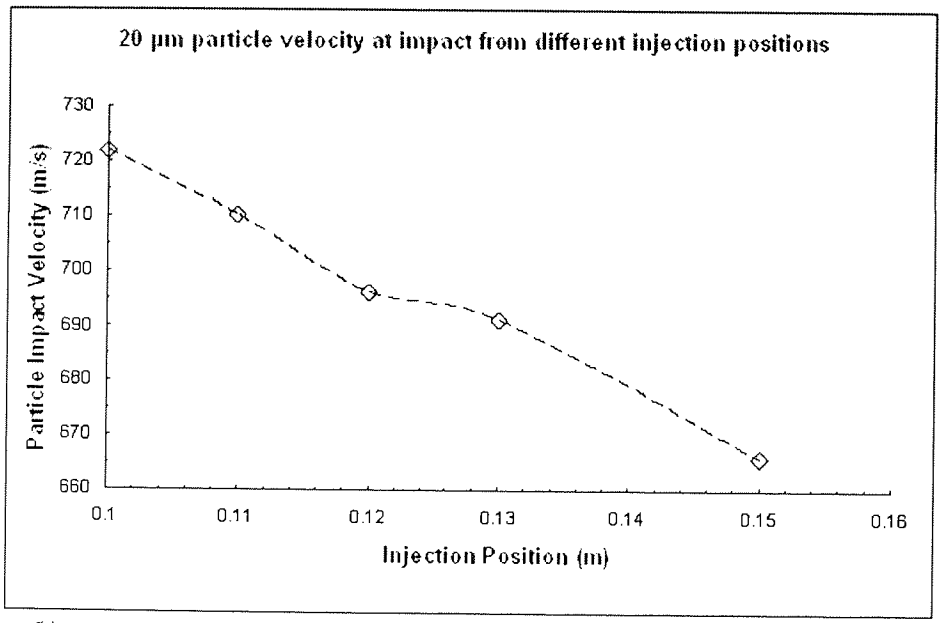

(b)

Figure 6.9: a,b Particle impact parameters from different injection positions.

Influence of Particle Size

Feedstock powder is generally supplied with a range of distribution. This study is to examine the effect of different particle sizes on particle behaviour to provide information on the optimum range within the nominal size distribution. In these calculations, different

sized Inconel 718 particles ranging from 5 μm to 40 μm were injected at axial distance of 0.12 m with a speed of 8 m/s. The particle trajectories in figure 6.10 show that the small particles are blown away by the gas flow, e.g. 5 μm particle travels along the edge of the barrel and spreads outwards at the external domain as the jet expands outside. The 10 μm particle remains at the outer region of the jet throughout the domain while the large particles e.g. 30 and 40 μm move cross the centre of the gun and spread outwards in the external domain. The particle velocity profiles in figure 6.11 clearly demonstrate that the smaller particles are accelerated more throughout the computational domain. When the particle velocity is higher than the gas velocity, as the gas jet decays outside the gun, the drag force on the particle then changes direction and becomes a resistance to the particle motion. The velocity of the particle is then decreased. The smaller the particle size, the more easily it is decelerated. A larger particle, on the other hand, has greater ability to maintain its velocity during the deceleration stage, because of its larger inertia. The velocity dependence on particle size is more clearly demonstrated in figure 6.12(a) which is a plot of particle velocity versus particle diameter at the point of impact on the substrate. The temperatures at the impact in relation to the particle size are given in figure 6.12(b). The surface temperature plots in figure 6.13 show the particles smaller than 10 μm undergo melting and solidification during the process which will be discussed in details in the following section.

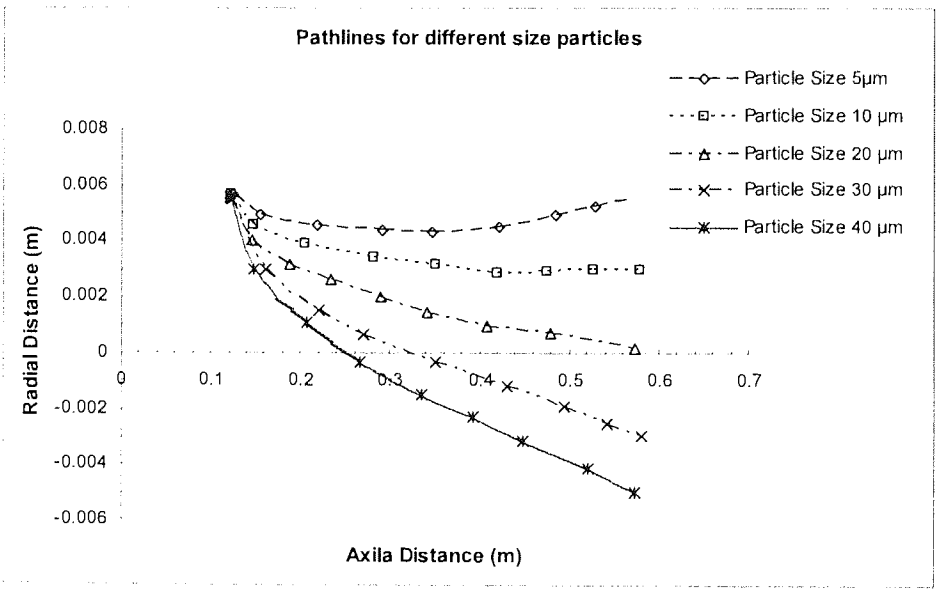

Figure 6.10: Trajectories for different size particles.

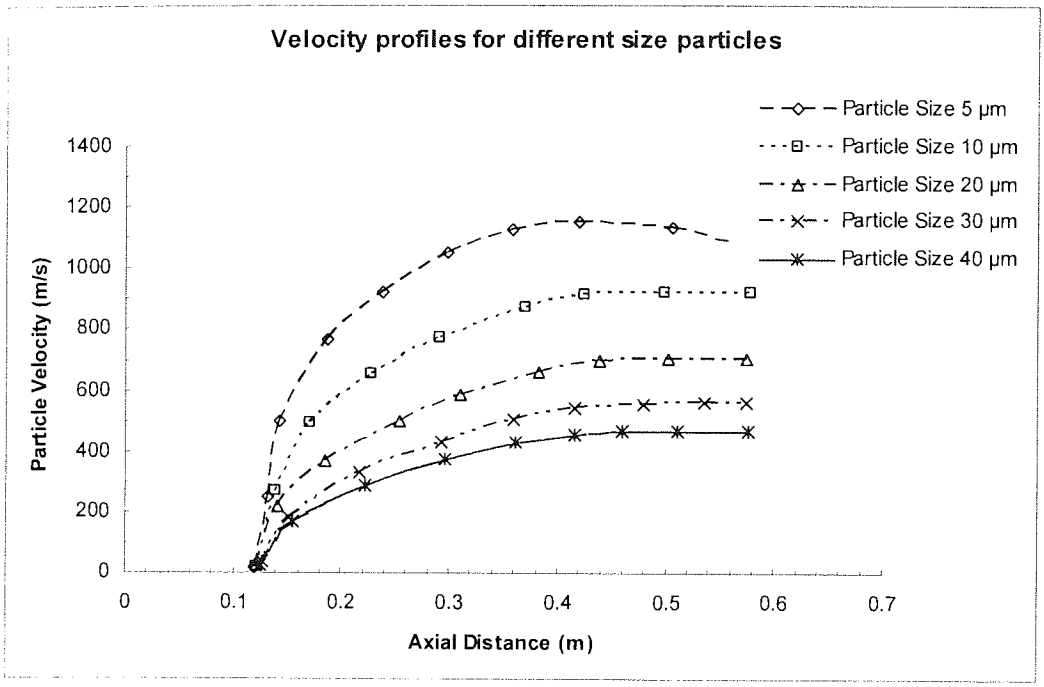

Figure 6.11: Velocity profiles for different size particles .

Melting and Solidification

The temperature evolution of 10 μm particle in figure 6.14 shows the rapid heating of particle is prevented when the surface temperature arrives at the solidus temperature (1528 K) at 0.18 milliseconds. The surface temperature increases slowly as the solidus isothermal surface moves towards the centre of the particle. At 0.29 milliseconds the surface temperature reaches the liquidus temperature (1610 K). At this point, the particle is still not in full liquid state, it takes another 0.0001 milliseconds for the liquidus temperature reaches the centre of the particle, which implies that the phase transformation is almost instantaneous once the surface reaches the liquidus temperature for this small 10 μm particle. When the particle is in full liquid state, the surface temperature starts to rise quickly and reaches the maxima. Figure 6.8 shows that the gas temperature declines sharply outside the gun and the heat transfer from gas to particle is reversed when the gas temperature drops below the particle temperature. From the maximum value, the surface temperature of particle starts to decrease, drops to liquidus temperature at 0.34 milliseconds and reach the solidus temperature at 0.41 milliseconds. From that point, the particle becomes solid instantaneously and the temperature of particle declines further. Figure 6.15 shows the surface temperature of 5 μm particle. In comparison to the profile of 10 μm particle, the 5 μm particle has much shorter melting and solidification periods

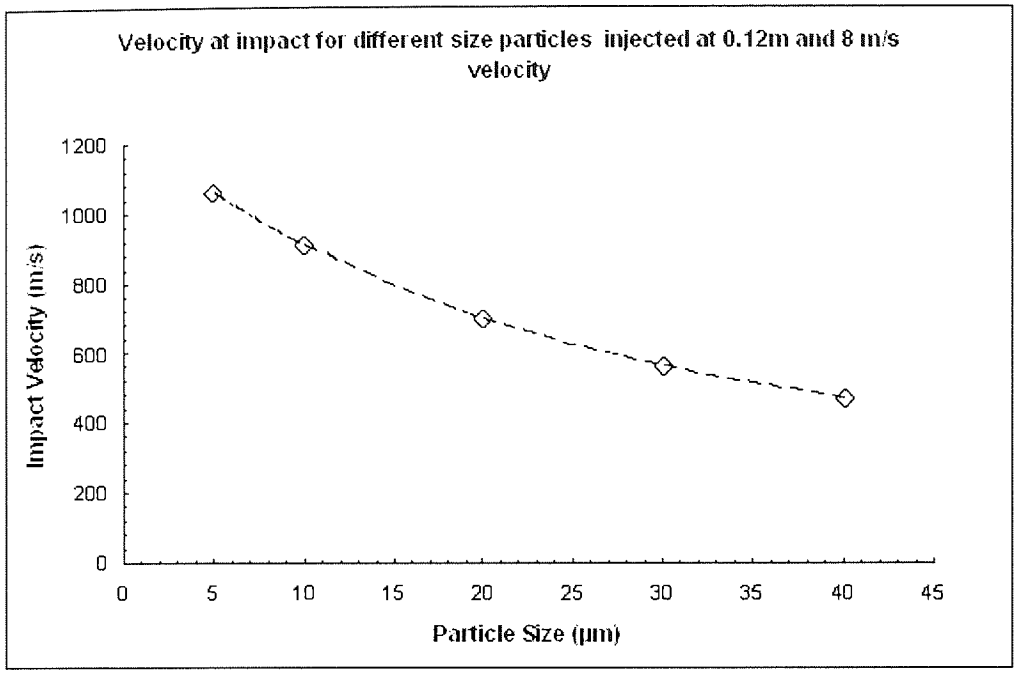

(a)

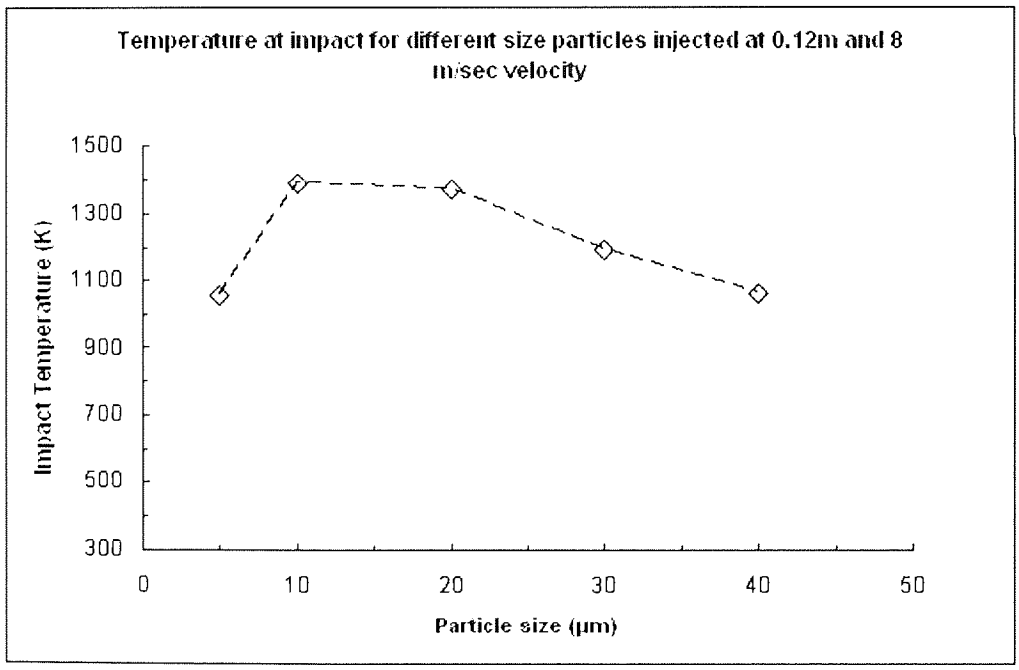

(b)

Figure 6.12: a,b Impact parameters for different size particles.

(0.003 milliseconds of melting for 5 μm particle against 0.11 milliseconds of melting for 10 μm particle); overheating in liquid state (up to 2000 K in 5 μm particle against up to

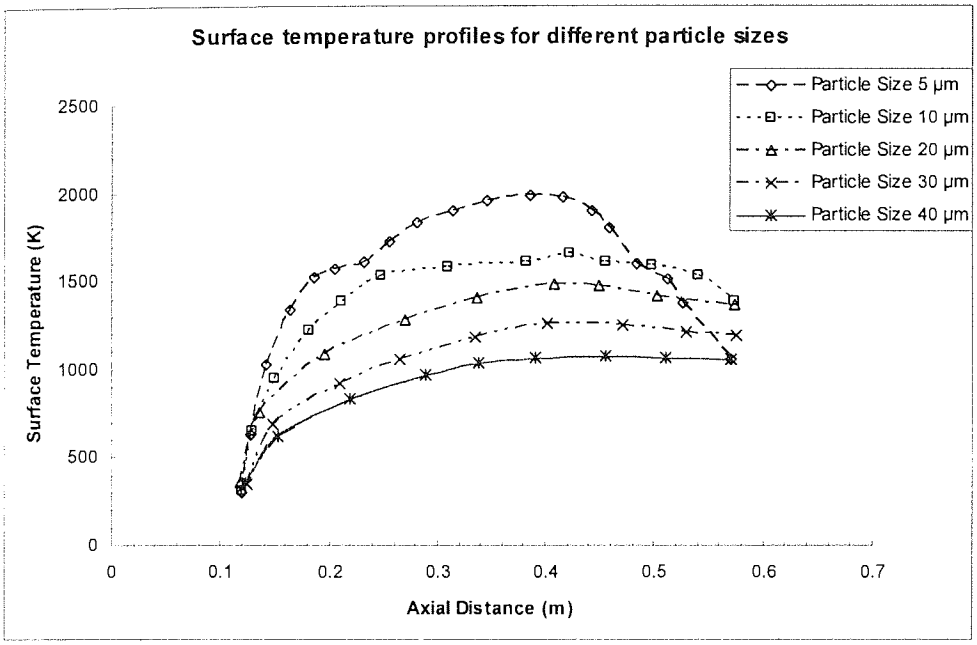

Figure 6.13: Temperature profiles for different size particles.

1700 K for 10 μm particle); and further cooling in solid state (down to 1000 K in 5 μm particle against down to 1400 K for 10 μm particle).

The numerical model results during melting and solidification are compared with the developed analytical solution to identify the accuracy of the correction function $\Psi(t)$. The analytical solution can be implemented when the material change's phase at a single temperature. Since Inconel 718 is an alloy the comparison between the models is made for the liquidus front times and temperature profiles. The results presented are for the melting time and temperatures within the particle after the particle surface has reached the liquidus temperature and the front starts to move towards the centre. This is only the last stage of the melting process as described earlier and it does not correspond to the complete process time. The analytical solution uses as an input the transient surface temperature obtained by the numerical model. The development of the melting front inside the 10 μm particle is shown in figure 6.16.

The melting front propagates gradually and progresses inwards steadily as the heat input from surface through convection is balanced by the increased rate of melting heat required. Near the centre of the particle, the propagation speed of melting front accelerates as the reduction of area prompts fast heat transfer. The numerical results show a more linear behaviour of the melting front where the liquidus temperature reaches the centre faster compared to analytical solution. The analytical solution looks more rea-

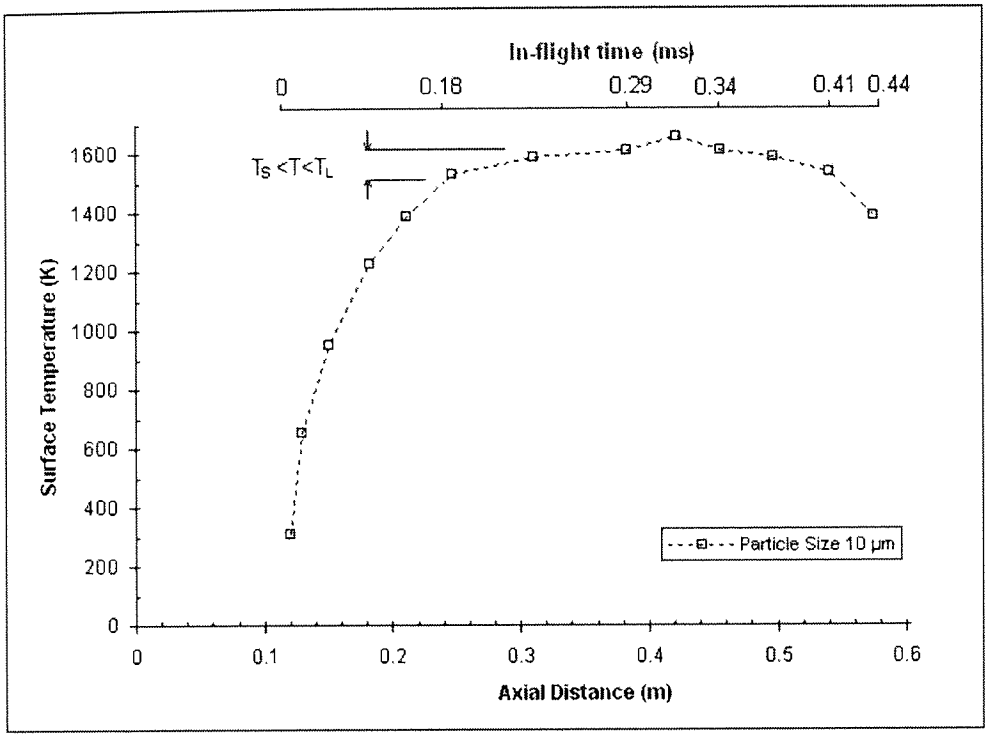

Figure 6.14: Surface temperature profile for 10μm size particle.

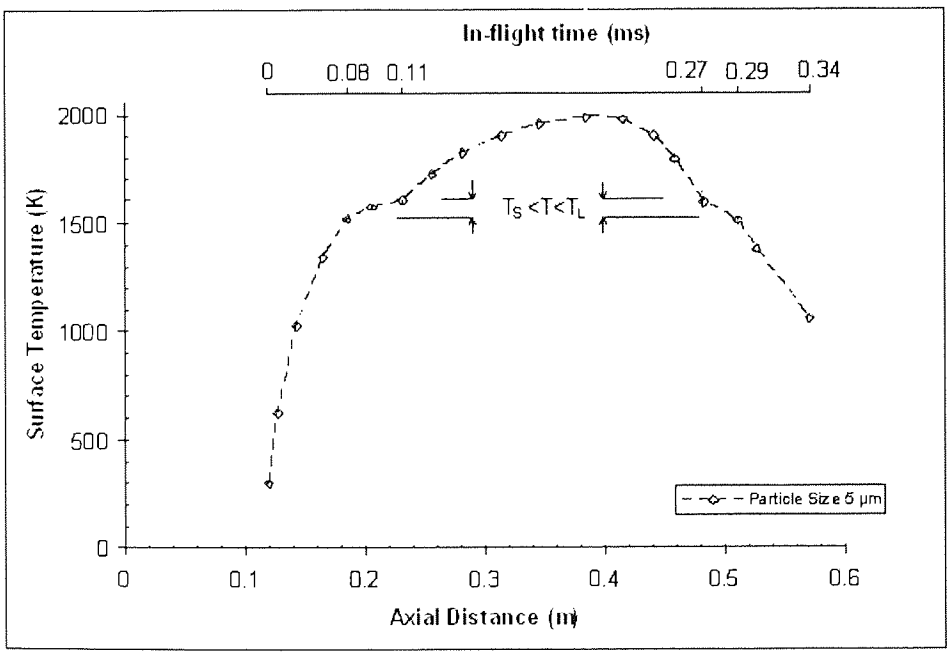

Figure 6.15: Surface temperature profile for 5μm size particle.

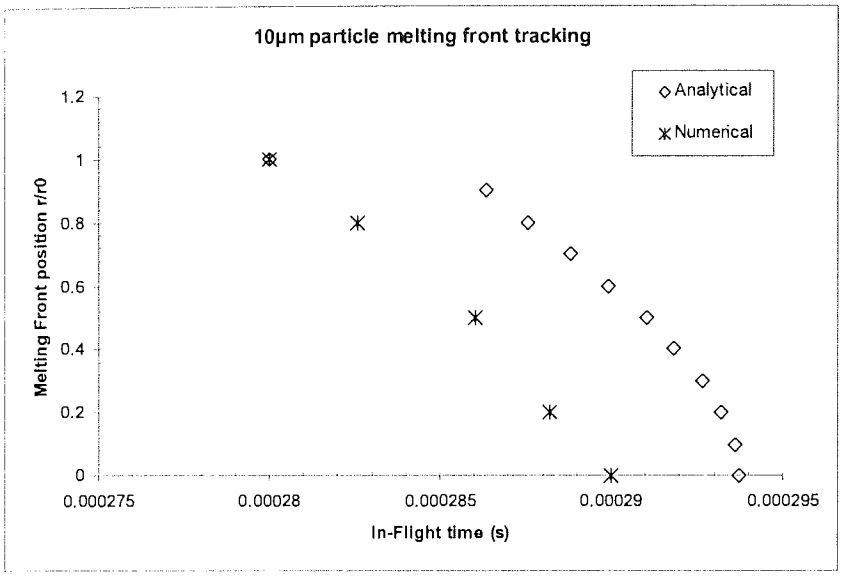

Figure 6.16: Melting front position plotted as a function of in-flight time.

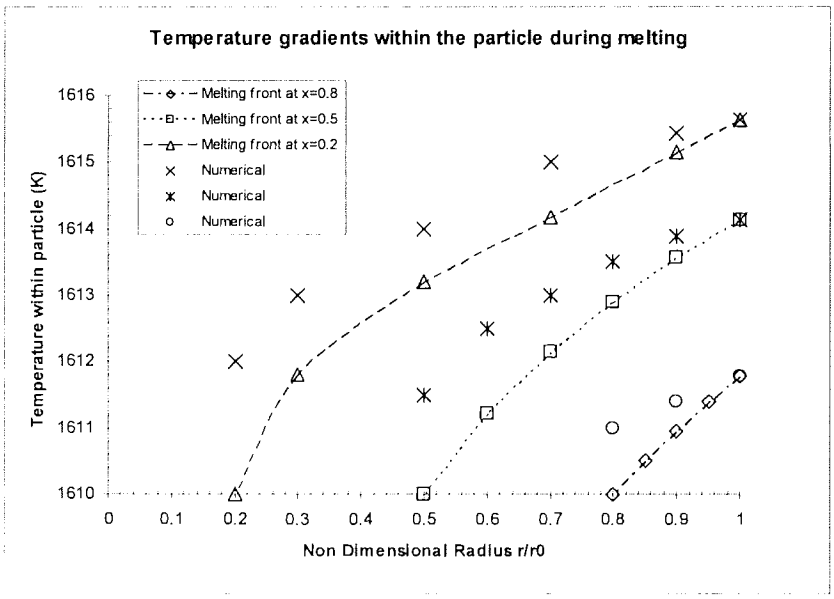

Figure 6.17: Temperature profiles within particle during melting.

sonable in terms of profile shape while the melting time is expected to be faster with the numerical solution. The resolution of the numerical solution can be improved by increasing the discretization points within the particle and by decreasing the simulation time step; on the contrary, overall computational time is increased considerably. The faster melting rate given by the numerical solution is a result of the elevating thermal

conductivity of the material with temperature. Similarly the temperature gradient predicted by numerical solution is smaller compared to the analytical solution, where the thermal conductivity is assumed constant (figure 6.17). Despite the several assumptions of the analytical solution, the results are compared well, implying that the correction function implemented in the numerical solution can provide an overall robust solution to the thermal behaviour of the in-flight particles.

6.1.4 Conclusions

A 3-D CFD model, has been developed to investigate the particle dynamic behaviour in a liquid fuelled HVOF spray gun using kerosene. The model employed a Lagrangian particle tracking frame coupled with the gas flow field to examine particle motion and heat transfer during HVOF spraying. The following conclusions have been obtained.

1. The computational results show that the particle dynamics vary at different injection velocity. For this Inconel 718 powder, 20 μm particles may hit the internal surface of the barrel and the trajectory may be changed to opposite direction as the result of elastic collision at injection velocity above 20 m/s. An optimal range is found between 8 to 10 m/s where most powder particles could be directly towards the centre of the gun.

2. Both velocity and temperature profiles of particle dynamics are improved with injection position closer the throat of the nozzle. A suitable location for powder injection is dependent on the powder feeding system to overcome the pressure fluctuation near the throat.

3. The particle trajectories show that the small particles are greatly affected by the gas flow, the particles smaller than 5 μm have good possibility to make direct contacts with nozzle wall and particles above 20 μm could cross the centre of the gun with a wide spread of coating area.

4. The history of particle temperature results show that the particles smaller than 5 μm will be overheated while the particles larger than 10 μm may never reach the liquid state during the process. For a typical stand-off distance used in this simulation (0.32 m from the gun's exit), all the particles are in full solid state prior to impact while the particle smaller than 10 μm undergo melting and solidification.

6.2 Modelling of Particle Oxidation

Further to the analytical solution of oxidation provided in section 5.3 a numerical solution to account for the growth of oxide layer on the surface of metal particles is implemented into Lagrangian particle tracking method. The two models are compared in this section for validation purposes. The numerical oxidation model is based on the Mott-Cabrera theory for very thin oxide films where it is assumed that oxidation is limited by the ion transport through the oxide layer. The computation of oxide layers is implemented as a user-defined function (UDF) into the discrete particle models. The simulation of multiphase flow with both gas and particle (without oxidation) phases was reported previously, therefore, the same HVOF process is used as test case for the oxidation model. The injection positions are shown in figure 6.18. The simulation of particle oxidation is coupled with the combusting gas flow which gives close-to-reality oxygen mass fraction rather than the assumption of constant oxygen fraction along the particle paths used in [142]. The analyzed metal powders are stainless steel which properties are given in table 6.2, but the oxidation model is generic and applicable to any thermal sprayed metal powders including alloys.

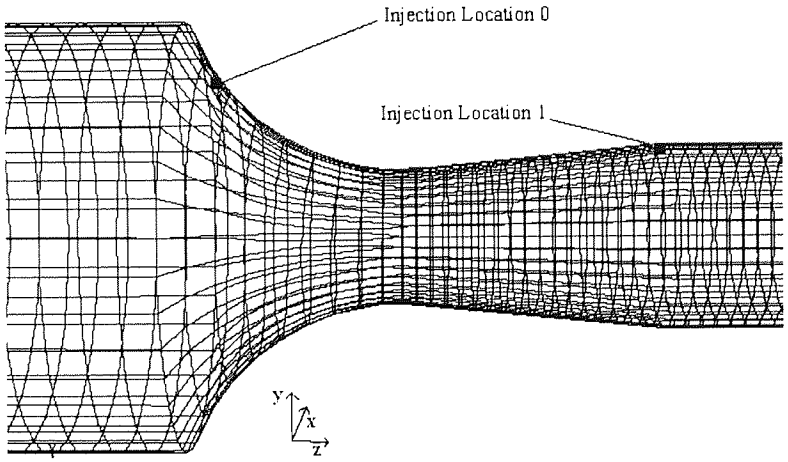

Figure 6.18: Injection locations.

Density	8000 [kg/m3]
Solidus temperature	1648 [K]
Liquidus temperature	1673 [K]
Specific heat	480 [J/kg K]
Latent heat	272000 [J/kg]
Thermal conductivity	26 [W/m K]

Table 6.2: Metal powder properties.

A0	5 x 10-6 A/s
Q	1.5 eV
K0	0.149 eV/torr0.5

Table 6.3: Constants of oxidation model [142].

6.2.1 Equations of Analytical Oxidation

The numerical model has been described in section 5.3. The constants of oxidation model are given in table 6.3. The analytical solution of the oxide layer growth was described in section. The oxygen mole fraction profile as a function of time at the particles surface is taken from the Lagrangian discrete phase analysis. The diffusion coefficient is given by the following expression:

$$D = A \times e^{\frac{-B}{RT}} = 1 \times 10^{-14} \tag{6.6}$$

The constants A and B are taken from [142]. The non-dimensional time is then converted to in-flight time for a 20 μm particle as follows:

$$\tau = \frac{Dt}{r_0^2} = \frac{1 \times 10^{-14} \times t}{10^{-10}} = 1 \times 10^{-4} \times t \tag{6.7}$$

The Pertubative parameter is given by:

$$a = \frac{C_0}{a^*} = 1 \times 10^{-4} \tag{6.8}$$

The oxide layer growth is expressed as:

$$\int x(x-1)\partial x = \int \frac{-1}{3} a^2 f(\tau)^2 + a f(\tau) \partial \tau + const \tag{6.9}$$

The analytical model assumes that oxidation reaction occurs at constant diffusion coefficient at an average particle temperature. The oxide layer growth only depends on the oxygen mole fraction in the surrounding gas. The reaction rate as expressed in equation (6.6) is valid according for a range of particles temperatures of 1000K to 1500K. For higher or lower temperatures errors are introduced to the analytical solution. For

large particles where the temperature is notably lower than 1100K different diffusion coefficient have to be used for more accurate prediction of the oxide layer growth. The pertubative number α is the ratio of the diffusive reactant concentration outside the particle over the density of the non-diffusive reactant at the particles surface. This ratio may be significantly altered according to metal composition and the number of oxides that are formed. The analytical model is tested for two different diffusion coefficient according to particle in-flight average temperature (large-small particle size).

6.2.2 Effect of Particle Size

Thermal spray powders are supplied within a range of distribution while uniform powders are not normally available. A typical range of HVOF sprayed powders are 10 to 80 μm, in this simulation, four different sizes are given namely, 10, 20, 50 and 80 μm to the particles injected at the supersonic region of the CDN. In this section, the particles are released at 0 m/s and named as SP-Particle for particles from the supersonic region of CDN. In the later discussion, SB-Particle is named for particles released from the subsonic region of CDN. It is known from the coating practice and existing models that smaller particles are heated more by the hot gas during thermal spraying, the temperature results are shown in figure 6.19. It is apparent that large particles (50 μm and 80 μm) have low temperature profiles (less than 700 K) during flight while small particles (10 μm) reach the maximum temperature of 1470 K. Given the liquidus temperature of the stainless steel is 1673 K, all the particles are still in solid state throughout the domain, which is consistent with the microstructure analysis showing that particles are hardly melted in the HVOF coating. The oxidation results in figure 6.20 show that the development of oxide layers on particles are strongly dependent on particle size. The amount of oxide for 50 μm and 80 μm particles are almost negligible and the oxidation progresses very slowly when particle temperatures are low. The variation of oxidation according to particle size is a direct result of temperature change.

The profile of oxidation rate in figure 6.21 demonstrates the fastest oxidation takes place when both temperature and oxygen concentration are close to their maximum values. The sudden drop of oxidation rate from its peak is caused by the rapid decline of oxygen surrounding the particles shown in figure 6.22. It needs to point out that figure 6.22 is the oxygen fraction surrounding the in-flight particles rather than the centre of the gas flow. As seen in the pathline of particle trajectory (figure 6.23), SP-Particles travel with a marginal distance from the centre of the gas flow. The oxygen contour plot in figure 6.24 shows the supersonic gas jet where excessive oxygen penetrating into the jet core is prevented, as a result, very low oxygen is available in the gas surrounding the particles. This result confirms that within the typical standing-off distance (from the gun

exit to substrates) this HVOF gun can produce metallic coating with low oxidation.

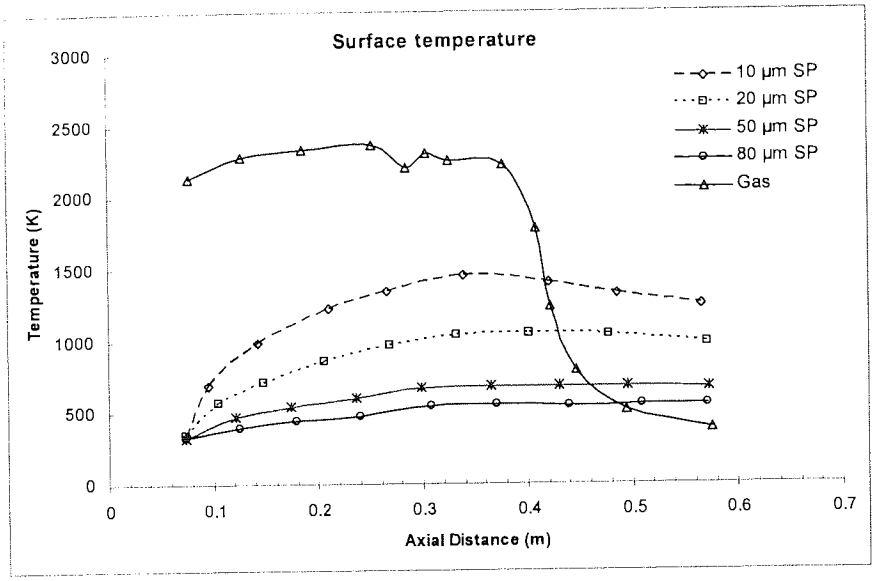

Figure 6.19: Surface temperatures for different particle size (SP-Particles).

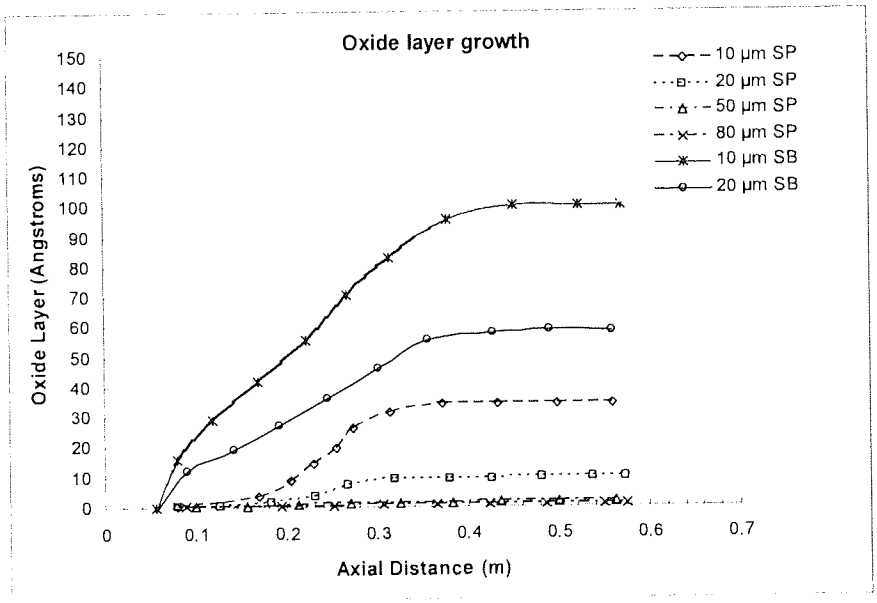

Figure 6.20: Oxidation at different particle size and injection location.

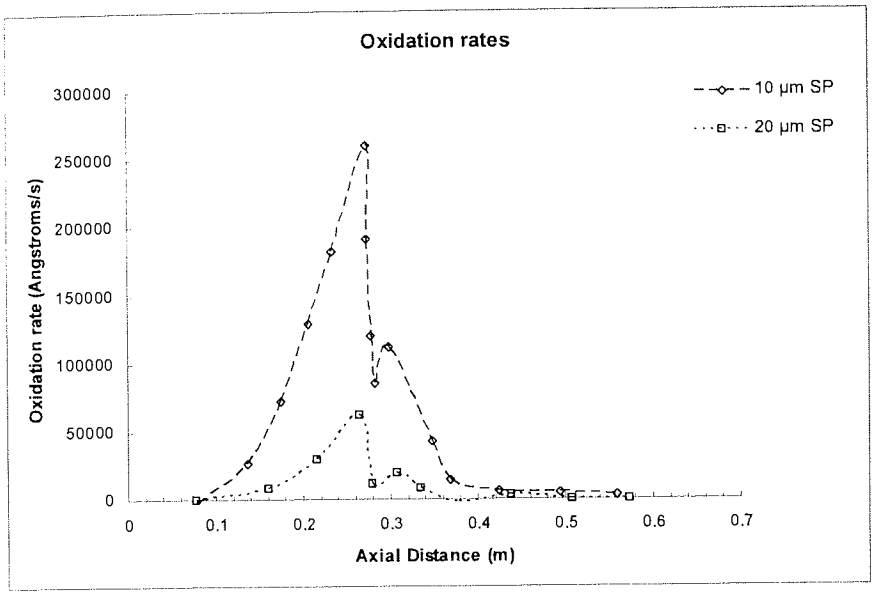

Figure 6.21: Oxidation rate for SP particles.

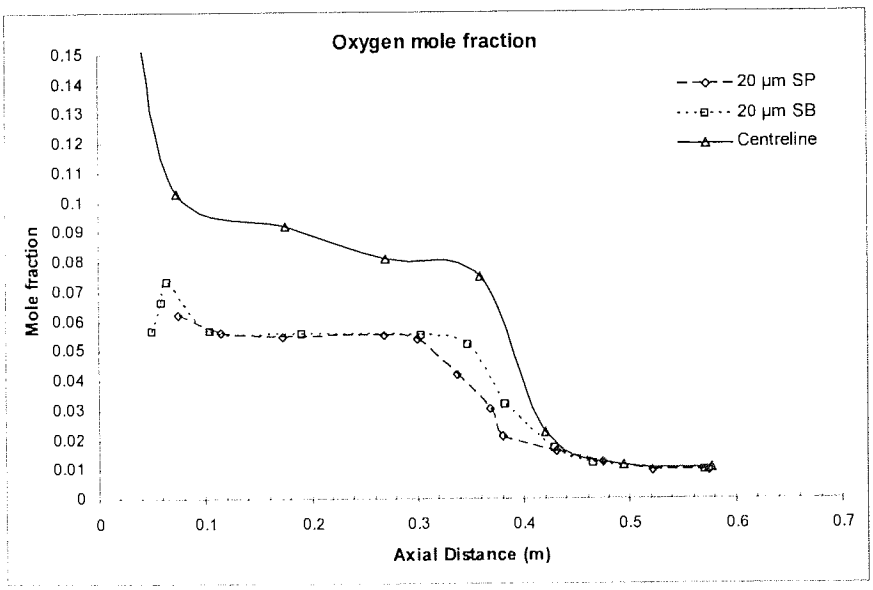

Figure 6.22: Oxygen concentrations in the particle computational cell and centreline of the domain.

6.2.3 Effect of Injection Location

It is a common feature in the commercial HVOF guns to inject powders at the end of CDN (supersonic region), in which case, it is believed that powders can effectively avoid direct contacts with the flame and hot gas in the combustion chamber, and suppress the

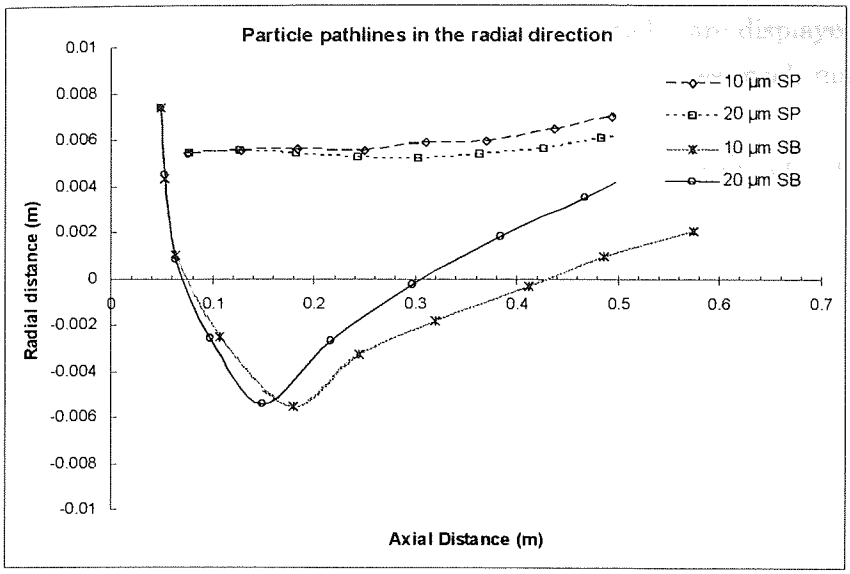

Figure 6.23: Particle trajectories in the radial direction.

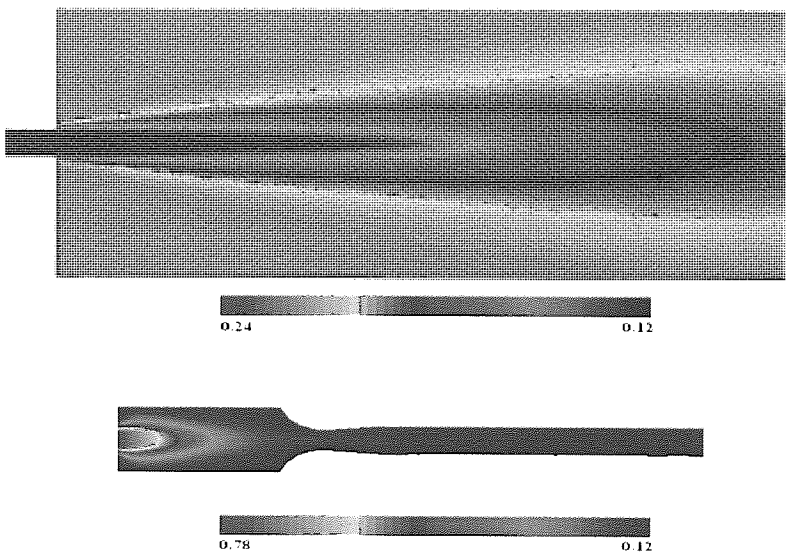

Figure 6.24: Oxygen concentration at the jet (top) and inside the gun (bottom).

undesirable overheating of particles. On the other hand, the later injection of powder could reduce the momentum transfer from the gas flow and give less acceleration to particles. To analyze the effect of injection location, in this simulation, powder is injected close to the combustion chamber and in the front of CDN (subsonic region). The particle is referred as SB-Particle. The results from SB-Particle and SP-Particle are compared in this section. Due to the low temperature profile and marginal oxidation for 50 μm and

80 μm particles, only the results from 10 μm and 20 μm particles are displayed for clear comparison. The temperature plot in figure 6.25 shows SB-Particles reach much higher temperatures than SP-Particles.

The temperature increase has dominant effect on the growth of oxides on the particles, e.g. 10 μm SB-Particles have oxide layer 3 times as thick as SP-Particles (figure. 6.26). As oxygen fraction varies within the gun and external domain shown by the contour plot in figure 6.24, the SB-Particles encounter a maximum oxygen concentration inside CDN and a delay of oxygen decline outside the gun shown in figure 6.22. The comparison between analytical and numerical model shows a satisfactory agreement. The numerical model can be considered more precise since oxidation is a function of both particle temperature and oxygen concentration. The analytical model inaccuracy rises from the fact that the oxide layer growth is driven only by the oxygen concentration. As shown in figure 6.26 the oxide layer thickness development follows the same pattern for both particle sizes and injection locations in contrast to numerical solution. The reason is that the analytical solution is not sensitive to any temperature variation on particle surface. In the case of small particles the oxide layer is under predicted significantly due to their large temperature variations that cannot be represented by an average temperature along the in-flight path. However, the developed analytical solution when is used with careful selection of the input parameters can provide a powerful validation tool.

The combined effect of temperature and available oxygen surrounding gives rise to two fastest oxidation regions shown in figure 6.27 while the growth of oxide layers for SB-Particles is three time as fast as that of SP-Particles. Although the Sub-Particles achieve slightly higher velocity due to the increase of residence time, the velocity difference at the end of the domain is relatively small; in this case, the benefit of increased momentum to the particles is overwhelmed by the large increase of oxidation in the particles which has detrimental effect on coating structure. The results approve that injecting powders at the end of CDN is able to reduce the contacts between powders and the hot gas flame minimizing consequently the undesirable oxidation.

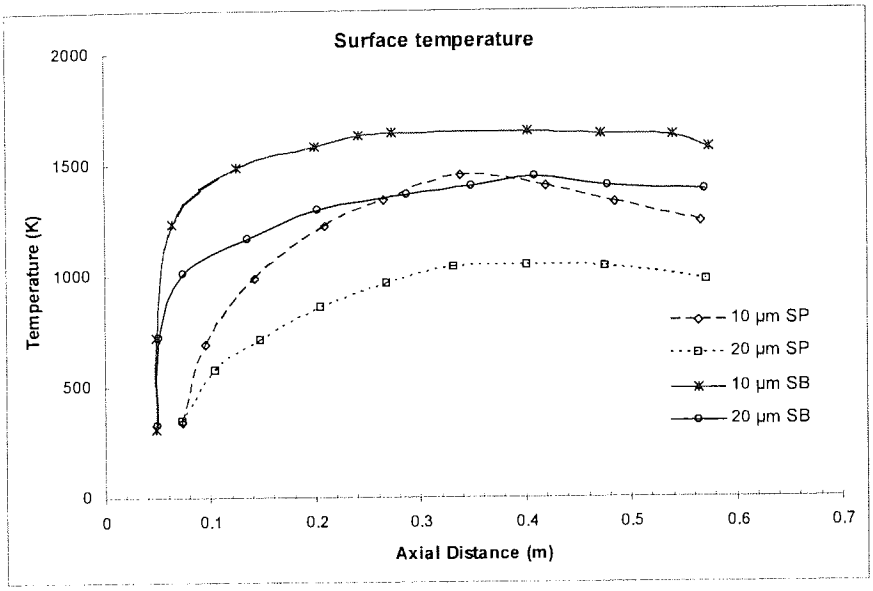

Figure 6.25: Particle surface temperatures SP and SB particles.

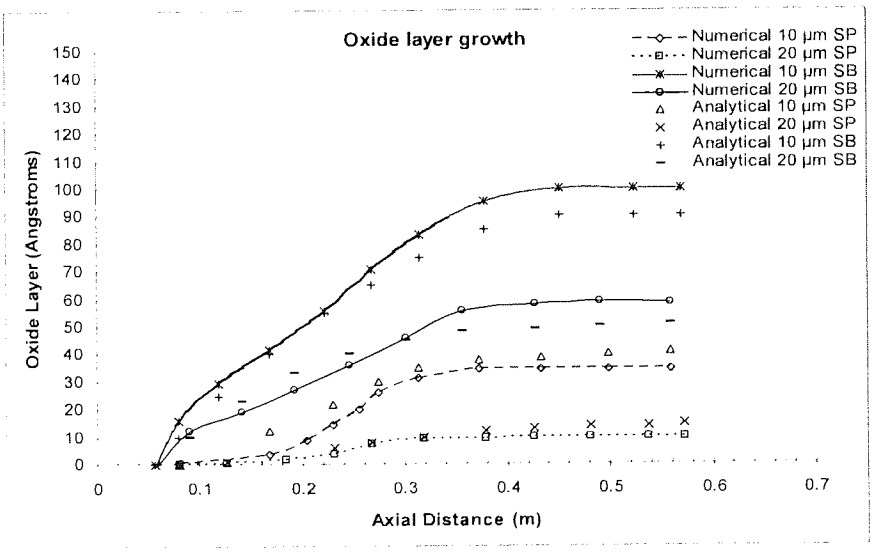

Figure 6.26: Comparison of oxide layer growth between analytical and numerical models.

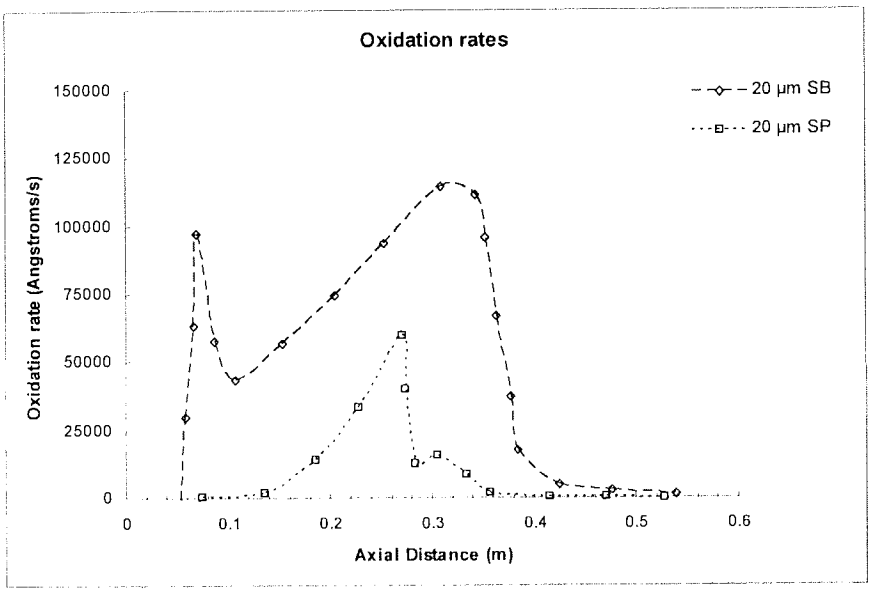

Figure 6.27: Oxidation rates at different injection locations

Chapter 7

Modelling of Droplet Impact

7.1 2-D Model Development

The large number of process parameters, in which the physical properties of coating are sensitive to, leads to expensive and time consuming trial and error optimization of thermal spray process. Better control of the process requires a fundamental understanding of the thermal-physics within and outside the gun. To date, progress has been made to study gas/particle dynamics within spraying guns and external free jet region; however, there is still lack of clear understanding of the impingement process where dynamic flow and heat transfer occur during the impact, spreading and solidification of molten droplets.

The study aims to develop a 2-D numerical model that is able to accurately simulate droplet impingement process. Detailed data of thermo-physical properties is implemented into the material model instead of using constant value, e.g. different thermal conductivity and density for liquid and solid, latent heat of freezing. Most assumptions that could affect prediction in existing droplet impingement models are replaced with close-to-reality algorithms, e.g. Marangoni stress boundary for substrate surface boundary where the shear stress is solved as a function of temperature, an additional heat transfer resistance in the governing equation to solve air entrapment and as a result, detailed physics could be revealed and many limitations for impingement modelling will be eliminated. It needs to point out that the geometric constraint for a 2-D model prohibits a correct prediction of the number of fingers formed around a droplet, which can only be solved with more computationally expensive 3-D model.

The droplet impingement model is solved with the computational domain shown in figure 7.1. Only half of the domain is actually computed with a symmetric boundary in the middle and very fine grid is used for the regions where impact, spreading and solidification occurs. The numerical method used in this study is a segregated solution algorithm with a control volume based technique. The pressure and velocity are coupled with SIMPLE

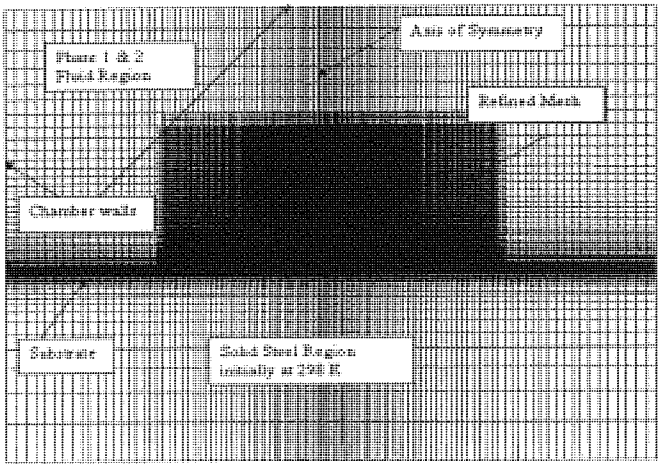

Figure 7.1: Computational domain for the impingement model

(semi-implicit method for pressure linked equations) algorithm which uses a guess-and-correct procedure for the calculation of pressure on the staggered grid arrangement. The QUICK (quadratic upwind interpolation) scheme is used for the discretization of the model equations. As a higher order scheme, the QUICK method can minimize false diffusion errors at cost of computational stability.

The droplet impingement model is developed and validated with the experimental measurement of Tin droplets [144]. Material properties being used in this model are listed in table 7.1. The numerical model works on the basis of two-dimensional, axi-symmetric, incompressible laminar flow. On the impingement, heat transfer is dominated by convection and conduction, therefore, radiation from the droplet surface to the surroundings is negligible.

7.1.1 Flow Modelling

Numerical models of the droplet impingement are solved by the Navier-Stokes and energy equations, coupled with the Volume of Fluid (VOF) surface tracking technique on a fixed Eulerian structured mesh. In the VOF model, a single set of momentum equations is shared by the fluids, and the volume fraction of each of the fluids in each computational cell is tracked throughout the domain. In this method, the volume fraction of 1^{st} fluid in the cell is denoted as ϕ: $\phi = 0$ for an empty cell; $\phi = 1$ for a full cell and $0 < \phi < 1$ when a cell contains the interface between the 1^{st} and 2^{nd} fluids. The following single momentum equation is solved throughout the domain:

Impinging Droplet	Tin (Sn)
Substrate	Stainless steel
Droplet Diameter	2.2 mm
Droplet Initial Temp	519 K
Substrate Initial Temp	298 K
Impinging Velocity	4 m/sec
Solidus temperature (Tsolid)	504 K
Liquidus temperature (Tliquid)	506 K
Thermal Conductivity Liquid Tin	33.6 W/mK
Thermal Conductivity Solid Tin	62.2 W/mK
Thermal Conductivity Steel	14.9 W/mK
Density Steel	7900 kg/m3
Density Liquid Tin	6980 kg/m3
Density Solid Tin	7200 Kg/m3
Droplet Surface Tension	0.566 N/m
Specific Heat Droplet	244 J/kgK
Specific Heat Steel	477 J/kgK
Latent Heat of Solidification	58500 J/kg

Table 7.1: Initial conditions and properties of tin and stainless steel used in the simulation.

$$\frac{\partial}{\partial t}(\rho\vec{u}) + \nabla\cdot(\rho\vec{u}\vec{u}) = -\nabla p + \nabla\cdot\left[\mu\left(\nabla\vec{u} + \nabla\vec{u}^{T}\right)\right] + \rho\vec{g} + F_{vol} \tag{7.1}$$

Equation (7.1) is dependent on the volume fractions of phases through the properties ρ and μ. The velocity differences between the two phases in this model are not pronounced so the shared-field approximation can be safely used without adversely affecting velocity computations near the interface. The face fluxes for the VOF model are calculated using the geometric reconstruction scheme available in FLUENT. The interface between fluids is solved by a piecewise-linear approach. The continuum surface force (CSF) proposed by [145] is used for the surface tension model. To include the surface tension effects in the calculation is necessary to compute a local curvature J (Figure 7.2(a)), in each free surface computational cell, so that a surface tension force F_{vol} can be evaluated.

The additional surface tension model to the VOF calculation results in a source term in equation (7.1) and is expressed as a volume force as follows:

$$F_{vol} = \sigma_{ij}\frac{\rho k_i \nabla\alpha_i}{\frac{1}{2}(\rho_i + \rho_j)} \tag{7.2}$$

The mathematical equation of the contact angle (figure 7.2(b)) is based on the study of [63] in which the curvature of the surface near the substrate wall surface is adjusted according to dynamics boundary conditions. The contact angle at the wall is given as θ_ω, and the surface normal to the cell next to the wall is:

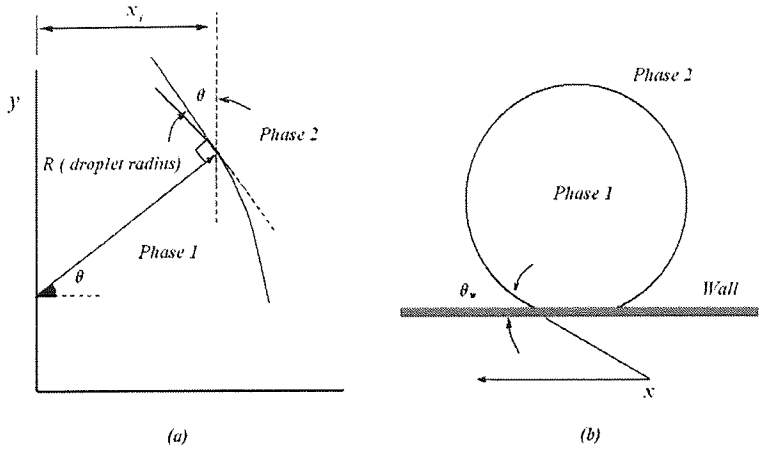

Figure 7.2: Interface boundaries: (a) Local free surface curvature (b) Wall contact angle.

$$\hat{n} = \hat{n}_\omega \cos\theta_\omega + \hat{t}_\omega \sin\theta_\omega \tag{7.3}$$

The values of the liquid-solid contact angle during spreading and recoiling of droplets are taken from the data produced by [144] as listed in table 7.2. The set of contact angles are universally applied to all the surface roughness in the current study and the later results show an excellent agreement between the predictions and experimental results. Accurate characterization of the substrate surface requires three input parameters, namely liquid-solid contact angles, thermal contact resistance and Marangoni stress. Given the universal variation of the contact angle and Marangoni stress boundary being applied to the contact surface, it is possible to specify the surface roughness using thermal contact resistance in this study.

Contact angle / θ^o	**Time /(ms)**
140	1 to 3
120	3 to 6
60	6 to 8

Table 7.2: Contact angle variation during impact.

The momentum equation (7.1) is in a general format for the numerical solution of the fluid flow and solidification. A definition of the source term that is used to modify the momentum equation in mushy zone (a region in which the liquid fraction lies between 0 and 1) is required; as the porosity decreases the velocity also decreases to zero when the mush becomes completely solid as represented by:

$$S_y = -Au \tag{7.4}$$

The form of A is derived from the Darcy law:

$$A = \frac{-C\left(1-\lambda\right)^2}{\left(\lambda^3+\eta\right)} \tag{7.5}$$

The value of C depends on the morphology of the porous media and measures the amplitude of the damping; a higher value C corresponds to a rapid deceleration to zero velocity on solidification. In the current model C is given a constant value of 150,000 that gives accurate prediction in comparison with experiments.

7.1.2 Solidification and Heat Transfer Modelling

An enthalpy porosity technique [146] is used for modelling the solidification process. In this technique, a variable named as liquid fraction is calculated instead of tracking the melt interface explicitly. The liquid fraction indicates the volume fraction of the cell in liquid form and is associated with each cell in the domain. The liquid fraction is computed at each iteration based on an enthalpy balance. The mushy zone is modelled as a pseudo porous medium in which the porosity decreases from 1 to 0 as the material solidifies.

The enthalpy of the material is computed as the sum of the sensible enthalpy, h, and the latent heat, ΔH, as follows:

$$H = h + \Delta H \tag{7.6}$$

where

$$h = h_{ref} + \int_{T_{ref}}^{T} c_p dT \tag{7.7}$$

The liquid fraction, β, is defined as
$\beta = 0$ if T $< T_{solid}$
$\beta = 1$ if T $> {}_{liquid}$

$$\beta = \frac{T - T_{solid}}{T_{liquid} - T_{solid}} \tag{7.8}$$

if T_{solid} < T < T_{liquid}
The Latent heat content is written in terms of the latent heat of freezing, L

$$\Delta H = \beta L \tag{7.9}$$

Heat transfer in the droplet is modelled by solving the energy equation. Due to high temperature difference between the droplet and substrate and the relative low droplet velocity (Eckert number:$E_c = \frac{U_0^2}{(C_p \Delta T)} \approx 3 \times 10^{-4}$), viscous dissipation is negligible and not included in the current model. The energy equation is written as:

$$\frac{\partial}{\partial t}(\rho H) + \nabla \cdot (\rho \vec{u} H) = \nabla \cdot (k \nabla T) + S_h \tag{7.10}$$

The source term appears on the right hand-sight is equal to:

$$S_h = \frac{\partial \rho \Delta H}{\partial t} + \nabla (\rho u \Delta H) \tag{7.11}$$

In isothermal cases, due to the step change of ΔH along with a zero velocity at the solid-liquid interface the convective part of this source term takes the value of zero. In a mushy region case this source term must be included. The temperature is solved from the energy equation (7.10) and the liquid fraction equation (7.8). Powder particles with 100% purity are rarely used in real engineering environment. For a wider application, the phase change in the solidification model is implemented within a temperature spectrum instead of giving a single melting point. Heat transfer within the substrate is solved as conduction alone and the governing equation is:

$$\rho_w c_{pw} \frac{\partial T_w}{\partial t} = \vec{\nabla} \cdot (k_w \vec{\nabla} T_w) \tag{7.12}$$

The model considers the presence of an air gap between the substrate wall surfaces and the solidified material, using an additional heat transfer resistance between walls and cells with liquid fraction less than 1. This contact resistance is included by modifying the conductivity of the fluid near the wall (figure 7.3). Thus, the wall heat flux is written as:

$$q = \frac{(T - T_w)}{\left(\frac{l}{k} + R(1 - \beta)\right)} \tag{7.13}$$

Values of R are provided according to the different substrate roughness. The values of contact resistance variation with surface roughness are listed in table 7.3.

Substrate Roughness /(μm)	Thermal Contact resistance $x10^{-6}/(m^2K/W)$
0.06	1.8
0.07	2.5
0.56	3.1
3.45	5.7

Table 7.3: Thermal contact resistance variation with surface roughness.

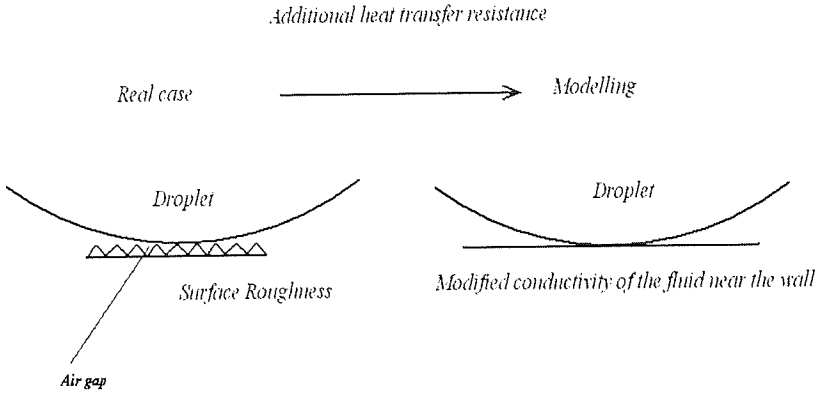

Figure 7.3: Modelling of surface roughness

As described earlier for the characterization of surface roughness, further to thermal contact resistance the model allows to specify the shear stresses caused by the variation of substrate surface tension due to temperature (Marangoni stress boundary condition). The shear stress applied at the wall is given by:

$$\tau = \frac{d\sigma}{dT} \nabla_S T \tag{7.14}$$

7.1.3 Results and Discussions

The dynamic impingement process is vividly shown in figure 7.4 in which the computing images have a good agreement with the experiment [144] given the same conditions as 2.1 mm diameter tin droplet at temperature of 510 K landing at velocity 4 m/s on the R=0.06μm rough stainless steel surface with temperature of 298 K. The spreading in dynamics shows that: the droplet spreads radially along the substrate surface after the impact; the break-off from edges is initiated at approximately 0.6 ms, get detached from the edges at 0.9 ms and form the satellite droplets. The droplet reaches its maximum spread at 1.8 ms as quantitatively illustrated in figure 7.5, and then surface tension pull the edges of the droplet inwards and the spreading stabilizes from 3.4 ms when the droplet mainly solidifies.

The solidification at different time frames is shown in figure 7.6. Thin solidification layers are developed at the centre and edges of the droplet right after the impact at 0.1 ms; the solidification layers progress to the most close to substrate surface as the droplet spreads at 0.6 ms; the solidification rapidly takes over the droplet by 2.0 ms; only a fraction of liquid remains within the internal edges of the droplet at 4.0 ms when the

droplet spreading becomes stabilized; and full solidification arrives at 6.5 ms.

The flow patterns during impingement are shown by pressure contour and velocity vector results in figures 7.7 and 7.8 respectively. On impact the high impact velocity generates a high pressure region under the droplet; shortly after the impact at 0.55 ms the high pressure at the centre of the droplet forces the liquid to flow over the contact surface while the surface tension is comparatively small; the maximum flow velocity is achieved at the edge where all the momentum is transferred to the radial direction and the cross-section area is small. The velocity at the edge is found to be 6 m/s, 2 m/s higher than the impact velocity. As the spreading and solidification develop, the flow slows down and the surface tension becomes significant which gives rise to the high pressure regions at the edges and eventually redirects the flow back towards the centre as clearly shown in the 2.2 ms time frame plot in figure 7.8. The flow rest mostly at 4.4 ms as a result of solidification and a small fraction of backflow with a velocity less than 0.5 m/s is found in the remaining liquid at the edges.

7.1.4 Surface Roughness

In this study, the surface roughness is evaluated by the thermal contact resistance as demonstrated in table 7.2. The temperature history at the impact point in figure 7.9 indicates that the temperature dependence on surface roughness or more precisely, high temperature profile is achieved at low thermal contact resistance on smooth surface. However, the droplet spreading is affected differently. The results in figure 7.5 show that the spread rate of the droplet is dependent on the surface roughness. At substrate temperature of 298 K, the droplet spreads much wider before recoiling with a significant increase of surface roughness from R = 0.07 μm to 3.45 μm while a slight increase of surface roughness from R = 0.07 μm to 0.56 μm give only a marginal effect. The computing results confirm the experimental observation [144] that the substrate surface roughness influence the spreading process through solidification, i.e. smooth surface has low thermal resistance that allows rapid solidification which prevents further droplet spreading; rough surface increases thermal contact resistance that slows down solidification process and allows the droplet to spread in a greater extent. Further examination of figure 7.5 shows that recoiling is substantially affected by the surface roughness: the droplet recoils marginally at R = 0.06 and 0.07 μm roughness, more pronounced at R = 0.56 μm and significantly at R = 3.5 μm.

7.1.5 Air Entrapment

It is anticipated that air could be trapped between droplet and substrate during the impingement, and as a matter of fact, air involvement reduces heat transfer rate between the droplet and substrate. The presence of air can be easily identified in the density plots where the density of tin is thousands time larger than that of air. The dynamic evolution of density distribution over the substrate surface is shown in figure 7.10. Air is trapped in the centre of the droplet on impact and that remains the only air entrapment region at early stage of spreading. As the spreading progresses at 0.55 ms, three identifiable air regions are presented within the droplet: zone 1 is in the centre, zone 2 is about 0.002 mm radial distance from the centre, and zone 3 is located near the edge. As the droplet continues to spread and solidification becomes significant, by 2.2 ms, zone 1 moves outwards, zone 2 remains mostly unchanged, zone 3 moves substantially outwards and replaced by two separate zones: a small adjacent air zone 3a is formed within the droplet and a big air gap zone 3b separates the main droplet and satellite droplets. As the droplet recoils at 4.4 ms, zone 1 moves inwards, zone 2 is steady and zone 3b expands as a result of the main droplet edge recoiling inwards. A possible explanation for the generation of air entrapment during the spreading is that the edge of droplet solidifies more quickly than the main body of the droplet, the liquid flow over the solidified edge and air is trapped consequently. Therefore, the air entrapment is closely linked to solidification.

The previous results already demonstrate that spreading and solidification are associated with the surface roughness. A comparison of density profile at different surface roughness in figure 7.10 shows that the air zone 2 disappears and zone 3b remains within the main droplet instead of separating the main and satellite droplets at high surface roughness R = 0.56 μm and 3.45 μm, which is consistent with experimental and previous findings that high thermal contact resistance at rough surface slows down solidification and suppresses splashing.

7.1.6 Conclusions

A numerical model has been implemented to investigate the impingement of tin droplets on a flat stainless steel plate. The following conclusions can be drawn:

1. The thermal contact resistance can be used effectively to characterize surface roughness and the numerical results demonstrate an excellent agreement with the experimental data.

2. The solidification of droplets is significantly affected by the thermal contact resistance/substrate surface roughness. On smooth surfaces where contact resistance is

low and heat is transferred rapidly from the droplet to substrate, droplet solidifies quickly which prompts the break-up and formation of satellite droplets.

3. Air is trapped in the droplet during the impingement. The air entrapment during spreading is dependent on substrate surface roughness, i.e. less air is trapped at high thermal contact resistance on rough surface.

7.2 3-D Modelling Results

The 2-D axis-symmetric numerical solution has been successfully applied and described in the previous section. The splashing droplet typically is not axisymmetric, which would require a three-dimensional model for realistic splat predictions. Here the method has been extended to fully three-dimensional computations to give a better visual understanding of the previous analyses. The grid consists of two levels of local refinement resulting to a maximum number of 4 million computational cells to enhance accuracy of the predictions in the areas of interest (i.e. the liquid–gas interface), with minimum computational cost. This is achieved by having relatively fine grid resolution at the regions of interest, and a coarse grid density where flow variable gradients are small. The numerical simulation has lasted for 1 month on an eight CPUs Linux cluster. Due to computational time limitations, it was almost impossible to simulate and post-process the entire range of cases described in the previous section. Instead only one case for substrate roughness of R=0.06 is presented.

Figure 7.11 is a sequence of photographs compared to the 3-D numerical predictions of a 2.2 mm diameter tin droplet impacting on a flat plate of R=0.06 μm with velocity of 4 m/sec. All the numerical parameters were described in the previous section. In subsequent frames we can see the droplet spread radially until it reaches its maximum spread. The outward motion of the spreading rim was arrested by surface tension and solidification. The numerical results of velocity temperature and solidification are shown in figure 7.13. A number of fingers were observed numerically and experimentally around the rim of the droplet (figures 7.11 and 7.12).

The surface roughness, results in discrepancies of the static pressure when air is trapped underneath the splat's surface as shown in figure 7.15 as well as decrease of the heat transfer from and to the substrate and solidification rate (figure 7.14). It can also trigger instabilities that cause fingering around the edge of the droplet. The fingers are produced by the Rayleigh-Taylor instability which occurs when the interface between two fluids of different density is accelerated. The number of fingers that are formed around the splat at its maximum spread, are 28, exactly the same number as it appears in the experimental observation at 1.4 ms (figure 7.11).

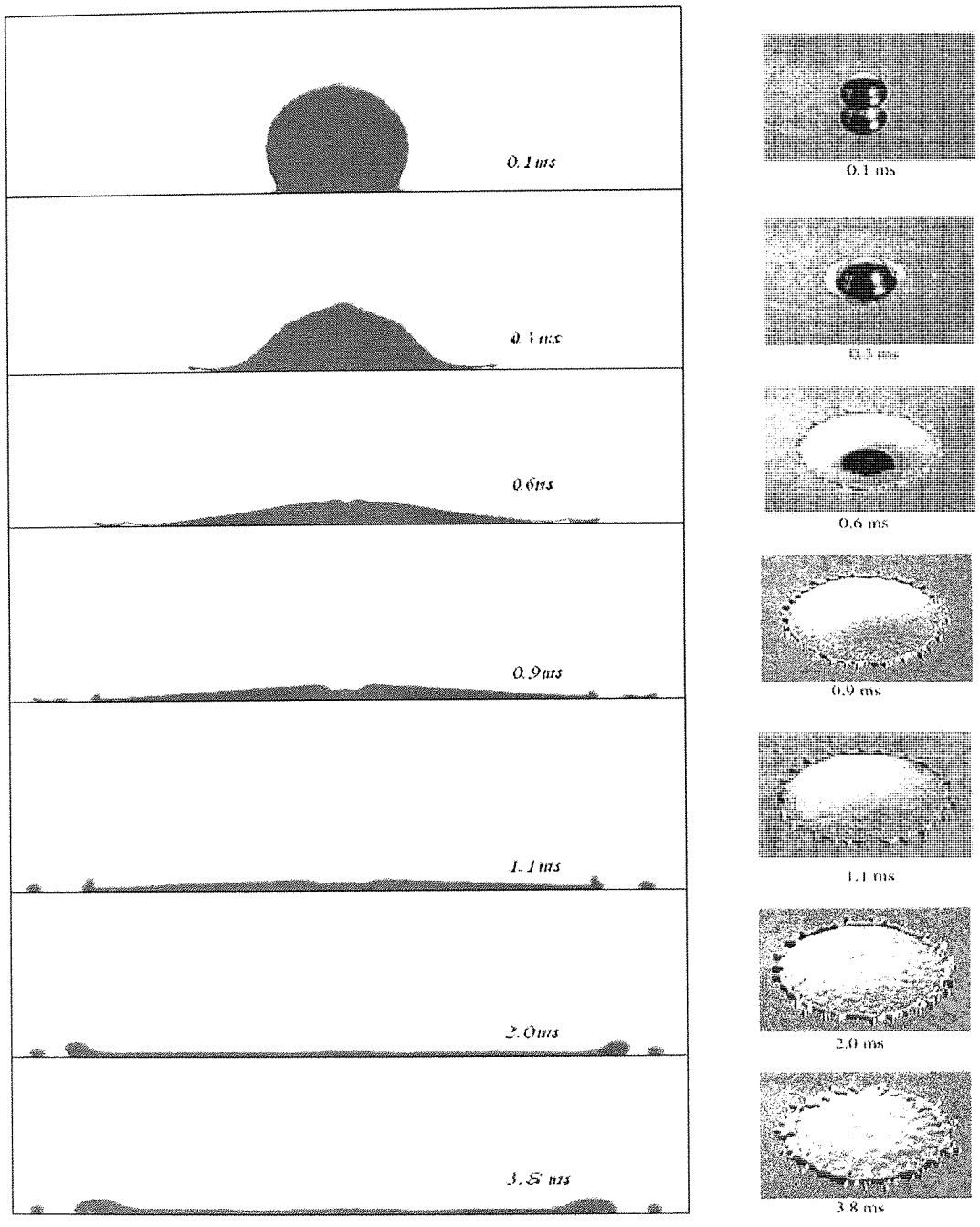

Figure 7.4: Comparison between simulation and photographic images taken from [144] at surface roughness 0.06m.

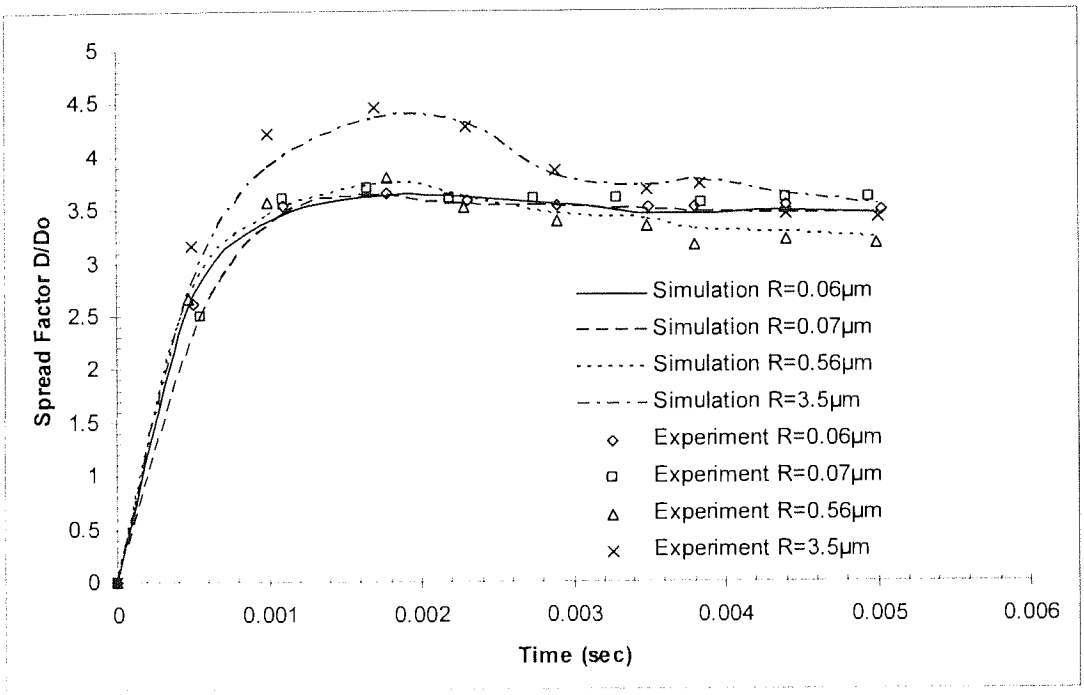

Figure 7.5: Variation of spread factor at different substrate surface roughness.

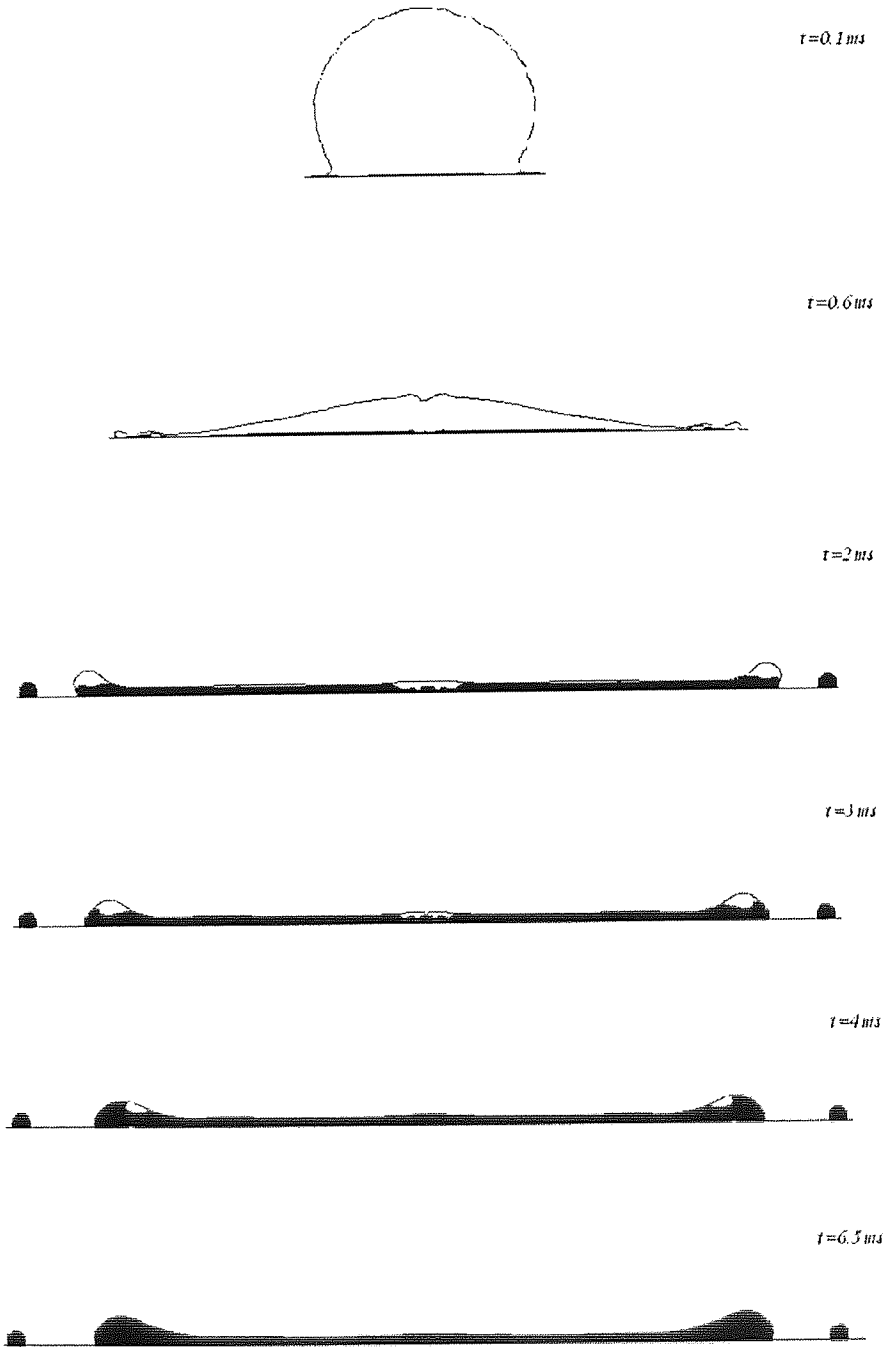

Figure 7.6: Solidification process at six time instants over the 0.06m surface roughness. The solidified tin is represented by black (the small magnitude of air is not identifiable in this diagram.

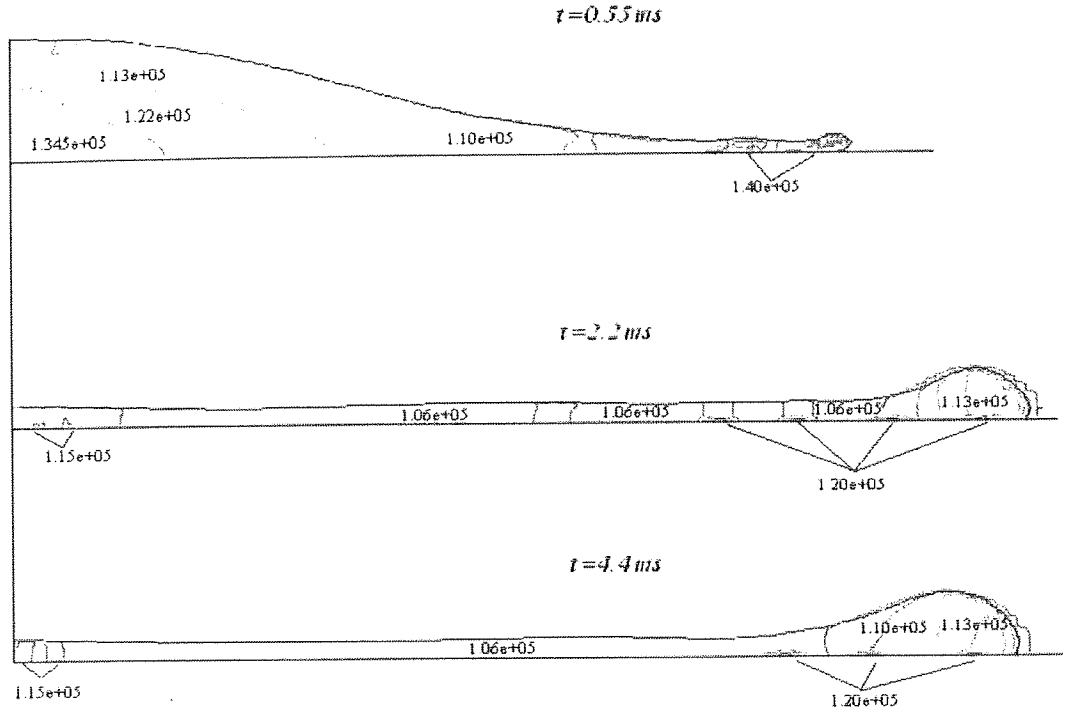

Figure 7.7: Pressure contours at three time instants inside the droplet landing at 0.06m surface roughness.

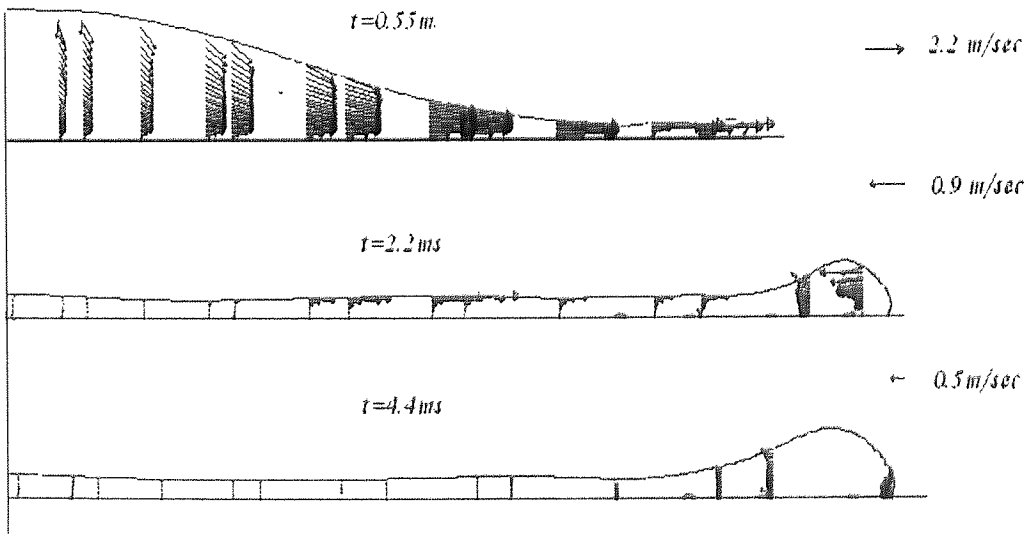

Figure 7.8: Velocity vectors at three time instants inside the droplet landing at the 0.06m surface roughness.

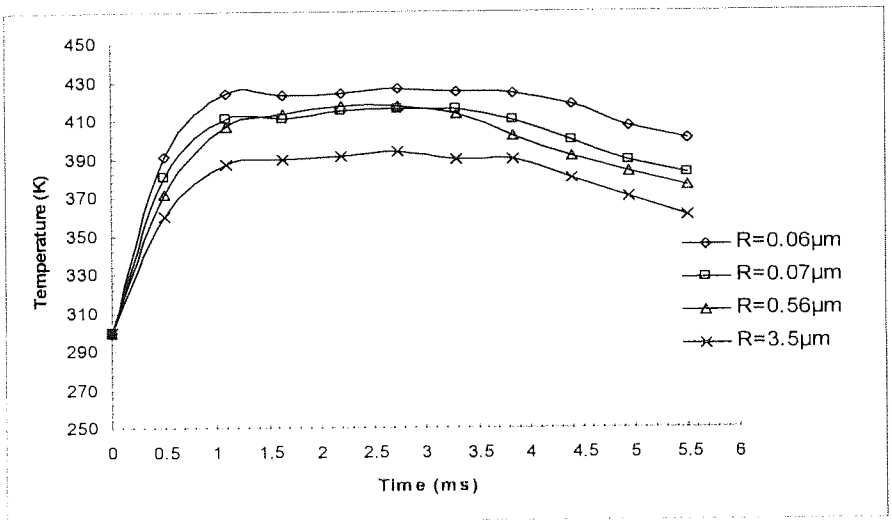

Figure 7.9: Substrate surface temperatures at point of impact for different roughness.

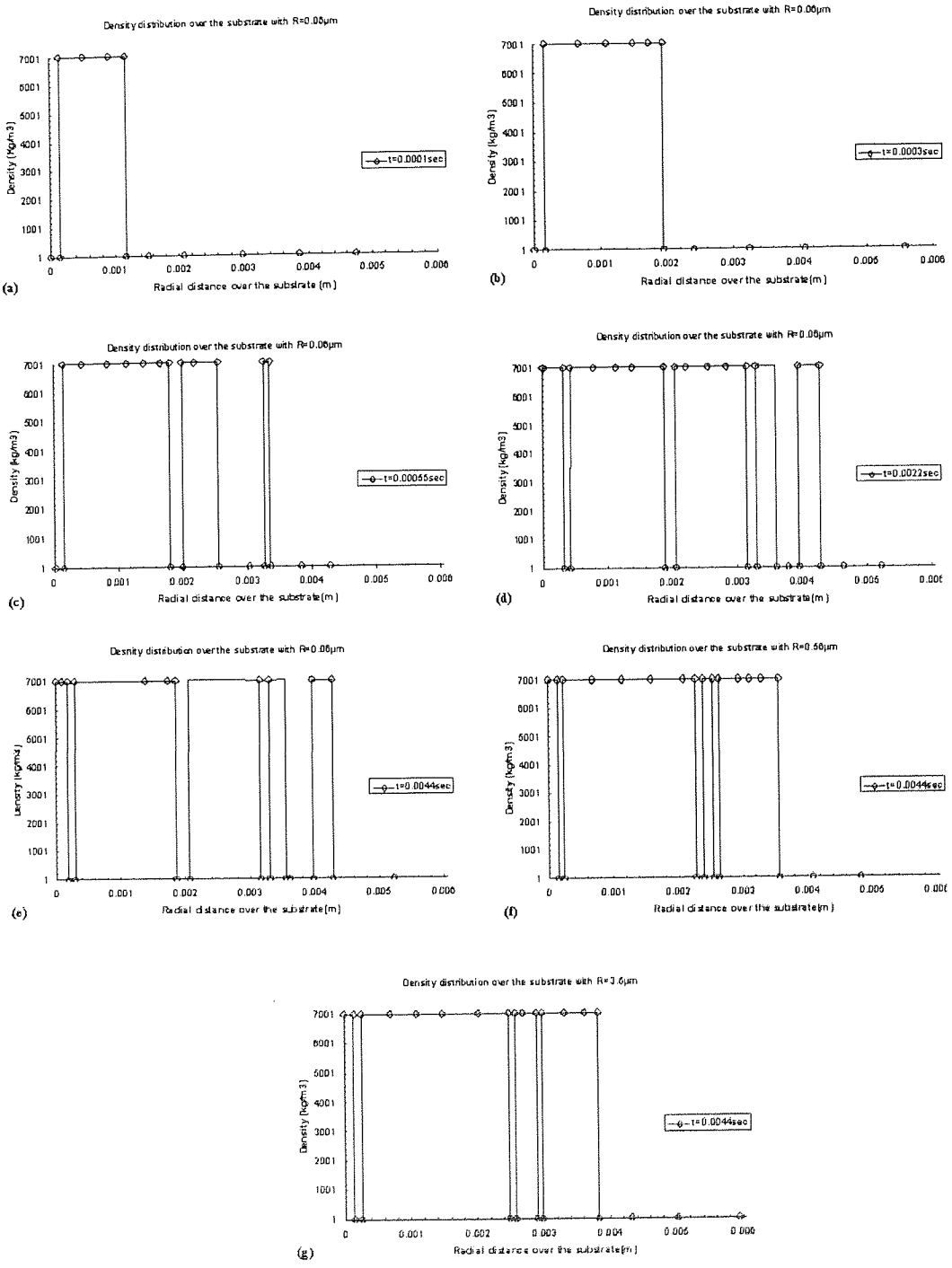

Figure 7.10: 10 Density profiles along the contact surface. Density distributions on 0.06μm surface roughness at (a) 0.1 ms, (b) 0.3 ms, (c) 0.55 ms, (d) 2.2 ms, (e) 4.4 ms. (f) Density distribution on 0.56m surface roughness at 4.4 ms. (g) Density distribution on 3.5m surface roughness at 4.4 ms.

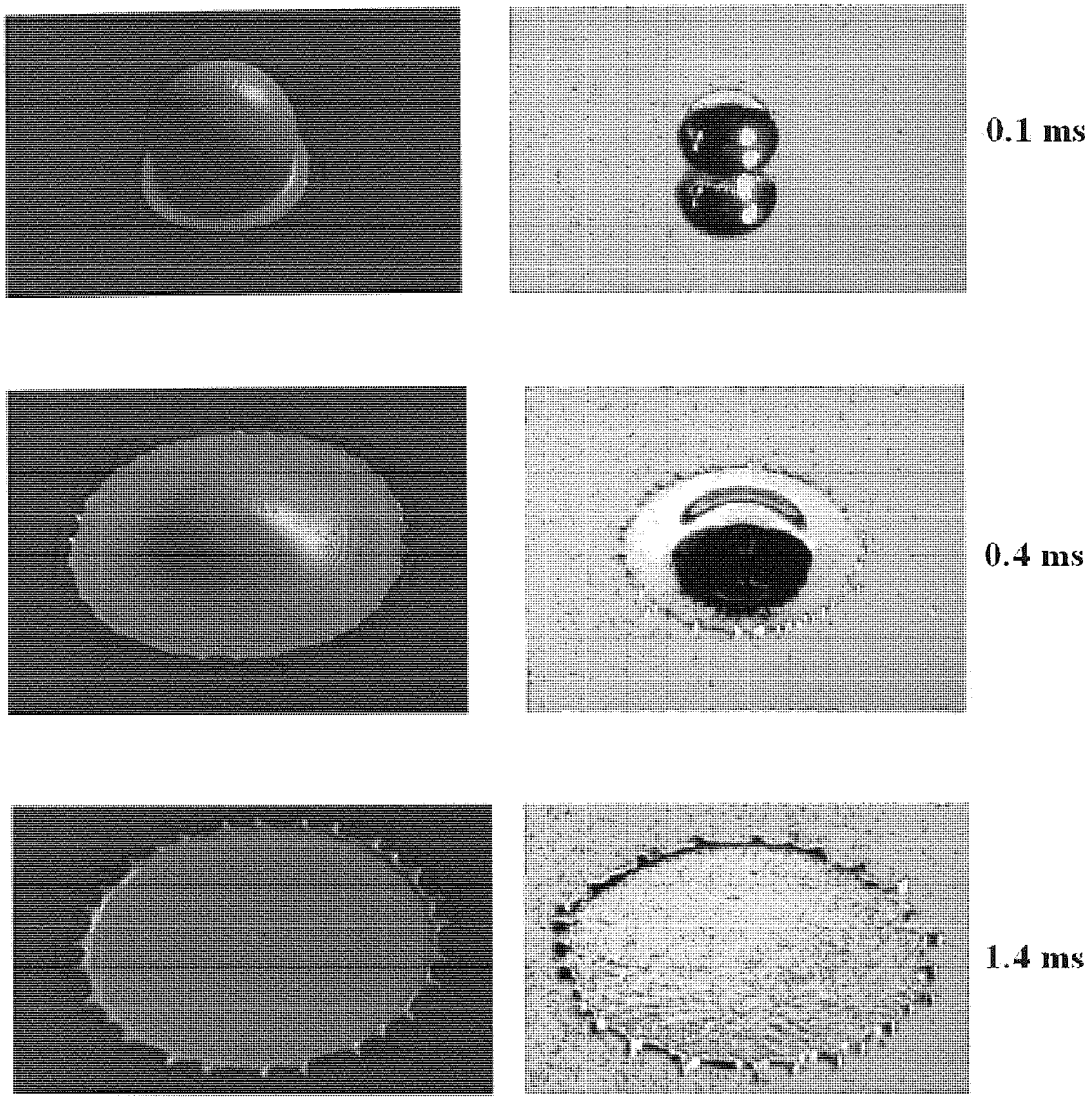

Figure 7.11: The impact of 2.2 mm diameter molten tin droplet with 4.0 m/s velocity on a stainless steel plate with surface roughness R=0.06 μm. On the left the numerical results are shown and compared on the right with photographs from experiment.

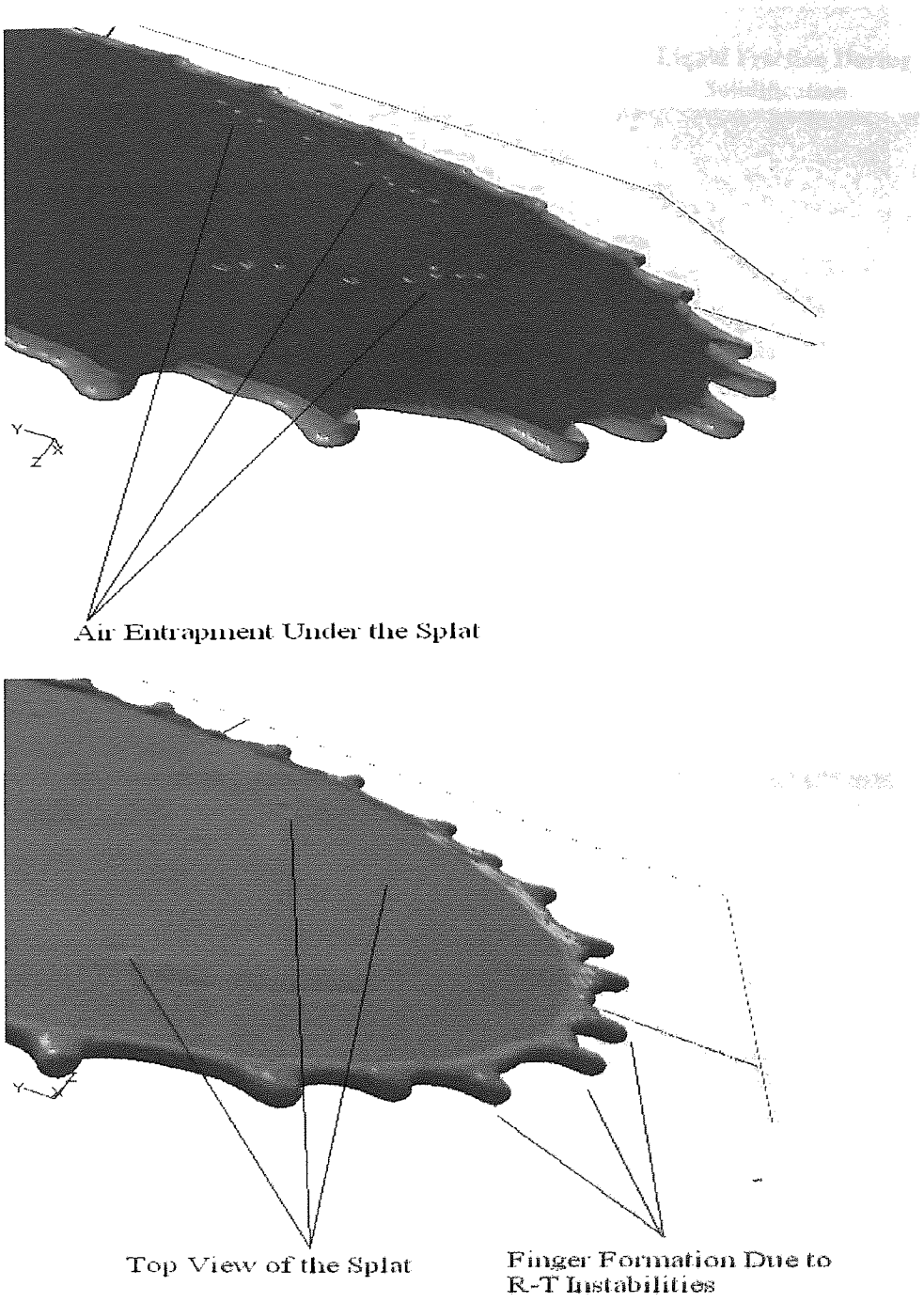

Figure 7.12: Top and bottom views of the splat at 1.4 ms showing the air cavities and the formation of fingers.

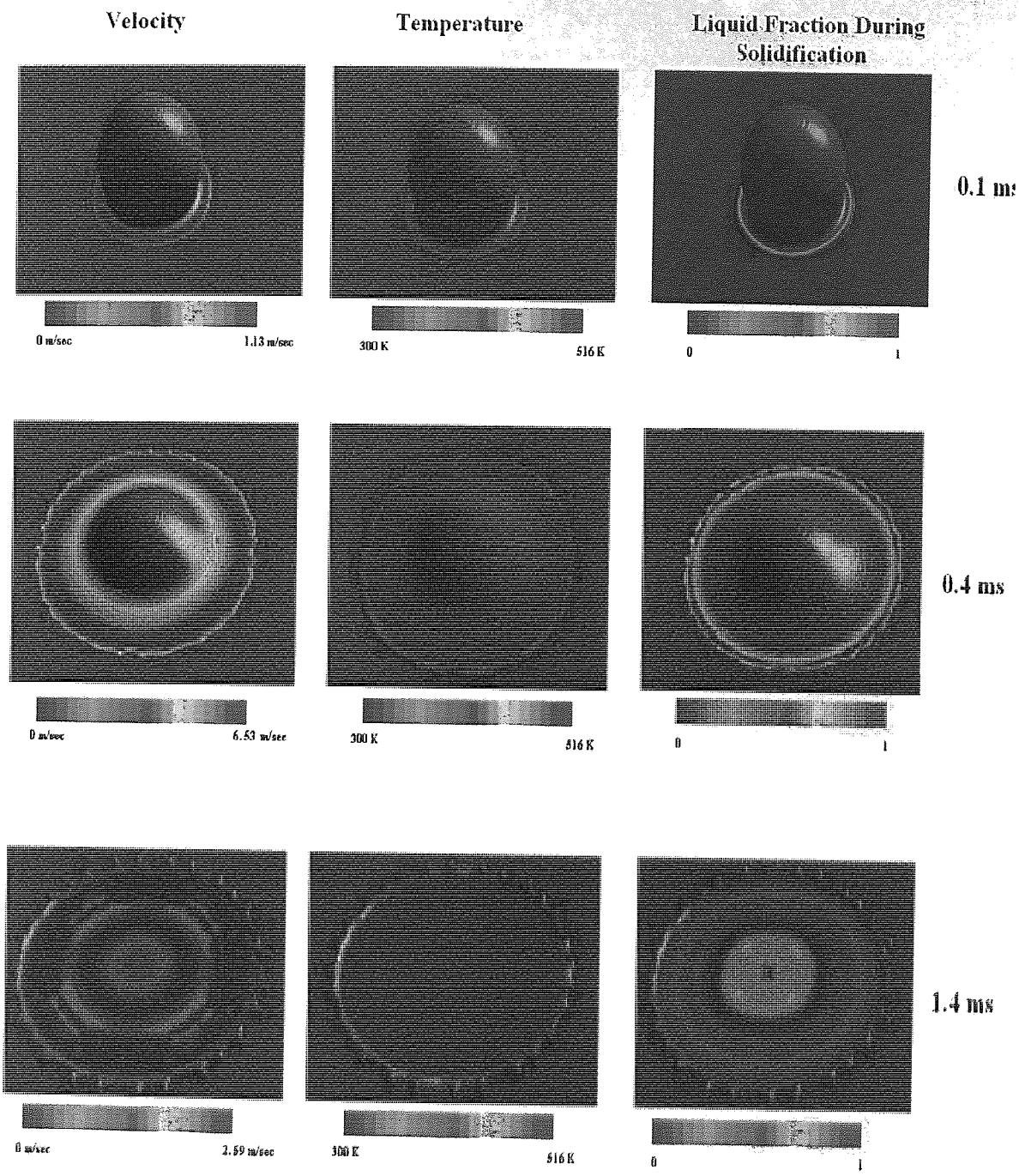

Figure 7.13: Numerical results showing the surface velocities temperatures and liquid fractions at three time instants.

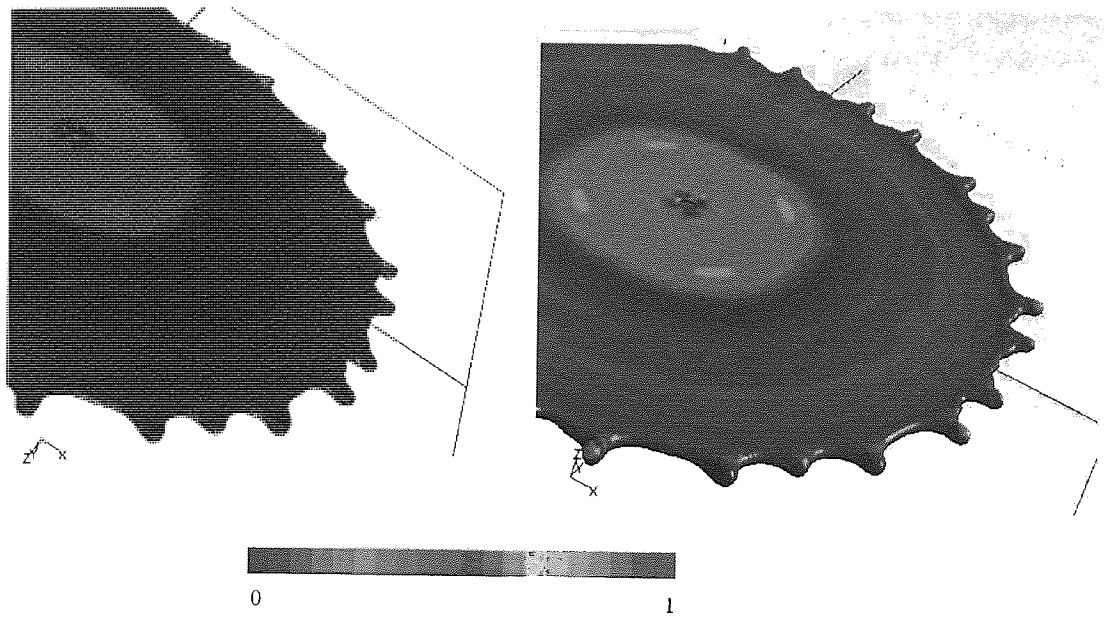

Figure 7.14: Top and bottom views of the surface liquid fraction during solidification at 1.4 ms.

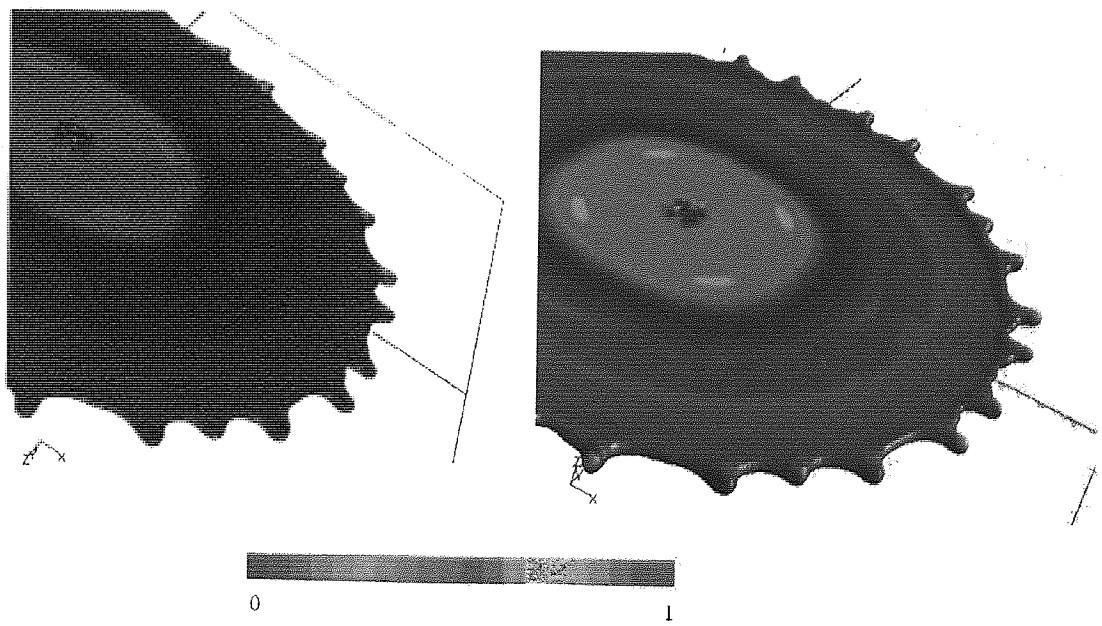

Figure 7.15: Top and bottom views of the surface static pressure distribution at 1.4 ms.

Chapter 8

Conclusions

8.1 Research Summary

The thesis has presented the research results obtained from focusing on the task to develop and implement mathematical models suitable for capturing the physical phenomena occurring during thermal spray process. The computational tasks were choosen according to involved process parameters such as combustion, heat transfer, particle modelling and powder impact dynamics on the substrate. The research presents how a commercial CFD code can be utilized and enhanced, in terms of numerical models, in a multidiscipline engineering process such as HVOF.

The numerical modelling presented in chapter 4 offers a viable analysis for moving to the next generation liquid fuelled HVOF technology. In the first section the combustion of propane was investigated where several mathematical models were tested. The results can be summarized as follows.

The third order descretization scheme (QUICK) is able to capture the supersonic shock diamonds closely aligned with the experimental observation in the free jet region. The model predicts that shock waves also exist inside the HVOLF gun where the high-pressure gas flow accelerates through the convergent-divergent nozzle and expands in the front of the barrel. The prediction of reacting flow in the combustion chamber is critically affected by turbulent fluctuations. Without the turbulent effect, the laminar finite rate combustion model predicts that the gas flow is confined to a narrow region around the centre of the gun. This computational pheromone is not consistent with experimental evidences in other HVOF guns that indicate small powder particles travel towards the internal surface of the gun as a result of gas flow dynamics. Both eddy dissipation and eddy dissipation-finite rate combustion models generate similar results with a conical shape flame naturally spreading in the combustion chamber. The global reaction model of propane combustion is able to give a reasonable prediction on heat

generation, in term of flame temperature. The same trend is found for the predicted maximum flame temperature and documented adiabatic flame temperature by varying fuel to oxygen ratio.

The second section of chapter 4 describes a three-dimensional simulation where the combustion and discrete particle models within the commercial numerical code were applied to solve the combustion of kerosene and couple the motion of fuel droplets with the gas flow dynamics in a Lagrangian fashion. The effects of liquid fuel droplets on the thermodynamics of the combusting gas flow were examined and the results are summarized here.

The combustion process of kerosene is dependent on the initial fuel droplet sizes. The small droplets generate a confined corn-shape flame and give more uniform temperature profile within the combustion chamber while large droplets have dispersed fan-shape flame structure and less uniform temperature profiles. Large areas of recirculation flow are generated around the fuel/oxygen injection ports and the location and magnitude of recirculation flow are dependent on droplet sizes, i.e. recirculation flows decline as the fuel droplet size increases. Generally small fuel droplets only endure short distances and are confined within a more uniform pattern while large droplets travel much further and disperse more widely into the gas flow. With the current gas flow rate, both 0.1 and 1 μm fuel droplets have similar core length of the flames and evaporation rate which implies that an optimized atomizer should produce droplet size around 1 μm to achieve cost-effective operation. The acceleration of powder particle is less sensitive to the variation of fuel droplet size while more dependency is predicted for the particle heating process. The current design of the three fuel/oxygen injection ports with large combustion chamber is able to generate uniform temperature and momentum output despite the variation of fuel droplet sizes. It is possible to overcome the problem of carbon deposition from the current design by changing the incoming angle of fuel and oxygen stream towards the centre, which will effectively reduce the contact between the combusting gas and the internal wall surfaces.

In the third section of chapter 4 a CFD water cooling model has been presented to examine the heat transfer between the cooling water and the solid copper in a HVOF thermal spray gun. The heat transfer mode was fully integrated with the hydrodynamic gas flow field and gives insights to heat transfer mechanism during the process. The following conclusions have been obtained.

The heat loss through water cooling is dependent positively on the water flow rate. The effect of water flow on the temperature of gun surface is more pronounced at low flow rate and less significant at high flow rate. The water flow has no noticeable influence on the gas temperature in the centre of the gun. Flow direction can affect the cooling

efficiency. The current cooling configuration points to a better cooling when water flows from combustion chamber towards the exit. The maximum temperature of gas flow within the combustion chamber is independent on water flow rate and direction. The gas flow dynamics relies on the internal design of the thermal spraying gun rather than water cooling configuration.

Chapter 5 presented several important considerations regarding the discrete particle modelling and validation of research results. The presented results in chapters 5 and 6 have been verified in terms of their ability to deal with the stated problem area (i.e. melting, solidification and oxidation modelling of powder particles) through integration with existing theories and methodologies and through implementation in an operative industrial HVOF design.

In Section 5.3 the concept of an analytical solution to the phase change problem was presented. The major advance of the improved analytical solution is to include surface convection without using complex numerical methods. The simplified solutions can be readily incorporated to numerical models in Lagrangian formulation to solve complicated multiscale modelling problems. The analytical model was based on several assumptions. Despite the benefit due to simplicity, the analytical solution can be used only when pure materials are examined. In section 5.4 a new approach that combines the Lagrangian particle modelling with numerical solution within the discrete particles is presented in an attempt to overcome the limitations of the analytical solution. The numerical model presented in this section is a novel "cheap to run version" of the expensive fixed grid methods described in section 5.1. The high thermal profiles endured for sprayed particles in conjunction with melting give rise to oxidation on the surface of metal powders. It was an objective of this study to include and predict numerically all the physical phenomena that occur during the process. The results and conclusions of the analytical and numerical solutions are presented in chapter6.

A 3-D CFD model has been developed to investigate the Inconel 718 particle dynamic behaviour in a liquid fuelled HVOF spray gun using kerosene. The model employed a Lagrangian particle tracking frame coupled with a steady-state gas flow field to examine particle motion and heat transfer during HVOF spraying. The model was used to investigate the effects of powder injection parameters on in-flight particle behaviour. The following conclusions have been obtained.

An increase in particle injection velocity from 0 to 40 m/sec increases the particle temperature development as well as the particle impact velocity. At speed above 20 m/s; the 20μm particle may hit the internal surface of the barrel and the trajectory may be changed to opposite direction as the result of elastic collision. The computational results imply that, to spray Inconel 718 powder with a mean diameter of 20μm, the injection

speed needs to be controlled between 8 to 10 m/s, in that case, most powder particles will stay in the centre of the gun. The set of results imply that the particular particles at the given injection speed of 8 m/sec will concentrate at the centre of the jet at the point of impact but the higher impact velocity and temperature can be achieve at axial injection position closer to the throat. The particle trajectories show that the small particles are blown away by the gas flow, whereas large particles of 30-40μm diameter move across the centre of the gun. The results show that particles smaller than 5μm will be greatly overheated, on the contrary particles larger than 10μm may never reach the liquid state during the process. All powder particles are hitting the substrate (i.e. 0.32m from the gun's exit) fully solidified although particles smaller than 10μm have been melted before at some point of their in-flight trajectory.

The oxidation of steel particles is investigated in section 6.2. The numerical oxidation model has been implemented in Lagrangian method for tracking powder particles in thermal spraying. Numerical simulation has been carried out for liquid fuelled HVOF gun with 3-D gas combusting gas flow same as in section 6.1. The numerical models were used for parametric study on particle size and injection location. The numerical model was validated against the analytical solution developed in the previous chapter. The results confirm that HVOF guns can produce metallic coating with low oxidation within the typical standing-off distance about 30 cm; injecting powders at the end of convergent divergent nozzle is able to reduce the contacts between powders and the hot gas flame to minimize the undesirable oxidation for metal powders. This investigation has used stainless steel powders, but the oxidation model can be generically applied to any metallic powders in thermal spray coating when experimental data on the material are available.

Chapter 7 presented a 2-D numerical model that is able to accurately simulate droplet impingement process. Detailed data of thermo-physical properties is implemented into the material model instead of using constant value, e.g. different thermal conductivity and density for liquid and solid, latent heat of freezing. Most assumptions that could affect prediction in existing droplet impingement models are replaced with close-to-reality algorithms. The 2-D computational domain was extended to a more realistic 3-D in section 7.2. The following conclusions can be drawn.

The thermal contact resistance can be used effectively to characterize surface roughness and the numerical results demonstrate an excellent agreement with the experimental data. The solidification of droplets is significantly affected by the thermal contact resistance/substrate surface roughness. On smooth surfaces where contact resistance is low and heat is transferred rapidly from the droplet to substrate, droplet solidifies quickly which prompts the break-up and formation of satellite droplets. Air is trapped in the

droplet during the impingement. The air entrapment during spreading is dependent on substrate surface roughness, i.e. less air is trapped at high thermal contact resistance on rough surface.

8.2 Scientific Contribution

A 'cheap to run' discrete phase particle numerical approach has been developed and added to the existing body of scientific knowledge. The analytical phase change solution is added as a possible extension (primarily in the discrete phase modelling) to overcome limitations and assumptions of previously developed models. The scientific contribution of this research is the suggestion of complete and accurate modelling methods for the prediction of the powder particle thermal behaviour during thermal spray. The implementation of the numerical and analytical models can be extended to different thermal spray processes such as plasma spray. The droplet impingement process has been analysed and enhanced with more reliable solution algorithms mainly regarding the heat transfer part. The successful validation with existing experimental data provide further evidence that the proposed concepts are valid and provide an extension to existing methods and theories.

8.3 Industrial Contribution

The ability to deal effectively and efficiently with HVOF thermal spray process, through a commercial general purpose CFD code, can provide insights into the core product design and a robust platform for further development. The gas and particle analysis of the liquid HVOF systems is interesting in such a way that transition phase to the next generation products can be supported and carefully assisted. The industrial contribution is the enhanced ability, through modeling, to effectively and efficiently develop high variety of products according to the market needs. The CFD results provided in this thesis can be a tool in the toolbox of an experienced designer as well as a fundamental enabler for the development and implementation of new generation product systems.

8.4 Recomentations for Future Research

8.4.1 Combustion modelling

Further understanding of combustion can be probably achieved using CFD, mainly at LES level. Standard steady RANS methods (based on the $\kappa - \varepsilon$ transport model) may

not be able to reproduce as accurate as LES the flame behaviour. RANS methods have a tendency to under predict, in the region inside the combustion chamber, the aerodynamic inflow jet of reactants into the flame. On the other hand LES, may give more accurate prediction of the velocity parameters controlling flame position, and predict flame stabilization inside the combustion chamber. Although fast burning fuels such as propane or kerosene can be modelled under equilibrium chemistry, more sophisticated multi-step reaction models can be implemented when experimental data are available. The study of kerosene combustion has shown that combustion process depends on the previously atomized fuel droplets. Modelling of the atomization process prior to combustion may be a necessary extension to this study.

8.4.2 Particle Modelling

Considering that the particle mass loading is relatively low in HVOF process the particle-particle interactions can be safely ignored. If the particle mass loading is large, particles are expected to interact each other therefore modelling of this behaviour may be necessary. Further studies on the particle modelling should be done considering the carrier gas effect on particle velocity upon entering the computational domain. In this study the particles are given an initial velocity which is not a result of the aerodynamic interaction with the carrier gas flow. Future studies should be contacted to correlate the carrier gas mass flow rate with particle velocity. This will require modelling of the particle flow inside the carrier gas tube. The effect of carrier gas on particle oxidation is also a process parameter that has not been studied yet.

8.4.3 Particle Impingement

Further efforts should be devoted to the modelling of solid particle impingement and the formation of coating structures. A challenging computational task is the prediction of multi-particle impingement including the hot gas stream onto substrate. The impingement of solid and irregular particles requires attention since most of the sprayed particles are not melted at impact.

Bibliography

[1] Davis, J.R. (Ed.). Handbook of Thermal Spray Technology. Thermal Spray Society, ASM International, Materials Park, OH, USA (2004), p. 338.

[2] Heinrich. P. Thermal spraying. Facts and state of the art. Sonderdruck, E10/92 (1992), p. 28.

[3] Pawlowski, L. The science and engineering of thermal spray coatings. John Wiley and Sons, New York, NY, USA (1995), p. 432.

[4] Kulkarni, A., Gutleber, J., Sampath, S., Goland, A., Lindquist, W.B., Herman, H., Allen, A.J.and Dowd, B. Studies of the microstructure and properties of dense ceramic coatings produced by high-velocity oxygen-fuel combustion spraying. Materials Science and Engineering A369 (2004), pp. 124.137.

[5] Ramm, D.A.J., Clyne, T.W., Sturgeon, A.J. and Dunkerton, S. Correlations between spraying conditions and microstructure for alumina coatings produced by HVOF and VPS. Proceedings of the 7th National Thermal Spray Conference, 20.24 June, 1994, Boston, Massachusetts, USA (1994, pp. 239.244.

[6] Sturgeon, A.J., Harvey, M.F.D. and Blunt, F.J. The influence of fuel gas on the microstructure and wear performance of alumina coatings produced by the High Velocity Oxyfuel (HVOF) thermal spray process. British Ceramic Proceedings, Vol. 54(1997), pp. 57.64.

[7] Sturgeon, A.J. Recent advantages and applications of thermal sprayed ceramic coatings, British Ceramic proceedings, Vol. 55(1996), pp. 3.12

[8] Kreye, H., Schwetzke, R. and Zimmermann, S. High velocity oxy-fuel flame spraying process and coating characteristics. Thermal Spray: Practical solutions for Engineering Problems. Berndt, C.C. (Ed.). Published by ASM International, Materials Park, Ohio-USA (1996), pp. 451.456.

[9] Li, M., Shi, D. and Christofides, P.D. Model-based estimation and control of particle velocity and melting in HVOF thermal spray. Chemical Engineering Science 59(2004), pp. 5647.5656.

[10] Nylen, P., Lemaitre, J. and Wigren, J. Sensitivity of four on-line diagnostic systems for plasma spraying. Thermal spray 2003: advancing the science and applying technology. Moreau, C. and Marple, B. (Eds.). Published by ASM International, Materials Park, Ohio-USA (2003), pp. 1101.1106.

[11] Steffens, H.-D. and Duda, T. Enthalpy measurement of direct current plasma jets used for ZrO2-Y2O3 thermal barrier coatings. Journal of Thermal Spray Technology, 9, 2(2000), pp. 235.240.

[12] Tucker, R.C. Jr. Integrated thermal spray systems. Some practical considerations. Thermal spray 2001: New surfaces for a new millennium. Berndt, C.C., Khor, K.A. and Lugscheider, E.F. (Eds.). Published by ASM International, Materials Park Ohio, USA (2001), pp. 1261.1266.

[13] Hamalainen, E., Vattulainen, J., Alahautala, T., Hernberg, R., Vuoristo, P. and Mantyla, T. Imaging diagnostics in thermal spraying. "Spray Watch" system. Thermal Spray Surface Engineering via Applied Research, Proceedings, 1st International Thermal Spray Conference (ITSC 2000), Montreal, Quebec, Canada; 8.11 May 2000, pp. 79.83.

[14] Fincke, J.R., Swank, W.D., Bewley, R.L. and Haggard, D.C. Control of particle temperature, velocity, and trajectory in thermal spray process. Thermal spray 2003: Advancing the science and applying technology. Moreau, C. and B. Marple, B. (Eds.). Published by ASM International, Materials Park, Ohio- USA (2003), pp. 1093.1099.

[15] Moreau, C., Gougeon, P., Lamontagne, M., Lacasse, V., Vaudreuil, G. and Cielo, P. On-line Control of the Plasma Spraying Process by Monitoring the Temperature, Velocity and Trajectory of In-Flight Particles. Proceedings of the 7th National Thermal Spray Conference 20.24 June 1994, Boston, USA (1994), pp. 431.437.

[16] Fincke, J.R., Haggard, D.C. and Swank, W.D. Particle Temperature Measurement in the Thermal Spray Process. Journal of Thermal Spray Technology, 10, 2(2001), pp. 255.266.

[17] Vuoristo, P., Ahmaniemi, S., Nuutinen, S., Mantyla, T., Hamalainen, E., Arola, N. and Vattulainen, J. Optimisation and monitoring of spray parameters by a CCD camera based imaging thermal spray monitor. Thermal spray 2001: New surfaces for a

new millennium. Berndt, C.C., Khor, K.A. and Lugscheider, E.F. published by ASM International, Materials Park Ohio, USA (2001), pp.727.736.

[18] Lugscheider, E., Fischer, E., Koch, D. and Papenfur, N. Diagnostics of in flight particle properties and resulting coating qualities on atmospheric plasma process, Thermal Spray 2001. New Surfaces for a New Millennium, Proceedings, International Thermal Spray Conference (ITSC 2001), Singapore; 28.30 May 2001, pp. 751.758.

[19] J.Westerweel,J., Digital Particle Image velocimetry, Theory and Application, Diss., Delft University Press, Netherlands, 1993.

[20] Thorpe, M., and Richter, H., 1992 Proc. Inter. Thermal Spray Conf. and Exposition, Orlando, Florida, USA, May 28-June 5, 1992 p 137

[21] Power, G.D., Smith, E.B., Barber, T.J., Chiappetta, L.M., 1991. Analysis of a combustion (HVOF) spray deposition gun. Report 91-8, United Technologies Research Centre, East Hartford, Connecticut, USA.

[22] Power, G. D., T. J. Barber, and L. M. Chiappetta, "Analysis of a High Velocity Oxygen-Fuel (HVOF) Thermal Torch," AIAA Paper No. 92-3598, AIAA/SAE/ASME/ASEE 28th Joint Propulsion Conf., Nashville, TN, July, 1993.

[23] Smith, E. B., G. D. Power, T. J. Barber, and L. M. Chiappetta, "Application of Computational Fluid Dynamics to the HVOF Thermal Spray Gun," International Thermal Spray Conf., Orlando, FL, May, 1992, 805-810.

[24] Oberkampf, W.L., Talpallikar, M., 1996. Analysis of a high-velocity oxygen fuel (HVOF) thermal spray torch part 2: computational results. Journal of Thermal Spray Technology 5, 62-68.

[25] Chang, C. H., and Moore, R. L., J. Therm. Spray Technol. 4 358 (1995)

[26] Eidelman, S., Yang, X., Lottati I and Grossmann 1995 Proc. 8th National Thermal Spray Conf. (Houston, Texas, 11-15 September) p 219

[27] B. P., Leonard, Order of accuracy of QUICK and related convection-diffusion schemes, Applied Mathematical Modelling, 19(11) (1995) 640-653.

[28] Cheng, D., Xu, Q., Trapaga, G., Lavernia, E.J., 2001b. A numerical study of high-velocity oxygen fuel thermal spraying process. Part I: gas phase dynamics. Metallurgical and Materials Transactions A 32, 1609-1620.

[29] T.H. Shih, W.W. Liou, A. Shabbir and J. Zhu, A new $\kappa - \varepsilon$ eddy viscosity model for high Reynolds number turbulent flows, Computers and Fluids, 24(3) (1995) 227-238, 1995.

[30] Yang, X., Eidelman, S., 1996. Numerical analysis of a high-velocity oxygen fuel thermal spray system. Journal of Thermal Spray Technology 5, 175-184.

[31] Gu, S., Eastwick, C.N., Simmons, K.A., McCartney, D.G., 2001. Computational fluid dynamic modelling of gas flow characteristics in a high-velocity oxy-fuel thermal spray system. Journal of Thermal Spray Technology 10, 461-469.

[32] Hassan, B., Lopez, A.R., Oberkampf, W.L., 1998. Computational analysis of a three-dimensional high-velocity oxygen fuel (HVOF) thermal spray torch. Journal of Thermal Spray Technology 7, 71-77.

[33] Lopez, A.R., Hassan, B., Oberkampf, W.L., Neiser, R.A., Roemer, T.J., 1998. Computational fluid dynamics analysis of a wire-feed, high-velocity oxygen fuel (HVOF) thermal spray porch. Journal of Thermal Spray Technology 7, 374-382.

[34] Dolatabadi, A., Mostaghimi, J., Pershin, V., 2003. Effect of a cylindrical shroud on particle conditions in high velocity oxy-fuel spray process. Journal of Materials Processing Technology 137, 214-224.

[35] Li, M., Christofides, P.D., 2005. Multi-scale modelling and analysis of HVOF thermal spray process. Chemical Engineering Science 60, 3649-3669.

[36] Gordon, S., and McBrid, B.J., Computer Program for Calculation of Complex Chemical Equilibrium Compositions, Rocket Performance, Incident and Reflected Shocks, and Chapman-Jonquet Detonations. NASA SP-273, 1976, new version 1989.

[37] Voronetsky A. V, Jagodnikov D. A, Filimono L. A, Suchkov S. A, Shirjaeva N. V, Elisseev A. A and Boronin E. V Proc. 15th International Thermal Spray Conf. (Nice, France, 25-29 May 1998) p 1393

[38] Mingheng Li, Panagiotis D. Christofides. Computational study of particle in-flight behaviour in the HVOF thermal spray process. Chemical Engineering Science 61 (2006) 6540 - 6552

[40] Lopez A R, Hassan B, Oberkampf W L, Neiser A R, Roemer T J 1996 Thermal Spray: Practical Solution for Engineering Problems ed C C Berndt (Materials Park, Ohio, USA: ASM International) p 531

[40] Lopez A R, Hassan B, Oberkampf W L, Neiser A R, Roemer T J 1996 Thermal Spray: Practical Solution for Engineering Problems ed C C Berndt (Materials Park, Ohio, USA: ASM International) p 531

[41] F.H. Harlow and J.P. Shannon, The splash of a liquid droplet, Journal of Applied Physics 38 (1967) 3855-3866.

[42] H. Jones, Cooling, freezing and substrate impact of droplets formed by rotary atomization, Journal of Physics D: Applied Physics 4 (1971) 1657-1660.

[43] J. Madejski, Solidification of droplets on a cold surface, International Journal of Heat and Mass Transfer 19(1976) 1009-1013.

[44] J. Madejski, Droplets on impact with a solid surface, International Journal of Heat and Mass Transfer 26 (1983) 1095-1098.

[45] G. Trapaga and J. Szekely, Mathematical modeling of the isothermal impingement of liquid droplets in spray processes, Metallurgical Transactions (B) 22 (1991) 901-914.

[46] K. Tsurutani, M. Yao, J. Senda and H. Fujimoto, Numerical analysis of the deformation process of a droplet impinging upon a wall, JSME International Journal (Series 2) 33 (1990) 555-561.

[47] T. Watanabe, I. Kuribayashi, T. Honda and A. Kanzawa, Deformation and solidification of droplet on a cold substrate, Chemical Engineering Science 47 (1992) 3059-3065.

[48] M. Pasandideh-Ford and J. Mostaghimi, Deformation and solidification of molten particles on a substrate in thermal spraying, in C.C. Berndt and S. Sampath (Ed.), Proceeding of the 7th National Thermal Spray Conference, Boston, MA, 1994, pp. 405-415.

[49] J.E. Welch, F.H. Harlow, J.P. Shannon, B.J. Daly, The MAC Method, Technical Report LA-3425, LANL, 1966.

[50] T. Bennet and D. Poulikakos, Heat transfer aspects of splat solidification: modelling and experiment, Journal of Material Science 29(1994) 2025-2039.

[51] B. Kang, Z. Zhao, D. Poulikakos, Solidification of liquid metal droplets impacting sequentially on a solid surface, ASME Journal of Heat Transfer 116 (1994) 436-445.

[52] H. Liu, E.J. Lavernia, R. Rangel, Numerical simulation of substrate impact and freezing of droplets in plasma spray process, Journal of Physics D: Applied Physics 26 (1993) 1900-1908.

[53] G. Trapaga, EF. Matthys, J.J. Valencia, J. Szekely, Fluid flow, heat transfer and solidification of molten metal droplets impinging on substrates: comparison of numerical and experimental results, Metallurgical Transactions B23(1992) 701-718.

[54] M. Pasandideh -Fard, Y.M. Qiao, S. Chandra, J. Mostaghimi, Capillary effects during droplet impact on a solid surface. Physics of Fluids 8(1996) 650-659.

[55] J.M. Waldvogel, D. Poulikakos, Solidification phenomena in picoliter size solder droplet deposition on a composite substrate, International Journal of Heat and Mass Transfer 40 (1997) 295-309.

[56] D. Sivakumar and H. Nishiyama. Spreading and solidification of a molten metal droplet impinging on a heated surface, International Journal of Heat and Mass Transfer 47 (2004) 4469-4478.

[57] R. Ghafouri Azar, Z. Yang, S. Chandra, J. Mostafhimi, Impact of molten metal droplets on the tip of a pin projecting from a flat surface, International Journal of Heat and Fluid Flow 26 (2005) 334-347.

[58] J.P. Van Doormal, G.D. Raithby, B.H. McDonald, The segregated approach to predicting viscous compressible fluid flows, ASME Journal of Turbomachinery 109 (1987) 268-277.

[59] M. Peric, Analysis of pressure-velocity coupling on non-orthogonal grids, Numerical Heat Transfer Part B: Fundamentals 17 (1990) 63-82.

[60] G.D. Raithby, G.E. Schneider, Numerical solution of problems in compressible fluid flow: Treatment of the velocity-pressure coupling, Numerical Heat Transfer 2 (1979) 417-440.

[61] B.P. Leonard, Order of accuracy of QUICK and related convection-diffusion schemes. Applied Mathematical Modelling 19 (1995) 640-653.

[62] S. Shakeri, S. Chandra, Splashing of molten tin droplets on a rough steel surface, International Journal of Heat and Mass Transfer 45 (2002) 4561-4575.

[63] J.U. Brackbill, D.B. Kothe, and C. Zemach, A continuum method for modelling surface tension, Journal of Computational Physics 100 (1992) 335-354.

[64] S.D. Aziz and S. Chandra, Impact, recoil and splashing of molten metal droplets, International Journal of Heat and Mass Transfer 43 (2000) 2841–2857.

[65] V.R. Voller, Modeling Solidification Processes, Technical report in Mathematical Modeling of Metals Processing Operations Conference, American Metallurgical Society, Palm Desert, CA, 1987.

[66] V. R. Voller, A. D. Brent, and K. J. Reid, A Computational Modeling Framework for the Analysis of Metallurgical Solidification Process and Phenomena, Technical report in Conference for Solidification Processing, Ranmoor House, Sheeld, 1987.

[67] V.R. Voller and C. Prakash, A Fixed-Grid Numerical Modeling Methodology for Convection-Diffusion Mushy Region Phase-Change Problems, International Journal of Heat and Mass Transfer 30 (1987)1709-1720.

[68] Van Dyke M., Album of Fluid Motion, Parabolic Press Inc, 1982;

[69] Smits A. J., Lim T.T., Flow Visualization: Techniques and Examples, World Scientific Publishing, 2000;

[70] Hinze J.O., Turbulence, McGraw-Hill Companies, 1975;

[71] Pope S.B., Turbulent Flows, Cambridge University Press, 2000;

[72] Bernard P.S., Wallace J.M., Turbulent Flow: Analysis, Measurement and Prediction, Wiley, 2002;

[73] Launder B.E., Sandham N. D.,Closure Strategies for Turbulent and Transitional Flows, Cambridge University Press, 2002;

[74] Moin P., Mahesh K., DIRECT NUMERICAL SIMULATION: A Tool in Turbulence Research, Annu. Rev. Fluid Mech., vol. 30, pp. 539-578, 1998;

[75] Reynolds O., On the Extent and Action of the Heating Surface for Steam Boilers. Proc. Manchester Lit. Phil. SOC., vol. 14, pp. 7-12, 1874;

[76] Wilcox D.C., Turbulence Modeling for CFD,DCW Industries Inc., La Cafiada, California, USA, 1993;

[77] Jones, W.P., Launder, B.E., The Prediction of Laminarization with a Two-Equation Model of Turbulence. Int. Journal of Heat and Mass Transfer,vol.5, pp. 301-314, 1972;

[78] Hartmann, J.,and Lazarus, F. The air jet with a velocity exceeding that of sound. Philosophical Magazine, 331, 35-50 (1941)

[79] Courant,R., and Friendrichs, K.O. Supersonic Flow and Shock Waves. Interscience Publishers, New York (1984) pp.387-392

[80] Poinsot, T., and Veynante, D. Theoretical and Numerical Combustion. Edwards, Inc. 2001

[81] V. Zimont. Gas Premixed Combustion at High Turbulence. Turbulent Flame Closure Model Combustion Model. Experimental Thermal and Fluid Science, 21:179 186, 2000.

[82] V. Zimont, W. Polifke, M. Bettelini, and W. Weisenstein. An Eficient Computational Model for Premixed Turbulent Combustion at High Reynolds Numbers Based on a Turbulent Flame Speed Closure. J. of Gas Turbines Power, 120:526 532, 1998.

[83] V. L. Zimont, F. Biagioli, and K. J. Syed. Modelling Turbulent Premixed Combustion in the Intermediate Steady Propagation Regime. Progress in Computational Fluid Dynamics, 1(1):14:28, 2001.

[84] V. L. Zimont and A. N. Lipatnikov. A Numerical Model of Premixed Turbulent Combustion of Gases. Chem. Phys. Report, 14(7):993:1025, 1995.

[85] B. Karlovitz, D.W. Denniston JR., D.H. Knapschaefer, and F.E. Wells. Studies on turbulent flames. Proc. Comb. Inst., 4:613n620, 1953.

[86] F.A. Williams. A review of some theoretical considerations of turbulent flame structure. In AGARD Conference Proceedings, volume 164, 1975.

[87] D. Bradley, How fast can we burn?, Proc. Combust. Inst. 24 1992, 247–262.

[88] N. Peters, Turbulent combustion, Cambridge Monographs on Mechanics, Cambridge University Press, Cambridge, 2000

[89] R. K. Cheng and I. G. Shepherd, The influence of burner geometry on premixed turbulent flame propagation, Combust. Flame 85 1991, 7-26.

[90] Chiu HH, Kim HY, Croke EJ 1982 Internal group combustion of liquid droplets. Proc Comb Inst 19:971

[91] L.P. Yarin and G.Hetsroni. Combustion of Two-Phase Reactive Media. Springer, New York 2004.

[92] J.P. Van Doormal, G.D. Raithby, B.H. McDonald, The segregated approach to predicting viscous compressible fluid flows. ASME Journal of Turbomachinery, 109(1987) 268-277.

[93] M. Peric, Analysis of pressure-velocity coupling on non-orthogonal grids, Numerical Heat Transfer, Part B: Fundamentals, 17(1990) 63-82.

[94] G.D. Raithby, G.E. Schneider, Numerical solution of problems in compressible fluid flow: Treatment of the velocity-pressure coupling, Numerical heat transfer, 2 (1979) 417-440.

[95] B.E Launder and D.B. Spalding, Lectures in Mathematical Models of Turbulence, Academic Press, London, England, 1972.

[96] T. Furuhata, S. Tanno, T. Miura, Y. Ikeda and T. Nakajima, Performance of numerical spray combustion simulation, Energy Conversion and Management, 38(10-13)(1997) 1111-1122.

[97] A.D. Hewitt, Technology of oxy-fuel gas processes, Welding and Metal Fabrication, (1972) 318-422.

[98] S. Gordon and B.J. McBride, Computer Program for Calculation of Complex Chemical Equilibrium Compositions and Applications, NASA Reference Publication 1311, Lewis Research Centre, Cleveland, OH, USA (1994).

[99] Lipatnikov and Chomiak, 2002 A.N. Lipatnikov and J. Chomiak, Turbulent flame speed and thickness: phenomenology, evaluation and application in multi-dimensional simulations, Progress in Energy and Combustion Science 28 (2002), pp. 1-74

[100] Reuss et al., Reuss, D.L., Kuo, T.W., Khalighi, B., Haworth, D.C., Rosilik, M., 1995. Particle image velocimetry measurements in a high-swirl engine used for evaluation of computational fluid dynamics calculations. SAE 952381

[101] Suh, E.S., Rutland, C.J., 1999. Numerical study of fuel/air mixture preparation in a GDI engine. SAE 1999-01-3657

[102] R.D. Reitz, Modeling atomization processes in high-pressure vaporizing sprays, Atomization and Spray Technology 3 (1987), pp. 309-337

[103] Swank, W.D., Fincke, J.R., Haggard, D.C., Irons, G., 1994. HVOF gas flow field characteristics. In: Proceedings of the Seventh National Thermal Spray Conference, pp. 313-318.

[104] S.A. Morsi and A.J. Alexander, An investigation of particle trajectories in two-phase flow systems, Journal of Fluid Mechanics 55 (1972), pp. 193-208

[105] A. Haider and O. Levenspiel, Drag coefficient and terminal velocity of spherical and nonspherical particles, Powder Technology 58 (1989), pp. 63-70.

[106] W.E. Ranz and W.R. Marshall, Evaporation from drops, Part II, Chemical Engineering Progress 48 (1952), pp. 173-180.

[107] Jayatilleke, C. (1969) Progress of Heat Mass Transfer, Vol. 1,pp.193-321.

[108] E. Loth. Numerical approaches for motion of dispersed particles, droplet and bubbles. Progress in Energy and Combustion Science, 26:161-223, 2000.

[109] Crowe, M.Sommerfeld, and Y. Tsuji. Multiphase Flows with droplets and particles. CRC press, Boca Raton, Florida, 1998.

[110] D. Migdal and D.V. Agosta. A source flow model for continuum gas-particle flow. ASME J. Applied Mechanics, 34:860, 1967.

[111] J.B. McLaughlin. Numerical computation of particles-turbulence interaction. International Journal of Multiphase Flow, 20:211-232, 1997.

[112] M.H.Wright. Direct search methods: once scorned, now respectable. pages 191-208. Addison Wesley Longman, 1996.

[113] M. Maxey and J. Riley. Equation of motion for a small rigid sphere in a non-uniform flow. Physics of Fluids, 24:883-889, 1983.

[114] O.R. Walton. Numerical simulation of inelastic, frictional particle-particle interaction. Particulate two-phase °ow, M. Roco (Ed.), pages 884{920, 1993.

[115] Stefan, J., Uber die theorie der eisbildung inbesondere uber die eisbildung im polarmeer, Annalen der Physik und Chemie, 42, pp. 269-86, 1891.

[116] Hashemi, H. T. and Sliepcevich, C. M., A numerical method for solving two-dimensional problems of heat conduction with change of phase, Chem. Eng. Prog. Symp. Series, 63, pp. 34-41, 1967.

[117] Poirier, D. and Salcudean, M., On numerical methods used in mathematical modeling of phase change in liquid metals, Transactions of ASME Journal of Heat Transfer, 110, pp. 562-70, 1988.

[118] Poirier, D., On numerical methods used in mathematical modelling of phase change in liquid metals, MSc Thesis, Department of Mechanical Engineering, University of Ottawa,1986.

[119] Voller, V. R., Swaminathan, C. R. and Thomas, B. G., Fixed grid techniques for phase change problems: a review, International Journal for Numerical Methods in Engineering, 30, pp. 875-98, 1990.

[120] N., Hartree, D. R., Ingham, J., Jackson, R., Sarjant, R. J. and Wagstaff, J. B., 1946, The calculation of variable heat flow in solid, Philosophical Transactions of the Royal Society of London. Series A, Mathematical and Physical Sciences, 240, pp.1-57.

[121] Gupta, R. S. and Kumar, D., 1980, A modified variable time step method for the one-dimensional Stefan problem, Computer Methods in Applied Mechanics and Engineering, 23, pp. 101-108.

[122] Heitz, W. L. and Westwater, J. W., 1970, Extension of the numerical method for melting and freezing problems, International Journal of Mass and Heat Transfer, 13, pp.1371-1375.

[123] Gupta, R. S., 1974, Moving grid method without interpolations, Computer Methods in Applied Mechanics and Engineering, 4, pp. 143-152.

[124] Basu B. and Date, A. W., 1988, Numerical modelling of melting and solidification problems: a review, Sadhana - Academy Proceedings in Engineering Sciences, 13, pp.169-213.

[125] Hu, H., Argyropoulos, S.A., 1996, Mathematical modelling of solidification and melting: A review, Modelling and Simulation in Materials Science and Engineering, 4, pp. 371-396.

[126] Neumann, F., 1912, Die Paruellen Differentialgleichungen der, Mathematischen Physik, 2, (Reimann-Weber) pp. 121.

[127] Goodman, T. R., 1958, The heat-balance integral and its application to problems involving a change of phase, Transactions of AMSE, 80, pp. 335-342.

[128] Pohlhausen, K., 1921, Zur naherungsweisen integration der differentialgleichunger der laminaren grenzschicht Zeitschrift fur angewandte, Mathematik und Mechanik 1, pp. 252-258.

[129] Kamnis, S., and Gu, S., 2005, Numerical modelling of droplet impingement, Journal of Physics D, 38, pp. 3664-3673.

[130] Tao, L. C., 1967, Generalized numerical solutions for freezing a saturated liquid in cylinders and spheres, AIChE Journal, 13, pp. 165-169.

[131] London, A. L. and Seban, R. A., 1943, Rate of ice formation, Transactions of ASME, 65, pp. 771-778.

[132] Pedroso, R. I. and Domoto, G. A., 1973, Perturbation solution for spherical solidification of saturated liquids, Transactions of ASME Journal of Heat Transfer, 95, pp. 42-46.

[133] Riley, D. S., Smith, F. I. and Poots, G., 1974, The inward solidification spheres and circular cylinders, International Journal of Heat and Mass Transfer, 46, pp. 1497-1501.

[134] Poots, G., 1962, On the application of integral methods to the solution of problems involving the solidification of liquid initially at fusion temperature, International Journal of Heat and Mass Transfer, 5, pp. 525-531.

[135] Lin, S. and Jiang, Z., 2003, An improved Quasi-Steady Analysis for solving freezing problems in a plate, a cylinder and a sphere, Transactions of ASME Journal of Heat Transfer, 125, pp. 1123-1128.

[136] Caldwell, J. and Chan, C. C., 2000, Spherical solidification by the enthalpy method and the heat balance integral method, Applied Mathematical Modelling, 24, pp. 45-53.

[137] Shih, Y. P., Chou, T. C., 1971, Analytical solution for freezing a saturated liquid inside or outside spheres, Chemical Engineering Science, 26, pp.1787-1793.

[138] Ismail, K. A. R. and Henriquez, J., R., 2000, Solidification of PCM inside a spherical capsule, Energy Conversion and Management, 41, pp. 173-187.

[139] M.C. Flemings, Solidification Processing, McGraw-Hill, New York, NY, 1974.

[140] Zhang, D., Harris, S.J., McCartney, D.G., Microstructure formation and corrosion behaviour in HVOF-sprayed Inconel 625 coatings, Material Science Engineering A, Vol 344 (01), 2003, pp. 45-56.

[141] S.L. Dai, J.-P. Delplanque, E.J. Lavernia, Microstructural characteristics of 5083 Al alloys processed by reactive spray deposition for net-shape manufacturing, Metal. Mater. Trans. A, Vol 29 (10), 1998, pp. 2597-2611.

[142] A.M. Ahmed, R.H. Rangel, V.V. Sobolev, J.M. Guilemany, In-flight oxidation of composite powder particles during thermal spraying, Int. Journal of Heat and Mass Transfer, Vol 44 (24), 2001, pp. 4667-4677.

[143] G. Pottlachera, H. Hosaeusa, B. Wilthana, E. Kaschnitzb, A. Seiftera: Thermophysikalische Eigenschaften von festem und flussigem Inconel 718, Thermochimica Acta 382 (2002) 255.

[144] S. Shakeri, S. Chandra, Splashing of molten tin droplets on a rough steel surface, International Journal of Heat and Mass Transfer 45 (2002) 4561-4575.

[145] J.U. Brackbill, D.B. Kothe, and C. Zemach, A continuum method for modelling surface tension, Journal of Computational Physics 100 (1992) 335-354.

[146] V.R. Voller and C. Prakash, A Fixed-Grid Numerical Modeling Methodology for Convection-Diffusion Mushy Region Phase-Change Problems, International Journal of Heat and Mass Transfer 30 (1987) 1709-1720

Appendix A

Turbulence Modelling

Based on the assumption of continuum the basics equations of fluid dynamics are derived according to the Reynolds's transport theorem. The integral form is given by the following equation:

$$\frac{d}{dt}\int_{V(t)} F(r,t)dV = \int_{V(t)} \frac{\partial F}{\partial t}dV + \int_{S(t)} F(\vec{u}\cdot\vec{n})dS \tag{A.1}$$

The dynamical behavior of fluid flow is completely described by the conservation of three quantities: mass, momentum and energy. An important feature of the fluid flow is the turbulence.

A.1 Flow Description

The complete system (in vector form) made by the integral expressions of the three conservation laws is:

$$\frac{\partial}{\partial t}\int_{\Omega} \vec{W}d\Omega + \int_{S}\left(\vec{F}_c - \vec{F}_v\right)dS = \int_{S}\vec{Q}dS \tag{A.2}$$

where Ω represents the control volume (fixed in space) and S is the surface that encloses Ω. The first term in the rhs, $\vec{W}$, has five components and is called the conservative variable vector. In the second surface integral, $\vec{F}_c$ is related to the convective transport of properties inside the fluid while $\vec{F}_v$ represents the viscous stress work and heat of diffusion: the former is called convective flux vector and the latter viscous flux vector. The vector $\vec{Q}$ includes the contribution of all volume sources (or sinks) due to external forces $\vec{f}_e$, heat sources $\dot{q}_H$ and work done by the external forces $W_{f_e} = \rho\vec{f}_e\cdot\vec{v}$. If $\vec{n}$ is the unit normal vector to the surface S (pointing outward of the volume) the component V of the flow velocity ($\vec{v}$) normal to the volume boundary can be expressed as:

$$V = \vec{v} \cdot \vec{n} = n_x u + n_y v + n_z w \tag{A.3}$$

The expanded expressions of the column vectors are:

$$\vec{W} = \begin{bmatrix} \rho \\ \rho u \\ \rho v \\ \rho w \\ \rho E \end{bmatrix} ; \vec{F}_c = \begin{bmatrix} \rho V \\ \rho u V + n_x p \\ \rho v V + n_y p \\ \rho w V + n_z p \\ \rho H V \end{bmatrix} ; \vec{F}_v = \begin{bmatrix} 0 \\ n_x \tau_{xx} + n_y \tau_{xy} + n_z \tau_{xz} \\ n_x \tau_{yx} + n_y \tau_{yy} + n_z \tau_{yz} \\ n_x \tau_{zx} + n_y \tau_{zy} + n_z \tau_{zz} \\ n_x \Theta_x + n_y \Theta_y + n_z \Theta_z \end{bmatrix} ; Q = \begin{bmatrix} 0 \\ \rho f_{ex} \\ \rho f_{ey} \\ \rho f_{ez} \\ \rho \vec{f}_e \cdot \vec{v} + \dot{q}_h \end{bmatrix} \tag{A.4}$$

The term τ is the viscous stress tensor (symmetric) and for a Newtonian (linear) viscous fluid is defined as:

$$\tau_{ij} = -p\delta_{ij} + \mu \left(\frac{\partial u_i}{\partial x_j} + \frac{\partial u_j}{\partial x_i} \right) + \delta_{ij} \lambda \vec{\nabla} \cdot \vec{v} \tag{A.5}$$

It is still not clear, how the coefficient of bulk viscosity λ can be considered: it appears to depend on frequency so that should not be a thermodynamic property. However, except for extreme condition (high temperature or pressure), the hypothesis done by Stokes (1845) is widely accepted.There are two phenomena in which bulk is relevant and are shock waves and sound wave absorption/attenuation and explicates the dependence of λ from μ as:

$$\lambda + \frac{2}{3}\mu = 0 \tag{A.6}$$

The first coefficient of viscosity (from now on *viscosity*) is calculated with the formula obtain by Sutherland from kinetic theory:

$$\mu \approx \mu_0 \left(\frac{T}{T_0} \right)^{3/5} \frac{T_0 + S}{T + S} \tag{A.7}$$

The constants are reference values (ex. for air T_0 =273 K and $\mu_0 = 1.71e{-}05 N \cdot s/m^2$). The vector Θ has the following components:

$$\begin{aligned} \Theta_x &= u\tau_{xx} + v\tau_{xy} + w\tau_{xz} + k\frac{\partial T}{\partial x} \\ \Theta_y &= u\tau_{yx} + v\tau_{yy} + w\tau_{yz} + k\frac{\partial T}{\partial y} \\ \Theta_z &= u\tau_{zx} + v\tau_{zy} + w\tau_{zz} + k\frac{\partial T}{\partial z} \end{aligned} \tag{A.8}$$

The external $\vec{f}_e$ forces (also called body forces) represent all the typology acting directly on the mass: examples are gravitational, Coriolis and buoyancy. The total

enthalpy H is given by the relation:

$$H = e + \frac{|v|^2}{2} + \frac{p}{\rho} \tag{A.9}$$

where e is the internal energy per unit of mass. For a perfect gas the internal energy is given by the equation:

$$e = \frac{p}{\rho(\gamma - 1)} \tag{A.10}$$

where γ is the specific heats ratio c_p/c_v. The equations system (A.2) is known as the Navier-Stokes equations.

A.2 RANS Equations

In order to explain the determinant aspects of turbulence, the differential form of the system (A.2) is used. Assuming that there are no sources or sinks, the differential Navier Stokes equations are:

$$\begin{aligned} &\frac{\partial \rho}{\partial t} + \frac{\partial}{\partial x_i}(\rho v_i) = 0 \\ &\frac{\partial}{\partial t}(\rho v_i) + \frac{\partial}{\partial x_i}(\rho v_j v_i) = -\frac{\partial p}{\partial x_i} + \frac{\partial \tau_{ij}}{\partial x_j} \\ &\frac{\partial}{\partial t}(\rho E) + \frac{\partial}{\partial x_j}(\rho v_j H) = \frac{\partial}{\partial x_j}(v_i \tau_{ij}) + \frac{\partial}{\partial x_j}\left(k \frac{\partial T}{\partial x_j}\right) \end{aligned} \tag{A.11}$$

where i and j are two index denoting the components of the tensor. The compact notation for the viscous stress tensor (according to Stokes hypothesis) is:

$$\tau_{ij} = 2\mu S_{ij} - \left(\frac{2\mu}{3}\right)\frac{\partial v_k}{\partial x_k}\delta_{ij} \tag{A.12}$$

According to the mass conservation in (A.11), the last term in the lhs disappears for incompressible flow. The strain rate tensor and the rotation rate tensor become:

$$S_{ij} = \frac{1}{2}\left(\frac{\partial v_i}{\partial x_j} + \frac{\partial v_j}{\partial x_i}\right); \quad \Omega_{ij} = \frac{1}{2}\left(\frac{\partial v_i}{\partial x_j} - \frac{\partial v_j}{\partial x_i}\right) \tag{A.13}$$

The basic concept in the statistical analysis is to decompose the flow u variables in a fluctuating u' part and its mean value $\bar{u}$:

$$u = \bar{u} + u' \tag{A.14}$$

In order to obtain the mean value, there are four possible averaging procedures:

1. time averaging (appropriate for statistically steady turbulence, the mean $\bar{u}$ value

varies only in space and not in time);

2. spatial averaging ($\bar{u}$ varies only in time);

3. ensemble averaging ($\bar{u}$ varies with both time and space);

4. density weighted averaging (known also as Favre decomposition, designed for compressible flow).

The first three methods are also known as Reynolds averaging: when the turbulent flow is stationary and homogeneous they are equivalent (ergodic hypothesis). The Favre method is necessary because, when density is fluctuating, an additional correlation between the variables arises: usually (for compressible flow) density and pressure are decomposed using the Reynolds approach while the other variables (velocity, temperature, enthalpy, internal energy...) undergo the density weighted procedure. The analytical expression of the four methods is respectively:

$$\begin{aligned} &a) \quad \bar{u}_i = \lim_{\Delta t \to \infty} \frac{1}{\Delta t} \int_t^{t+\Delta t} u_i dt; \qquad b) \quad \bar{u}_i = \lim_{\Omega \to \infty} \frac{1}{\Omega} \int_\Omega u_i d\Omega; \\ &c) \quad \bar{u}_i = \lim_{N \to \infty} \frac{1}{N} \sum_{n=1}^{N} u_i; \qquad d) \quad \overline{\overline{u_i}} = \frac{1}{\bar{\rho}} \lim_{\Delta t \to \infty} \frac{1}{\Delta t} \int_t^{t+\Delta t} \rho u_i dt; \end{aligned} \tag{A.15}$$

It is important to note that the main fluctuation term is zero, $\overline{u_i'} = 0$, while the average product of two fluctuating term not $\overline{\overline{u_i' u_j'}} \neq 0$. In case of Favre decomposition $\overline{\overline{\rho u_i}} = \bar{\rho}\overline{\overline{u_i}}$ and $\overline{\overline{\rho u_i''}} = 0$. The application of the Favre averaging to the equations (A.11) yields the so called RANS system:

$$\begin{aligned} &\frac{\partial \bar{\rho}}{\partial t} + \frac{\partial}{\partial x_i}\left(\bar{\rho}\overline{\overline{v_i}}\right) = 0 \\ &\frac{\partial}{\partial t}\left(\bar{\rho}\overline{\overline{v_i}}\right) + \frac{\partial}{\partial x_i}\left(\bar{\rho}\overline{\overline{v_j}}\,\overline{\overline{v_i}}\right) = -\frac{\partial \bar{p}}{\partial x_i} + \frac{\partial}{\partial x_j}\left(\overline{\overline{\tau_{ij}}} - \bar{\rho}\overline{\overline{v_i'' v_j''}}\right) \\ &\frac{\partial}{\partial t}\left(\bar{\rho}\overline{\overline{E}}\right) + \frac{\partial}{\partial x_j}\left(\bar{\rho}\overline{\overline{v_j}}\,\overline{\overline{H}}\right) = \frac{\partial}{\partial x_j}\left[\overline{\overline{v_i}}\left(\overline{\overline{\tau_{ij}}} - \bar{\rho}\overline{\overline{v_i'' v_j''}}\right)\right] + \frac{\partial}{\partial x_j}\left(k\frac{\partial \overline{\overline{T}}}{\partial x_j} - \bar{\rho}\overline{\overline{v_j'' h''}} + \overline{\overline{\tau_{ij} v_i''}} - \bar{\rho}\overline{\overline{v_j'' K}}\right) \end{aligned} \tag{A.16}$$

The equations in (A.16) have a new unknown quantity, called Reynolds-stress tensor:

$$\tau_{ij}^R = -\bar{\rho}\overline{\overline{v_i'' v_j''}} \tag{A.17}$$

The turbulent kinetic energy is given by the sum of the normal stresses:

$$\bar{\rho}\overline{\overline{K}} = \frac{1}{2}\bar{\rho}\overline{\overline{v_i'' v_i''}} \tag{A.18}$$

Usually, in transonic and supersonic flow, the term expressing the molecular diffusion, $\frac{\partial}{\partial x_j}\left(\overline{\overline{\tau_{ij} v_i''}}\right)$, and turbulent transport of K, $\frac{\partial}{\partial x_j}\left(\bar{\rho}\overline{\overline{v_j'' K}}\right)$, are neglected. The Reynolds-stress tensor is symmetric, so that after the averaging procedure we introduce six more

unknown terms in the equations describing the flow. Further there are other three unknowns coming from the components of the turbulent heat-flux vector $\frac{\partial}{\partial x_j}\left(\bar{\rho}\widetilde{v_j''h''}\right)$. In conclusion, nine more relations are necessary to close the problem.

A.3 Boussinesq Hypothesis

The basic approach to solve the closure problem belongs to Boussinesq. After noticing that the momentum transport in turbulent flow is enhanced by the mixing activity of the big energetic vortex, he theorized a linear relation between turbulent shear stress and mean rate of strain:

$$\tau_{ij}^{R} = -\bar{\rho}\widetilde{v_i''v_j''} = 2\mu_T\widetilde{S_{ij}} - \left(\frac{2\mu_T}{3}\right)\frac{\partial\widetilde{v_k}}{\partial x_k}\delta_{ij} - \frac{2}{3}\bar{\rho}\widetilde{K}\delta_{ij} \tag{A.19}$$

The proportionality μT coefficient is called turbulent viscosity, that is not a physical property of the fluid (like molecular viscosity), but it is function of the local flow condition. Especially in the simplest models, like algebraic ones, the last term in the right hand side is removed. According to the Reynolds analogy, the turbulent heat-flux vector can be modeled as:

$$\bar{\rho}\widetilde{v_j''h''} = -k_T\frac{\partial\widetilde{T}}{\partial x_j} \tag{A.20}$$

The turbulent thermal conductivity coefficient is given as a function of the turbulent Prandtl number (generally considered constant in the flow,$\approx$ 0.9 for air) and turbulent viscosity:

$$k_T = c_p\frac{\mu_T}{\mathrm{Pr}_T} \tag{A.21}$$

It is now clear, that when the value of the turbulent viscosity is known, the equations (A.16) are ready to be solved (the value of $\widetilde{K}$ in the last term on the rhs of (A.16) is usually neglected or deducted as a product of the specific model). However, although the simply formulation, Boussinesq hypothesis is not generally valid. It is not accurate in cases like sudden variation in the mean strain rate, secondary flows, separated flow, rotating and stratified flows. The limit of this approach relies on the assumptions of local equilibrium between turbulence and main strain and of system rotation independence.

A.4 Reynolds Stress Transport

The exact Reynolds stress transport description can be derived averaging the product of second equation in (A.11) and fluctuating quantity:

$$\begin{aligned}\frac{\partial \tau_{ij}^R}{\partial t} + \frac{\partial}{\partial x_k}\left(\overline{\overline{v}_k}\tau_{ij}^R\right) = &-\tau_{ik}^R\frac{\partial \overline{\overline{v}}_j}{\partial x_k} - \tau_{jk}^R\frac{\partial \overline{\overline{v}}_i}{\partial x_k} + \varepsilon_{ij} - \Pi_{ij} + \frac{\partial}{\partial x_k}\left[-\overline{\tau_{kj}v_i'' + \tau_{ki}v_j''} + C_{ijk}\right] \\ &+\bar{v}_i''\frac{\partial \bar{p}}{\partial x_j} + \bar{v}_j''\frac{\partial \bar{p}}{\partial x_i}\end{aligned} \tag{A.22}$$

where

$$\begin{aligned}\Pi_{ij} &= \overline{p'\left(\frac{\partial v_i''}{\partial x_j} + \frac{\partial v_j''}{\partial x_i}\right)}; \quad \varepsilon_{ij} = \overline{\tau_{kj}\frac{\partial v_i''}{\partial x_k} + \tau_{ki}\frac{\partial v_j''}{\partial x_k}} \\ C_{ijk} &= \bar{\rho}\overline{\overline{v_i''v_j''v_k''}} + \overline{p'v_i''}\delta_{jk} + \overline{p'v_j''}\delta_{ik}\end{aligned} \tag{A.23}$$

Because of the nonlinearity of the momentum conservation equation, additional unknowns (e.g.$\overline{\overline{v_i''v_j''v_k''}}$) are generated every time a higher moment (averaging level) is taken. The closure of equation (A.22) is done using empirical model.

A.5 The κ-ε model

This is the most used 2 equations model: a detailed description can be found in [95]. It relies on the solution of two additional transport equations, one for the turbulent kinetic energy $\overline{\overline{K}}$ and the other for its dissipation rate . For high value of the Reynolds number the transport of the turbulent kinetic energy can be written as:

$$\begin{aligned}\bar{\rho}\frac{\partial \overline{\overline{K}}}{\partial t} + \overline{\rho\overline{v}_j}\frac{\partial \overline{\overline{K}}}{\partial x_j} = &\tau_{ij}^R\frac{\partial \overline{\overline{v}}_i}{\partial x_j} - \overline{\tau_{ji}\frac{\partial v_i''}{\partial x_j}} + \frac{\partial}{\partial x_j}\left[\overline{\tau_{ji}v_i''} - \tfrac{1}{2}\overline{v_j''v_i''v_i''} - \overline{p'v_j''}\right] \\ &-\overline{v_i''}\frac{\partial \bar{p}}{\partial x_i} + \overline{p'\frac{\partial v_i''}{\partial x_i}}\end{aligned} \tag{A.24}$$

However, in the standard κ-ε a modelled expression is implemented, instead of (A.24):

$$\frac{\partial \bar{\rho}\varepsilon}{\partial t} + \frac{\partial \bar{\rho}\varepsilon\overline{\overline{v_j}}}{\partial x_j} = \left(-C_{\varepsilon 1}\rho\overline{v_i''v_j''}\frac{\partial \overline{\overline{v_i}}}{\partial x_j} - C_{\varepsilon 2}\bar{\rho}\varepsilon\right)\frac{\varepsilon}{K} + \frac{\partial}{\partial x_j}\left[\left(\bar{\mu} + \frac{\bar{\mu}_T}{\mathrm{Pr}_\varepsilon}\right)\frac{\partial \varepsilon}{\partial x_j}\right] \tag{A.25}$$

The exact equation that expresses the dissipation rate transport is extremely complicate and would introduce new terms with double and triple correlation between the fluctuating parts of flow variables. Further those quantities are almost impossible to measure at any level of accuracy, so that a closure model would be impossible. In order to overcome this difficulty an approximate expression for ε is used and is the same used for incompressible flows:

$$\frac{\partial \bar{\rho}\varepsilon}{\partial t} + \frac{\partial \bar{\rho}\varepsilon\overline{\overline{v_j}}}{\partial x_j} = \left(-C_{\varepsilon 1}\rho\overline{v_i'' v_j''}\frac{\partial \overline{\overline{v_i}}}{\partial x_j} - C_{\varepsilon 2}\bar{\rho}\varepsilon\right)\frac{\varepsilon}{K} + \frac{\partial}{\partial x_j}\left[\left(\bar{\mu} + \frac{\bar{\mu}_T}{\mathrm{Pr}_\varepsilon}\right)\frac{\partial \varepsilon}{\partial x_j}\right] \tag{A.26}$$

The eddy viscosity is:

$$\mu_T = C_\mu \rho \frac{K}{\varepsilon} \tag{A.27}$$

The closure coefficients are:

$$C_{\varepsilon 1} = 1.44;\ \ C_{\varepsilon 2} = 1.92;\ \ C_\mu = 0.09;\ \ P_k = 1.0;\ \ P_\varepsilon = 1.3; \tag{A.28}$$